Observational signatures of the simulated solar photosphere

ISBN 978-90-8570-714-1

Cover image: A woodcut from the graphic novel "The Sun" (page 32) by Flemish artist Frans Masereeel (1889-1972). The novel is an allegorical story of modern Icarus trying to reach the ideals symbolized by the Sun.

Observational signatures of the simulated solar photosphere

Waarnemingsdiagnostieken van de numeriek nagebootste zonnefotosfeer

(met een samenvatting in het Nederlands)

Proefschrift

ter verkrijging van de graad van doctor aan de Universiteit Utrecht op gezag van de rector magnificus, prof. dr. J. C. Stoof, ingevolge het besluit van het college voor promoties in het openbaar te verdedigen op donderdag 13 januari 2011 te 10.30 uur .

door

Nikola Vitas

geboren op 12 december 1974 te Belgrado, Servië

Promotoren: Prof. dr. C. U. Keller
Prof. dr. R. J. Rutten

Ever tried. Ever failed. No matter.
Try again. Fail again. Fail better.

— Samuel Beckett, *Worstward Ho*, 1983

Dedicated to the memory of Yugoslavia.

Contents

Chapter 1

Introduction

1.1 Setting the scene

The Sun is a star. It is a yellow dwarf, a rather normal small star in the middle of its life. Astronomically speaking, its spectral class is G2, and it belongs to the V class of luminosity. The Sun can roughly be divided into the solar interior and the solar atmosphere. The interior itself has three zones (from the center outward): the core, the radiative zone and the convection zone. The atmosphere is divided into the photosphere, the chromosphere and the corona. The solar wind blows out of the corona and fills the entire heliosphere that embeds the solar systems.

The photosphere is a narrow shell separating the interior from the outer atmosphere. The thickness of this shell is only a few hundred kilometers. The plasma in the photosphere changes from optically thick at the bottom to optically thin at the top, allowing the photons emitted in the photosphere to leave the Sun carrying the energy away. The major mode of energy transfer turns from convection in the layers below the photosphere to radiation in the solar atmosphere and beyond.

There are two important observational implications of the abrupt change in opacity. First, the edge of the visible solar disk is sharp: the radius of the photosphere (696 000 km) is commonly considered as the radius of the Sun[1]. Secondly, almost all of the radiation that leaves the Sun originates in the photosphere[2]. The temperature distribution of the photosphere thus determines the effective temperature of the star (5778 K).

The distance from the Earth to the Sun is 149 million kilometers on average, or one astronomical unit. From the perspective of life on Earth, this is sufficiently close to avoid global glaciation, and sufficiently far away to allow oceans to condense[3]. From

[1]For illustration, the ratio between the solar radius and the thickness of the photosphere is about ten times larger than the ratio between the size of an apple and the thickness of its skin.

[2]Mean, integrated radiative losses from the photosphere are $\sim 6.4\times10^{10}$ erg cm^{-2}s^{-1}; losses from all other layers are only $\sim 6\times10^{6}$ erg cm^{-2}s^{-1}.

[3]The habitable zone (zone in which life is possible) in the solar system extends between 0.95 and 1.37 astronomical units (Kasting et al. 1993).

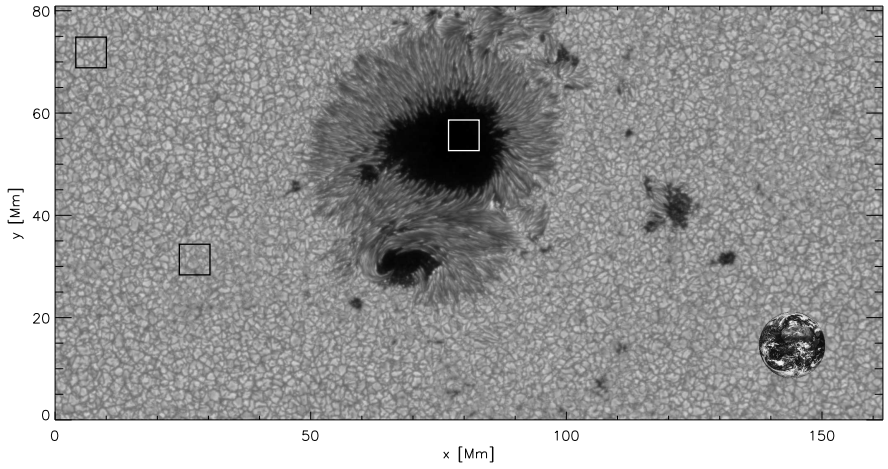

Figure 1.1: The solar photosphere observed in the G-band by the BFI instrument on Hinode. The image was taken on 21 May 2007. Three regions indicated by the boxes represent the quiet Sun (upper black box), faculae (lower black box) and umbra (white box). Enlarged images of the boxes are shown in Fig. 1.3. The Earth is shown in the bottom right corner for size comparison.

the perspective of an astronomer, the Sun is the only star in the Universe sufficiently close to allow direct observations of its surface details. At the highest currently available angular resolution, the linear dimension of the smallest detail of the solar photosphere that can be directly observed is around 35 km[4] (Solanki et al. 2010).

Figure 1.1 shows a continuum intensity image of the solar photosphere obtained with the Broadband Filter Imager (BFI) on the Hinode satellite (Suematsu et al. 2008). At any moment in time, the photosphere is largely or completely covered with a granular pattern of bright cells and intermittent, dark lanes. The pattern shows the top of the convection zone: the material in the bright granules is moving upward; the material in the dark lanes downward. The magnetic field associated with this pattern is weak (10-100 G, Nordlund et al. (2009)). However, magnetic activity in the Sun occasionally creates active regions that become visible in the continuum images as dark sunspots and bright faculae. The darkest central region of a sunspot is the umbra; it is surrounded by a brighter penumbra. The size of granules is around 1000 km, whereas the size of sunspots varies from several thousand kilometers (small sunspots without penumbrae, so-called pores) to several hundreds of thousands of kilometers (for the groups of sunspots in large active regions). On scales smaller than 1000 km, the continuum images show the large variety of fine structure, both in the quiet sun and in the active regions. The structure and evolution of the solar photosphere is mainly driven by the gas pressure. The layers higher up in the atmo-

[4]This is about the size of the province of Utrecht.

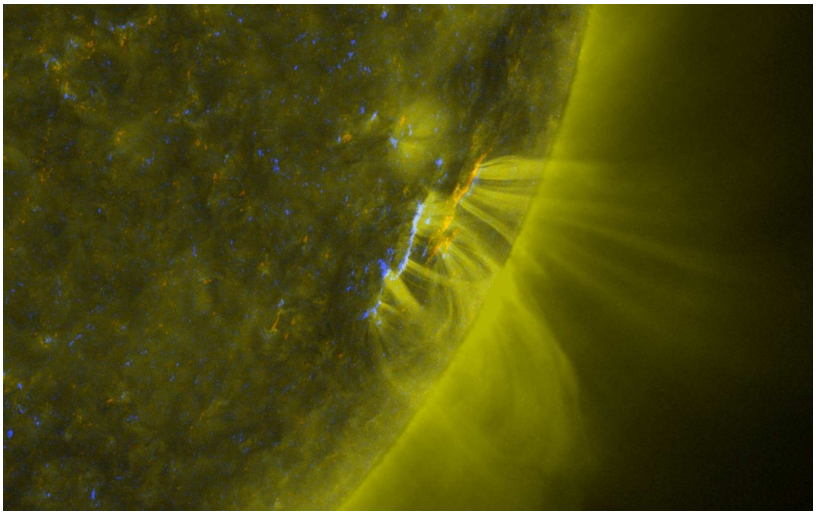

Figure 1.2: Composite image of photospheric magnetic fields (blue-orange patches) and an image of the outer atmosphere observed in the extreme UV. The data was recorded by the Solar Dynamics Observatory.

sphere, where the magnetic pressure becomes predominant, show more dynamics and a rather different organization of the plasma.

The photosphere is obviously the most observed part of the Sun owing to the number of photons originating in this layer. Nevertheless, the radiation coming from the photosphere is also important for indirectly sensing the layers below and above it. One example is the retrieval of the convection zone structure from the observed variations of photospheric spectral lines using the techniques of helioseismology. Another example is the reconstruction of the magnetic field in the chromosphere and corona by extrapolation of the observed photospheric magnetic field. In space weather studies the first step is naturally the analysis of the photospheric images: many important phenomena have their roots or leave fingerprints in the photosphere. Figure 1.2 shows a composite image of the magnetic field measured in the photosphere (yellow and blue patches) and the nearly simultaneous image of the outer atmosphere. The arcs in the higher layers are clearly connected to the photospheric concentrations of the magnetic field.

High-resolution studies of the solar photosphere also offer a guideline for studying the photospheres of other stars that have an outer convection zone.

Although observations provide an enormous amount of data, to describe physical conditions of the photosphere we also need suitable algorithms to retrieve physical parameters from the observables. Moreover, we need theoretical models to give us deeper insight into the physical processes on the scales and in the layers that cannot be observed directly. The inversion of observations and the forward modeling are often

viewed as distinct approaches. However, these approaches are complementary and, indeed, inseparable. Before I present the outline of this thesis, I will briefly describe the basic concepts of these two approaches and summarize recent achievements.

1.2 Forward modeling and inversions

1.2.1 Forward modeling

The first step of *forward modeling* consists of building a model atmosphere that obeys the basic laws of physics and has as few free parameters as possible. In practice, a model atmosphere is a stratification of several physical parameters that are discretized on a given grid. The physical parameters of a model are usually the components of the magnetic field and velocity vectors and two thermodynamic variables suc as the density and the internal energy. The grid can be one-, two- or three-dimensional (1D, 2D, 3D). Models in 2D and 3D usually result from time-dependent simulations[5].

Over the last twenty years, the rapid development of computing facilities enabled highly realistic 3D simulations of the solar atmosphere. Progress was made in the relevant physics that is incorporated in the computer codes, but also in the numerical and programming schemes. For example, the MURaM[6] code used extensively in this thesis solves the non-ideal magnetohydrodynamic (MHD) equations on a Cartesian grid including a realistic equation-of-state and non-local and non-gray radiative transfer. The code has a parallel design based on domain decomposition that enables excellent performance on supercomputers with a distributed memory architecture.

In the second step of the forward modeling, the model atmosphere is used for the detailed radiative transfer computation of the spectrum. The result of this computation represents an ideal *synthetic observation*. In the case of 3D simulations, its spatial resolution is determined by the size of the horizontal simulation grid, whereas its spectral resolution is virtually unlimited. In addition, the ideal synthetic observation is not contaminated by noise or any kind of stray light. The third step of the forward modeling is the degradation of the ideal synthetic observations to mimic the limited angular and spectral resolution, and noise present in real observations.

The amount of information in the synthetic observations is significantly smaller than in the model atmosphere. In the second step the reduction of the information content has three sources. (1) The levels below the surface do not directly contribute to the emergent intensity. (2) The stratification of the physical quantities along the line-of-sight is smeared and translated into the wavelength dependence of the intensity due to the intrinsic integro-differential nature of the radiative transfer equation. (3) The information contained in several physical quantities of the model is combined into the computed intensity for four polarization states. In the third step of the

[5] A a model corresponding to one instance in the simulation sequence is also refered to as a *simulation snapshot*.

[6] MPS/University of Chicago Radiative MHD (Vögler & Schüssler 2003, Vögler et al. 2005).

forward modeling, the reduction is due to the intrinsic limits of the instrument, but also due to the imperfections of the instrument and seeing in the Earth's atmosphere.

The three steps of the forward modeling can be summarized as:

$$\begin{aligned} \text{PL + A + FP} &\xrightarrow{1^{\text{st}}\text{step}} M(P(x,y,z,t)) \\ &\xrightarrow{2^{\text{nd}}\text{step}} O(S(x',y',\lambda,t')) \\ &\xrightarrow{3^{\text{rd}}\text{step}} O'(S(x',y',\lambda,t')), \end{aligned} \tag{1.1}$$

where PL+A+FP represent physical laws, approximations and free parameters, $M(P(x,y,z,t))$ is the 3D time-dependent model of the physical variables P, S specifies the polarization state, and $O(S(x',y',\lambda,t'))$ and $O'(S(x',y',\lambda,t'))$ are the ideal and degraded synthetic observations.

1.2.2 Inversions

Two types of measurements exist: direct measurements and remote-sensing. Almost all measurements in astrophysics belong to the remote-sensing category. Remote-sensing consists of observations and inversions of the observations. *The inversions of observations* (or simply *inversions*) thus represent a very broad and diverse class of techniques and methods whose aim is to give a physical meaning to the observations. Mathematically speaking, an inversion technique should aim to reverse eq.(1.1), hence to start from the real observation $o'(S(x',y',\lambda,t'))$ and to retrieve the empirical model $m(P(x,y,z,t))$. However, this is an impossible goal in the case of solar observations because of the inevitable reduction in the information content related to the nature of the radiative transfer as well as observational limits. Instead, the inversion problem in this case has to be described as

$$M_0 + \text{AI} + o'(S(x',y',\lambda,t')) \rightarrow \{p_1, p_2, \dots p_n\} \tag{1.2}$$

where M_0 stands for an a-priori model with a number of free parameters, AI for additional information (physical approximations, geometry of the structures present in the atmosphere, see Ruiz Cobo, 2007), $o'(S(x',y',\lambda,t'))$ for the real observation and $\{p_1, p_2, \dots p_n\}$ for a set of values of the free parameters of the model M_0. In principle, within the error limits, the values p can be derived from the model $M(P(x,y,z,t))$ but they do not provide a unique description of the model. This difference is important when a strategy for comparison between the theoretical model and the observations has to be selected.

1.2.3 Comparison and interpretation

Two possibilities exist for comparing theoretical simulations and observations. First, the synthetic observation O' can be compared to the real one o'. Secondly, the set of parameters p retrieved by inversions of o' can be compared to the set of parameters

derived from the synthetic observation O' derived from the model M. The first method obviously tests the model, whereas the second tests both the model and the inversion technique. However, examples can be found in the literature where the values of the parameters p inferred from the real observations are compared quantitatively to the theoretical model That often leads to misinterpretation of the observations.

Three points have to be stressed. First, any conclusion derived from the comparison between the theoretical models and observations inevitably includes all the approximations and assumptions of the forward modeling and all the uncertainties of the measurement. Secondly, the o' can take the form of many different observational signatures. If the result of comparison is positive in one signature, it does not imply a positive result in another. Thirdly, a unique recipe for comparison between the theoretical models and the simulations does not exist.

The comparison between synthetic and real observations is an important too to validate the theoretical models. Once it is proven that a theoretical model reproduces the basic observational signatures correctly, the model can be used for interpreting or predicting other observational signatures. For example, once a simulation of the quiet Sun provides the correct rms contrast of the granulation (Danilovic et al. 2008), center-to-limb variation of the continuum intensity (Pereira et al. 2009a) and satisfactory agreement between the profiles averaged over many snapshots with an atlas of the solar spectrum (Asplund et al. 2000a), it can be used to study the solar granulation in detail and to predict the signatures of small-scale phenomena that are not fully resolved in observations (e.g. Chapter 4 of this thesis).

1.3 Numerical simulations of the solar photosphere

Since the first hydrodynamic simulations of the solar convection (Nordlund 1982) the fraction of the relevant physics incorporated in the simulations of the photosphere has gradually increased. The early history of convection simulations is summarized by Spruit (1997). However, several recent breakthroughs in numerical simulations produced a true avalanche of new results.

The simulation of Stein & Nordlund (1998) provided a detailed picture of the quiet sun convection and enabled comparison with observations. Asplund et al. (2000a) employed the results of the simulation of Stein & Nordlund to explain the profile shapes, wavelength shifts and asymmetries of iron spectral lines. Asplund et al. (2000b), Asplund (2000) used the same simulation to determine the photospheric abundance of iron. Following the same line of research, Asplund et al. (2004) showed that the abundance of oxygen is significantly lower when using the results of 3D simulations instead of 1D semi-empirical models leading to the so-called *oxygen crises*. The recent improvement of this family of simulations reproduced the center-to-limb variation of the quiet-Sun continuum intensity and photospheric spectral lines remarkably well(Pereira et al. 2009a). The effect of convective motions on small-scale magnetic elements has been studied in detail in the simulation of Stein &

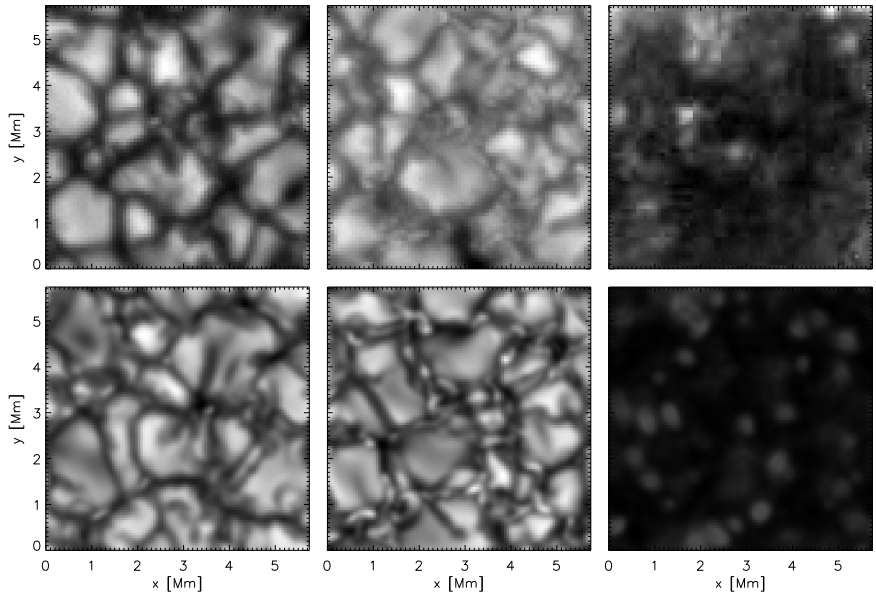

Figure 1.3: Quiet Sun granulation (*left*), faculae (*center*) and a sunspot umbra (*right*). The enlarged versions of the boxes in Fig.1.1 (*upper row*) are compared to the synthetic observations computed from the MURaM simulations (*lower row*). These three simulations are used in Chapters 3, 4 and 5 of this thesis.

Nordlund (2006).

Another family of numerical simulations of the solar photosphere rely on the MURaM code (Vögler & Schüssler 2003, Vögler 2004, Vögler et al. 2005), which puts more emphasis on highly realistic modeling of magneto-convection. Results of the quiet-Sun and plage simulations are described by Vögler (2003). Vögler (2005) studied the interactions between magnetic fields, convective flows and the radiation field in detail. The simulations of Vögler (2003) have been extensively used to synthesize various observational signatures (Shelyag et al. 2004, Khomenko et al. 2005a, Asensio Ramos 2009) and to test different inversion techniques (Khomenko et al. 2005b, Khomenko & Collados 2007a,b, Asensio Ramos 2009, Orozco Suárez et al. 2007a, 2010a,b). The reversed granulation phenomenon observed in the wings of the Ca II K&H lines is successfully reproduced in the quiet-Sun simulations of Leenaarts & Wedemeyer-Böhm (2005) using the CO^{5}BOLD code and of Cheung et al. (2007b) using MURaM.

The quiet sun simulations at high resolution demonstrated that a turbulent local dynamo can operate near the solar surface (Vögler & Schüssler 2007). In addition, Schüssler & Vögler (2008) showed that the local-dynamo mechanism produces predominantly horizontal fields in the low photosphere in agreement with Hinode ob-

servations. Danilovic et al. (2008) used snapshots from the same simulation to show that the granular root-mean-square contrast in the simulations matches the values found in the Hinode measurements. This result has been confirmed by Wedemeyer-Böhm & Rouppe van der Voort (2009) using simulations performed independently with CO^{5}BOLD. Further comparison between the local dynamo simulations and observations (Danilovic et al. 2010) provided additional support for the local-dynamo mechanism.

The MURaM simulation of faculae has been employed by Keller et al. (2004) to explain the facular brightening toward the solar limb. The explanation is confirmed by Carlsson et al. (2004) and Steiner (2005) using different codes. In addition, Shelyag et al. (2007) studied the spectropolarimetric signatures of the facular simulations.

Another event simulated with high realism is magnetic flux emergence. Cheung et al. (2007a, 2008) showed that a magnetic flux tube can rise from the near-surface layers of the convection zone into the photosphere causing distinct changes in the granular pattern and magnetic field distributions comparable with Hinode observations. Yelles Chaouche et al. (2009) has analysed the observational signatures of rising-flux-tube simulations in detail. The advection of the flux tube from the convection zone into the outer atmosphere and the formation of the magnetic loops has been simulated by Martínez-Sykora et al. (2008, 2009), Tortosa-Andreu & Moreno-Insertis (2009) and Stein et al. (2010).

Significant progress has also been made in modeling sunspots. Schüssler & Vögler (2006) simulated an isolated sunspot umbra and explained the nature of bright umbral dots. The recent work of Rempel et al. (2009b,a) reproduced full-scale sunspots with an umbra, a penumbra and the surrounding granulation. Yet another step forward was made by Cheung et al. (2010a). Their impressive large-scale simulation shows the birth of an active region with a pair of sunspots at the locations where a gigantic flux-tube penetrates the solar surface.

This list of recent results in the physics of the solar photosphere is long, but far from complete. It must also be emphasized that significant progress has been achieved in related fields. Carlsson (2009) reviewed the current status and perspectives of models that extend into the chromosphere. The progress of local helioseismology and the numerical simulations used in that field is summarized in the recent review of Gizon et al. (2010). Finally, the past decade has witnessed rapid progress in modeling of convection and atmospheres of stars of other spectral classes (e.g. Kochukhov et al. (2007) for A stars; Freytag & Höfner (2008) for AGB stars; Freytag et al. (2010) for M and brown dwarfs).

1.4 Outline of the thesis

The five studies collected in this thesis present different examples of comparing theory and observations of the solar photosphere. They all employ different models and analyze different observational signatures. Chapter 2 is based on semi-empirical 1D models, whereas Chapters 3 to 6 use the results of four 3D simulations performed with

the MURaM code (plage, quiet-Sun, isolated umbra and isolated umbra extended in height). The simulation of the isolated umbra extended in height in Ch. 6 has never been published before. In Chapters 2, 3 and 4, I analyze unpolarized spectral lines (In I 4511.3 Å, Mn I 5394.7 Å and Fe I 6301.5 Å); in Ch. 5 continuum intensities in the visible and near-infrared; in Ch. 6 full Stokes vectors of Fe I 6301.5 Å and Fe I 6302.5 Å. The study presented in Ch. 2 is the only abundance analysis in this thesis. The line formation in Ch. 3 is analyzed exclusively at the simulation resolution as the studied phenomena depend on the activity cycle and cannot be directly reproduced from the high-resolution simulations of the photosphere. In Ch. 4 we discuss the synthetic observations at the SP/SOT Hinode resolution; in Ch. 6 at the resolution of SP/SOT and at the resolution of CRISP at the SST. In Ch. 5 the synthetic observations are spatially and spectrally smeared to mimic real observations with different telescopes and different resolutions.

On the solar abundance of indium. The motivation for the study presented in Chapter 2 is the large photospheric overabundance of indium (relative to the meteoritic value) reported by several authors. We employ semi-empirical 1D models of a sunspot to synthesize the single spectral line of indium found in the solar spectrum. The synthetic profile is compared to the profile in a spectral atlas of a sunspot umbra. A good match between the profile synthesized in the umbral model using meteoritic abundance with the atlas is obtained after the synthetic profile has been artificially contaminated with stray light. We conclude that the line observed in the quiet-Sun spectrum and used in previous determinations of the indium abundance has been misidentified, while the actual photospheric abundance is consistent with the meteoritic value.

Explanation of the activity sensitivity of Mn I 5394.7 Å. The unusual activity sensitivity of the photospheric Mn I 5394.7 Å spectral line is the topic of Chapter 3. Narrow photospheric lines loose their activity sensitivity due to their thermal and granular Doppler broadening. However, we show that the hyperfine structure of Mn I 5394.7 Å dominates over other broadening mechanisms in this line and causes the observed intensity variation with the solar cycle. The activity sensitivity of the Mn I line is thus purely photospheric contrary to some other hypotheses. This conclusion is demonstrated using 1D models and verified with 3D simulations of faculae.

Fast horizontal flows and their spectroscopic signatures In Chapter 4, we study the granular supersonic flows in a quiet-Sun MHD simulation. We synthesize Stokes I profiles of Fe I 6301.5 Å from the snapshots at different viewing angles and select the lines-of-sight sampling the supersonic horizontal flows. At the spatial resolution of the simulation, the profiles show large variations in their asymmetries depending on the viewing angle and the particular flow properties. At the Hinode resolution, the profiles are significantly smoother, though distinct signatures of supersonic motion

remain visible. The synthetic observations are used to test a recently proposed criterion for the detection of these flows. We conclude that the criterion is indeed applicable, though it is sensitive to ad-hoc parameter choices.

Observational signatures of a simulated sunspot umbra In Chapters 5 and 6 we study the observational signatures of simulations of an isolated sunspot umbra. In Ch. 5, we demonstrate that the morphology, size and contrast of umbral dots in the synthetic continuum disk-center observation is consistent with recent high-resolution observations. Away from disk center, the morphology of umbral dots changes depending on their orientation relative to the center-limb direction. We suggest that, at the resolution of the next generation of solar telescopes, upflows associated with umbral dots can be observed in continuum intensity images near the limb. Along with the morphology of umbral dots, we also evaluated the center-to-limb variation of the umbral intensity at different wavelengths. The result is discussed in the context of available observations.

The research presented in Ch. 6 is motivated by recent observational attempts to reconstruct the structure of the velocity and magnetic fields associated with umbral dots. Four different spectropolarimetric diagnostics are applied to the observations in Fe I 6301.5 Å and Fe I 6302.5 Å synthesized from the simulated umbra. The results of the different diagnostics are compared, and an optimum strategy for measuring the magnetic field and the velocity in the umbra is suggested. In the layers where the spectral lines are sensitive to the physical parameters of the atmosphere, the structure of umbral dots reconstructed from the synthetic observations is consistent with the simulations and with actual observations. In the layers above and below, the retrieved values are not reliable, thus the actual structure of the umbral dots in those layers cannot be retrieved from observations in the Fe I 6302 Å lines.

1.5 Future directions

The examples of the detailed comparison between the theory and observations presented in this thesis offer solutions to particular problems associated with the solar photosphere. However, some questions remain unanswered, and some new questions are raised. I list some topics for future research.

- Does the normal granulation cause all observed supersonic horizontal flows or is there an additional mechanism? And if so, how can one distinguish between supersonic horizontal flows that are caused by different mechanisms?

- How much do the supersonic horizontal flows contribute to the heating in the upper photosphere and, consequently, to the brightening in the images of the reversed granulation?

- Do high-resolution observations of magnetic elements in other lines broadened by hyperfine structure support our explanation of activity sensitivity of Mn I 5394.7 Å?
- How high do the upflows in umbral dots extend? Are they related to chromospheric umbral flashes?
- What is the transition between the magneto-convection regime in faculae and umbra? Do umbral dots represent an isolated phenomenon or do they belong to a family of similar phenomena?
- How can inversion techniques be combined to provide better and more efficient determinations of physical parameters in umbrae, but also in the quiet sun?
- Is it possible to retrieve the fine umbral structure in the upper photosphere using information from simultaneous measurements in many spectral lines?

Furthermore, a guideline for the detailed comparison between numerical 3D simulations and high-resolution observations of the solar photosphere is presented in this thesis. It should help with the assimilation of observational data in future MHD codes as well as the application of MHD constraints in future codes for inversion of spectropolarimetric observations.

Chapter 2

On the solar abundance of indium

N. Vitas, I. Vince, M. Lugaro, O. Andriyenko, M. Gošić and R. J. Rutten*

Abstract

The generally adopted value for the solar abundance of indium is over six times higher than the meteoritic value. We address this discrepancy through numerical synthesis of the 451.13 nm line on which all indium abundance studies are based, both for the quiet-sun and the sunspot umbra spectrum, employing standard atmosphere models and accounting for hyperfine structure and Zeeman splitting in detail. The results, as well as a re-appraisal of indium nucleosynthesis, suggest that the solar indium abundance is close to the meteoritic value, and that some unidentified ion line causes the 451.13 nm feature in the quiet-sun spectrum.

*Published in *Monthly Notices of the Royal Astronomical Society*, 384, 370 (2008)

2.1 Introduction

The solar abundance of indium is controversial because its generally accepted value significantly exceeds the meteoritic value. At a factor of six difference, this remains the largest unexplained discrepancy between meteoritic and solar abundance values. In this paper we address this problem by considering the nucleosynthesis of indium and through indium line synthesis for the quiet solar photosphere and sunspot umbrae including hyperfine structure in detail.

The meteoritic indium abundance is $A_{\rm In}^{\rm m} = 0.80 \pm 0.03$ (Lodders 2003 and references therein) where $A_{\rm In} \equiv \log(n_{\rm In}/n_{\rm H}) + 12$ with $n_{\rm In}$ and $n_{\rm H}$ the indium and hydrogen particle densities, respectively. Table 2.1 summarises the determinations of the solar indium abundance in the literature. All measurements are based on a single, very weak feature in the quiet-sun spectrum at $\lambda = 451.1307$ nm which is commonly identified as one of the In I resonance lines. The initial result of Goldberg et al. (1960) was based on an erroneous oscillator strength. The other three determinations scatter around $A_{\rm In}^{\odot} = 1.6$, the value listed in the compilation of Asplund et al. (2005). The 0.8 dex discrepancy with the meteoritic value cannot be explained by the usual uncertainties of abundance determination such as line strength measurement, imprecise atomic data and solar modeling deficiencies.

The origin of elements heavier than Fe is mostly attributed to neutron-capture processes (see Meyer 1994, for a review). *Slow* neutron capture (the *s* process) occurs for relatively low neutron densities ($\simeq 10^7$ cm^{-3}), while *rapid* neutron capture (the *r* process) occurs for relatively high neutron densities ($> 10^{20}$ cm^{-3}). Allen (1978) analysed the Sn/In abundance ratio. He found that 'no combination of *r*- or *s*-process products even remotely resembling those which generally predict the solar system abundances very successfully can give Sn/In as low as 1.4' (which results from taking $A_{\rm In}^{\odot} = 1.71$).

Recently, Gonzalez (2006b) suggested that because of its low condensation temperature (536 K, Lodders 2003), indium may have been depleted in chondritic meteorites to an abundance much smaller than the solar one. However, we note that, e.g., thallium has a similar condensation temperature (532 K, Lodders 2003) and a similar meteoritic abundance (0.78 ± 0.04) whereas its well-determined photospheric abundance (0.9 ± 0.2.) is only slightly higher than the meteoritic one. In a sequel paper Gonzalez (2006a) studied the indium abundance in a sample of 42 sun-like stars of which five are known to host planets. He found a strong negative correlation between the [In/Fe] and [Fe/H] logarithmic abundance ratios. This trend is much steeper than the comparable relation for europium, which is a pure *r*-process element. However, one would expect a less steep trend for indium because it received contributions both from the *s*- and the *r*-processes.

In this paper we once again scrutinize the solar indium abundance, paying specific attention to indium nucleosynthesis (Sect. 2.2.1), indium line identification and appearance in the solar spectrum (Sect. 2.2.2), and indium line synthesis accounting for hyperfine structure both for quiet sun and sunspot umbrae (Sect. 2.2.3). The conclusion is that, after all, the solar indium abundance is likely to be close to the

Table 2.1: $A^{\odot}_{\rm In}$ determinations

Authors	$A^{\odot}_{\rm In}$	Specified error
Goldberg et al. (1960)	1.16	
Lambert et al. (1969)	1.71	
Grevesse & Sauval (1998)	1.66	0.15
Bord & Cowley (2002)	1.56	0.20

Table 2.2: Sn/In from different nucleosynthetic processes.

	Sn/In
s process (classical)[a]	39
s process (classical)[b]	46
s process (stellar)[a]	38
s process (GCE)[c]	34
r process (weak)[d]	32
r process (main)[d]	6
solar value [e]	2.51
meteoritic value [f]	20.42

[a]Arlandini et al. (1999), [b]Simmerer et al. (2004), [c]Travaglio et al. (2004), [d]Kratz et al. (2007), [e]Asplund et al. (2005), [f]Lodders (2003)

meteoritic value.

2.2 Analysis

2.2.1 Nucleosynthesis and the Sn/In ratio

In this section we update the analysis of Allen (1978) considering the latest models for the origin of heavy elements. The indium and tin abundances in the solar system are believed to have received contributions from both the *s* and the *r* processes, with roughly 30 and 60 per cent *s*-process production to In and Sn, respectively (e.g. Travaglio et al. 2004, Arlandini et al. 1999).

In Table 2.2 we present the Sn/In ratios associated to the most recent models of the *s* and the *r* processes. For the *s*-process we list different estimates of the ratio: two of them were derived using the classical approach for the *s* process, where abundances are calculated via a parametric model, and another via the stellar model, where the building up of *s*-process abundances is modeled inside an asymptotic giant branch (AGB) stars (see Arlandini et al. 1999 for details). A further, more realistic description of the solar system distribution of abundance is given by models of the galactic chemical evolution (GCE), where yields from different generations of AGB stars are integrated in order to build up the solar system abundances at the time and location of the formation of the sun. In all descriptions the Sn/In ratios remain

very similar among the *s*-process estimates because during the *s*-process, and far from nuclei with closed neutron shells, *s*-process abundances are determined by the $\sigma_A N_A \simeq constant$ rule, where σ_A is the neutron capture cross section of isotope with atomic mass A, and N_A its abundance during the *s*-process. The σ_A of In and Sn are determined with roughly 10 per cent uncertainties[1] and thus the Sn/In ratios from the *s* process have small nuclear uncertainties.

For the *r* process we take the recent parametric models of Kratz et al. (2007). Two *r*-process components, generated assuming different neutron densities, are introduced to build up the *r*-process abundances in the solar system: the 'weak' *r* process produces elements up to tellurium, and the 'main' *r* process produces elements from tellurium up to the actinides. The Sn/In ratio for the main *r* process component is equal to 6 (Table 2.2), which confirms the estimate of Allen (1978) made using the simple argument that the *r* process would produce similar yields for close-by isotopes and that In and Sn have 1 and 6 stable isotopes that can be produced by the *r* process, respectively.

Finally, we note that recent *r*-process calculations indicate that the situation is likely to be much more complex, with several different components involved (Farouqi 2005). However, also in these more recent models no component with Sn/In < 8 is found (K.-L. Kratz, personal communication).

2.2.2 Indium in the solar spectrum.

The 451.13 nm line. The resonance line of In I at 451.13 nm ($5p^2P_{3/2} \rightarrow 6s^2S_{1/2}$) is the only indium line that has been identified in the solar spectrum. Figure 2.1 shows this region in the disc-centre quiet-sun Kitt Peak spectral atlas of Wallace et al. (1998b). The small frame in Fig. 2.1 is enlarged in Fig. 2.2 and shows the region around 451.13 nm in detail. There are no significant differences with the Jungfraujoch atlas (Delbouille et al. 1973). In the Kitt Peak atlas the relatively strong feature at 451.1155 nm is attributed to Ti I, but this identification does not agree with Kurucz & Bell (1995) whose table instead suggests a line of Cr I at 451.1134 nm.

Other lines that may be expected in this narrow region are listed in Table 2.3 and indicated in Fig. 2.2. The lines of Ru I and Sc II are fully blended by the wing of the line at $\lambda = 451.1155$ nm. The four Fe II lines have high excitation energy (> 10 eV) and low oscillator strengths, hence they should not be present in the quiet-sun spectrum. There are three candidate blends of the In line due to Sc I, V I and Sm I. All three belong to elements with a large nuclear spin, so that hyperfine splitting must be taken into account. Scandium and vanadium have only one stable isotope with $I = 7/2$. Samarium has 7 stable isotopes, two (^{147}Sm and ^{149}Sm) having nonzero nuclear spin $I = 7/2$. Unfortunately, data on hyperfine splitting are only available for the V I line (Kurucz & Bell 1995). The ground level of Sm I is split in 7 sub-levels, giving numerous weak transitions as indicated in Fig. 2.2. The Sm I 451.1317 nm line,

[1] http://nuclear-astrophysics.fzk.de/kadonis/

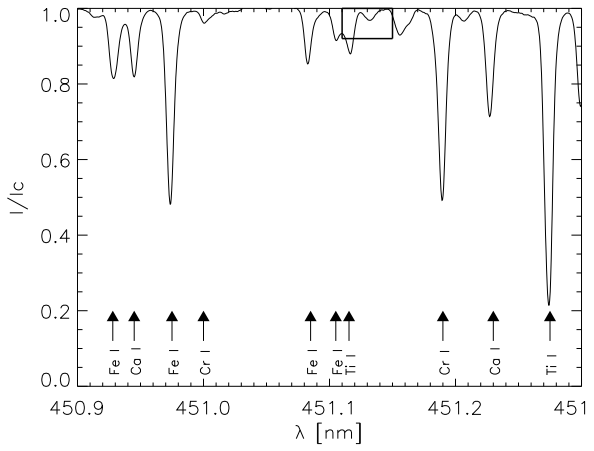

Figure 2.1: The spectral region around 451.13 nm in the Kitt Peak atlas of the quiet-sun disc-centre photosphere. The intensity scale is normalised by the adjacent continuum value. The arrows specify line identifications copied from the Kitt Peak atlas.

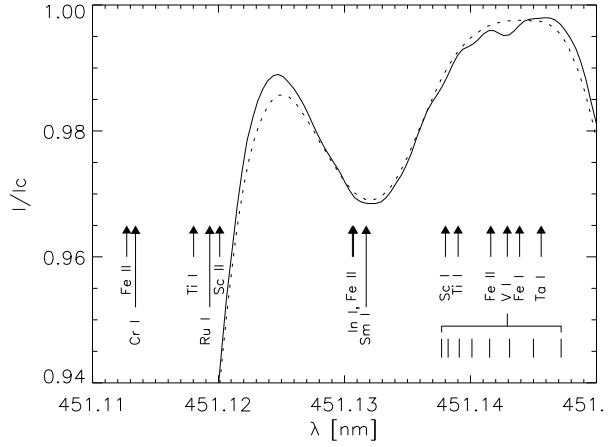

Figure 2.2: Enlargement of the frame in Fig. 2.1. Solid: Kitt Peak atlas. Dotted: Jungfraujoch atlas. The candidate lines of Table 2.3 are indicated by arrows. Positions of hyperfine components of the V I line are also indicated.

attributed to Sm II by Gonzalez (2006a), is one of them. The In I line is not affected by the Ta I 451.1456 nm line as it is sufficiently far away.

The umbral spectrum in the Kitt Peak Sunspot Atlas of Wallace et al. (2000) shows a much stronger line at λ = 451.13 nm as illustrated in Fig. 2.3. Its core is clearly split in two strong components, with the red peak slightly stronger than the blue

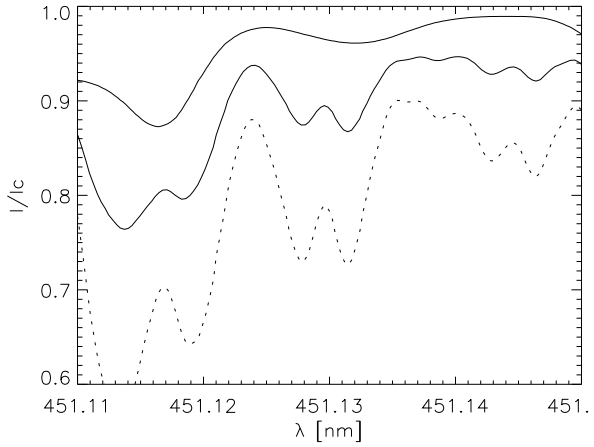

Figure 2.3: The spectral region around the 451.13 nm line in the Kitt Peak sunspot atlas. Lower solid curve: sunspot spectrum. Dotted: after subtraction of 60 per cent straylight. Upper solid curve: Kitt Peak quiet-sun atlas for comparison. Each atlas profile is normalised to its own adjacent continuum.

Table 2.3: Possible blends of In I 451.13 nm. The data are from Kurucz & Bell (1995) (K&B) and Kupka et al. (1999) (VALD).

Element	λ [nm]	E_l [eV]	log(gf)	Reference
Fe II	451.1127	11.31	−2.811	K&B
Cr I	451.1134	3.17	−2.366	K&B
Ti I	451.1170	0.50	−3.300	VALD
Ru I	451.1193	1.69	−1.070	K&B
Sc II	451.1201	7.87	−1.694	K&B
Fe II	451.1306	10.60	−3.338	K&B
In I	451.1307	0.27	−0.213	K&B
Sm I	451.1317	0.50	−0.013	K&B
Sc I	451.1380	1.85	−1.193	K&B
Ti I	451.1390	3.29	−4.076	VALD
Fe II	451.1416	11.29	−2.063	K&B
V I	451.1429	2.13	−1.520	K&B
Fe II	451.1439	10.72	−3.405	K&B
Ta I	451.1456	0.70	−1.730	K&B

one. Gonzalez (2006a) attributes them to Zeeman splitting of the In I line. The upper solid curve in Fig. 2.3 represents the photospheric spectrum as a reference. The dotted curve is the observed umbral spectrum with sizable correction for straylight following Zwaan (1965), setting its amount to 60 per cent (i.e., the observed spectrum

Table 2.4: Candidate lines of In I and In II and their appearance in the Kitt Peak atlas (K, Wallace et al. 1998b) and the SUMER atlas (S, Curdt et al. 2001). The wavelengths and oscillator strengths are from CD-ROM No. 23 of Kurucz & Bell (1995).

Ionisation stage	λ [nm]	$\log(gf)$	E_l [eV]	Atlas	Comment
I	303.9357	−0.143	0.000	K	In the wing of Fe I 303.9321 nm
I	325.6087	0.170	0.274	K	In the wing of a strong line at λ = 325.613 nm
I	325.8559	−0.620	0.274	K	Between two strong lines
I	410.1765	−0.550	0.000	K	In the core of Hδ
I	451.1307	−0.213	0.274	K	The only identified line of In I
I	684.7440	−1.200	3.022	K	No line
I	690.0132	−1.510	3.022	K	Strong telluric line
II	78.3892	−3.092	0.000	S	No line
II	91.0951	−1.777	0.000	S	No line
II	92.7324	−3.170	0.000	S	Heavily blended
II	158.6450	0.393	0.000	S	Very weak unidentified line

contains 60 per cent photospheric and 40 per cent umbral light). The choice of this value is discussed below. The broad triple-peaked feature to the right of the indium line is likely due to the hyperfine splitting of the V I line indicated in Fig. 2.2.

Other indium lines. Table 2.4 lists the other candidate lines of neutral and singly ionised indium. The other component of resonance multiplet (1) is $5p^2P_{1/2} \rightarrow 6s^2S_{1/2}$ at λ = 410.1765 nm. It is located close to the centre of the Balmer Hδ line and is not recognizable in the quiet-sun Kitt Peak atlas. The other indium lines are absent or completely blended or located in spectral regions that are not covered by the present solar atlases.

Since indium is mostly ionised (over 99 per cent throughout the photosphere assuming the Saha distribution), one would expect that the In II resonance line at 158.6 nm should be the strongest in the solar spectrum, but also this line is not clearly present in the SUMER atlas of Curdt et al. (2001).

2.2.3 Synthesis of the solar In I 451.13 nm line

Model atom. Oscillator strengths for the indium transitions were taken from Kurucz & Bell (1995) except for the 451.13 nm line for which Table 2.5 lists various values from the literature. We adopted the value of Fuhr & Wiese (2006). The indium hyperfine structure must be taken into account because the nuclear spin of In is $I = 9/2$. Values of the magnetic dipole (A) and electric quadrupole (B) constants of the hyperfine interaction for the lower and upper levels of the In I multiplet 1 were taken from Jackson (1981) and Zaal et al. (1978).

Table 2.5: Values of $\log(gf)$ for In I 451.13 nm transition.

$\log(gf)$	A [10^8 s^{-1}]	Source
−0.308	0.806	L
−0.265	0.890	M
−0.213	1.003	K&B
−0.206	1.019	F&W
−0.167	1.115	C&B
−0.360	0.715	G&K W
−0.590	0.421	G&K D

L = Lambert et al. (1969), M = Morton (2000), K&B = Kurucz & Bell (1995), F&W = Fuhr & Wiese (2006), C&B = Corliss & Bozman (1962), G&K = Gurtovenko & Kostyk (1989a) (W = value determined from the equivalent width, D = from the line depth)

Table 2.6: Hyperfine components of In I 451.13 nm with r the intensity of the component relative to the strongest one and $\Delta\lambda$ the wavelength shift from the centre of gravity.

F_l	F_u	r	$\Delta\lambda$ [pm]
5	4	33.84	3.14
4	4	50.76	2.38
3	4	53.84	1.93
6	5	100.00	−1.38
5	5	50.76	−2.58
4	5	18.46	−3.34

The level splitting was evaluated from:

$$\Delta E_F = \frac{C}{2}A + \frac{3C(C+1) - 4I(I+1)J(J+1)}{8I(2I-1)J(J-1)}B,$$

where $C = F(F+1) - J(J+1) - I(I+1)$, $F = J+I, J+I-1, \ldots, |J-I|$, and J is the electronic angular momentum (e.g., Sobelman 1992). For the upper level with $J = 1/2$ only the first member in the Hamiltonian of the hyperfine interaction is present and is split into two sublevels ($F = 4, 5$), while the upper level is split into four sublevels ($F = 3$, 4, 5, 6). Hence, the selection rule ($\Delta F = -1, 0, 1$) implies that 6 hyperfine components are expected in the 451.13 nm transition. Relative intensities of these components were calculated from Wigner $6j$ coefficients assuming analogy with LS coupling (cf. Sobelman 1992). Table 2.6 specifies the resulting hyperfine structure components. Indium has two stable isotopes, but since the ratio of their abundances is ^{115}In : ^{113}In = 95.7 : 4.3, the second isotope can be neglected.

Quiet-sun profile synthesis. The radiative transfer code MULTI 2.2 of Carlsson (1992) was used for detailed synthesis of the In I 451.13 nm line profile.

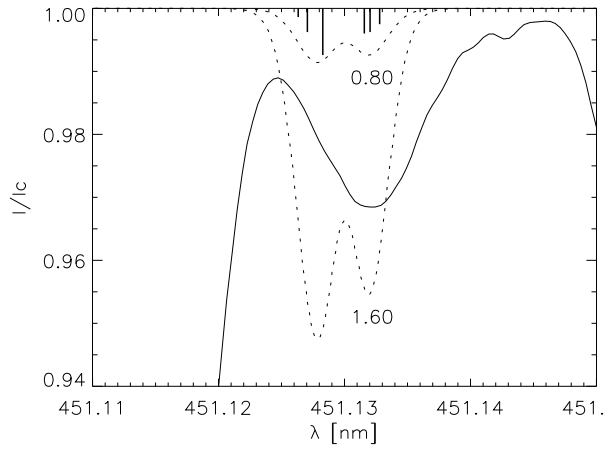

Figure 2.4: Synthetic profiles (dotted) of the In I 451.13 nm line for $A_{\rm In}^{\odot} = 0.80$ and 1.60 compared with the Kitt Peak atlas (solid). The vertical bars at the top specify the wavelengths and relative intensities of the hyperfine components. They produce double peaks in the synthetic profiles.

As commonly done in solar abundance analysis (see Rutten 2002), we assume local thermodynamical equilibrium (LTE) and the HOLMUL model of Holweger & Müller (1974) for the solar photosphere, including its microturbulence stratification. For the oscillator strength of In I 451.13 nm we take the value of Fuhr & Wiese (2006). We computed line profiles both for the meteoritic abundance value $A_{\rm In}^{\rm m} = 0.80$ and for the solar value $A_{\rm In}^{\odot} = 1.60$ listed by Asplund et al. (2005). The resulting profiles are compared with the observed quiet-sun profile in Fig. 2.4. The vertical bars specify the hyperfine structure components. It is obvious that neither computation fits the observed feature at all.

Figure 2.5 illustrates the steps that are required to force a better match. The synthesized line was convoluted with a broad Gaussian profile with FWHM = 1.58 pm (1 pm = 10^{-3} nm), much wider than the instrumental broadening of the FTS spectrometer at Kitt Peak, and it was shifted redward over $\Delta\lambda = 2.35$ pm. With these ad-hoc measures a reasonable fit is obtained for indium abundance $A_{\rm In}^{\odot} = 1.50$ (Fig. 2.5) but the assumptions made to obtain it are not justified. We conclude that the solar line at this wavelength in the quiet-sun spectrum is probably not due to indium.

Umbral profile synthesis. We use the appearance of the 451.13 nm line in the sunspot spectrum to provide an independent estimate. In order to include Zeeman splitting we estimate the magnetic field to be 3000 G from the Ti I 464.52 nm line observed at the same day as the In I 451.13 nm in the Kitt Peak Sunspot atlas. Lines with hyperfine structure split in complex manner in the presence of magnetic fields (Landi degl'Innocenti 1975). We employed the code by Landi degl'Innocenti (1978). The result is shown in Fig. 2.6. We assume that the orientation of the magnetic field

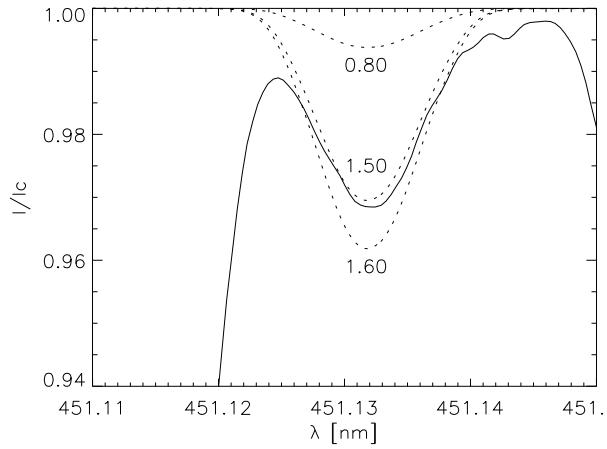

Figure 2.5: Synthetic profiles (dotted) of the In I 451.13 nm line compared with the Kitt Peak atlas (solid) after ad-hoc convolution and wavelength shift.

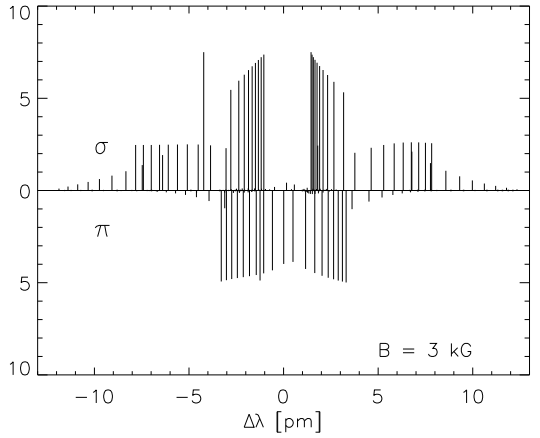

Figure 2.6: Combined Zeeman and hyperfine splitting of the In I 451.13 nm line a magnetic field of 3 kG.

in the observed sunspot is purely vertical and maintains only the σ components.

For the model atmosphere we use the semi-empirical umbral model M of Maltby et al. (1986). Figure 2.7 compares the synthesized profile assuming the meteoritic abundance value $A_{\rm In}^{\rm m} = 0.80$ to the observed profile assuming 60 per cent straylight. The dotted curve is the computed profile after convolution with instrumental broadening corresponding to the FTS resolution of one million. No ad-hoc wavelength shift is applied. The match is quite satisfactory, including the separation and amplitude

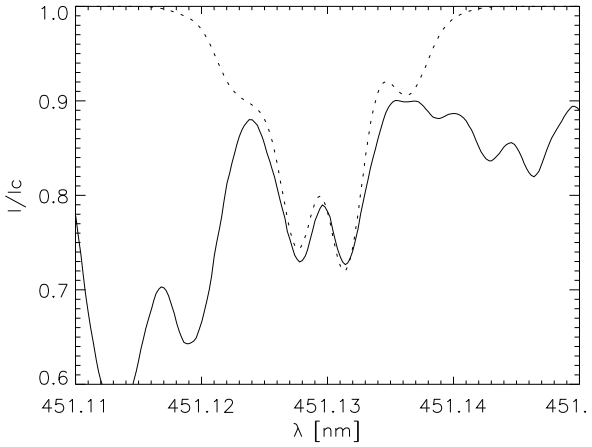

Figure 2.7: Profiles of the In I 451.13 nm line in the sunspot spectrum. Solid: Kitt Peak sunspot atlas with 60 per cent straylight subtraction. Dotted: computed profile with instrumental broadening corresponding to the Kitt Peak FTS (Gaussian with FWHM = 0.47 pm).

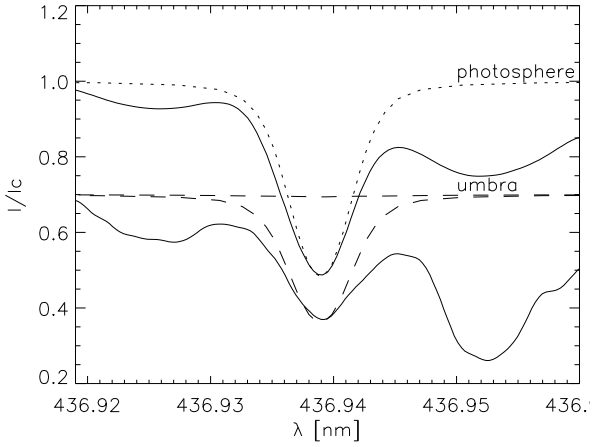

Figure 2.8: Profiles of the Fe II 436.9 nm line in quiet-sun (upper pair) and umbral spectra (lower curves). The latter are shifted down over 0.3 of the relative intensity scale. Solid: observed profiles from the Kitt Peak photosphere and sunspot atlases. Dotted: computed profile from the HOLMUL model. Dashed: computed profiles using the Maltby M model without and with 65 per cent photospheric straylight addition.

ratio of the two peaks.

Obviously, the good match in Fig 2.7 requires 60 per cent straylight subtraction. We first argue and then show that this is a reasonable value. In their introduction

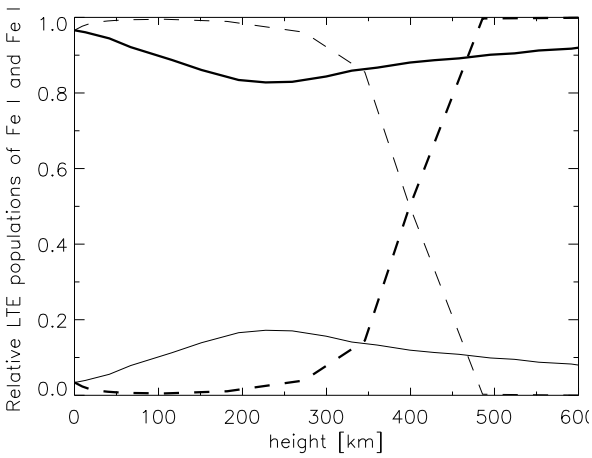

Figure 2.9: The relative LTE populations of neutral (thin curves) and once-ionised iron (thick) in the HOLMUL photosphere model (solid) and the Maltby M umbral model (dashed).

to the Kitt Peak sunspot atlas, Wallace et al. (2000) already remark that photospheric straylight fully dominates the violet part of the spectrum. Its contribution scales as λ^{-2} (see Staveland 1970) so that it is still large in the blue around 450 nm. Berdyugina et al. (2003) used 25 per cent to fit their TiO lines at 705 nm which translates into 61 per cent at 450 nm with the λ^{-2} dependence. In order to quantify this estimate more precisely, we have performed spectral synthesis of the Fe II 436.9 nm line chosen because it is the closest Fe II line without Zeeman splitting to the In I 451.13 nm line. The oscillator strength of the line was adapted to obtain a good fit to the photospheric spectrum as shown in Fig. 2.8. The lower curves demonstrate that the Fe II line vanishes in the intrinsic umbral spectrum and only appears due to the contribution by photospheric stray light. The good fit to the atlas spectrum was obtained with 65 per cent addition of the computed photospheric spectrum. The reason why the Fe II line vanishes in the umbral spectrum is shown in Fig. 2.9. The dominant ionisation stage is Fe II in the photosphere, but Fe I throughout the low umbral photosphere. Fe II lines that are weak in the photospheric spectrum can therefore not appear in the intrinsic umbral spectrum.

2.3 Discussion

Our update in Sect. 2.2.1 of the analysis of Allen (1978) did not change the conclusion that there is no combination of nucleosynthetic processes that can produce a Sn/In ratio as obtained using the most recent solar values, while the chondritic ratio can be easily accounted for. This is a strong indication that the solar abundance of indium cannot be much higher than the meteoritic value. This also suggested by the absence

of the In II resonance line at 158.6 nm.

Furthermore, Fig. 2.4 shows that standard line synthesis including hyperfine structure does not fit the observed profile for either the high or the low abundance value. In contrast, its appearance in the sunspot spectrum is well reproduced, including hyperfine Zeeman splitting, using the low meteoritic abundance value (Fig. 2.7) and assuming a reasonable straylight fraction (60 per cent) and umbral field strength of 3000 G.

These results together suggest that the line at 451.13 nm in the quiet-sun spectrum is not due to indium but to some other species. It should be from an ion with low ionisation energy of the neutral stage since the line disappears in the sunspot spectrum (cf. Fig. 2.9). The observation by Gonzalez (2006a) of significant trends of the assigned indium abundance with $T_{\rm eff}$ and [Fe/H] in a sample of stars cooler than the sun suggests that the unidentified transition should have high excitation energy. The best possible candidate in the list of Gonzalez (2006a) would be the Sm II line, but as noted in Sect. 2.2.2 this is actually a resonance transition of Sm I.

Finally, an alternative explanation of the In I 451.13 nm line formation might be NLTE effects. In particular, the appearance of the 451.13 nm line as emission line in the spectra of long-period variables during the downward modulation phase was explained already by Thackeray (1937) as optical pumping between Hδ and a In I line at 410.1 nm which shares its upper level with In I 451.13 nm. However, we this mechanism does not operate at all in the deep solar photosphere where the formation of the hydrogen Balmer lines is close to LTE (cf. Fig. 30 of Vernazza et al. 1981).

In conclusion, we suggest that the solar indium abundance is close to the meteoritic value as evidenced in the sunspot spectrum, whereas the feature at 451.13 nm in the quiet-sun spectrum remains unidentified and is likely to be an ion line at high excitation energy from a species with low first ionisation energy.

Acknowledgments

We are indebted to Stevan Djeniže for drawing our attention to the solar indium abundance and to Pit Sütterlin and Karl-Ludwig Kratz for discussions. We thank the referee for suggesting the analysis in Fig. 2.8. This research project has been supported by a Marie Curie Early Stage Research Training Fellowship of the European Community's Sixth Framework Programme under contract number MEST-CT-2005-020395. ML is supported by NWO (VENI fellow). The Ministry of Science of Serbia partially supported this research (project 'Stellar and Solar Physics', Contract No. 146003).

Whenever a theory appears to you as the only possible one, take this as a sign that you have neither understood the theory nor the problem which it was intended to solve.
— Karl Popper

Chapter 3

Explanation of the activity sensitivity of Mn I 5394.7 Å

N. Vitas, B. Viticchiè, R. J. Rutten and A. Vögler*

Abstract

There is a long-standing debate why the Mn I 5394.7 Å line in the solar irradiance spectrum brightens more at higher activity than other photospheric lines. The claim that this is caused by spectral interlocking to chromospheric emission in the Mg II h & k lines is disputed. In this paper we settle this issue, using classical one-dimensional modeling for demonstration and modern three-dimensional MHD simulation for verification and analysis. The unusual sensitivity of the Mn I 5394.7 Å line to solar activity is due to its excessive hyperfine structure. This overrides the thermal and granular Doppler smearing through which the other, narrower, photospheric lines lose such sensitivity. We take the nearby Fe I 5395.2 Å line as example of the latter, and analyze the formation of both lines in detail to demonstrate and explain the granular Doppler brightening which affects all narrow photospheric lines. Neither the chromosphere nor Mg II h & k emission play a role, nor is it correct to describe the activity sensitivity of Mn I 5394.7 Å in terms of plage models with outward increasing temperature contrast. The Mn I 5394.7 Å line represents a proxy diagnostic of strong-field magnetic concentrations in the deep solar photosphere comparable to the G band and the blue wing of Hα, but not a better one than these. The Mn I lines are more promising as diagnostics of weak fields in high-resolution Stokes polarimetry.

*Published in *Astronomy & Astrophysics*, 499, 301 (2009)

3.1 Introduction

The formation of the solar Mn I 5394.7 Å line has received considerable attention with respect to its global sensitivity to solar activity, based on the extensive observations of this line by Livingston and coworkers and Vince and coworkers (Livingston & Wallace (1987); Vince & Erkapic (1998); Danilovic & Vince (2004, 2005); Malanushenko et al. (2004); Danilovic et al. (2005); Vince et al. (2005a,b) Livingston et al. (2007)).

In hindsight, the first publications of interest were by Thackeray (1937), who pointed out that the violet wing of Mg II k (line center k_3 at 2795.53 Å) overlaps with Mn I 2794.82 Å and so may produce optical pumping of that and other Mn I lines in stellar spectra, and by Abt (1952), who pointed out that the unusual widths of the Mn I lines in the solar spectrum are due to hyperfine structure. These two points remained key ones in almost all later work on solar Mn I lines, effectively dividing it into two categories. The first addresses the unusual sensitivity of the Mn I 5394.7 Å line to global solar activity, mostly debating the forceful claim by Doyle et al. (2001) that this is explained by Thackeray's Mg II k coincidence operating in the solar chromosphere. This activity response is also our subject here, but we establish and explain that neither Mg II k nor the chromosphere has anything to do with it.

We first summarize the observations and discuss these conflicting views in the remainder of this introduction, and then demonstrate that Abt's hyperfine structure is the key agent through reducing spectral-line sensitivity to thermal and convective Dopplershifts outside magnetic concentrations.

The second category of solar Mn I papers concentrates on quantitative measurement of weak internetwork fields exploiting the intricate line-center opacity variation with wavelength imposed by hyperfine structure to disentangle weak- and strong-field signatures in Stokes polarimetry (López Ariste et al. (2002, 2006a,b) Asensio Ramos et al. (2007); Sánchez Almeida et al. (2008)). This potentially more fruitful topic is not addressed here.

3.1.1 Activity modulation

Livingston's inclusion of the Mn I 5394.7 Å line in his long-term full-disk "Sun-as-a-star" line profile monitoring from 1979 onwards was prompted by Elste, who suggested that their large hyperfine structure makes the Mn I lines less sensitive to the questionable microturbulence parameter than other ground-state neutral-metal lines that may serve as temperature diagnostic (Elste & Teske (1978); Elste (1987)). Livingston found that this line is the only photospheric line in his full-disk monitoring that exhibits appreciable variation with global activity, in good concert with the Ca II K full-disk intensity variation. Its equivalent width in the irradiance spectrum varies by up to 2% (Livingston & Wallace (1987)). Figure 16 in the overview paper of Livingston et al. (2007) displays the variation as line-depth fraction of the full-disk continuum intensity (plotted in reverse and therefore labeled "central intensity" in the caption).

The same data are plotted as relative line depth in Fig. 2 of Danilović et al. (2007),

overlaid by a theoretical modeling curve. The relative line-center intensity increases by about 2% from cycle minimum to maximum, slightly more than the corresponding decrease in equivalent width.

Vince et al. (2005a) used observations at the Crimea Observatory including Zeeman polarimetry to measure the changes in Mn I 5394.7 Å between plages with different apparent magnetic flux density. They found that the line weakens with increasing flux, as concluded already by Elste & Teske (1978) and Elste (1987).

3.1.2 Chromospheric interpretation

Doyle et al. (2001) gave their paper the title "*Solar Mn I 5432/5395 Å line formation explained*", which we paraphrase in our title above. They used NLTE computations to claim that these Mn I lines are sensitive to optical pumping through the overlap coincidence with Mg II k noted by Thackeray. The demonstration consisted of displaying Mn I profiles for different solar atmosphere models with and without taking Mg II h & k into account. The models imposed ad-hoc variations in the onset heights of the temperature rises that described the chromosphere and the transition region. Appreciable variation of the two Mn I lines was found and attributed to the spectral interlocking.

However, closer inspection undermines this claim. Large changes, of the order of 30% in line depth, were shown to occur when Mg II h & k and all other blanketing lines were not taken into account. However, this is not a relevant test since deletion of the ultraviolet line haze invalidates the ionization equilibrium evaluation for any species of intermediate ionization energy. The same test would be as dramatic for any optical Fe I line. The changes in the profile of Mn I 5394.7 Å between the cases of Mn I – Mg II coupling and no coupling were negligible, unless the model possessed a very deep-lying chromosphere and transition region, producing unrealistic high peaks in Ca II H & K and Mg II h & k. Even then, the computed brightening of Mn I 5394.7 Å amounted to only a few percent, which must be further diluted through a filling factor of the order of 0.01 to represent the contribution of active-Sun plage in full-disk averaging.

Doyle et al. (2001) added no further analysis (such as specification of NLTE departures, radiation fields, source functions) but only verbal explanation, literally: "*because of the huge absorption in Mg II, the local continuum for the Mn I UV lines changes. There is less flux and thus fewer photons to be absorbed and hence the ground level is consequently more populated*". Actually, in such coupling the quasi-continuous Mg II wing opacity increases the height of photon escape and enforces LTE behavior to considerably larger heights than the Mn I lines might maintain on their own, up to the height where Mg II k photon loss causes source function departure from the Planck function. Thus, due to the wavelength coincidence, departures from LTE set in only at exceptionally large height, and these anyhow represent a much larger fractional population change for the upper level than for the ground level, affecting the source function far more than the opacity.

The concept of optical pumping, also part of the paper's verbal explanation, is

perhaps more easily grasped. Super-Planckian radiation in a pumped transition may overpopulate its upper level and so induce super-Planckian source function excess and apparent brightening in subordinate lines from the same upper level, in this case Mn I multiplet 4, and perhaps also in other lines through upper-level coupling. Such pumping was earlier demonstrated for a variety of emission lines in the extended wings of Ca II H & K (e.g., Canfield (1971); Rutten & Stencel (1980); Cram et al. (1980)), but these arise through coupling to more deeply escaping super-Planckian radiation outside the H & K wings, an entirely different mechanism. No such pumping affects the Mn I lines, nor did it operate in the computation of Doyle et al. (2001) who obtained slight brightening of Mn I 5394.7 Å for deep-lying chromospheres only from their effect on the outer tail of the contribution function.

In any case, the computation of Doyle et al. (2001) was intrinsically wrong because the Mn I multiplet UV1 lines do not coincide with the Mg II h & k cores but are located $\Delta\lambda = 0.7$ Å away in their wings, of which the intensity is considerably overestimated when assuming complete redistribution instead of partially coherent scattering – one of the worst features in the solar spectrum to adopt this simplification for. In the computations, deep onsets of the chromospheric temperature rise resulted in bright extended Mg II h & k wings, but in reality the independent radiation fields in the inner wings decouple from the Planck function already in the photosphere (Milkey & Mihalas (1974)). This error is obvious when comparing the computed profiles in Fig. 3 of Doyle et al. (2001) with observed Mg II h & k profiles, such as the pioneering ones by Lemaire & Skumanich (1973) in which even the strongest plage emission exhibits deep k_1 minima at $\Delta\lambda = \pm 0.5$ Å from line center. The Mn I 2794.82 Å line actually appears as an absorption dip within the deep Mg II k_1 minimum, not only in the reference spectrum in Fig. 1 of Staath & Lemaire (1995) but also in all Mg II h & k profiles displayed in their Fig. 2, and it remains located within the k_1 dip even in all limb spectra in their Fig. 11, outside as well as inside the limb. These spectra represent summation of chromospheric Mg II k emission along the tangential line of sight, so that the peak widths represent a maximum. Therefore, everywhere across the solar surface Mn I 2794.82 Å lies in the deep k_1 dip, which has a sub-Planckian source function due to coherent scattering and does not respond at all to chromospheric activity.

In summary, although both the Mn I 5394.7 Å line and the peaks in Mg II h & k are observed to track solar activity, the blending of the Mn I UV1 lines into the opaque Mg II h & k wings does not imply a viable causal relationship, nor was one proven by Doyle et al. (2001). The Mn I UV1 lines are too far outside the chromospheric h & k emission peaks to be affected by these. In addition, the Mn I multiplet 1 lines are formed at much smaller height (Vitas & Vince (2007)).

3.1.3 Photospheric interpretation

The height of formation estimates for the optical Mn I lines of Gurtovenko & Kostyk (1989b) and Vitas (2005) suggest that these lines are purely photospheric. Observational evidence that Mn I 5394.7 Å is indeed photospheric has been collected by Vince

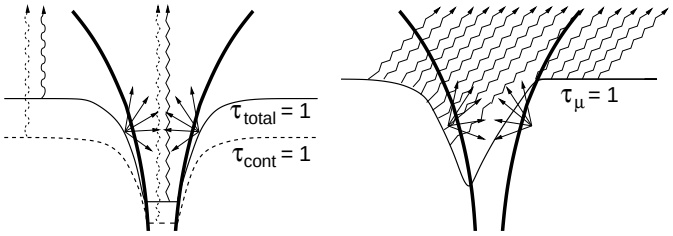

Figure 3.1: Schematic G-band bright-point enhancement in a magnetic concentration, portrayed here as a vertical cut through an idealized, flaring fluxtube (thick curves) containing strong field, embedded in a field-free quiet photosphere. *Left*: in radial viewing the Wilson depression due to magnetic-pressure evacuation deepens the photon escape layer characterized as $\tau = 1$ surface to deep below the outside surface. The magnetic concentrations are much cooler there than the subsurface surroundings due to suppressed convection, but hotter than the outside photon escape layer due to the large depth and hot-wall irradiation, and have flatter temperature gradients. The correspondingly larger degree of dissociation of the CH molecules that make up the G band cause a yet larger effective Wilson depression in this spectral feature, producing larger brightness enhancement than in the continuum. *Right*: In near-limb viewing the same lack of opacity along the slanted line of sight causes deeper, facular "bright-stalk" sampling of hot granules behind magnetic concentrations. From Rutten (1999); see also Fig. 1 of Spruit (1976).

et al. (2005b), who showed that Mn I 5394.7 Å bisectors show characteristic photospheric shapes and center-limb behavior, and by Malanushenko et al. (2004) who compared spectroheliogram scans in Mn I 5394.7 Å and the nearby Mn I 5420.4 Å line with other lines and a magnetogram. The Mn I lines show network bright, closely mimicking the unsigned magnetogram signal which is purely photospheric.

The arguments above against a chromospheric interpretation and these observational indications of photospheric formation together suggest that the propensity of Mn I lines to track solar activity in their line-center brightness may be akin to the contrast brightening that network and plage show in the G band. We therefore summarize G-band bright-point formation, where "bright points" stands for kilo-Gauss magnetic concentrations. Their enhanced photospheric brightness in continuum intensity and further contrast increase in G-band imaging has been studied extensively and is well understood, both for their on-disk appearance as filigree and near-limb appearance as faculae, in terms of the magnetostatic fluxtube paradigm of Zwaan (1967) and Spruit (1976) which is schematized in Figure 3.1. A brief review of the subsequent literature was given in the introduction of de Wijn et al. (2005); the latest numerical verifications of this concept are the MHD simulations of Keller et al. (2004), Carlsson et al. (2004), and Shelyag et al. (2004). The upshot is that the G band shows magnetic concentrations with enhanced contrast because its considerable line opacity lessens through molecular dissociation within the concentrations while its LTE formation implies good temperature mapping. Similarly, the extended blue wing of Hα brightens in magnetic concentrations through reduced collisional broadening

plus LTE formation (Leenaarts et al. (2006b)).

Hence, for manganese we seek a property that enhances the effect of reduction of line opacity in fluxtubes over that in comparable lines such as from Fe I, enhancing the corresponding "line gap" phenomenon. A first consideration is that Mn I 5394.7 Å is relatively sensitive to temperature, as pointed out already by Elste & Teske (1978), because it originates from a neutral-metal ground state. Resonance lines do not suffer from the cancellation in LTE response to temperature increase that chracterizes lines from excited levels because for these temperature increases are masked by higher-up formation where they sample lower temperatures (see Fig. 4 of Leenaarts et al. (2005)). In addition, Mn I 5394.7 Å is also a somewhat forbidden intersystem transition which causes its source function to obey LTE more closely than for higher-probability lines. However, both these properties are unlikely to play an important role since Malanushenko et al. (2004) found that Mn I 5420.4 Å, a member of multiplet 4 at 2.14 eV excitation, brightens about as much in network.

The obvious remaining property which makes Mn I lines differ from others is their large hyperfine structure. How can this cause unusual brightness enhancement in strong-field magnetic concentrations? Elste & Teske (1978) pointed out that it lessens sensitivity to the "turbulence" that was needed to explain other lines in classical one-dimensional modeling of the spatially-averaged solar spectrum. The infamous "microturbulence" and "macroturbulence" parameters were supposed to emulate the reality of convective and oscillatory inhomogeneities that make a solar-atlas line profile represent a spatio-temporal average over widely fluctuating and Doppler-shifted instantaneous local profiles. Lines that should be deep and narrow are so smeared into shallower average depressions. However, lines that are already wide intrinsically by hyperfine broadening suffer less shallowing by being less sensitive to Dopplershifts. The culprit may therefore not be the hyperfine structure of Mn I lines but rather the heavy hydrodynamic smearing of all the other, narrow lines that occurs in the granulation outside magnetic concentrations. We test this idea below, finding it is correct. The analysis so becomes a study of general Fe I line formation rather than specific Mn I line formation.

We first demonstrate this idea with classical one-dimensional modeling in Sect. 3.3.1, verify it by means of three-dimensional MHD simulation in Sect. 5.2, and add explanation by analyzing the simulation in Sect. 3.3.3. The next section presents our assumptions, input data, and methods.

3.2 Assumptions and methods

3.2.1 Line selection

We started this project with a wider line selection but for the sake of clarity and conciseness we limit our analysis to Mn I 5394.7 Å and the neighboring Fe I 5395.2 Å line, following the example of Danilović et al. (2007) who show and modeled the activity modulation of both lines in parallel. The Fe I 5395.2 Å line serves here

Table 3.1: Line parameters.

Line	Mn I	Fe I
Wavelength [Å]	5394.677	5395.215
Transition	$a^6S_{5/2} - z^8P^0_{7/2}$	$z^5G^0_2 - g^5F_1$
Excitation energy [eV]	0.0	4.446
Oscillator strength ($\log gf$)	−3.503	−1.74
Landé factor	1.857	0.500
$\mathcal{A}_{\rm lower}$	−2.41	–
$\mathcal{A}_{\rm upper}$	18.23	–
Ionization energy [eV]	7.44	7.87
Abundance ($\log N_{\rm H} = 12$)	5.35	7.51

as prototype for all comparable narrow lines. The line parameters are given in Table 3.1. The Mn I hyperfine structure constants $\mathcal{A}$ come from Blackwell-Whitehead et al. (2005). All other values were taken from the NIST database[1].

3.2.2 Line synthesis

We perform line synthesis in the presence of magnetic fields with the code of Sánchez Almeida et al. (2008), which solves the radiative transfer equation for polarized light in a given one-dimensional atmosphere via a predictor-corrector method. It yields the full Stokes vector, but we only use the intensity here. The code includes evaluation of the Zeeman pattern for lines with hyperfine structure using the routine of Landi degl'Innocenti (1978). This pattern depends on the magnetic field and on the hyperfine structure constants, the quantum numbers of the upper and lower level, the relative isotopic abundance, and the isotope shifts. The splitting depends on the hyperfine structure constants $\mathcal{A}$ and $\mathcal{B}$, which account for the two first terms of the Hamiltonian describing the interaction between the electrons in an atomic level and the nuclear magnetic moment. $\mathcal{A}$ specifies the magnetic-dipole coupling, $\mathcal{B}$ the electric-quadrupole coupling. We neglect the latter, again following Sánchez Almeida et al. (2008) who successfully reproduced multiple Mn I line profiles with different HFS patterns.

3.2.3 Assumption of LTE

The source function of Fe I 5395.2 Å is likely to share the characteristic properties of weak subordinate Fe I lines that possess LTE source functions, with the equilibrium maintained by the much stronger Fe I resonance lines, while having lower-than-LTE opacity in the upper photosphere in locations with steep temperature gradients (as controlled by radiative overionization of iron in the near ultraviolet; see the review by Rutten (1988)).

[1] `http://physics.nist.gov/asd3`

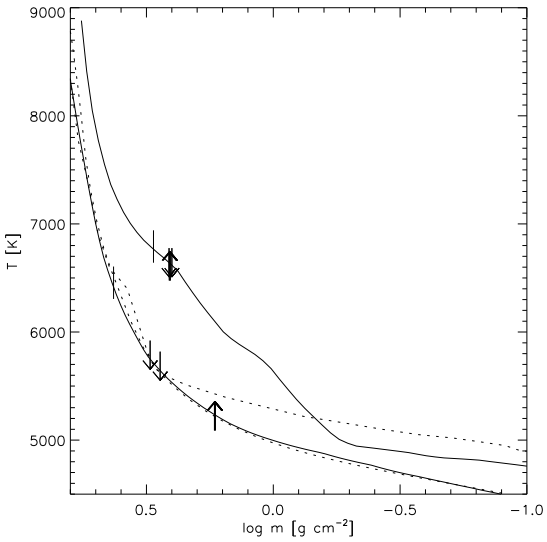

Figure 3.2: One-dimensional standard models plotted as temperature against column mass. The lower solid curve is the quiet-Sun MACKKL model of Maltby et al. (1986); the upper solid curve is the PLA model for fluxtubes in plage of Solanki & Brigljevic (1992). The tick marks on these two curves specify $\tau_\lambda = 1$ locations for the line-center wavelength of Mn I 5394.7 Å (upward arrows), the line-center wavelength of Fe I 5395.2 Å (downward arrows), and the continuum in between (arrowless). Extra $\tau_\lambda = 1$ ticks are added for line synthesis without turbulent smearing, but these differ significantly only for the Fe I line and MACKKL. The two dotted models were defined by Unruh et al. (1999) as basis for solar irradiance modeling and are discussed in Sect. 5.5.4. The lower one, close to MACKKL, is for quiet Sun, the upper one for plage.

The source function of Mn I 5394.7 Å should also remain rather close to LTE because it is an intersystem transition with rather small oscillator strength, although not as forbidden as the well-known LTE Mg I 4571.1 Å line. Indeed, Mn I behaves as most minority-species metals in the NLTE abundance study by Bergemann & Gehren (2007) for a one-dimensionsal solar atmosphere model assuming radiative equilibrium, by showing only minor (0.05 dex) NLTE weakening of the central intensity of Mn I 5394.7 Å, mostly due to the effect of ultraviolet overionization on the opacity. Such overionization is likely to be more important in locations with steeper radial temperature gradients, but similarly for Fe I. Apart from their large hyperfine structure, Mn I lines should not behave differently from Fe I lines.

Within magnetic concentrations the radial temperature gradients are close to local radiative equilibrium throughout their photospheres (Sheminova et al. (2005)), so that NLTE overionization is likely to affect both lines similarly also within magnetic concentrations.

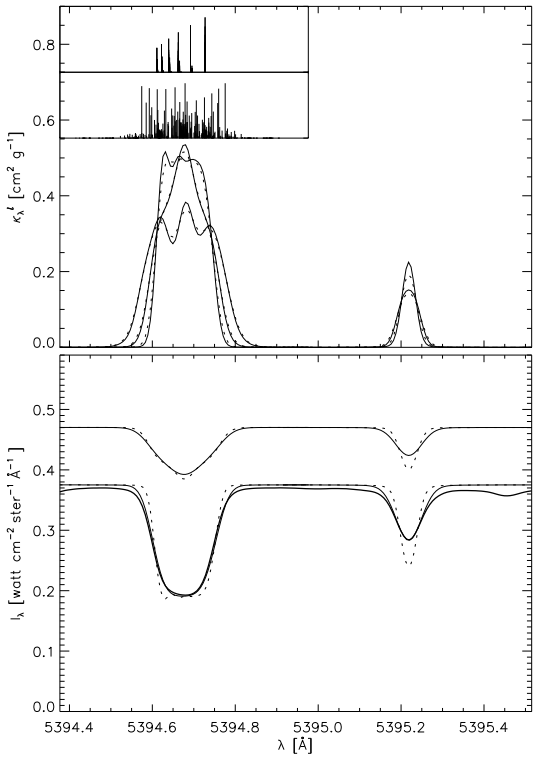

Figure 3.3: *Upper panel*: line extinction coefficient α_λ^1 for Mn I 5394.7 Å (left) and Fe I 5395.2 Å (right), for temperature $T = 5000$ K and longitudinal magnetic field strength $B = 0$ G (top solid curve), and 2000 G (lowest solid curve). For the Mn I line there is also an intermediate profile for $B = 1000$ G. The dotted curves result when temperature $T = 7000$ K is inserted into the Dopplerwidth. The insets specify the splitting pattern of Mn I 5394.7 Å for $B = 0$ G (upper) and $B = 2000$ G (lower). *Lower panel*: line profiles resulting from classical one-dimensional spectral synthesis. The lower solid curve in the lower trio is the quiet-Sun disk-center spectrum in the atlas of Neckel (1999) which is an absolute-intensity version of the NSO/FTS atlas of Wallace et al. (1998a). The other solid curve in the lower trio is the spectrum computed from the MACKKL model including micro- and macroturbulence. The dotted curve results when these fudge parameters are omitted. The two upper spectra result from the PLA model with $B = 1000$ G, also with and without turbulent smearing.

3.2.4 One-dimensional modeling

We use the standard model PLA for fluxtubes constituting plage derived by Solanki and coworkers from spectropolarimetry of photospheric lines (Solanki (1986); Solanki & Steenbock (1988); Solanki & Brigljevic (1992)) and shown in Fig. 1 of Bruls & Solanki (1993). Since we employ it only for demonstration, we do not apply spatial averaging

over upward-expanding and canopy-merging magnetostatic fluxtubes as in Buente et al. (1993), but simply use it as on-axis representation of a fully-resolved fluxtube as in the cartoon in Fig. 3.1, with constant field strength along the axis, again following the example of Sánchez Almeida et al. (2008). PLA is shown in Fig. 3.2 together with the standard MACKKL quiet-Sun model of Maltby et al. (1986) which we use to represent the non-magnetic atmosphere outside fluxtubes. In such a graph PLA appears to be far hotter than MACKKL, but when PLA is shifted over the Wilson depression in fluxtube modeling it is actually far cooler at equivalent geometrical height. Figure 3.2 shows two additional models from Unruh et al. (1999), which are discussed in Sect. 5.5.4.

3.2.5 Three-dimensional simulation

We use a single snapshot from a time-dependent simulation with the MURaM (MPS/University of Chicago Radiative MHD) code (Vögler & Schüssler (2003); Vögler (2004); Vögler et al. (2005)). MURaM solves the three-dimensional time-dependent MHD equations accounting for non-local and non-grey radiative transfer and for partial ionization.

The particular snapshot used here was taken from a simulation similar to the one of Vögler et al. (2005). Its horizontal extent is 6 Mm sampled in 288 grid points per axis, its vertical extent 1.4 Mm with 100 grid points. It was initiated with a homoge-

Figure 3.4 (facing page): Results from the MURaM snapshot. *First row*: magnetic field strength, temperature, and gas density across the $\tau_5 = 1$ continuum-escape surface. Greyscale calibration bars are shown on top. The field is monopolar. The white line specifies the cut used in Figs. 3.5–3.8 to display formation parameters in a vertical plane through the simulation volume. It represents a spectrograph slit in Fig. 3.7. The three superimposed ticks specify locations analyzed in detail in Fig. 3.7: a magnetic concentration, an intergranular lane, and the edge of the large granule in the center. *Second row*: synthetic intensity images for the continuum between the two lines and the nominal wavelengths of Fe I 5395.2 Å and Mn I 5394.7 Å. They share the same intensity greyscale. These images represent predicted observations with a telescope matching the MURaM resolution by being diffraction-limited at 2.4-m aperture. The magnetic concentrations (point-like locations with the largest field strength) are about equally bright at all three wavelengths, but the non-magnetic granules (in the center and at the top of the field) are much darker in Mn I 5394.7 Å than in the other two panels. *Third row*: the same intensities plotted as scatter diagrams per pixel against the magnetic field strength at the $\tau_5 = 1$ level for that pixel. The upward tails of bright values at large field strength reach the same maxima in all three plots, but the granulation ($B < 200$ G) is much darker in Mn I 5394.7 Å than in Fe I 5395.2 Å and the continuum. The first two panels display a pronounced hook shape, but this hook is not present in the Mn I panel. Adding more field therefore gives more spatially-averaged brightening in the Mn I line than in the Fe I line and the continuum. The Mn I line thanks its "unhooking" to its hyperfine structure through which it is less sensitive to the Doppler brightening that affects the Fe I line (and all similar lines) in the granulation.

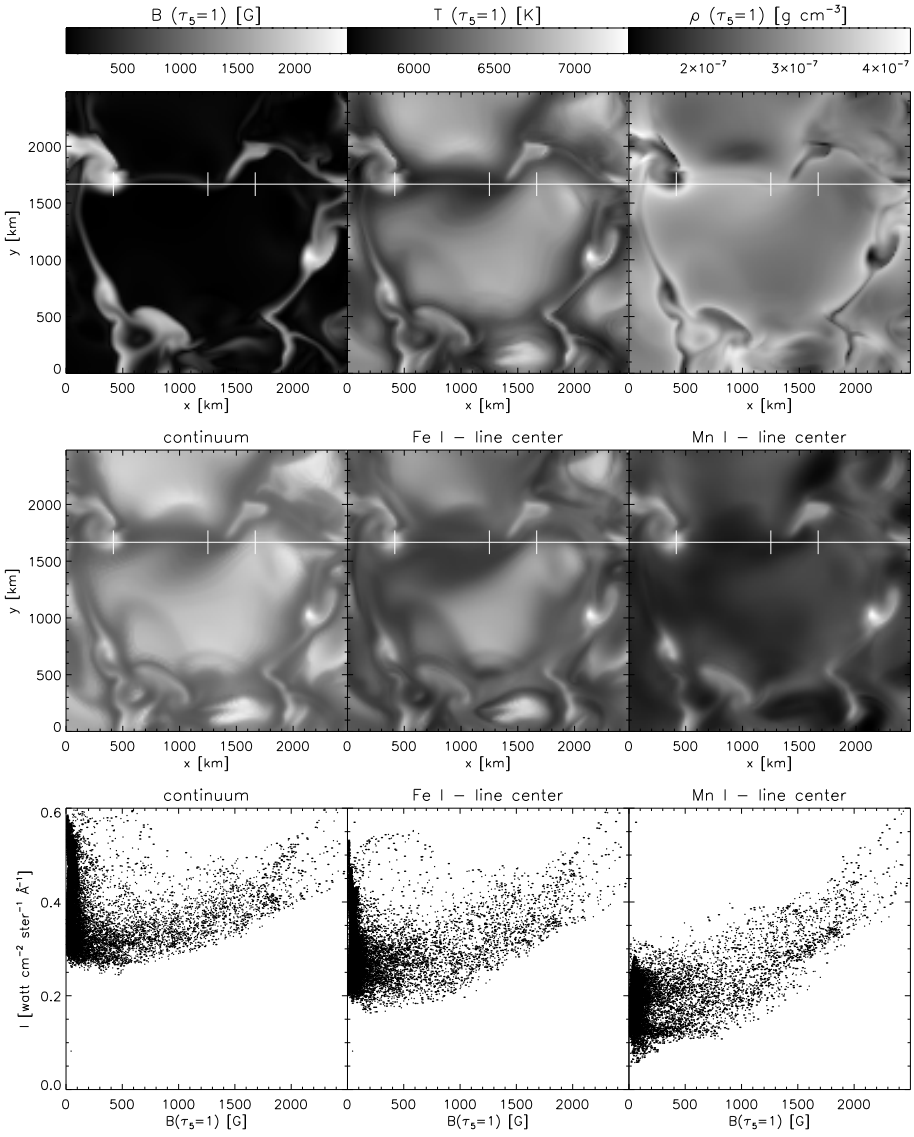
B (τ_5=1) [G]
T (τ_5=1) [K]
ρ (τ_5=1) [g cm^{-3}]
500 1000 1500 2000
6000 6500 7000
2×10^{-7} 3×10^{-7} 4×10^{-7}
y [km]
x [km]
continuum
Fe I − line center
Mn I − line center
I [watt cm^{-2} ster^{-1} Å^{-1}]
B(τ_5=1) [G]

neous vertical seed field of 200 G. The subsequent magnetoconvection produced an appearance similar to active network, with strong-field magnetic concentrations in intergranular lanes. A relatively quiet subcube was selected for our line synthesis. It has 2.5×2.5 Mm horizontal extent and contains a large granule and a field-free intergranular lane, in addition to lanes containing magnetic concentrations of varying field strength (Fig. 3.4).

The line synthesis performed for this paper used the code described above, treating the vertical columns in the subcube as independent lines of sight. The displays below are restricted to the nominal NIST wavelengths of the two lines in Table 3.1, corresponding to the line centers in a spatially-averaged disk-center intensity atlas as in Fig. 3.3.

3.3 Results

3.3.1 One-dimensional demonstration

Figure 3.3 presents the results of our one-dimensional modeling. The solid curves in the upper panel show the spectral variation of the extinction coefficient for both lines for temperature $T = 5000$ K and field strengths $B = 0$ G and $B = 2000$ G, plus the intermediate profile for $B = 1000$ for the Mn I line. For the Fe I line the Zeeman effect produces simple broadening but for the Mn I line the many hyperfine components, each with its own magnetic splitting, cause an intricate pattern shown in the lower part of the inset. The resulting profile widens in the wings, but the core first becomes peaked at $B = 1000$ G and then splits into three collective peaks at $B = 2000$ G.

The dotted curves result from inserting temperature $T = 7000$ K into the Doppler-width but not into other variables, in order to show the effect of larger thermal broadening while keeping all other things equal. The Fe I profile for $B = 0$ G looses appreciable amplitude while the Mn I profile does not.

The lower panel of Fig. 3.3 shows the emergent intensity profiles for the two lines. The lowest solid curve is the observed, spatially-averaged, disk-center spectrum. It is closely matched by the MACKKL modeling when applying standard microturbulence (1 km s^{-1}) and best-fit macroturbulence (1.28 km s^{-1} for Mn I 5394.7 Å, 1.55 km s^{-1} for Fe I 5395.2 Å). When this artificial broadening is not applied the computed Fe I line becomes too deep, but the depth of the Mn I line does not change due to its flat-bottomed core. The upper curves result from the PLA model with $B = 1000$ G, again with (solid) and without (dotted) turbulent smearing. The smearing again affects only the Fe I line. It causes a corresponding shift of the $\tau_\lambda = 1$ location for this line along MACKKL in Fig. 3.2.

Comparison of these MACKKL and PLA results shows that the spectrum increases in intensity at all wavelengths, but the most in the Mn I line, by a factor 2. Turbulent smearing does not affect this line but it produces significant difference for the Fe I line. In particular, if it is applied to the MACKKL quiet-Sun prediction but not to the PLA profile, the Fe I line-center brightness increases by only a factor 1.4.

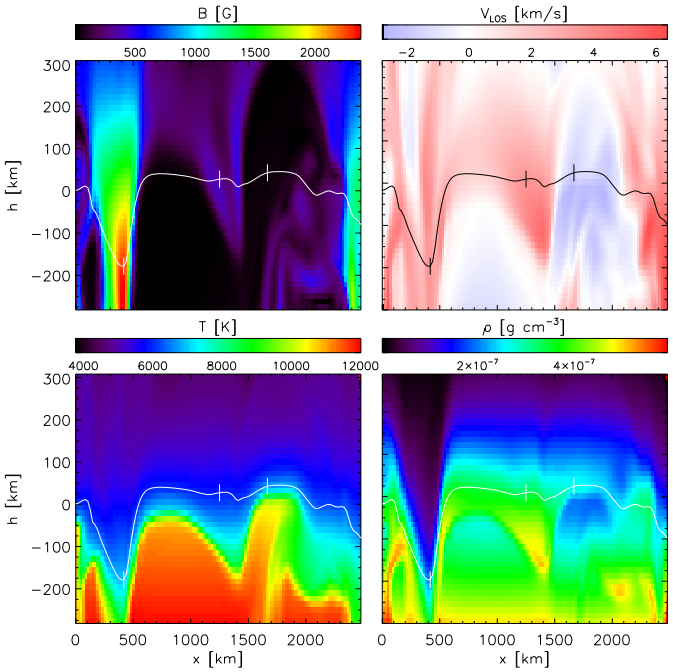

Figure 3.5: Various quantities in the MURaM snapshot across the vertical plane marked by the white horizontal line in Fig. 3.4. The upper panels show the magnetic field strength and radial velocity as a function of geometrical height versus horizontal location along the cut. The height scale has $h = 0$ km at the mean $\tau_5 = 1$ level, averaged over all columns. It extends 882 km below and 518 km above that level in the simulation but only the pertinent height range is shown here. The velocity coloring is red for downdraft (redshift) and blue for updraft (blueshift). The lower panels show the temperature and the gas density. The overlaid curves specify $\tau_5 = 1$ continuum formation depths. The three ticks mark the locations analyzed in Fig. 3.7.

This difference in line-center brightening suggests that the Fe I line suffers more from thermal broadening and from the thermodynamic fine structuring that was traditionally modeled with micro- and macroturbulence. The apparent sensitivity of the Mn I line to magnetic activity may indeed actually reflect decrease in the sensitivity of the Fe I line by its non-magnetic quiet-Sun Doppler smearing.

3.3.2 Three-dimensional verification

The results from the MURaM simulation are shown in Fig. 3.4. The three panels in the upper row show basic state parameters across the $\tau_5 = 1$ surface where τ_5 is the continuum optical depth at $\lambda = 5000$ Å determined separately for each simulation column. The middle row displays synthetic intensity images for our three diagnos-

tics: the continuum between the two lines and the nominal line-center wavelengths of Fe I 5395.2 Å and Mn I 5394.7 Å. The bottom row shows these intensities in the form of pixel-by-pixel scatter plots against the magnetic field strength at $\tau_5 = 1$.

The three images demonstrate directly why Mn I 5394.7 Å shows higher brightness contrast between non-magnetic and magnetic areas: the magnetic bright points reach similar brightness in all three panels but the granulation is markedly darker in this line. Darker granulation implies higher sensitivity to activity, i.e., addition of more magnetic bright points. The three scatter plots in the bottom row of Fig. 3.4 quantify this behavior. In the continuum plot at the left, the darkest pixels are located in field-free or weak-field intergranular lanes. The addition of more magnetic field within the lanes brightens the latter, the more so for stronger fields, and for the strongest fields almost up to the maximum brightness of the field-free granular centers. The large brightness of the latter at left and of the strongest-field pixels at right causes a prominent hook shape.

In slanted near-limb viewing, the magnetic concentrations do not add brightness to dark intergranular lanes but permit deeper viewing into the bright granules behind them, adding brightness to the already brightest features and so making faculae brighter than the granular background (see Fig. 3.1).

The scatter diagram for Fe I 5395.2 Å (bottom-center panel) shows a similar hook shape as the continuum panel. The cloud of granulation pixels at the left is at lower intensity since the line is an absorption line. However, the intensities of the strongest-field pixels still brighten to the same values as in the continuum panel, implying that the line vanishes completely at its nominal wavelength.

The scatter diagram for Mn I 5394.7 Å exhibits similar behavior but it loses the hook shape. The line is yet darker in field-free granulation. In this case, the corresponding dark cloud of low-field pixels at the left does not have an upward tail. However, the upward tail of pixels with increasing field still stretches all the way from the dark lanes to the continuum values, which again implies that the line vanishes for the strongest-field pixels.

If magnetic field is added to field-free granulation, this addition removes points from the bottom left of the distribution (corresponding to dark intergranular lanes) and adds "magnetic bright points" at the upper right. Its effect is more dramatic in the ensemble average of the Mn I line than in that of the Fe I line because the latter already has bright contributions from field-free granules; in the Fe I line, the field-free granulation covers the same brightness range as the field-filled lanes. Thus, field addition produces a higher spatially-averaged brightness increase in the Mn I line than in the Fe I line.

We conclude that the MURaM synthesis duplicates the Sun in exhibiting higher brightness response to more activity in the Mn I line than in the Fe I line – not by means of chromospheric emission from magnetic concentrations but by showing the non-magnetic granulation darker in the Mn I line.

3.3.3 Explanation

Unlike the Sun, the MURaM simulation not only allows us to inspect the emergent spectrum but also to dissect the behavior of pertinent physical parameters throughout the simulation volume. Instead of ending our paper here with the above conclusion that neither a chromosphere nor NLTE coupling to Mg II h & k are required to reproduce the activity sensitivity of Mn I 5394.7 Å, we provide additional analysis of the MURaM results to diagnose why the granulation appears darker in the Mn I line – or rather, why it appears brighter in the Fe I line – and so justify our use of the term "explanation" in the title of this paper.

The white line with three ticks in the grey-scale panels of Fig. 3.4 indicates the spatial samples selected in Figs. 3.5–3.8. These cut and tick locations were chosen to sample a strong-field magnetic concentration that appears as a bright point in the intensity images (left-hand tick), a non-magnetic dark lane (middle tick), and a granule (right-hand tick). Unfortunately, the cut samples only the edge rather than the center of the large granule covering the center part of the field, but other cuts would not have sampled both a bright point and a non-magnetic lane. A magnetic lane less extreme than the bright point is sampled at the far right.

Figure 3.5 diagnoses MURaM physics in the vertical plane defined by this cut. It shows behavior that is characteristic of solar magnetoconvection close to the surface. The overlaid curves specify the $\tau_5 = 1$ continuum surface. The low gas density (4th panel) in the magnetic concentration at $x \approx 400$ km produces a large Wilson depression of about 200 km. The deep dip in the $\tau_5 = 1$ curve samples a relatively high temperature and a relatively flat vertical temperature gradient. The intergranular lane at $x \approx 1300$ km combines low temperature with high density and strong downdraft; the granule edge at $x \approx 1650$ km combines higher temperature with gentler updraft and lower subsurface density.

Figure 3.6 repeats this vertical-plane display of temperature and density but per column on the radial optical depth scale that belongs to each diagnostic. The panels in the first and second columns show the atmosphere "as seen" by each spectral feature at its nominal wavelength. The dotted horizontal lines at $\log \tau_\lambda = 0$ indicate their formation heights. The solid curves are the $\tau_5 = 1$ locations. The third column illustrates the relative behavior of the corresponding opacities in the form of fractional lower-level population variations.

The top panels of Fig. 3.6 exhibit only slight differences between the $\tau = 1$ locations along the cut. The magnetic concentration has an appreciable hump in $T(\tau_\lambda)$ and dip in $\rho(\tau_\lambda)$ around $\tau_5 = 1$. The relatively high temperature and low density there combine into increase of the electron-donor ionization. This is illustrated by the sixth panel showing the fractional population variation of the lower level of Mn I 5394.7 Å, which is the Mn I ground state. Its behavior equals the depletion by manganese ionization apart from a minor correction for the temperature sensitivity of the Mn I partition function. Manganese has too small an abundance to be an important electron donor, but ionizes similarly to iron (Table 3.1) so that this panel illustrates general electron-donor ionization, with neutral-stage depletion occurring

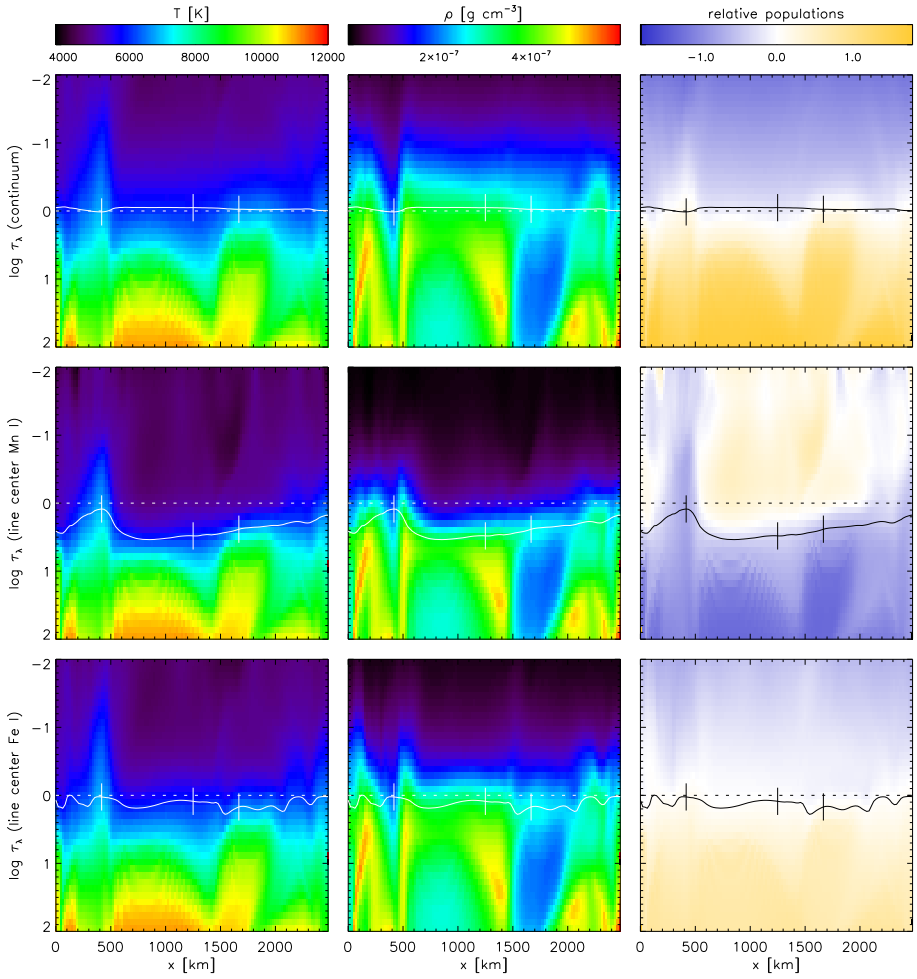

Figure 3.6: Temperature, gas density, and population variations across the vertical cut through the MURaM simulation plotted per column on radial optical depth scales for the nominal continuum (top row), Mn I 5394.7 Å (middle row), and Fe I 5395.2 Å (bottom row) wavelengths. The solid curves specify $\tau_5 = 1$ depths, the horizontal dotted lines feature-specific $\tau_\lambda = 1$ depths. The third column displays fractional population offsets. These are the lower-level populations for H^- bound-free transitions, the Mn I line, and the Fe I line, each normalized by the total element density (hydrogen, manganese, iron) per location and shown in logarithmic units scaled to the mean value at $\tau_\lambda = 1$ along the cut. Positive offsets are colored amber, negative bluish. The scale runs from −1.8 to +1.8.

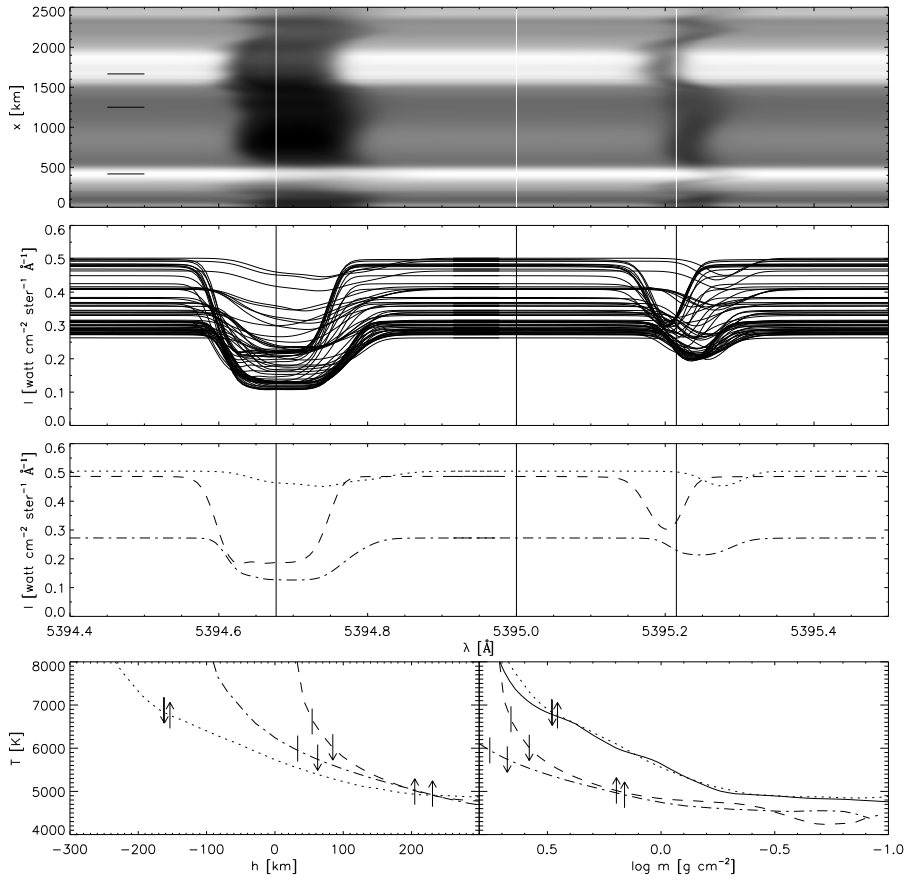

Figure 3.7: Further analysis of the formation of Mn I 5394.7 Å, Fe I 5395.2 Å, and the intermediate continuum in the MURaM simulation. *Top panel*: spectrum synthesized from the computed emergent intensities. The vertical coordinate corresponds to the x sampling along the cut specified in Fig. 3.4. The three black horizontal markers correspond to the ticks selecting the bright point (lowest), field-free intergranular lane (middle), and granule edge (highest). The three vertical lines specify the nominal wavelengths for Mn I 5394.7 Å (left), Fe I 5395.2 Å (right), and the intermediate continuum (center). *Second panel*: spectral profiles for every second pixel along the cut. *Third panel*: spectral profiles for the three locations specified by ticks in Fig. 3.4 and black markers in the top panel. *Dotted*: magnetic concentration. *Dot-dashed*: intergranular lane. *Dashed*: granule edge. *Bottom panels*: temperature stratifications for the three selected locations, at left against geometrical height, at right against column mass as in Fig. 3.2. The solid curve is the PLA model, as in Fig. 3.2. The tick marks specify the $\tau_\lambda = 1$ locations for the nominal wavelengths of Mn I 5394.7 Å (upward arrows), of Fe I 5395.2 Å (downward arrows), and of the continuum in between (arrowless). In the magnetic concentration the Fe I 5395.2 Å tick coincides nearly with the continuum one. The Wilson depression is much larger for the Mn I line than for the continuum and the Fe I line.

within magnetic concentrations and at large depth. The corresponding increase in the free-electron density produces larger H^- opacity, evident as an overall color gradient reversal between the top and center panels in the third column. It results in an upward enhancement peak at the magnetic concentration in the H^- population panel. This relative increase in continuum opacity explains why $\tau_\lambda = 1$ is reached at lower density in the magnetic concentration than in the adjacent intergranular lane (second panel), the Wilson depression being smaller than one would estimate from pressure balancing alone. The flat temperature gradient in the magnetic concentration produces a marked upward extension in $T(\tau_\lambda)$ in the first panel. It contributes brightness enhancement along much of the intensity contribution function, and so causes magnetic concentrations to appear bright with respect to non-magnetic lanes. However, the hook pattern in the continuum scatter plot in Fig. 3.4 shows that this lane brightening does not exceed the maximum granular brightness.

The center row of Fig. 3.6 shows that Mn I 5394.7 Å is generally formed higher in the solar atmosphere than the continuum, but not in the magnetic concentration where the upward hump in the $\tau_5 = 1$ curve almost reaches the $\tau_\lambda = 1$ level. This is because the relatively high temperature and low density there increase the degree of manganese ionization, as is evident as a marked upward blue extension in the third panel. The line weakens so much that the brightest Mn I pixels in Fig. 3.4 reach the same intensity as in the continuum, also sampling the upward high-temperature extension (first column). In contrast, the highest line-to-continuous opacity ratio (i.e., the largest separation between the $\tau_\lambda = 1$ and $\tau_5 = 1$ locations) is reached along the intergranular lane where the neutral-stage population is higher due to relatively large density and low temperature. Thus, the curve separation maps the variation in fractional ionization along the dotted line. Since the temperature increases inwardly anywhere, the deeper sampling within the magnetic concentration and the higher sampling in the granulation, especially in the lanes, together increase the brightness contrast between bright points and granulation with respect to that in the continuum. The effect of this increased ionization is similar to the effect of CH dissociation in the G band and reduced damping in the Hα wings within magnetic concentrations. It enhances the magnetic lane brightening, so that this exceeds the granular brightnesses, undoing the hook shape of the continuum scatter plot.

The bottom row of Fig. 3.6 shows the corresponding plots for Fe I 5395.2 Å. Iron and manganese ionize similarly so that low-excitation Fe I lines experience the same depletion in magnetic concentrations. However, Fe I 5395.2 Å is a high-excitation line; its Boltzmann sensitivity to higher temperature largely compensates for the enhanced ionization. The panel in the third column therefore resembles the top one for H^- much more than the second one for Mn I 5394.7 Å: the overall color gradient reverses. The line again vanishes in the magnetic concentration, so that the strongest-field pixels in Fig. 3.4 reach the continuum intensities. One might expect that the curve separation in the bottom panels would follow the temperature pattern under the dotted line in the first column, but this is not the case; for example, the line also nearly vanishes (at its nominal wavelength) in the intergranular lane. This discordant variation is caused by the Dopplershifts imposed on the line extinction by the flows displayed in

the upper-right panel of Fig. 3.5. A precise comparison confirms that the unsigned amplitude of the flow variation along the cut at 100 − 200 km above the $\tau_5 = 1$ curve in the Dopplershift panel is mapped into reversed modulation of the $\tau_5 = 1$ curve for Fe I 5395.2 Å in the last panel of Fig. 3.6. Thus, the line weakens because it is systematically shifted away from its nominal wavelength.

We demonstrate the Doppler-related formation differences between the two lines further in Fig. 3.7. The upper two panels display spectral representations along the cut defined in Fig. 3.4, as a spectral image and as sample profiles. The top panel displays the spectrogram which would have been obtained with a telescope with MURaM resolution. Both lines show a bright "line gap" in the magnetic concentration close to the bottom. At $x \approx 2500$ km, the intergranular lane with weaker field still causes a noticeable gap. Large Dopplershifts occur in the field-free lane and the granular edge.

The second panel displays spectral profiles taken from the spectrogram. Both panels show that the line-center intensity of the Mn I line is not very sensitive to Dopplershifts, whereas the Fe I line is almost everywhere shifted significantly away from its nominal wavelength. It also weakens more in the granule due to larger thermal broadening (Fig. 3.3). Taking the spatial mean at each nominal wavelength does a fair job of intensity averaging for the Mn I line but misses nearly all dark cores in the Fe I line, especially in the lanes but also in granules. We note that this particular cut does not represent hot granules well; more samples of these would add many profiles with weakened cores blueward of the nominal Fe I wavelength.

The third panel selects the spectral profiles for the three sample locations along the cut. The nominal Fe I line-center wavelength misses all three cores! Thus, the brightness average at this wavelength is much higher than it would be for an undisturbed line of this opacity. The Mn I line-center wavelength, however, only misses the deepest part of the magnetic-concentration profile, which is weak anyhow. This disparity in Doppler sensitivity explains why the granulation in Fig. 3.4 is much darker in Mn I 5394.7 Å than in Fe I 5395.2 Å.

We also note that the Mn I line profile changes from boxy to more pointed in some of the intermediate profiles in the second panel. This sharpening follows the extinction coefficient behavior in Fig. 3.3. It contributes to the decrease in equivalent width of Mn I 5394.7 Å at higher activity, which is not analyzed here.

The bottom panels of Fig. 3.7 show the vertical temperature stratifications at the three sample locations, at left against geometrical height with $h = 0$ at $\tau_5 = 1$ for the simulation mean, at right against column mass per feature. These graphs link the simulation results to the classical fluxtube modeling in Sect. 3.3.1. They exhibit familiar properties of granulation and magnetic concentrations: the temperature gradients are steepest within granules, flatter in intergranular lanes with mid-photospheric cross-overs producing "reversed granulation", and flattest in fluxtubes. The heights of formation, marked by ticks specifying the $\tau_\lambda = 1$ locations, are similar per line in the granular edge and the lane but much deeper in the magnetic concentration, which is the coolest feature at equal geometrical height but the hottest at equal column mass and at the $\tau_{\rm cont} = 1$ location per feature. The Wilson depression is about 200 km in

the continuum and twice as large for the Mn I line due to enhanced ionization within the magnetic concentration, but not for the Fe I line due to its Doppler-deepened granulation sampling. Both lines weaken severely in the magnetic concentration due to this deep sampling, and both are redshifted away from their nominal wavelength, Fe I 5395.2 Å so much that its $\tau_\lambda = 1$ tick coincides with the continuum one.

3.4 Discussion

3.4.1 Comparison of 1D modeling and 3D simulation

We have used both classical empirical fluxtube modeling (Sect. 3.3.1) and modern MHD simulation (Sect. 5.2). The bottom panels of Fig. 3.7 relate the latter with the former. The right-hand panel shows remarkably close agreement between the PLA model and the MURaM magnetic-concentration stratification. This may be taken as mutual vindication of these very different techniques, but not as proof of their correctnesses since both assumed LTE ionization (discussed below) while the Sun does not.

The simulation resolves the granular Dopplershifting emulated by turbulence in classical modeling. The simulation analysis in Sect. 3.3.3 confirmed that Mn I 5394.7 Å activity-brightens more than Fe I 5395.2 Å because its intrinsic hyperfine-structure broadening suppresses the thermal and Doppler brightening in non-magnetic granulation. This was already suggested by the 1D demonstration in Fig. 3.3.

3.4.2 Validity of LTE

We have assumed LTE throughout this paper. In Sect. 3.2.3, we noted that the most likely departure from LTE affecting our two lines is a decrease of opacity by radiative overionization in locations with steep temperature gradients, where the angle-averaged intensity exceeds the Planck function in ultraviolet photo-ionization edges (see e.g., Rutten (2003) for more explanation). The steepest temperature gradients in Fig. 3.5 occur not radially along columns but transversely across the magnetic concentration. Therefore, the ionization which causes the vanishing of both lines from the corresponding bright point may be underestimated. If so, the H^- opacity is equally underestimated. However, the MURaM simulation itself assumes LTE with coarse spectral sampling and is likely to differ intrinsically if NLTE overionization affecting the H^- opacity is taken into account. Such overionization was similarly neglected in the empirical construction of the PLA model from Fe I-line spectropolarimetry, by assuming LTE to define the optical depth scales. Improvement requires non-trivial evaluation of the ultraviolet line haze.

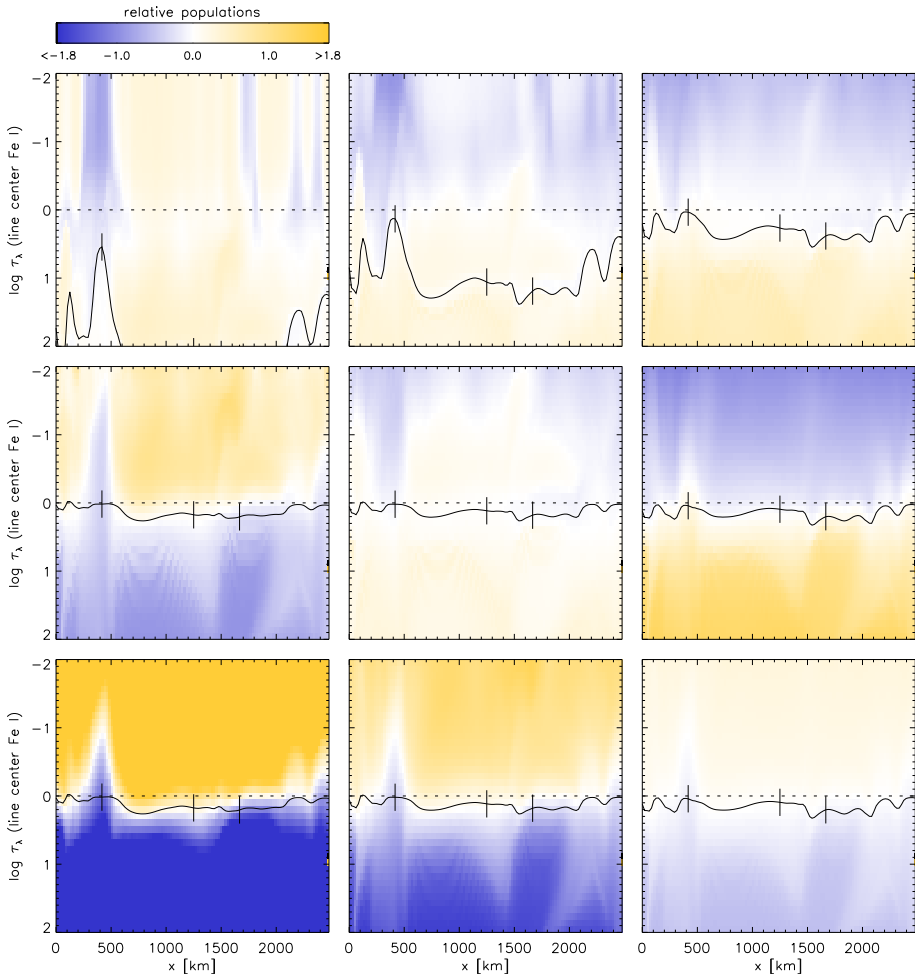

Figure 3.8: The effect of excitation energy and line strength on Fe I line formation. Each panel is the fractional population of the lower level of an artificial line comparable to Fe I 5395.2 Å along the cut through the MURaM simulation defined in Fig. 3.4, again shown on nominal line-center optical depth scales, normalized to the mean value along the dotted line, and with the same logarithmic color coding as in the third column of Fig. 3.6, clipped at offsets −1.8 and +1.8. The solid curves are again the $\tau_5 = 1$ locations for the continuum at 5000 Å, the dashed lines the line-center $\tau_\lambda = 1$ formation indication. *Top row*: the Fe I 5395.2 Å line at excitation energy 2, 3, and 4 eV, respectively. The corresponding mean Boltzmann factors at $\tau_\lambda = 1$ are 1.2×10^{-3}, 1.7×10^{-4}, and 5.2×10^{-5}. *Second row*: the Fe I 5395.2 Å at excitation energy 0, 3, and 6 eV but with the oscillator strength scaled to maintain the same line strength in the emergent spectrum that Fe I 5395.2 Å shows (by 25×10^{-3}, 25 and 25×10^{3}, respectively). *Bottom row*: idem, but the color coding now measures deviations from the Milne-Eddington approximation by showing the lower-level population divided by the H^- population. The leftmost panel is severely clipped. The Milne-Eddington approximation improves dramatically with higher excitaton.

3.4.3 Extension to other lines

We have demonstrated and analyzed Doppler brightening in detail only for Mn I 5394.7 Å and Fe I 5395.2 Å. The first line may be taken to exemplify all lines with wide boxy extinction profiles, the second line all others with narrow peaked profiles, i.e., almost all other photospheric lines. Figure 3.8 illustrates this generalization by extending the MURaM synthesis to a range of artificial Fe I lines with other excitation energies. The first two rows again display relative population variations across the simulation cut, using the same color coding as in the third column of Fig. 3.6. The top row of Fig. 3.8 combines the effects of the Boltzmann factor both on the amplitude of the line extinction and on its temperature sensitivity. The second row isolates the latter by making each line as weak as Fe I 5395.2 Å.

The first panel of Fig. 3.8 is included for illustration purposes only, because this artificial line is already too strong for reliable synthesis from our simulation. If it existed in reality it would also suffer appreciable departures from LTE (see Rutten & Kostik (1982)). It originates near the top of the simulation volume, which sets the columnar structure of the upper part; the sizable vertical flows there impose the separation between the two $\tau = 1$ curves. In reality, very strong Fe I lines suffer less convective and thermal Doppler weakening in their cores, which explains the observation by Malanushenko et al. (2004) that the strongest Fe I lines exhibit some (but only slight) global activity modulation. Even this modulation, however, has nothing to do with the chromosphere! The second and third panel illustrate deeper line formation with steeper gradients. Their $\tau = 1$ separations also exhibit Doppler modulation. Thus, Doppler weakening affects these three lines just as it affects Fe I 5395.2 Å.

The second row of Fig. 3.8 illustrates the effect of Boltzmann temperature sensitivity at a given emergent line strength. The first panel describes the Fe I ground state and is nearly the same as the sixth panel of Fig. 3.6. Towards higher excitation energy, the Boltzmann increase compensates more of the depletion by ionization. In the center panel, the population offset gradients are flat; at right, they are reversed so that the population variation closely mimics the behavior of H^- in the third panel of Fig. 3.6, although at slightly smaller amplitude. The Doppler modulation of the $\tau = 1$ separation remains similar, irrespective of this gradient reversal in fractional population distribution. Thus, Doppler brightening affects all photospheric Fe I lines similarly.

The third row of Fig. 3.8 displays results from repeating this test in terms of the Milne-Eddington approximation (constant line-to-continuum opacity ratio with height) often assumed in photospheric polarimetry (e.g., Auer et al. (1977); Skumanich & Lites (1987); Westendorp Plaza et al. (1998); Orozco Suárez et al. (2007b)). At the left, the combination of Fe I depletion by ionization and the corresponding increase in H^- opacity implies taking the square of the population offsets, or twice steeper gradients in this logarithmic plot than in the second row. The Milne-Eddington approximation fails badly, but least so within the magnetic concentration. It improves with excitation energy through Boltzmann compensation. The rightmost

panel shows the residuals that remain from subtracting the sixth panel in this figure from the third panel in Fig. 3.6, resulting in rather small deviations. This behavior was shown earlier in Fig. 3 of Rutten & van der Zalm (1984; reprinted in Fig. 9.2 of Rutten (2003)).

3.4.4 Irradiance modeling

In this paper, we have not extended the analysis from radial viewing to full-disk averaging. The demonstration in Sect. 3.3.1 adopted Solanki's one-dimensional empirical model for a fluxtube in plage but without adding flaring fluxtube geometry, granular presence around fluxtubes and behind fluxtubes in slanted facular viewing, multiple-tube interface geometry, spatial averaging over these geometries, the multi-angle evaluation needed to emulate center-to-limb viewing, and did not incorporate full-disk averaging, consideration of spatial distributions over the solar surface, and their variations with the solar cycle. All of these non-trivial aspects would need careful quantification to expand the demonstration of enhanced sensitivity in Sect. 3.3.1 into a quantitative estimate for comparison with Livingston's irradiance data. The simulations in Sect. 5.2 yielded profile synthesis for a small solar-surface area containing strong-field concentrations that may be considered more realistic than idealized magnetostatic fluxtubes but, nevertheless, generation of full-disk signals comparable to Livingston's data would still require all the above evaluations. This effort is not attempted here.

In contrast, the step from one-dimensional line synthesis to emulation of the full-disk and cycle-dependent integrated signal was recently achieved by Danilović et al. (2007) using the SATIRE (Spectral And Total Irradiance Reconstruction) approach of Fligge et al. (2000), Krivova et al. (2003) and Wenzler et al. (2005, 2006) In this technique, the spatial distributions of spots and plage are extracted from full-disk magnetograms and continuum images to derive disk-coverage distributions throughout recent activity cycles. Each component (i.e., quiet Sun, plage, spots) is represented by a standard one-dimensional model atmosphere. The first two components are shown as dotted curves in Fig. 3.2. The lower one for quiet Sun is the radiative-equilibrium model of Kurucz (1979, 1992a,b) which is virtually identical to MACKKL. The upper one for plage was constructed by Unruh et al. (1999) by smoothing model P of Fontenla et al. (1993) and deleting its chromospheric temperature rise. For spots, a Kurucz radiative-equilibrium model with low effective temperature is used, which is not shown here. Danilović et al. (2007) found that the use of these models with the empirically established SATIRE coverage fractions produces a good reproduction of Livingston's data, both for Mn I 5394.7 Å and Fe I 5395.2 Å.

This use of the dotted models in Fig. 3.2 can be regarded as an ad-hoc trick to reproduce the higher brightness of plage. The Mn I 5394.7 Å line brightens more than Fe I 5395.2 Å in this simplistic modeling simply because it is a stronger line, hence formed higher, hence getting more out of the divergence between the two models with height. Any line as strong would show the same brightening. Stronger lines would brighten more; in particular, Fe I lines with deeper cores than Mn I 5394.7 Å

would show yet larger activity modulation, in conflict with the observations.

Actually, as illustrated in Fig. 3.1 and demonstrated in Figs. 3.4–3.8, plage produces disk-center brightening in any photospheric diagnostic not by being hotter at equal height, but through below-the-surface viewing of hot-wall heat within magnetic concentrations. The SATIRE modeling does not evaluate Wilson depressions, but as long as the SATIRE models are used in a one-dimensional radial fashion on their own column mass or optical-depth scale, this does not matter. In this sense, the Unruh plage model does recognize that the local temperature gradient around local $\tau = 1$ within magnetic concentrations tends to be less steep than in the granulation, as in the bottom panels of Fig. 3.7. However, the approximation breaks down for non-vertical fluxtube viewing, for which the "Zürich wine-glass" geometry of Buente et al. (1993) with slanted rays passing through the glasses was a far more realistic description, and it fails for limbward faculae because slanted viewing of hot granule innards through empty fluxtubes (Fig. 3.1) should not be described by the vertical temperature stratification within magnetic concentrations.

Plage and faculae were much more realistically treated by the older Solanki-style fluxtube models, which diverge with depth instead of with height between magnetic and non-magnetic components (compare the PLA and Unruh plage models in Fig. 3.2 and PLA with the MURaM stratification in Fig. 3.7). Obviously, outward divergence with height supplies a zero-order approximation to increasing facular contrast in limbward viewing, but no more than that and inherently wrong.

The same criticisms apply to the similar photospheric-feature modeling through outward-diverging temperature stratifications by e.g., Fontenla et al. (1993, 2006) who added more ad-hoc adjustment parameters in the form of a deep-seated chromospheric temperature rise, comparable to those invoked by Doyle et al. (2001), which were rightfully removed by Unruh et al. (1999) in their plage model – the chromosphere has nothing to do with network and plage visibility in photospheric diagnostics.

Nevertheless, the success of the SATIRE modeling by Danilović et al. (2007) implies that, given any trick to make a single magnetic concentration brighter in Mn I 5394.7 Å than in Fe I 5395.2 Å by the amount given by SATIRE's two-model divergence, that trick will reproduce Livingston's data similarly. Thus, although we have not performed any full-disk modeling, our trick is likely to reproduce these data too. Ours entails better understanding of why Mn I lines activity-brighten more than other lines: the latter brighten more in normal granulation.

3.5 Conclusion

The explanation of the activity sensitivity of Mn I 5394.7 Å concerns only deep-photosphere line formation. Intergranular magnetic concentrations brighten with respect to field-free intergranular lanes in any photospheric diagnostic by deep radiation escape that samples relatively high and flat-gradient temperatures (Figs. 3.5 and 3.6). For normal, narrow, photospheric lines this brightening has less effect in

full-disk averaging due to their loss of line depth in normal granulation (Fig. 3.7), which was traditionally mimicked by applying micro- and macroturbulent smearing (Fig. 3.3). Mn I 5394.7 Å has a flat-bottomed profile due to its hyperfine structure (Fig. 3.3), which makes this line less susceptible to granular Doppler smearing and thermal broadening. It weakens less in normal granulation (Fig. 3.7) and so displays larger mean brightness contrast between quiet and magnetic areas (Fig. 3.4).

The Mn I 5394.7 Å line is therefore an unsigned proxy magnetometer sensitive to the magnetic concentrations ("fluxtubes") that constitute on-disk network and plage and near-limb faculae, through Wilson-depression viewing of subsurface bright-wall heat at disk center and through slanted facular viewing into hot granules near the limb (Fig. 3.1). In solar irradiance monitoring, Mn I 5394.7 Å tracks the Ca II H & K and Mg II h & k core brightness varations because these also respond to magnetic concentrations, although by unidentified magnetic chromosphere heating that does not affect the Mn I lines, neither directly nor through interlocking to Mg II h & k.

As a proxy magnetometer, Mn I 5394.7 Å is similar to the G band in which the contrast enhancement arises from the general addition of CH line opacity and local reduction of that in magnetic concentrations through dissociation. Similar contrast enhancement occurs in the extended blue wings of strong lines by the addition of line opacity and reduction of that in magnetic concentrations from lesser damping, plus Doppler flattening of the granular contrast (Leenaarts et al. (2006b)). These diagnostics are all sufficiently wide in wavelength not to suffer from the granular Doppler smearing that spoils the contrast for the centers of narrow lines. The G band is the most useful by being a wide-band spectral feature in the blue. Qua contrast, the blue wing of Hα is probably the best proxy (Leenaarts et al. (2006a)), but not for full-disk irradiance monitoring since its photospheric magnetic-concentration brightening is sometimes obscured by overlying dark blue-shifted and/or heat-widened chromospheric fibril absorption.

We conclude that the principal usefulness of photospheric Mn I lines lies not in their unusual activity sensitivity but in their hyperfine-structured richness as weak-field diagnostic in full-Stokes polarimetry of high angular resolution and sensitivity (e.g., Sánchez Almeida et al. (2008)).

Acknowledgments

We thank J. Sánchez Almeida for bringing us together and H. Uitenbroek for valuable interpretation and many text improvements. N. Vitas is indebted to I. Vince for suggesting this research topic. His research is supported by a Marie Curie Early Stage Research Training Fellowship of the EC's Sixth Framework Programme under contract number MEST-CT-2005-020395. B. Viticchiè thanks V. Penza for invaluable help and J. Sánchez Almeida for introducing him to Mn I lines. His research is supported by a Regione Lazio CVS (Centro per lo studio della variabilità del Sole) PhD grant. R.J. Rutten thanks the National Solar Observatory/Sacramento Peak for much hospitality and the Leids Kerkhoven-Bosscha Fonds for travel support.

Watch the sun until it becomes square.
— Yoko Ono, *Sun piece*, 1962

Chapter 4

Fast horizontal flows in a quiet sun MHD simulation and their spectroscopic signatures

N. Vitas, C. E. Fischer, A. Vögler and C. U. Keller*

Abstract

Numerical simulations of solar surface convection have predicted the existence of supersonic horizontal flows in the photospheric granulation. Recently, Bellot Rubio (2009) reported the detection of such flows in data from the Hinode satellite. We study supersonic granular flows in detail to understand their signatures in spectral lines and to test the observational detection method of Bellot Rubio. We perform time-dependent 3D radiative MHD numerical simulations and synthesize the spectral lines used by Bellot Rubio at the resolution of the Hinode data for different viewing angles covering the center-limb variation. There is very large variation in the detailed shape of the emergent line profiles depending on the viewing angle and the particular flow properties and orientation. At the full simulation resolution the supersonic flows can even produce distinct satellite lines. After smearing to the Hinode resolution sufficient signature of supersonic motion remains. Our analysis shows that the detection method of Bellot Rubio is indeed applicable. However, the detection is very sensitive to ad hoc parameter choices and can also misidentify supersonic flows.

*Accepted for publication in *Astronomy & Astrophysics*s

4.1 Introduction

Continuum images of the solar surface show a pattern of isolated bright cells called granules that are separated by dark intergranular lanes. The physics causing this pattern is well understood and has been successfully reproduced in highly realistic 3D hydrodynamical simulations (Stein & Nordlund 1998, Vögler & Schüssler 2003, Wedemeyer et al. 2004). A detailed review of solar granulation is given by Nordlund et al. (2009). In this paper we employ numerical MHD simulations to study high velocity flows and shocks in granular outflows and their observational signatures.

We briefly summarize the physics of solar granulation: Bright granules are locations where hot, high-entropy and low density gas parcels reach a height at which the continuum opacity is sufficiently low to allow photons to escape. The temperature and entropy of the parcel are reduced by radiative losses in a thin layer at the solar surface. The parcel expands and reaches a characteristic surface granule size of around 1 Mm. The horizontally outflowing, radiatively cooled, dense material collides with neighboring granular flows and sinks in the dark intergranular lanes.

A closer look at particle trajectories within the parcel shows that, once at the surface, the particles continue to move upwards and penetrate into a stable layer (e.g., Fig. 18 of Stein & Nordlund (1998) and Fig. 8 of Cheung et al. (2007b)). There the entropy temporarily increases due to a small amount of radiative heating from below. Finally, due to mass conservation and the horizontal pressure gradient, the flows diverge horizontally outwards. The particle trajectories in this overshooting zone differ depending on the individual initial velocity and location within the granule. In some cases the accelerated flows reach large horizontal velocities that occasionally become supersonic at the granular edges (Cattaneo et al. 1990, Malagoli et al. 1990, Stein & Nordlund 1998). Gas parcels that are located initially at the granule center have the longest trajectories and so are likely to reach the highest velocities (Stein & Nordlund (1998)).

At disk center, Doppler measurements of supersonic horizontal flows in the granulation are not possible. Therefore Nesis et al. (1993) proposed to use line broadening as an indirect indicator of such flows. However, Solanki et al. (1996) compared the velocity field in 2D granulation simulations with synthesized line profiles and showed that, at disk center, other properties of the downflow lanes can cause comparable line broadening, and pointed out that unresolved vertical velocity gradients can also produce apparent line broadening. They concluded that all line widths observed by Nesis et al. (1993) can be attributed to limited resolution.

At the limb, the broadest profiles found by Solanki et al. (1996) were all associated with strong horizontal velocity gradients. However, the inverse was not true, as not all supersonic horizontal flows resulted in large line broadening. Solanki et al. (1996) and Gadun & Hanslmeier (2000) analyzed 2D granulation simulations and concluded that limb observations are more favorable than disk center observations for the detection of such fast horizontal flows. Rybák et al. (2004) performed spectroscopy with high angular resolution at a viewing angle corresponding to $\mu = 0.65$, found shock signatures in spectral line widths, and presented the first observation of the time evolution of such a granular shock. In high-resolution data obtained with the IMaX instrument on the balloon-borne Sunrise telescope, Khomenko et al. (2010) observed line profiles with small FWHM at the granular edges. They compared the observations with results of magneto-convection simulations and concluded that the narrow profiles originate from regions where the granular flows bend.

Recently, Bellot Rubio (2009) detected granular shocks in spectra obtained with the SOT/SP

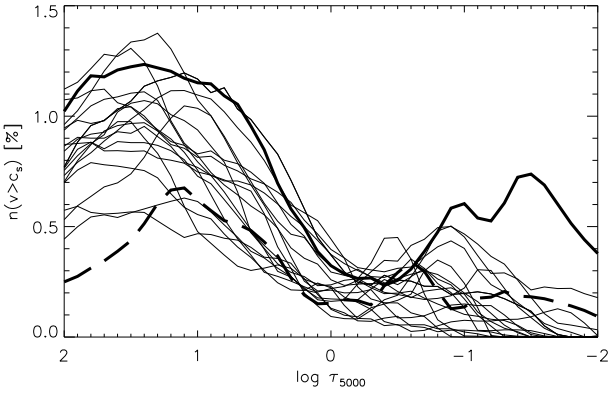

Figure 4.1: The fraction of $\mathrm{d}x \times \mathrm{d}y \times \mathrm{d}(\log\tau)$ cells with supersonic flows versus optical depth for disk center viewing with $\mu = 1$. Each curve represents one of the 20 analyzed snapshots. The supersonic flow may be in any direction. The thick solid curve corresponds to the snapshot with the largest abundance of supersonic flows (S1, lower row in Fig. 4.3), while the thick dashed curve corresponds to the initial snapshot (S0, upper row in Fig. 4.3).

instrument on Hinode (Suematsu et al. 2008). At its high-angular resolution, individual line profiles sometimes show shock signatures as considerable profile distortions, even as separate blue-wing satellite components. These high-quality observations motivated the present study in which we synthesize spectral line profiles from numerical simulations snapshots and compare them to the SP/SOT Hinode measurements of Bellot Rubio (2009).

4.2 Computational method

Model atmosphere. We use snapshots from a time-dependent 3D radiative magnetohydrodynamics (MHD) simulation of the quiet sun. The simulation was performed with the MURaM (MPS/University of Chicago Radiative MHD) code (Vögler & Schüssler 2003, Vögler et al. 2005) that successfully has reproduced multiple phenomena in the solar photosphere (e.g. Schüssler & Vögler (2006), Vögler & Schüssler (2007), Cameron et al. (2007), Cheung et al. (2007a), Schüssler & Vögler (2008), Rempel et al. (2009a), Cheung et al. (2010b)). The simulated box spans 6 Mm in the horizontal direction, evaluated at 288 grid points, and 1.4 Mm in the vertical axis with 100 grid points. This simulation setup was chosen by Khomenko et al. (2005b) in their study of quiet-sun Stokes diagnostics. Our simulation was restarted from one of their snapshots, which contains an average magnetic field of 30 G. We continued the simulation for approximately an hour of solar time. From this time sequence we extracted 20 snapshots at intervals of 3 minutes for further analysis.

Speed of sound. The local sound speed is computed from the results of the simulation. Since MURaM takes partial ionization into account, we evaluate the sound speed, c_s, from its

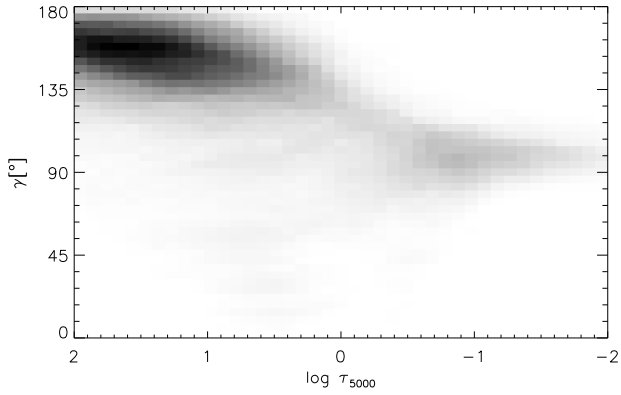

Figure 4.2: Two-dimensional histogram of the distribution of supersonic flows in optical depth and orientation ($\gamma = 0°$ corresponds to an upflow, $\gamma = 90°$ to a horizontal flow, and $\gamma = 180°$ to a downflow). The histogram is made from all snapshots. The populations of the horizontal flows and the vertical flows are separated in height. The horizontal flows are found mainly above the surface; the vertical flows below it.

general definition:

$$c_s = \left(\frac{\partial p}{\partial \rho}\right)_S = \left(\frac{\partial p}{\partial \rho}\right)_\varepsilon + \left(\frac{\partial p}{\partial \varepsilon}\right)_\rho \left(\frac{\partial \varepsilon}{\partial \rho}\right)_S ,$$

where p is the total gas pressure, ρ the density, ε the internal energy, and S the entropy. In the case of an isentropic process the last term is given by the first law of thermodynamics :

$$\left(\frac{\partial \varepsilon}{\partial \rho}\right)_S = \frac{p}{\rho^2}.$$

The partial derivatives of the pressure at constant density and internal energy are found from the precomputed tables of the equation of state $p(\rho, \varepsilon)$ (see Vögler et al. (2005)).

Skewing the snapshot. Since we are interested in the properties of the snapshot at different viewing angles μ, where $\mu = \cos\theta$ with θ the angle between the line of sight (LOS) and the vertical, we skewed the snapshots to mimic the center-to-limb variation of the quiet sun at $\mu = 0.4$ and 0.6. The periodic horizontal boundary conditions of the simulation enable evaluation along any LOS through the skewed snapshot. The skewing was done along the x-axis, in negative (towards the "left" limb) and positive ("right" limb) directions. The skewing method was adopted from Keller et al. (2004) and is described in detail by Vitas et al. (2010).

Line synthesis. We assume local thermodynamic equilibrium (LTE) for the spectral line synthesis, employing the LILIA code of Socas-Navarro (2001). The one-dimensional spectral synthesis was done assuming that the columns of the simulation snapshot along the LOS are independent, each representing a one-dimensional model atmosphere. We so synthesized the

two Fe I lines at 6301.5012 Å and 6302.4936 Å with a wavelength sampling of 12 mÅ. The atomic data for these lines were taken from Khomenko et al. (2005b).

Image degradation. To degrade the computed line profiles to the diffraction-limited angular resolution of the SOT on Hinode we adopt the ideal part of the empirical point spread function (PSF) of Wedemeyer-Böhm (2008). After the smearing, the computed intensities were resampled to the pixel size of 0.16 ″. It is important to note that, at disk center, roughly 6×6 simulation pixels correspond to one pixel in the SOT observations. Due to geometrical foreshortening, the number of simulation pixels per SOT pixel increases linearly with $1/\mu$ and, at $\mu = 0.4$, that number becomes as large as 90. In addition to that, the convolution with the PSF increases the number even further.

4.3 Velocity field

4.3.1 Statistics of supersonic events

We identified supersonic flows by comparing the magnitude of the velocity with the local sound speed at constant τ_{5000} surfaces in the simulation snapshots. The fraction of the surface occupied by supersonic flows, without distinguishing between different orientations, versus optical depth is shown in Fig. 4.1. It shows that shocks occur only rarely, less than 1.5% in any snapshots and at any optical depth in the plotted range. In the upper half of the range, that fraction is even smaller, exceeding 0.3% only occasionally as in the thick curve for snapshot S1. Projection of the horizontal supersonic flows in snapshot S1 to the horizontal plane occupies 2.5% of the surface, while projection of the vertical flows covers 1.6%. Projections of horizontal and vertical supersonic flows in snapshot S0 cover similar area of ∼1%. Similar to that, Stein & Nordlund (1998) found: "The shocks at the edges of intergranular lanes are [...] a rare occurance. At any one time, supersonic flow occurs in only ∼3%-4% of the surface".

Figure 4.1 shows that the amount of supersonic events in our simulation varies with time. This is in qualitative agreement with the findings of Malagoli et al. (1990), who identified distinguishable episodes of increased supersonic occurrences in their less realistic simulations.

Furthermore, Figure 4.1 suggests two different populations of supersonic cells: one below the surface ($2 > \log \tau_{5000} > 1$), and one roughly peaking at $\log \tau_{5000} > -1$. That finding is in agreement with results obtained by Gadun et al. (2000) in 2D simulations and by Stein & Nordlund (1998) in 3D.

The two-dimensional histogram in Fig. 4.2 shows the inclination angles γ of the supersonic flows versus optical depth for all snapshots. There are two distinct areas of increased occurence. The supersonic flows above the surface are predominantly horizontal with a slight tendency towards downflow, while the supersonic downflows are located in the layers just below the surface.

The largest Mach number of the predominantly horizontal supersonic flows is 1.37 and is reached at $\log \tau_{5000} = -1$. This is in a good agreement with Fig. 32 of Stein & Nordlund (1998).

4.3.2 Selection of events

In Fig. 4.3 we show the continuum intensity at 6300 Å, temperature, horizontal velocity and total magnetic field strength at the surface of constant optical depth $\log \tau_{5000} = -1$ for two snapshots. The upper row is taken from the initial snapshot which is characterized by a

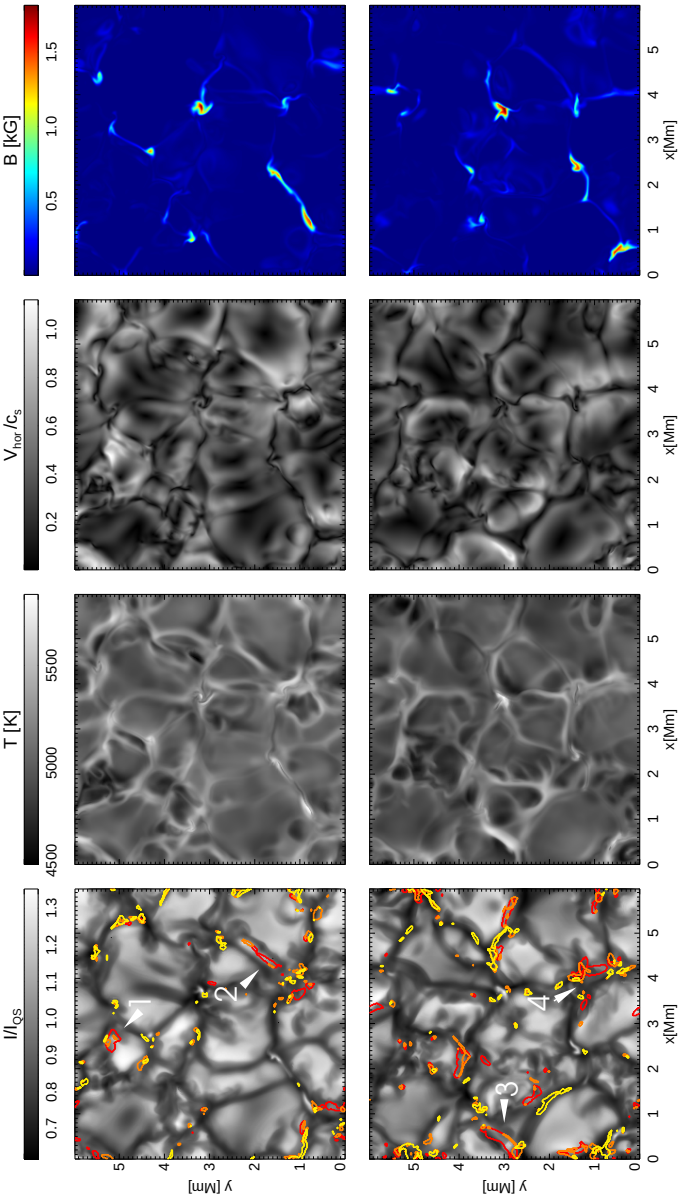

Figure 4.3: Maps of the two snapshots analyzed in detail (*top*, S0; *bottom*, S1). *From left to right:* continuum intensity at 6300 Å, temperature, magnitude of the horizontal velocity in units of the local sound speed, and total magnetic field strength at the log $\tau_{5000} = -1$ surface. Contours show the projection on the horizontal plane of cells containing supersonic flows (red specifies flows that are nearly horizontal $120° > \gamma > 60°$ and; yellow nearly vertical flows $180° > \gamma > 150°$ and $30° > \gamma > 0°$; orange flows with inclinations $150° > \gamma > 120°$ and $60° > \gamma > 30°$). The four numbered markers point to selected events discussed in detail in Sect. 4.3.2.

relatively small number of supersonic events in the photosphere (S0, thick dashed curve in Fig. 4.1). The lower row shows the snapshot with the largest abundance of supersonic flows (S1, thick solid curve in Fig. 4.1). The time separation between the two snapshots is only 6 minutes of solar time. Although that time is sufficient for the convective scenery to be largely changed, the magnetic field did not evolve as strongly.

The contours obtained by outlining the projection of the volume occupied by supersonic flows on a horizontal plane are overplotted on the continuum images. Different colors correspond to different inclination angles γ. The patches of horizontal supersonic flows occur above granular edges, whereas the vertical supersonic flows are located mainly in the downdrafts beneath the dark lanes.

The temperature maps in Fig. 4.3 show reversed granulation. This phenomenon has been studied extensively by Cheung et al. (2007b) as adiabatic heating at the granular edges. Superimposed on this pattern, the temperature maps in Fig. 4.3 show enhanced values at the locations where horizontal supersonic flows are present, indicating the presence of shock heating.

The horizontal velocity map (Fig. 4.3) shows "fountain-like" topology (Stein & Nordlund 1998). The horizontal velocity increases towards the granular edges, and vanishes at the very edge where the horizontal flows turn into downflows. The horizontal supersonic flows are not exclusively associated with large granules as it might be expected from a simple description of the solar granulation. Moreover, even in the large granules in our sample these flows do not occur symmetrically arround the granular rim, but only at a small fraction of the rim (Fig. 4.3).

Figure 4.3 also shows that large horizontal flows are generally not related to strong magnetic concentrations.

We select four events of fast horizontal flow in snapshots S0 and S1 for a more detailed analysis. They are indicated by markers in Fig. 4.3. Vertical cross-sections through the temperature and velocity stratification for events 1, 2 and 4 are shown in Fig. 6.9, while Event 3 is studied in more detail in Fig. 4.6.

Event 1 samples the edge of a small granule. The vertical cross-section in the first panel of Fig. 6.9 has an irregular shape with supersonic upward and downward flows close together. There is no clear shock front related to this event in the temperature distribution.

Event 2 (Fig. 6.9) is characterized by fast, mainly subsonic horizontal flows, containing only a few areas of supersonic velocities. An area of enhanced temperature is located at the front of the horizontal flow. It is a hot and coherent front where the velocities of a decaying shock have already dropped below the sound speed. The convection roll visible as a vortex flow in the vertical plane is very similar to the features analyzed by Steiner et al. (2010).

Event 3 is analyzed in Figs. 4.5 and 4.6. It is located at the edge of a large granule. The area contaning supersonic velocities is almost 1 Mm wide (extent of the red contour in Fig. 4.3) and extends over 300 km vertically (see Fig. 4.6). The time evolution of this event is shown in Fig. 4.5. Before the shock (bottom curve in the plot) the temperature at the granular edge is lower than at the center of the granule whereas the density increases towards the edge. This results in a pressure difference that accelerates the horizontal flow. In addition to that, the sound speed is locally reduced, and the flow reaches supersonic velocities. This leads to compression and a shock front. A well-defined shock front occurs in the temperature distribution (Fig. 4.3). It is also evident in the entropy in the middle right panel of Fig. 4.5. The subsequent upstream drift of the shock front can be traced in all six parameters shown in Fig. 4.5. When the velocity becomes subsonic, the temperature enhancement persists for some time, as in Event 2.

Finally, Event 4 is located in an area with supersonic flows on both sides of an intergranular

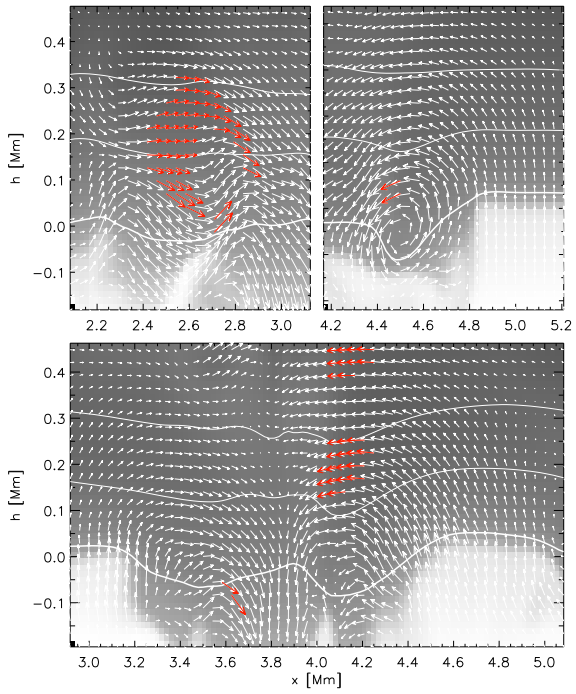

Figure 4.4: Vertical cross-section of temperature (gray scale) and velocity (arrows) for events 1 and 2 (upper panels) and 4 (lower panel) (cf. Fig. 4.3). Subsonic velocities are indicated by white arrows, red arrows correspond to supersonic velocities. White curves represent the $\log \tau_{5000} = 1, 0.1$ and 0.01 levels, respectively.

lane which contains strong magnetic field ($\approx$ 0.5 kG). This is the only case of supersonic horizontal flow close to a a strong-field concentration in these snapshots. As shown in 2D simulations (Steiner et al. 1998), granular flows and magnetic flux concentrations can interact in a complex manner leading, for example, to the bending and displacement of flux sheets. Such flux sheet dynamics are also capable of triggering shocks, providing an alternative shock production mechanism in addition to purely hydrodynamic, fast granular flows.

Event 3 seems to be the best example of a shock produced by a granular outflow; we select it for further analysis in the next section.

4.4 Shock signatures in Fe I 6301.5 Å

4.4.1 At full resolution

Figures 4.6 and 4.7 show parameters of Event 3 at five viewing angles obtained by skewing snapshot S1 to $\mu = 0.6$ and 0.4 towards the "left" and "right" limbs as described in Sect. 6.2.

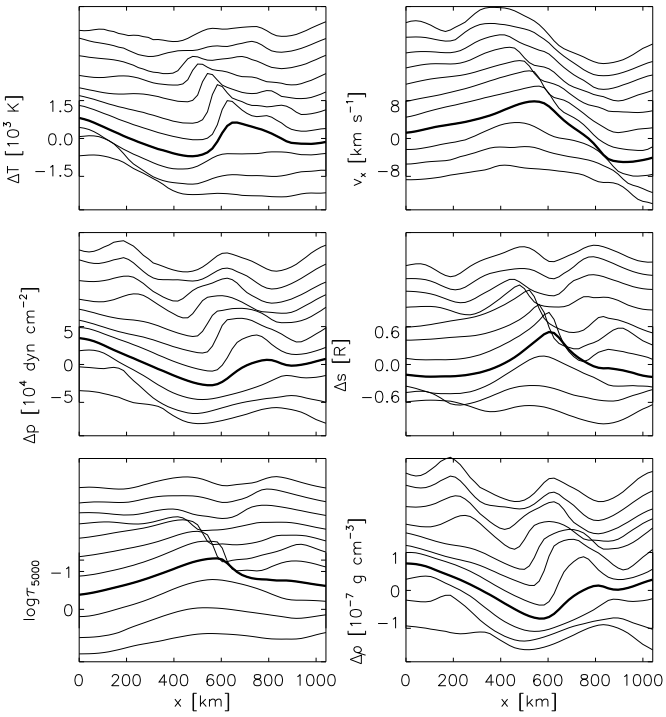

Figure 4.5: Temporal evolution of the shock front in event 3 at a fixed geometrical height of ~100 km above the average $\log \tau_{5000} = 0$ level. From the bottom up, the curves represent time samples at 25 s intervals. The scale on the vertical axis is for snapshot S1 (thick curve). The range of the horizontal axis is same as in Fig. 4.6. *Upper left panel*: temperature deviation from the horizontal mean; *upper right*: horizontal velocity (positive along x); *middle left*: pressure deviation from the horizontal mean; *middle right*: entropy deviation from the horizontal mean in units of the universal gas constant; *lower left*: $\log \tau_{5000}$; *lower right*: density deviation from the horizontal mean.

The upper row of Fig. 4.6 shows cross-sections in the x–h plane, where h measures height along the LOS and x is the simulation coordinate specified in arcsec to show the foreshortening. The grey scale shows the temperature, the arrows the velocity with red specifying supersonic values. The second row shows x–λ spectrograms synthesized along the cross-sections, with line profiles along the six LOS's indicated by color markers shown in the upper row of Fig. 4.7. Since the two lines behave so similarily, we only present results for Fe I 6301.5 Å in this paper. The stratification of the temperature and the velocity along the specified LOS's are plotted in Fig. 4.7 (middle and bottom row, respectively). The third row shows the x–y maps of the emergent continuum intensity.

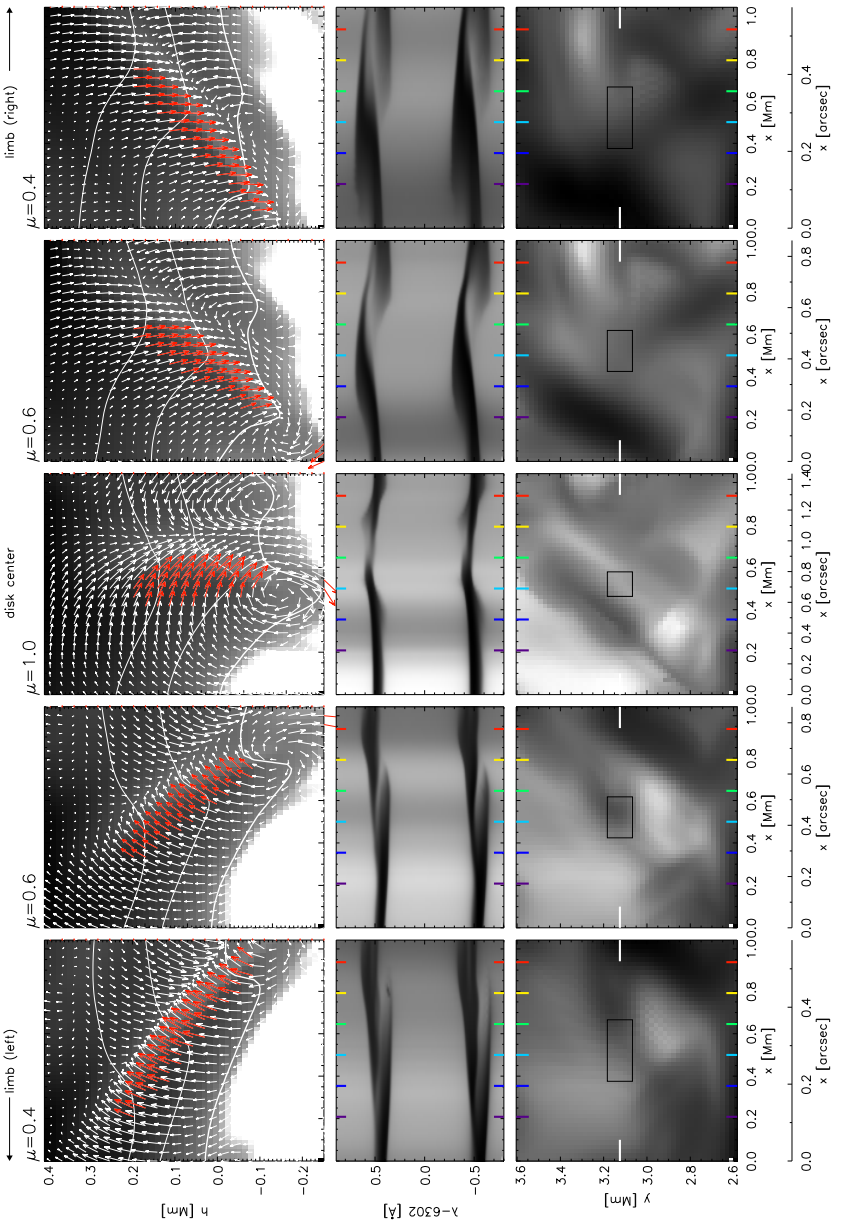

Figure 4.6: *Top row:* Vertical cross-section through event 3. Subsonic velocities are indicated by white arrows, whereas red arrows correspond to supersonic velocities. The temperature distribution is shown as a background in gray-scale. White curves represent the $\log \tau_{5000} = 1, 0.1$ and 0.01 levels, respectively. *Middle row:* Spectrogram of Fe I 6301.5 and 6302.5 Å synthesized from the cross-section; *Bottom row:* Continuum intensity maps of the area of the flow. The white markers specify the location of the vertical cross-section in the top panels. The five columns correspond to the five viewing angles specifed at the top. The h coordinate is measured along the line of sight (LOS). The x coordinate is the horizontal simulation coordinate in the center-to-limb plane containing the LOS, not the projected skewed coordinate. The projected extent in arcsec x' is added underneath. The color markers specify six LOS's shown in detail in Fig. 4.7. The box in the bottom row specifies the size of a SP/SOT pixel.

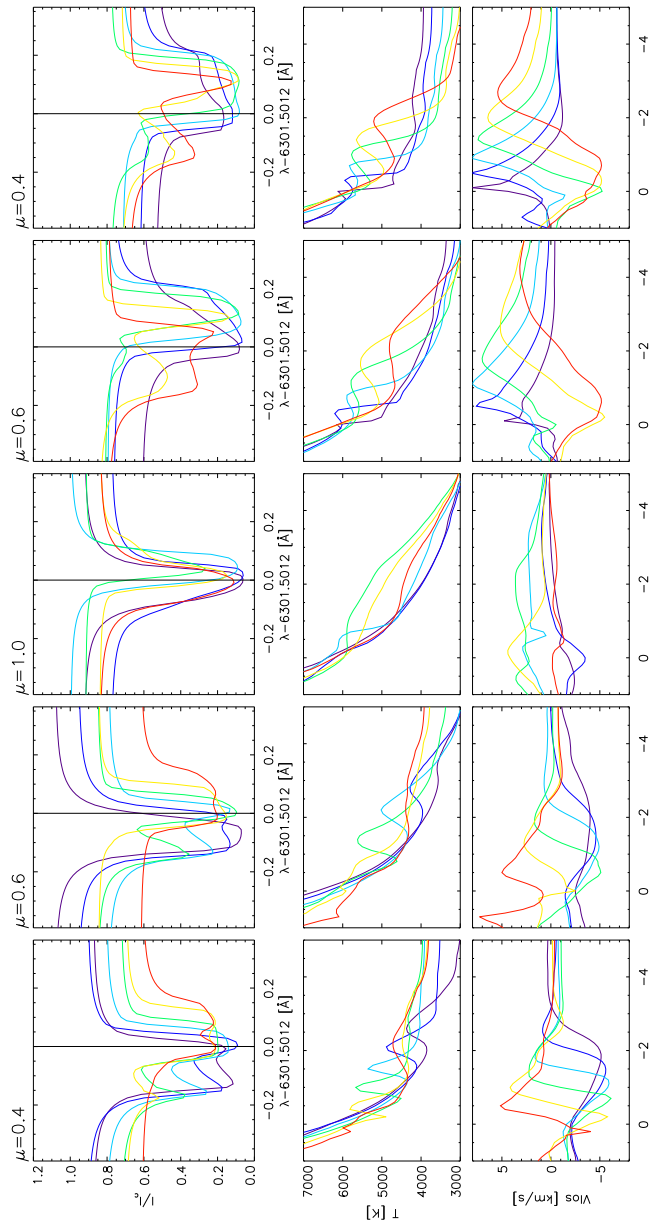

Figure 4.7: Profiles of the Fe I 6301.5 Å line computed for six LOS's corresponding to the colors (purple, blue, pale-blue, green, yellow, red) indicated in Fig. 4.6 for every μ (*top row*). Temperature and velocity distributions along these LOS's are shown in the *middle* and the *bottom rows*. Positive velocities correspond to motions away from the observer.

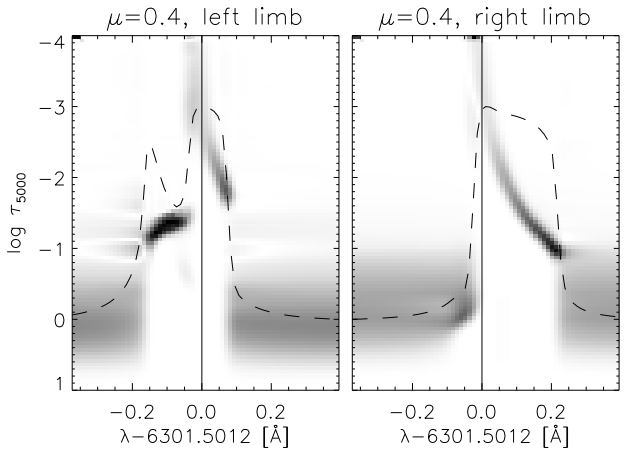

Figure 4.8: Response function of intensity to temperature variation computed for Fe I 6301.5 Å at $\mu = 0.4$ at opposite limbs. It is computed for the LOS that cuts through the center of the shock at the two disk locations (pale blue, first and fifth column of Fig. 4.6 and Fig. 4.7). Corresponding line profiles (dashed line) are overplotted in an arbitrary and inverted intensity scale.

Disk center

The velocity field in the shock is largely horizontal and has a negligible effect on the emergent line profiles (central columns of Figs. 4.6 and 4.7).

The pale-blue LOS defined in Fig. 4.6 cuts through the supersonic flow, the green and yellow LOS's cut through the hot shock front. The corresponding line profiles are slightly red shifted due to the flow turning downward.

The continuum intensity map (Fig. 4.6, center, bottom) is mainly determined by the deformation of the optical depth unity surface (specified with the white solid curve in the top row Fig. 4.6) due to the formation of the horizontal roll at the bottom edge of the shock. A dark stripe is clearly seen behind the shock where the optical depth unity surface is slightly elevated into higher and cooler layers as the density is locally increased. Similar dark zones are visible behind several of the other shock fronts in the simulated time sequence. The horizontal vortex tubes corresponding to bright granular edges were recently found in an MHD simulation analyzed in detail by Steiner et al. (2010). In IMaX/Sunrise observations they apear as a leading bright rim and following dark zone. The observed vortex tubes move toward the center of a granule, consistent with the upstream drift of a shock front we found in Fig. 4.5.

Away from disk center

Away from disk center, the velocity in the shock front is increasingly aligned with the LOS, and discrete features from Doppler shifts appear in the synthesized line profiles. These become quite complex as seen in the spectrograms (Fig. 4.6) and the individual profiles (Fig. 4.7).

As the different LOS's at a given μ at one limb sample the flow and shock front at varying heights, the profile asymmetries caused by the Doppler shifts appear at different positions

in the line profile. Where large velocities along the LOS combine with a local temperature enhancement, the line profiles extended strongly in one of the wings, or become even double-peaked with clearly visible satellites. Such satellites can appear in either wing depending on how the LOS samples the shock. An example can be seen at the "left" limb ($\mu = 0.4$) in the red and purple profiles where satellites appear in opposite wings. The LOS represented by the purple markers samples the shock at roughly $\log\tau = -2$, and the fast flow towards the observer broadens the blue wing. Along the LOS represented by the red markers the blueshift in the line profile is invisible because the shock sits below the $\log\tau = 1$ surface. The redshift observed in this line profile is actually caused by the horizontal flow towards the intergranular lane seen at the righthand side of the top center $\mu = 1$ panel of Fig. 4.6.

The flow directions in the shock also have a strong effect on the line profiles. The nearly horizontal motions in the shock at $\mu = 1$ lead to a clear separation of the core and the satellite when viewed head-on ("left" limb) and to profile smearing when viewed from the other side ("right" limb).

In Event 3 the fast flow is seen moving towards the observer at the "left" limb and the LOS cuts through the upper layers of the adjacent, centerward granule and through the intergranular lane. At the "right" limb, where the fast flow is seen moving away from the observer, the LOS cuts through the granular material behind the shock that has a locally increased opacity (cf., Fig. 4.5). As a consequence, at the "left" limb the hot shock front appears slightly narrower and higher up in the corresponding optical depth scale (compare the humps at the "left" and "right" limb in the temperature panels in Fig. 4.7).

Figure 4.8 shows response functions of the emergent intensity to temperature perturbations computed following Ruiz Cobo & del Toro Iniesta (1994) and Cabrera Solana et al. (2005) at the "left" and "right" limb in order to estimate where the line asymmetries are formed along the LOS. They are computed for the pale-blue LOS that cuts through the center of the shock at both limbs. At the "left" limb, the line has a blue-wing satellite with very localized temperature contribution which comes from the granular side of the shock where the temperature decreases with optical depth and the velocity along the LOS drops from 5 to 0 km/s. In contrast, at the "right" limb the extended red wing is formed in the layers where both temperature and velocity increase with optical depth, with the velocity ranging from nearly zero to supersonic values.

At the "left" limb, the temperature and source function increase with height in this region (Fig. 4.7), producing a reversal in the blue wing of the line and a full separation of the satellite component. In contrast, along the LOS at the "right" limb, due to the higher opacity, the shock front is shifted to slightly deeper layers and extends over a wider range in optical depth. The majority of these profiles do not show intensity reversals, as the temperature decreases monotonically with height in the regions of largest response in the wing.

The corresponding line profiles synthesized for the other three events show similar asymmetries.

4.4.2 At Hinode resolution

The line profiles are computed from the skewed snapshot. As the field of view is foreshortened away from disk center, we expand it to a square by replicating the 2D images in the limb direction at every wavelength. The images are then smeared to the angular resolution of the SP/SOT and resampled at the SP/SOT pixel size. After the spatial smearing and resampling, the profiles are also smeared to the SP/SOT spectral resolution and resampled at the wavelength step of this instrument. The large asymmetries seen in the high-resolution profiles vanish. In Fig. 4.9 a selection of emergent profiles for the 4 events is shown for the five viewing angles.

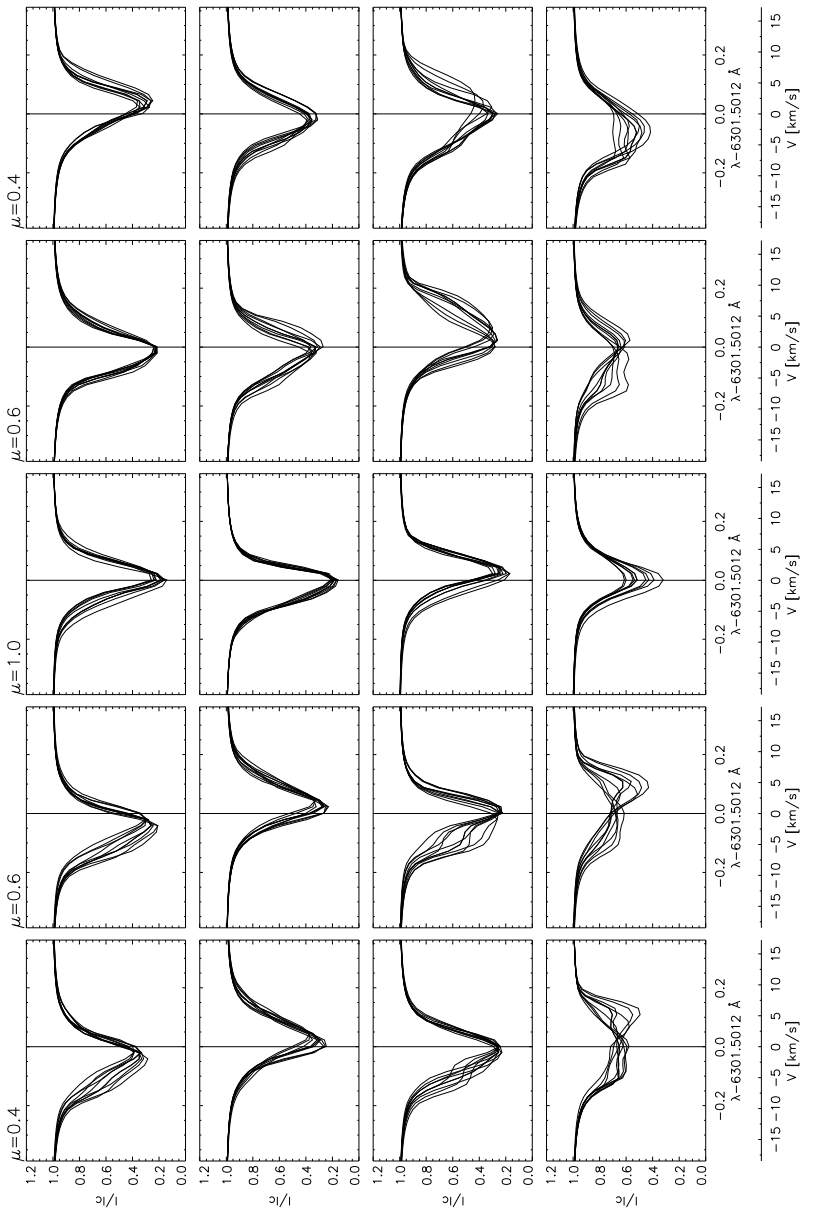

Figure 4.9: Profiles of Fe I 6301.5 Å computed for four events (see Fig. 4.3) after the images at every wavelength were degraded to the resolution of the SP/SOT Hinode. Rows from top to bottom correspond to Events 1, 2, 3 and 4, respectively. Columns correspond to five locations of the snapshot on the solar disk. We also the wavelength axis in terms of corresponding Doppler shifts.

The third row of Fig. 4.9 corresponds to the top row of Fig. 4.7. For each event, Fig. 4.9 plots the line profile for the central pixel and for the 8 surrounding pixels.

In all 4 events the disk-center profiles are only slightly broadened and/or shifted in comparison to their full-resolution counterparts. Away from disk center, the profiles of Events 1 and 2 are somewhat broadened but no clear satellites are visible at $\mu = 0.4$ or $\mu = 0.6$.

Event 3, identified as a supersonic flow with a well developed shock front, only shows the presence of the blue wing satellite when it is observed at $\mu = 0.4$ at the "left" limb. The profiles at the same μ at the "right" limb show only a hint of the second component, but the line in the central pixel corresponding to the shock area is redshifted as a whole.

Event 4 shows profile deformations in both line wings at both limbs. This event exhibits fast horizontal granular flows hitting the intergranular lane from opposite sides, causing two distinct components in the emerging line profiles.

Azimuthal dependence

Figure 4.6 shows how the line profile for Event 3, in the full spectral and spatial resolution, changes at the two limbs depending on whether the shock front is seen head-on ("left" limb) or from the other side ("right"). Thus, the orientation of the flow in the shock relative to the LOS determines the size and shape of the emergent profile. This projection effect will also affect the signature of the shock for different azimuth angles of the LOS (φ), which is defined here as having $\varphi = 0$ for the "left" limb with counter-clockwise rotation around the z axis of the snapshot seen from the top. To simulate this effect, the snapshot S1 was first rotated at disk center by multiples of 45° and then skewed to $\mu = 0.4$ to position the simulation box at 8 different limb locations[1]. The line profiles computed and degraded for every location are shown in Fig.4.10.

The shock front is curved and is seen nearly head-on for azimuth values between $\varphi = 0°$ and 45°. At $\varphi = 0°$ two separate components are clearly seen, one at the rest wavelength and the other shifted towards the blue by ≈ 7 km/s. In contrast to that, at $\varphi = 45°$ the line is broadened, entirely shifted to the blue, but no satellite component is present. Towards $\varphi = 180°$ where the shock is seen from the other side, the line core exhibits a red shift, whereas the asymmetry in the blue wing (satellite component or extended wing) diminishes. At $\varphi = 180°$ the profile is very broad with an extended red wing. Rotation from $\varphi = 180°$ to $\varphi = 360°$ shows the same change in the opposite direction.

Line asymmetries and shifts

The contours in the first row of Fig.4.11 show projections of volumes occupied by horizontal supersonic flows to the plane perpendicular to the LOS at every μ. Flows moving away from the observer are specified in red and flows moving towards the observer in blue. The projected area increases from ~2.5% at disk center to ~3.5% at $\mu = 0.4$.

Bellot Rubio (2009) searched for signatures of these flows in several parameters infered from the observed lines. He analyzed continuum intensity, equivalent width, full width at half maximum, line core velocity and used, in particular, bisector velocities $V_{\rm bi}$ to detect supersonic events[2]. In an empirical way, Bellot Rubio estimated that the value $V_{\rm bi} = \pm 2.6$ km/s at the 70%

[1] When the snapshot is rotated by 180° and then skewed towards the "left" limb, it is equivalent to a mirror-image of the non-rotated snapshot skewed to the "right" limb.

[2] The bisector velocity is the wavelength distance between the bisector of a line and its rest wavelength at a given fraction of the line intensity (cf. Grossmann-Doerth (1994)). Note that the bisector velocity

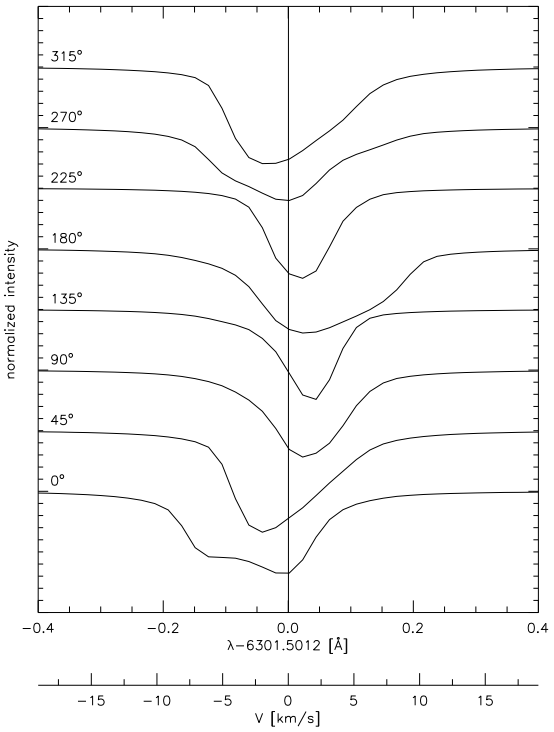

Figure 4.10: Line profiles of Fe I 6301.5 Å computed for Event 3 at $\mu = 0.4$ for eight azimuth values φ. All profiles are normalized to their local continuum. The vertical line indicates the rest wavelength of the spectral line.

intensity level represents an optimal threshold for the detection of supersonic flows. Using that criterion, he found that 0.3% of the field of view at $\mu = 0.55$ is covered by pixels with profiles showing $V_{\rm bi} < -2.6$ km/s, while pixels with $V_{\rm bi} > 2.6$ km/s occur very rarely. The negative velocities are observed at the edges of large granules, whereas the positive ones are observed "almost exclusively in intergranular lanes".

To test the robustness of the criterion and the chosen threshold, we measured $V_{\rm bi}$ of the profiles synthesized from snapshot S1 and degraded to the SP/SOT Hinode resolution, again for our five viewing angles. For the rest wavelength we adopt the value that we used to synthesize the profiles (6301.5012Å). The detection results are plotted over the continuum intensity maps in the second row of Fig.4.11. Pixels with $V_{\rm bi} < -2.6$ km/s and $V_{\rm bi} > 2.6$ km/s are indicated with blue and red contours, respectively.

In contrast to Bellot Rubio's identification of predominantly negative bisector velocities

does not say anything about line asymmetry with respect to the line core, but only with respect to the rest wavelength. For example, if the radial velocity is constant with height, the spectral line will be shifted by the value of the bisector velocity, but relative to the line core, it will remain symmetric.

above the threshold, events with both positive and negative velocities are similarily abundant in the synthetic observations. Event 3 is detected at the "right" limb where the flow is moving away from the observer (red contour), while it is invisible at the opposite limb. The line profiles in the supersonic flow of Event 4 show bisector velocities above the threshold at both limbs. At the "right" limb the flow is towards the observer (blue contour), and at the "left" limb it moves away from the observer (red contour). In addition to these two events, another small supersonic flow is correctly identified at the "right" limb at both $\mu = 0.6$ and 0.4, while all other supersonic flows remain undetected. Apart from these detections, there are few wrongly-identified pixels, all with negative bisector velocities.

Therefore, the fraction of pixels correctly detected as supersonic varies significantly with the viewing angle. For example, at $\mu = 0.6$ at the "left" limb, the method detects horizontal supersonic flows moving away from the observer in ∼0.6% of the area (red contour), in comparison to ∼1.4% found in the simulation. At $\mu = 0.6$ at the "right" limb, the detected area of the supersonic flows moving away (∼1.3%) agrees well with the area found in the simulation.

Bellot Rubio speculated that the difference in the number of identified flows with positive and negative bisector velocities and the presence of satellites in the blue wings exclusively may be due to the flows at the far side of the granules occuring below the optical depth unity surface. However, our analysis shows that supersonic horizontal flows do produce observable asymmetries in both line wings, i.e., at both disk-center and limb side of a granule. Another reason for the unequal abundance of detected supersonic flows moving in opposite directions in the observations of Bellot Rubio (2009) may be presence of an offset in the rest wavelength determined as the location of the minimum of the average line profile over the entire field of view. To estimate the influence of such an offset, we apply artificial shifts to our adopted rest wavelength.

The third and fourth row of Fig. 4.11 show results after the rest wavelength has been shifted toward the red by $\Delta\lambda = 5$ mÅ and 10 mÅ, corresponding to Doppler velocities of 240 m/s and 480 m/s, respectively. The detection of supersonic events changes significantly. As expected, the number of pixels exhibiting $V_{\rm bi} < -2.6$ km/s increases, while the number of pixels with $V_{\rm bi} > +2.6$ km/s decreases. Events 3 and 4 are clearly detected as fast flows moving towards the observer, whereas the contours identifying motions away from the observer are strongly reduced. At the "left" limb, Event 4 disappears, whereas Event 3 appears. Hence, the precise determination of the reference wavelenght is very important for the correct detection of supersonic horizontal flows.

Finally, to estimate how the detection of the flows depends on the chosen value of the threshold, we reduce that value from 2.6 km/s to 2.0 km/s in steps of 0.2 km/s. Obviously, the number of pixels identified as supersonic increases with decrease of the threshold causing a clear detection of Events 3 and 4 at both limbs. However, the area of pixels misidentified as supersonic also increases. This result supports the empirically determined threshold of Bellot Rubio (2009).

4.4.3 Line broadening

Nesis et al. (1992) argued that the spectral line broadening they observed at disk center in the dark intergranular lanes was evidence of post-shock turbulence caused by supersonic horizontal flows. Solanki et al. (1996) made a comperative study using 2D granulation simulation. They found that even without supersonic horizontal flows a significant line broadening was observed in the synthetic spectral lines that were smeared to mimic observations. They

showed that, at disk center, both, horizontal gradients in the vertical and horizontal velocity at the full resolution are able to reproduce the broadend line profiles after smearing. They concluded that the broadend profiles observed in the dark lanes by Nesis et al. (1992) were not necessarily an indication of supersonic flows, whereas the observations in Nesis et al. (1993) of line broadend profiles at the edges of granules, between the granule and the intergranular lane, were more likely due to turbulence caused by supersonic flows.

Keller (2006) suggested a simple mechanism able to produce broadend line profiles at the edge of granules with no additional turbulence needed. We perform the computation for Fe I 6301.5 Å, the less-magnetic of the two iron lines and illustrate the result in Fig. 4.12. The normalized continuum intensity along a spatial direction is compared to the variation in FWHM of the unsmeared and smeared profiles in the upper panel. As a smearing function we employ a Gaussian with a width comparable to the width of the PSF of SOT on Hinode. At $x = 2.4$ Mm and 5.4 Mm, we find enhanced line broadening at locations of steep intensity gradients. This is seen even clearer after smearing of the profiles. At $x = 0.5$ Mm, the spectral line shows a greater FWHM after smearing, even though that was not the case before smearing.

To demonstrate the effect of the smearing on the FWHM, we alter the line profiles to artificially keep the FWHM constant throughout the sample. In the lower panel of Fig.4.12, we show that even in that simple case, when the profiles have the same FWHM and differ only in Doppler velocity and intensity, the smearing produces line broadening, especially at locations of steepest continuum intensity gradient, as seen at $x = 4.2$ Mm and $x = 0.6$ Mm. Line broadening is therefore not a reliable indicator for supersonic horizontal flows.

4.5 Discussion and conclusions

Although the large asymmetries in the computed Fe I 6301.5 Å profiles are smeared out almost completely at the SP/SOT Hinode resolution at $\mu = 0.4$ and 0.6, various line-profile deformations remain visible, even with a few discernable satellites in the blue wing (Fig. 4.9). This is in good agreement with the measurements of Bellot Rubio (2009) who identified satellite components of the Fe I 6301.5 Å line exclusively in the blue wing of the observed profiles. In addition, we find extended red wings corresponding to the supersonic flows moving away from the observer at the limb side of granules.

Figure 4.11: Continuum intensity map computed from snapshot S1 at $\mu = 0.4$ and 0.6 at the "left" limb, at disk center, and at $\mu = 0.6$ and 0.4 at the "right" limb (from *left* to *right*). Away from disk center, the foreshortened maps are replicated to fill a square. *First row*: Contours show projection of volumes with supersonic horizontal flows to the plane perpendicular to the line of sight. Flows moving towards the observer are specified in blue; flows moving away from the observer in red. *Second row*: Supersonic flows detected as pixels with bisector velocity smaller than −2.6 km/s (blue contours) and larger than 2.6 km/s (red). The zero wavelength for the bisector measurement is the laboratory wavelength of the Fe I 6301.5012 Å line. *Third* and *fourth row*: The zero wavelength is shifted by 5 and 10 mÅ towards the red, respectively. In the bottom three rows, the zero wavelength is the laboratory wavelength for all panels, but the threshold for the determination of supersonic flows varies: ±2.4 km/s (*fifth row*), ±2.2 km/s (*sixth*) and ±2.0 km/s (*seventh*)

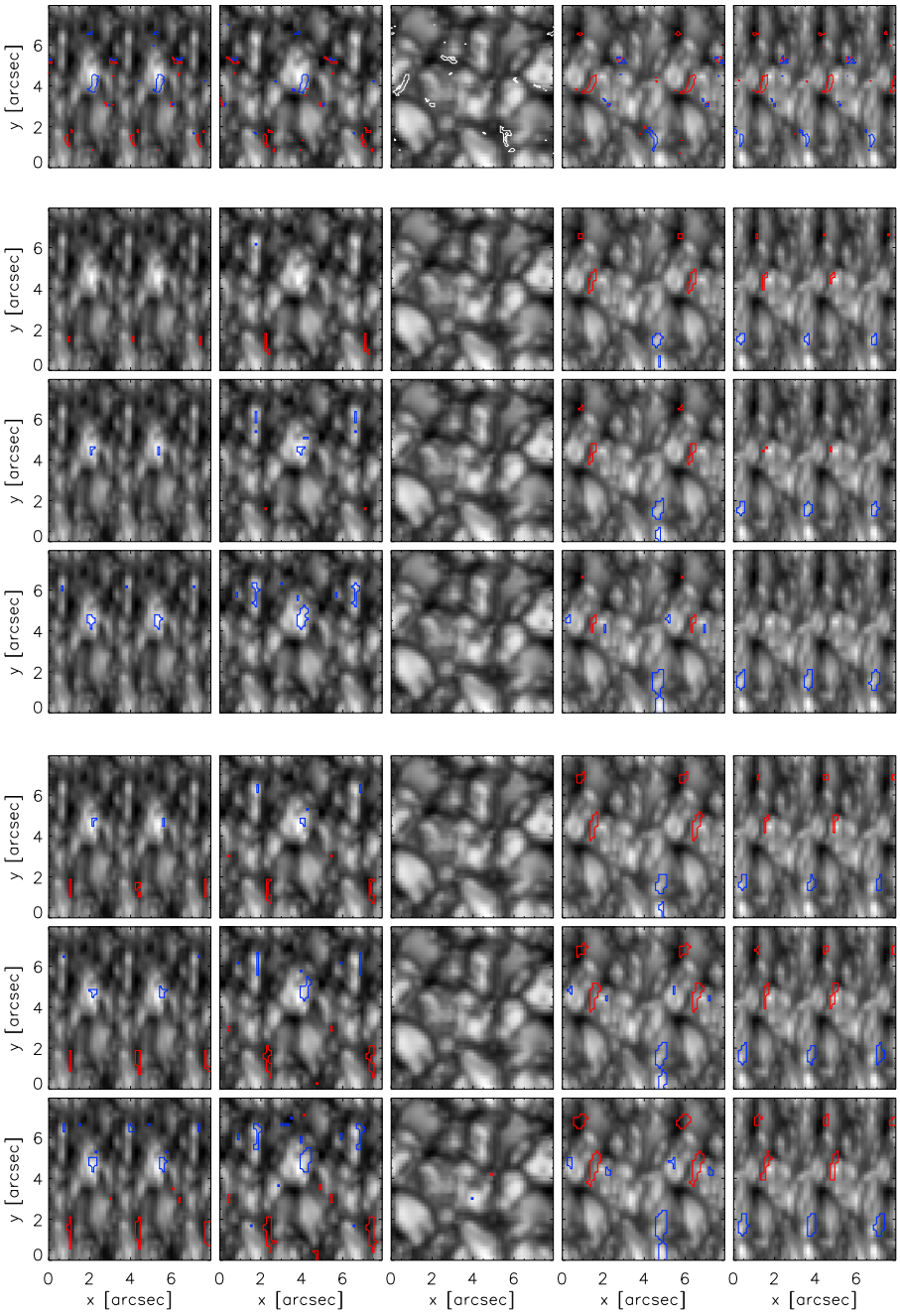
y [arcsec]
0
2
4
6
x [arcsec]
0
2
4
6

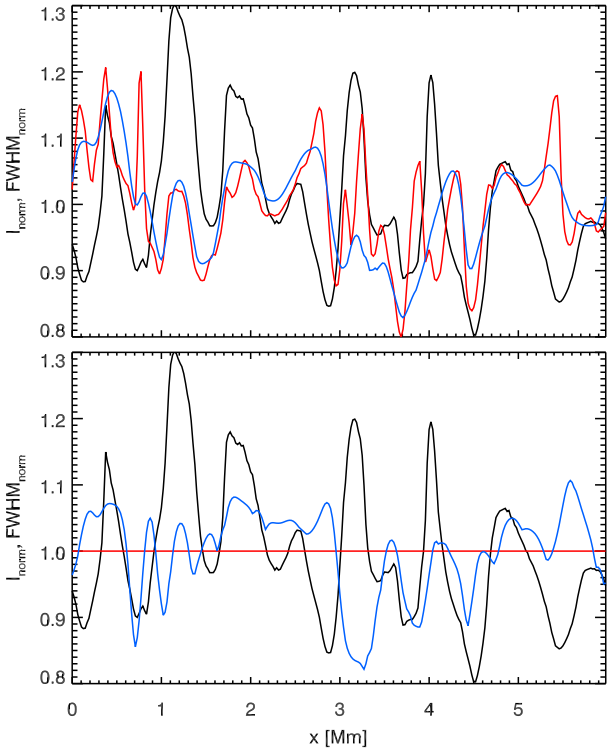

Figure 4.12: Comparison of FWHM before and after smearing. *Upper panel:* The black curve shows the normalized continuum intensity along a spatial direction at the full resolution of the snapshot. The red curve shows the FWHM of the spectral line profile corresponding to the spatial location at the full resolution snapshot; the blue curve, the FWHM of the spatial location in the smeared snapshot. The quantities are normalized to their average. *Lower:* same as in the upper panel, after the FWHM was fixed to a single value.

Bellot Rubio (2009) defined an empirical criterion for automatic detection of supersonic horizontal flows through bisector measurements, setting a treshold of 2.6 km/s for the absolute bisector velocity at 70% of the line intensity to indicate such flows. Our analysis shows that his method of detection is generally applicable and supports his conclusion that this ±2.6km/s threshold is rather conservative. However, we note that the bisector velocity analysis can be used to identify only a certain class of horizontal supersonic flows as was already pointed out by Solanki et al. (1996). Only large volumes with directionally coherent supersonic flows can be unambiguously detected. Furthermore, the LOS has to be sufficiently aligned with the flow. This alignment obviously depends on the azimuthal direction of the flow and the heliocentric angle. The number of pixels detected as supersonic is also critically sensitive to ad hoc parameter choices. For a lower threshold value we indeed obtain more supersonic flow detections, but with an increasing fraction of false identifications. In addition, this supersonic

flow detection method critically depends on a precise wavelength calibration.

In our simulation, at disk center, projection of the supersonic horizontal flows covers ~2.6% of the surface. The surface coverage increases limbward, in snaphsot S1 it reaches ~3.5%. Using the bisector velocity analysis, Bellot Rubio (2009) identified supersonic flows in 0.3% of the field of view. The difference between this number and the abundance of the flows found in the simulation of Stein & Nordlund (1998) has been attributed by him to the projection effects. In Sect. 4.4.2 we simulated the measurements of Bellot Rubio (2009). The results of this simulation show that the fraction of correctly identified supersonic pixels depends on the viewing angle, threshold used, and the position of the reference wavelength. This fraction can vary from almost zero (e.g., first column, second row of Fig.4.11) to more than one (e.g., fourth column, third row of Fig.4.11).

However, our analysis is based on 20 simulation snapshots covering in total an area ~10 times smaller than the area observed by Bellot Rubio (2009). It would be necessary to employ much larger numbers of snapshots to quantify the fraction of supersonic pixels that can be detected by Bellot Rubio's method. Without such a quantification we cannot rule out an additional mechanism able to accelerate the flows to supersonic velocities. One possible mechanism that is not present in our simulation and can trigger supersonic flows is magnetic flux emergence as shown by Cheung et al. (2007a) in their large-scale simulation. Bellot Rubio has considered the possibility that a similar mechanism can operate on small-scales as well, but no clear evidence was found in the observations. The next step consists in simulating flux emergence at granular scales, studying how it affects the dynamics of horizontal granular outflows, and synthesizing the corresponding observational signatures.

Acknowledgments

We thank to R. J. Rutten for carefully reading the manuscript and making numerous comments and suggestions that significantly improved it. We thank J. de la Cruz Rodríguez, L. Bellot Rubio, R. Keppens and R. F. Stein for useful discussions. We also thank S. Wedenmeyer-Böhm for making available the point spread function of the SOT on Hinode, E. Khomenko for providing the initial snapshot of our simulation, and H. Socas-Navarro for the opportunity to run the simulations on the LaPalma Supercomputer. The authors thankfully acknowledge the technical expertise and assistance provided by the Spanish Supercomputing Network (Red Española de Supercomputación), as well as the computer resources used: the LaPalma Supercomputer, located at the Instituto de Astrofsica de Canarias. This research is supported by a Marie Curie Early Stage Research Training Fellowship of the EC's Sixth Framework Programme under contract number MEST-CT-2005-020395. This research has made use of NASA's Astrophysics Data System.

There are painters who transform the sun into a yellow spot, but there are others who, thanks to their art and intelligence, transform a yellow spot into the sun.
— Pablo Picasso

Chapter 5

Observational signatures of a simulated sunspot umbra: I. Continuum intensity from 4000 to 16500 Å

N. Vitas, A. Vögler and C. U. Keller*

Abstract

The fine structure of sunspot umbrae is a key to understanding the structure and evolution of sunspots. A break-through was made in the theory of umbral dots when a realistic 3D radiative MHD simulation reproduced the general appearance of a sunspot umbra for the first time (Schüssler and Vögler, 2006). We investigate the emergent monochromatic continuum radiation computed from a state-of-the-art 3D MHD simulation of a sunspot umbra in the context of the available observations at various wavelengths and heliocentric angles. A snapshot from a 3D MHD simulation is used to synthesize the continuum intensity in the visible and near-infrared as a function of the heliocentric angle. The simulation explains the morphology of umbral dots at disk center as well as their brightness relative to the dark background. Away from disk center, it predicts a characteristic change in the appearance of the umbral dots depending on their orientation relative to the center-limb direction. The overall brightness of the simulated umbra at disk center is lower than in the observations. The center-to-limb variation of the emergent continuum intensity computed from the 3D simulated umbra is smaller than the one computed from 1D models. This difference is produced by the umbral inhomogeneities.

*Accepted for publication in *Astronomy & Astrophysics*

5.1 Introduction

High-resolution images of sunspot umbrae reveal their inhomogeneous nature with features of different size, brightness and lifetime (e.g., light bridges, central and peripheral umbral dots, dark voids) embedded in a grainy and/or filamentary dark background (DB) (e.g., Sobotka (1997), Sobotka & Puschmann (2009)). Biermann (1941) already realized that the darkness of sunspot umbrae relative to the quiet sun (QS) is basically due to strong magnetic fields inhibiting the convective energy transport. On the other hand, early magnetohydrostatical models (Schlüter & Temesváry 1958, Deinzer 1965, Gokhale & Zwaan 1972) indicated that some form of convection must take plase, and the umbral fine structure is a signature of it (Thomas & Weiss (2008), and references therein).

There were two main aproaches in the theoretical modeling of umbral inhomogeneities. The small and bright umbral dots (UDs; first observed by Thiessen (1950)) may be explained either as a consequence of oscillatory convection in a flux tube (overstable oscillatory convection, Danielson (1965); non-linear oscillatory convection, Knobloch & Weiss (1984); overshooting by oscillatory convection from deeper layers, Weiss et al. (1990)) or as penetrations of hot material due to convective overstability of field-free plasma in the regions below the radiative layer (Severnyi 1965, Obridko 1974, Parker 1979). Both approaches (known as "monolithic" and "cluster" model, respectively) were able to interpret the existence of the umbral dots, though a direct comparison with observations has been missing.

The details of the formation of UDs were revealed for the first time in an ab initio 3D MHD simulation of magnetoconvection in strong magnetic fields performed by Schüssler & Vögler (2006). The recent, large scale MHD simulations of sunspots (Rempel et al. 2009a,b) put that simulation of an isolated umbra in a wider context. In these simulations oscillatory convection columns below the surface become overturning cells in the layers where the radiative cooling is significant, giving it an appearance of bright dots on a dark background in intensity maps (Fig.1 of Schüssler & Vögler (2006)). Moreover, the simulations predict a characteristic UD morphology with a single or multiple dark lanes in its center. That prediction was confirmed in observations by Bharti et al. (2007), Rimmele (2008) and Ortiz et al. (2010).

In a recent paper, Bharti et al. (2010) studied a long simulation run started from the last snapshot of the sequence described by Schüssler & Vögler (2006). They demonstrated that the simulation run has two distinctive phases: the thermal relaxation phase characterized by radiative cooling and the quasy-stationary phase in which convection becomes more efficient. These authors also analyzed in detail statistical properties of the simulatied time sequence in its original resolution (in bolometric intensity and continuum intensity at 6300 Å).

Although overall qualitative agreement between the results of the simulation and the available observations was obtained, a more detailed quantitative comparison between the umbral simulation and the observations is needed. The major difficulty is that there is no standard sunspot observation to compare to theoretical models of an umbra as it is the case, for example, with the quiet sun (see Nordlund et al. (2009)).

This is particularly problematic when an isolated umbra is considered because it does not take into account the variety of sunspots that are observed, the horizontal gradients, and the large scale inhomogeneities present in each individual umbra. The simulation snapshot studied here represents a portion of a sunspot umbra located between a dark umbral core (where no UDs are present) and the umbral periphery (where the magnetic field becomes inclined toward the penumbra).

In this paper we analyze monochromatic continuum intensities computed in a broad spectral range (from 4000 to 16500 Å) from a single snapshot of a 3D MHD simulation run similar to the one of Schüssler & Vögler (2006). We discuss our results in the context of the available continuum observations. The simulation run and the details of the continuum computation are described in Sect. 5.2. In Sect. 5.3 we discuss the general properties of the studied snapshot. Sect. 5.4 presents the results of the emergent continuum computation when the snapshot is viewed from above as in disk-center observations. We describe the morphology of the simulated umbral inhomogeneities and the automatic identification of UDs, and compare our simulation to a semi-empirical 1D sunspot model. The variation of the emergent continuum radiation of the simulated umbra with heliocentric angle is the topic of Sect. 5.5. We summarize our findings in Sect. 6.5.

5.2 Method of computation

5.2.1 Simulation setup

We use a single snapshot from a time-dependent simulation with the MURaM (MPS/University of Chicago Radiative MHD) code (Vögler & Schüssler 2003, Vögler et al. 2005). MURaM solves the three-dimensional, time-dependent MHD equations including non-local and non-gray radiative transfer and accounting for partial ionization. It has already been successully applied to various problems of solar surface magnetism (e.g., Keller et al. (2004), Schüssler & Vögler (2006), Vögler & Schüssler (2007), Cameron et al. (2007), Cheung et al. (2007a), Schüssler & Vögler (2008), Rempel et al. (2009a,b)). The simulation run has been started as the one described by Schüssler & Vögler (2006) with a homogeneous, vertical seed field of 2.5 kG. After it has reached a stationary state, the radiative transfer evaluation was changed from gray to non-gray with four opacity bins (Vögler (2004)), and the computation was continued until a stationary state was reached again.

The horizontal extent of the snapshot is 5.76 Mm sampled in 288 equally-spaced grid points per axis and the vertical extent is 1.6 Mm with 160 grid points. The size of a horizontal grid cell corresponds to 0.027''at the solar disk.

5.2.2 Continuum computation

To compute monochromatic continuum intensities from the snapshot, we used the continuum opacities by Kurucz (1993). The optical depth at the top boundary of the

simulation box is found assuming hydrostatical equilibrium[in the layers above the boundary]. The values of $\log \tau_{5000}$ at the top boundary are between -6 in DB and -2 in the central parts of UDs. The larger opacity of the UDs makes this snapshot not suitable for computation of even medium-strength lines (e.g., the Fe I 6302 Å lines), though the simulation box extends high enough to allow the computation of the emergent continuum.

For the continuum computation, vertical columns in the simulated cube were treated as independent lines-of-sight. All intensity computations were performed assuming local termodynamical equilibrium (LTE) with LILIA (Socas-Navarro 2001) for wavelengths from 4000 to 16500 Å in 100 Å intervals. In the following analysis we focus on the continuum at 6300 Å because continuum observations at that wavelength come as a by-product of the observations in Fe I 6302 Ålines that are one of the most common spectropolarimetric diagnostics.

5.2.3 Skewing the snapshot

The periodic lateral boundary condition of the simulated snapshot makes it possible to study the center-to-limb variation of the synthetic continuum radiation emerging from the complete cube. We follow the approach of Keller et al. (2004) and skew the snapshot to easily calculate the intensity emerging under an angle. All intrisic variables of the simulation (density, magnetic field, velocity, total energy, pressure and temperature) were interpolated to the new, inclined grid. Since every horizontal cross-section of the simulated box is periodic, the Fourier shift theorem provides an excellent tool for sub-pixel interpolation (Chen & Weinhous 1999). Every horizontal slice is transformed to the Fourier space, the phase is changed to represent a shift dependent on the height of the slice in the simulated box, and inverse Fourier transformed. Additionally, components of magnetic field and velocity are projected corresponding to the new line-of-sight. Optical depth is then calculated along the new line-of-sight and all variables are interpolated to an equidistant scale in optical depth. The emergent continuum is finally computed from the skewed snapshot along the lines-of-sight.

5.3 General properties

The temperature, local density fluctuation, line-of-sight velocity, vertical and horizontal component of the magnetic field of the snapshot at the $\tau_{5000} = 1$ surface are shown in Fig. 5.1. The simulated umbra is indeed similar in appearance to a dark sunspot umbra with strong and predominantly vertical magnetic field and local excesses of temperature that are reminiscent of UDs. According to Schüssler & Vögler (2006) these hot spots at $\tau_{5000} = 1$ correspond to cusp-like overturning cells that are a consequence of oscillatory convection in the layers below the surface. In the surface layers, where radiative losses become significant, the density in the cusp is enhanced and the level of the $\tau_{5000} = 1$ surface is elevated to higher and cooler layers (cf. Fig. 2

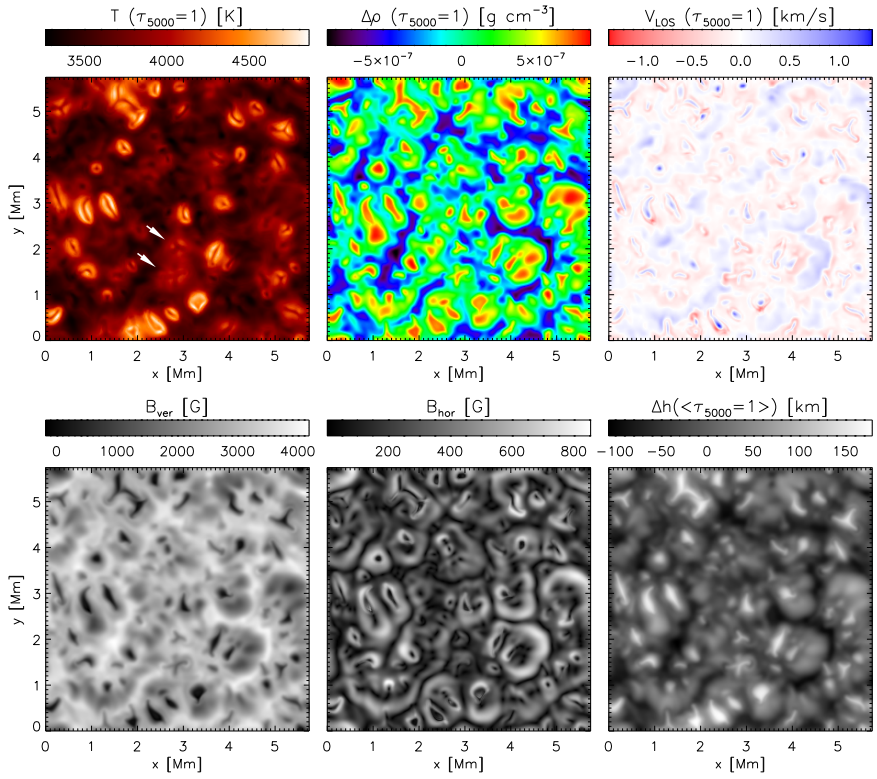

Figure 5.1: Sections through a snapshot of a simulated sunspot umbra. *Upper row*: temperature (left, arrows show two examples of decaying UDs), deviation from the local mean density (center) and line-of-sight velocity (right, blue corresponds to an upflow and red to a downflow); *Lower row*: vertical (left) and horizontal (center) component of the magnetic field vector, and differential Wilson depression (right, see text for details). All quantities are shown at constant optical depth $\tau_{5000} = 1$.

and Fig. 3 of Schüssler & Vögler (2006)). Consequently, most of the simulated UDs show single or multiple central lanes of low temperature that correspond to local density enhancements ($\approx 10^{-6}$ g cm^{-2}), upflows ($\approx 2 \times 10^4$ cm s^{-1}) and relatively low magnetic fields (< 1 kG).

If the UDs are masked out from the snapshot with a temperature threshold $T(\tau_{5000} = 1) < 4100$ K, the remaining background is not homogeneous either but additional features can be identified, particularly in the panels showing the distribution of temperature, horizontal ($B_{\rm hor}$) and vertical ($B_{\rm ver}$) magnetic field. Some of them can be attributed to decaying UDs (arrows in the temperature panel of Fig. 5.1). In the intensity map (see Sect. 5.4.1) these features appear as a low contrast grainy component of the background. In addition to that, elongated cool ($T(\tau_{5000} = 1) \approx 3000$ K)

structures characterized by strong (> 3 kG) and almost completely vertical (< 5°) magnetic fields, low densities and very slow motions can be identified. These structures can be traced to the bottom of the simulation box. They roughly outline regions were the UDs are formed. We call them "magnetic barriers".

The lower-right panel of Fig. 5.1 shows the deviation of the $\tau_{5000} = 1$ surface from the height where the average optical depth $\langle\tau_{5000}\rangle = 1$. It is a measure of the differential Wilson depression and roughly shows the difference in height between the continuum formation layers in the UDs and in the DB (cf. Socas-Navarro et al. (2004)).

5.4 Disk center

5.4.1 Morphology

Figure 5.2 shows continuum intensity maps at 6300 Å synthesized from the selected snapshot. The lefthand panels show the entire field of view and one selected and enlarged UD at the intrinsic resolution of the simulation, while the central and righthand maps show the same after the image was degraded. The blurring function in the central and righthand panel is a Gaussian with a FWHM of 0.16″and 0.32″, respectively. The pixel size in the degraded images is half of the FWHM used for the smearing.

Umbral dots in the synthetic intensity maps have rounded, elongated or iregullar shapes with single or multiple dark central lanes. Schüssler & Vögler (2006) suggested that the manifold of the dark lanes is due to different modes of the fluting instabilities in the upper parts of the UDs. Simulated UDs appear either as individual dots or grouped in clusters. The clusters observed in low resolution might appear as oversized umbral dots with central darkening (e.g., the cluster of UDs at the top of FOV). The surrounding diffuse background is inhomogeneous. The faint small and/or decaying dots visible at limited spatial resolution might appear as grainy structures (see Sobotka & Puschmann (2009)). "Magnetic barriers", described in Sect. 5.2, correspond to the darkest regions free of UDs in the intensity maps (Fig. 5.2).

Automatic identification of UDs. It is a common observational practice to identify UDs as features that occupy pixels with intensity ratios $I_c/\langle I_c\rangle$ larger than an arbitrary threshold, where I_c is the continuum intensity at a fixed wavelength (Sobotka et al. (1997))[1].

Additionally, to minimize the influence of noise, it is required that the features identified in this way are larger than a certain size (e.g., 3 pixels= 0.48″ in Watanabe et al. (2009b)). In Fig. 5.3 isophotes corresponding to thresholds of 1.2 (red contours) and 1.6 (blue) are shown. With the high threshold, all UDs are clearly identified and

[1]For more sophisticated methods of automatic identification see Riethmüller et al. (2008b) and Bharti et al. (2010).

separated from the background. If the identification is performed in the $T(\tau_{5000} = 1)$ map, very similar results are obtained for a temperature threshold of $T = 4100$ K (orange contours in Fig. 5.3). The green contours outline UD pixels that would be identified by the method of Sobotka if the intensity map was blurred to a resolution of 0.32''and rebinned so that the pixel size is 0.16''. It is important to emphasize that the threshold for the UD identification depends on many parameters (wavelength, heliocentric angle, instrumental diffraction, stray light contribution, etc).

Size and filling factor. It is clear that the effective radii D (Sobotka & Hanslmeier 2005) of the UDs depend strongly on the chosen intensity threshold. We computed values of D of the UDs selected in Fig. 5.3 assuming two different thresholds. With an intensity threshold of 1.2 (1.6), D is in the range 0.13''to 0.46''(0.08''to 0.36''). For the smaller (larger) threshold the bright component occupies 18% (10%) of the total FOV. These values agree well with the most recent observational data: Sobotka & Hanslmeier (2005) found that the typical observed size of UDs is 175 km (≈0.23''), and the ratio of the total area of UDs to the area of the umbra is 9% at an intensity treshold of 1.5. In a detailed analysis of a high-resolution observation Riethmüller et al. (2008b) found the UD filling factor to be 11% and a typical size of UDs of 229 km (≈0.39'') at an intensity threshold of 2. On the other hand, according to a study of a long simulation run with a similar setup (Bharti et al. 2010), the size of the simulated UDs can change with time and, in particular, to increase when the thermal relaxation is reached.

5.4.2 One-dimensional models

Semi-empirical one-dimensional (1D) sunspot models are based on observations of the continuum and/or spectral lines and/or their center-to-limb variation (CLV) (for a review see Solanki (2003)). To compare a snapshot from our 3D MHD simulation with a 1D semi-empirical model, we average the temperature stratifications of the snapshot over surfaces of constant optical depth in continuum at 5000 Å. This 1D model, henceforth called the ⟨3D⟩ model, is shown in Fig. 5.4 and compared with the semi-empirical 1D model of Maltby et al. (1986) representing an average umbral core (Maltby M). The ⟨3D⟩ model is cooler than the Maltby M model throughout the whole atmosphere. The difference is smallest (280 K) at $\log \tau_{5000} = 0$ and increases considerably upward. On the other hand, the temperature gradients of the two models are very similar in the lower photosphere ($-2.5 < \log \tau_{5000} < 0$). In subphotospheric layers the gradient of the Maltby M model is significantly larger than the simulated one, while above the level of $\log \tau_{5000} = -2.5$ the gradient of the average snapshot exceeds the semi-empirical one which becomes close to zero.

5.4.3 Intensity ratio

The monochromatic continuum intensity computed from the snapshot, normalized to the quiet sun continuum and averaged over the simulated box is presented in

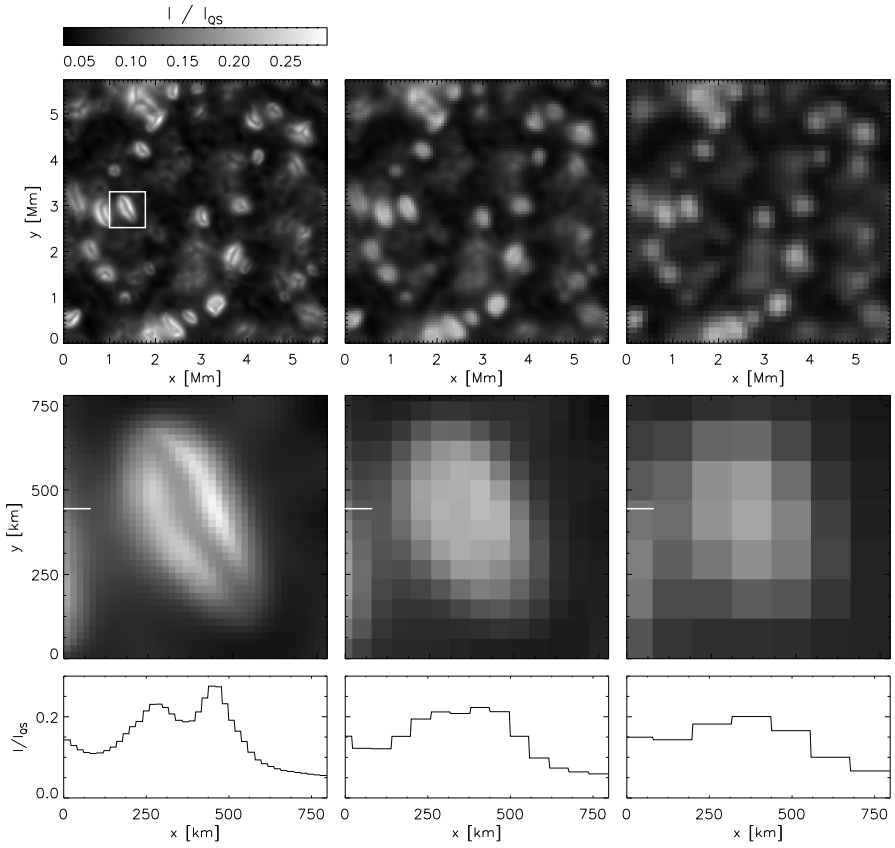

Figure 5.2: Synthetic continuum observations of the simulated umbra at 6300 Å at disk center. *First row*: the full field of view in the resolution of the simulation (left) and after it was blurred with a Gaussian with a FWHM of 0.16″(center) and 0.32″(right). The blurred images have been resampled so that the pixel size is half of the smearing FWHM. *Second row*: Enlarged umbral dot marked by the white square in the upper row is shown at three different resolutions. *Third row*: Intensity ratio along the row marked by the horizontal bars in the middle row. Note the decrease of the intensity ratio with decreasing resolution. In the central panel one darker pixel corresponding to the dark lane is still visible though the contrast is very small. If the resolution is comparable to the resolution of SP/SOT Hinode (right), the dark lane is completely washed out and the brightest pixel is at its location.

the upper panel of Fig. 5.5 (black solid curve).[2] For comparison, we computed the

[2]All *intensities* in this paper are normalized to the monochromatic continuum intensity of the HSRA model (Gingerich et al. 1971) at disk center. The term *intensity ratio* is used to describe the relative intensity of two models (e.g., dark and bright umbral component) or one model at two different heliocentric angles (see Sect. 5.5.2).

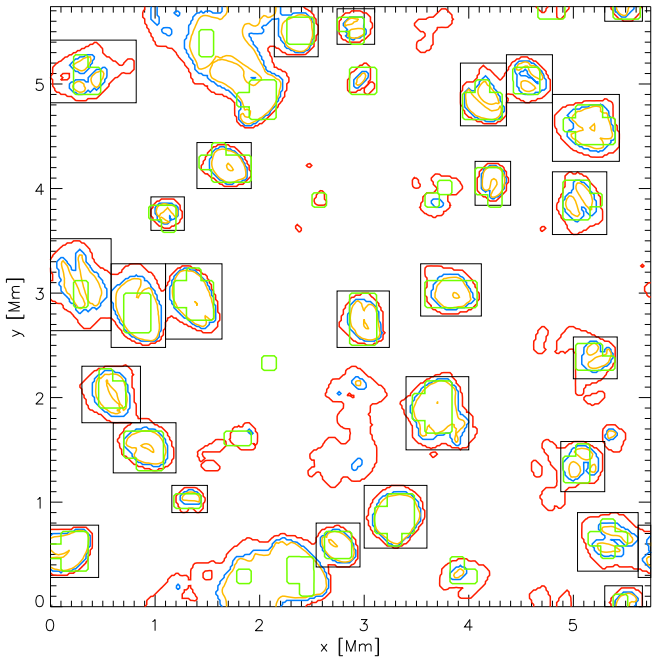

Figure 5.3: Identification of umbral dots: automatic identification based on the intensity map at 6300 Å in the original resolution of the simulation with thresholds of $I_c/\langle I_c\rangle > 1.2$ (red contour) and $I_c/\langle I_c\rangle > 1.6$ (blue); after the intensity map was blurred with a Gaussian with FWHM=0.32″and with threshold value of $I_c/\langle I_c\rangle > 1.2$ (green); identification based on temperature at the $\tau_{5000} = 1$ level with a threshold of $T = 4100$ K (orange); manually selected UDs used for the determination of the effective diameters (black squares).

continuum from the Maltby M model (dashed curve, cf. Fig. 2 of Maltby et al. (1986)). The Maltby M model produces higher continuum intensities at all wavelengths than the simulation snapshot. The average intensity of the bright and dark components separated as in Fig. 5.3 (at 6300 Å with threshold of 1.6) is also shown (middle panel). The intensity of the bright component exceeds the values computed from Maltby M at all wavelengths. However, due to the small UD filling factor it represents a minor contribution to the total umbral intensity.

The intensity ratio between the umbral dots and the dark background ($I_{\rm UD}/I_{\rm DB}$) is shown in the lower panel of Fig. 5.5. In the visible part of the spectrum, this ratio drops with wavelength by factor of 2 (from ≈ 4 to ≈ 2) and becomes almost constant in the range between 1 and 1.5 μm.

Limited spatial resolution. Even in the case of a perfect telescope and no terrestrial atmosphere the image resolution is limited due to difraction at the telescope aperture,

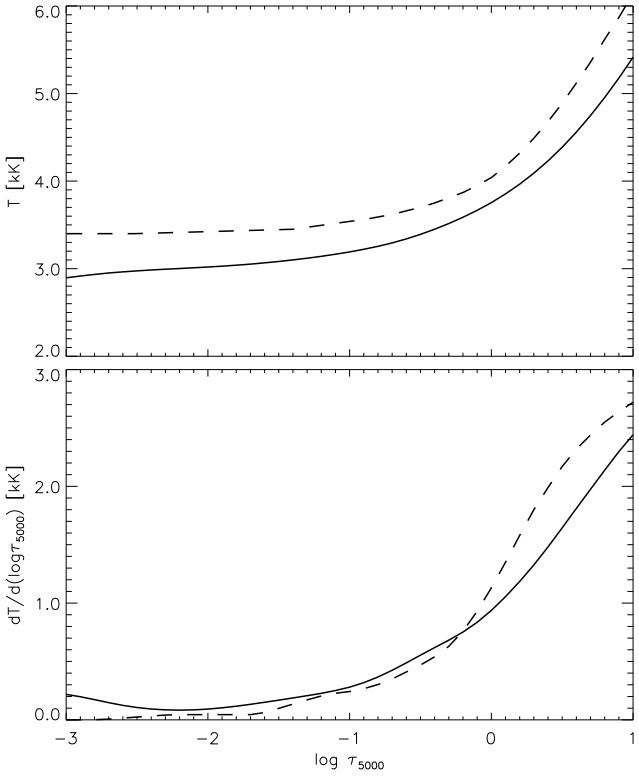

Figure 5.4: Temperature stratification of the average of the 3D snapshot over iso-τ surfaces (solid curve) versus semi-empirical 1D model of Maltby et al. (1986) (dashed): *Upper panel*: temperature; *Lower panel*: gradient of temperature in logarithmic scale of optical depth.

which is described by an ideal point spread function (PSF). In the most simple case of a circular aperture that is homogeneously illuminated, the PSF is the Airy function with a FWHM equal to the resolution of the instrument $\alpha_{\rm res} = 1.22\ \lambda/d$ where λ is the wavelength and d is the diameter of the aperture. In practical applications a more complex geometry has to be treated, and it is necessary to modify the ideal PSF to account for the central obscuration, spiders, etc. (for example, for the PSF of the SOT on Hinode, see Wedemeyer-Böhm (2008), Danilovic et al. (2008)).

Image blurring due to the difraction-limited resolution lowers all intensity ratios in an image. In particular, if we consider an observation of a sunspot umbra, with increasing wavelength it becomes more difficult or even impossible to resolve and identify the umbral fine structure. Since our aim in this paper is not to compare with a particular solar telescope but rather a general analysis, the synthetic images are

blurred with a Gaussian with a fixed FWHM of 0.11″(equal to $\alpha_{\rm res}$ of an aperture of 0.5 m at 4500 Å and to $\alpha_{\rm res}$ of 1 m at 9000 Å). The degraded intesities $I_{\rm UD}/I_{\rm QS}$ and $I_{\rm DB}/I_{\rm QS}$ and their ratio $I_{\rm UD}/I_{\rm DB}$ are shown in Fig. 5.5 (dash-dotted curves).

Influence of stray light. The amount of the stray light in the observed signal is specified by the far wings of the PSF. As a blurring function in this study we adopted a Gaussian to represent the central peak of an Airy function, and, in that sense, we neglect the contribution of the far wings of the PSF. To account for stray light present in real observations, we add an a-posteriori fraction α of the quiet sun intensity to the computed umbral intensities:

$$I^{\rm obs}(\lambda) = I^{\rm true}(\lambda) + \alpha(\lambda) I_{\rm QS}(\lambda)$$

where $I^{\rm true}$ is the intensity computed from the umbral simulation, $I_{\rm QS}$ the intensity computed from the HSRA model of the quiet sun and $I^{\rm obs}$ is the intensity after the stray light contribution has been added (see Zwaan (1965), Martinez Pillet (1992)).

The dependence of the stray light contribution factor $\alpha(\lambda)$ on wavelength is determined by the nature of the processes that scatter light into the beam along the line-of-sight. The major contributor to the instrumental stray light at visible and near-infrared wavelengths is scatter on dust and micro-roughnesses (see Spyak & Wolfe (1992a)). Spyak & Wolfe (1992b) found that the amount of the scattered light in that case varies as λ^{-2}. Here we follow their conclusions and define wavelength-dependent stray light factor α as

$$\alpha(\lambda) = \frac{\alpha_0}{\lambda^2},$$

where α_0 is an arbitrary constant different for every instrument, selected here to give 10% of stray light at 4000 Å, $\alpha_0 = 1.6 \times 10^6$. The effect of the stray-light contamination on the intensity ratio $I_{\rm UD}/I_{\rm DB}$ is shown in Fig. 5.5. The effect is obviously most pronounced at the shortest wavelength (4000 Å) where the intensity ratio between UDs and DB drops by a factor of 2.6 due to the stray light.

5.4.4 Comparison to observations

There is no systematic observational study of $I_{\rm UD}/I_{\rm DB}$ in a wide spectral range to compare with our simulation. The lack of such a study is understandable, since in the blue part of the spectrum the diffraction-limited resolution is high enough to separate UDs from the background, but the uncertainties due to stray light are large. On the other hand, in the near-infrared the stray light is negligible, but the resolution of the largest instruments currently available is insufficient to resolve UDs.

There is a large scatter of single-wavelength intensity measurements ($I_{\rm UM}/I_{\rm QS}$, $I_{\rm UD}/I_{\rm QS}$ and $I_{\rm UD}/I_{\rm DB}$) in the literature (e.g., Sobotka et al. (1993), Tritschler & Schmidt (1997), Kitai et al. (2007), Sobotka & Hanslmeier (2005), Sobotka & Puschmann (2007), Socas-Navarro et al. (2004), Riethmüller et al. (2008b), Watanabe et al. (2009a)). These

results were obtained at different telescopes (space-borne and ground-based), at different wavelengths in the visible, with different methods for UD detection and with different approaches to the stray light correction. The observed values of I_{UD}/I_{DB} are typically smaller than those computed from the simulation, and the computed values of I_{UM}/I_{QS} and I_{UD}/I_{QS} are smaller than the observed ones. These trends suggest that most of the cited observations are (at least partly) contaminated with some stray light contribution and other effects related to the data analysis (UD identification, threshold ambiguities, etc.).

If we assume, for example, that the simulation represents the umbra observed by Watanabe et al. (2009a), who found $I_{UD}/I_{DB} = 1.51$ in SOT/Hinode measurements at 4504.5 Å, a stray light contribution of $\alpha = 0.08$ is sufficient to explain the difference between the observations and our simulations (dash-triple-dotted curve in the lower panel of Fig. 5.5 shows the computed intensity after the image is blurred and the stray light is added, and "×" represents the value found by Watanabe et al.). In the blue part of the spectrum that value of α is realistic for a SOT/Hinode observation (cf. Wedemeyer-Böhm (2008)). Due to these observational limitations a comparison between the simulated intensity I_{UM}/I_{QS} and intensity ratio I_{UD}/I_{DB} with observations remains inconclusive.

5.5 Center-to-limb variation

The continuum-intensity variation with μ ($\mu = \cos\theta$ where θ is the heliocentric angle) is an important diagnostic of the temperature stratification in a stellar atmosphere (e.g., see Gray (2008)). In the case of sunspot observations, there are four main difficulties concerning CLV measurements: (1) different sunspots show significantly different intensities, making it difficult to combine observations; (2) a sunspot evolves and often changes significantly while rotating towards the limb; (3) the path of a sunspot often does not cross the disk center; (4) CLV measurement at very small μ is virtually impossible because of foreshortening. Additionally, the dependence of the stray-light correction on μ also has to be taken into account. To compare the CLV of the continuum intensity computed from the simulation to the available observational data, and to study the umbral morphology at small μ, we tilted the snapshot following the procedure described in Sect. 5.2.3 and computed emerging continuum intensities along the lines-of-sight.

5.5.1 Morphology

The monochromatic continuum intensity maps at 6300 Å computed for $\mu = 1.0$, 0.8, 0.6, 0.4 and 0.2 are shown in Fig. 5.6. The filling factor of UDs increases with decreasing μ because an increasing fraction of the dark background becomes "shadowed" by clustering of elevated UDs. The morphology of UDs significantly changes with distance from the disk center. If an UD has a dark lane perpendicular to the selected center-limb direction, that lane vanishes already at $\mu = 0.8$ (UD A in Fig. 5.6), but if

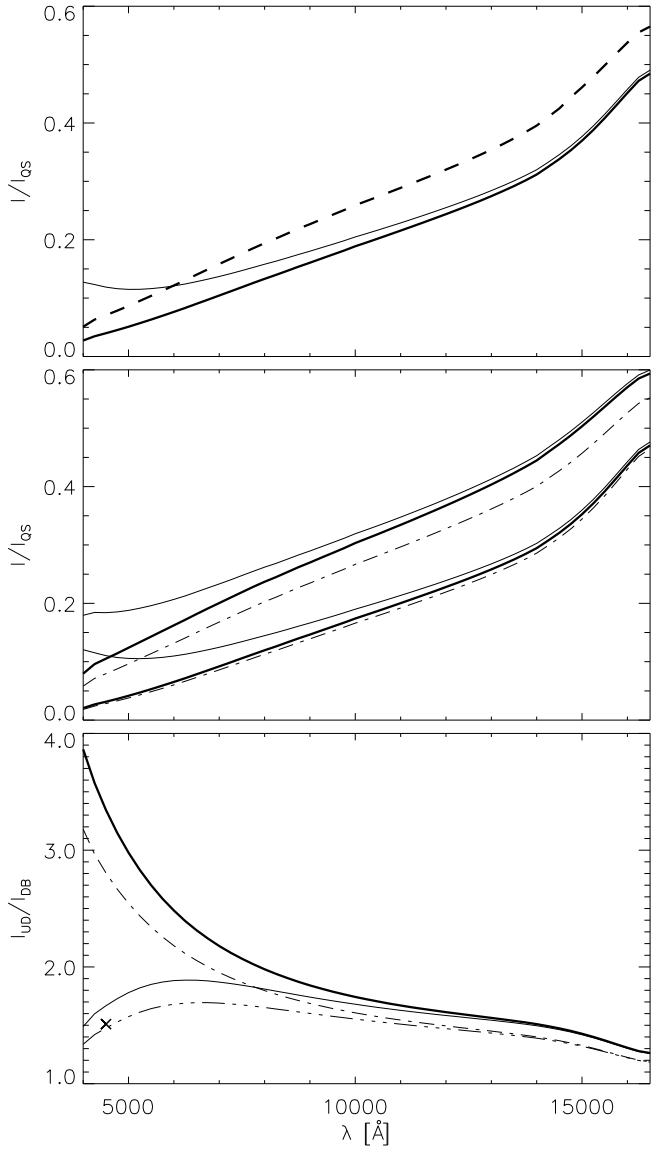

Figure 5.5: Monochromatic continuum intensities and intensity ratios at disk center as a function of wavelength: *Upper panel*: the umbral intensity computed from the 3D snapshot and averaged over the whole snapshot (solid thick curve), the same intensity after adding a wavelength-dependent (λ^{-2}) stray-light contribution (solid thin), and the intensity computed from the Maltby M model (dashed). *Middle panel*: the intensities of UDs and DB (solid thick) after they are separated in the intensity map (blue contours in Fig. 5.3), the same intensities after the stray-light contribution is taken into account (solid thin), and after the image resolution has been degraded (dashed-dotted) as in Sect. 5.5.2. *Lower panel*: the intensity ratio between the bright and the dark component in the full resolution of the snapshot (solid thick), after blurring (dash-dotted), after stray-light addition (solid thin), and after the combined effect of blurring and stray-light (dashed-triple-dotted).

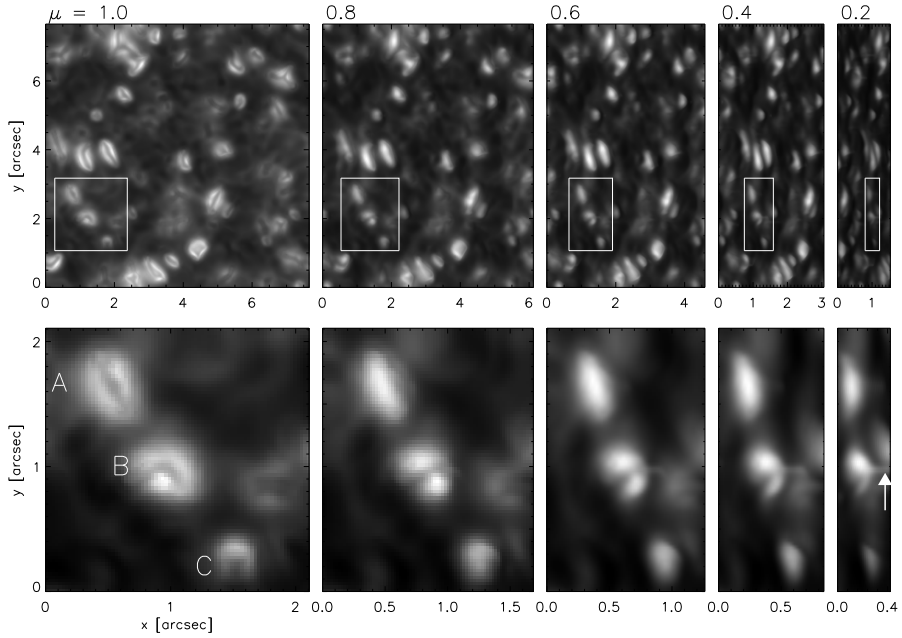

Figure 5.6: Center-to-limb variation of the simulated umbra at 6300 Å: *Upper row*: Monochromatic continuum intensity computed from the snapshot as observed at disk center (leftmost) and at $\mu = 0.8$, 0.6, 0.4 and 0.2 (from left to right). In the upper panels the intensity at all values of μ is shown at the same grey scale. *Lower row*: Blow-up of the regions outlined by the white boxes in the upper row. The appearance of UDs depends on their orientation. If the dark lane is almost perpendicular to the center-limb direction it vanishes already at $\mu = 0.8$ (UD A). In contrast, the dark lane remains visible even at large heliocentric angles if it is oriented parallel to that direction (UD B). At very large angles it also shows a "tail" (pointed to by arrow). A small UD without dark lane does not change its appearance significantly with μ (UD C). To enhance the contrast of the small features at large angles, the intensity in the lower panels was normalized separately for each value of μ.

the lane is close to the center-limb direction, it remains partly visible for even smaller values of μ (UD B). The change in shape is less pronounced for a tiny, rounded UD (UD C), though all the shapes appear more elongated toward the limb.

Close to the limb many dots show long, very thin "tails" pointing away from disk center (Fig. 5.6). Their location, size and limb-side orientation suggest that they correspond to the "jet-like upflows" described by Schüssler & Vögler (2006). The tails are more prominent next to dots that have dark lanes oriented in the center-limb direction. The orientation of a dot is important because the jet-like upflows vary in size and shape and, in general, their horizontal cross-section follows the shapes of

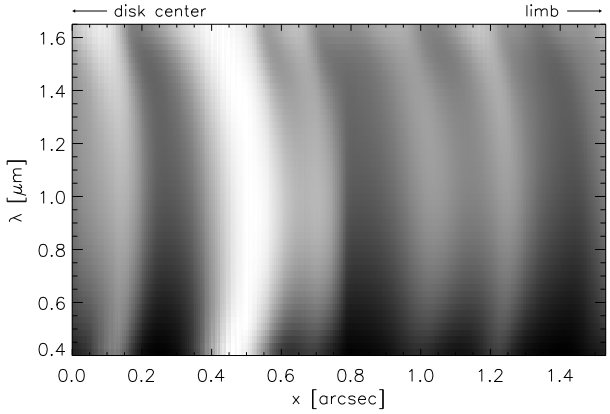

Figure 5.7: Variation along a cross-section (at $y \approx 2.0$ Mm) of the intensity map at $\mu = 0.2$ with wavelength (the x-axis points toward the limb). The arc-like shapes are due to the continuum opacity variation with wavelength. The bright arcs are due to UDs; the brigthest arc is due to the UD *B* in Fig. 5.6. The image is normalized row-by-row to remove the overall intensity variation with wavelength.

the corresponding dark lanes.

Let us assume, for simplicity, that a typical upflow has the shape of a hot and thin wall, denser than the surrounding material. Then, if an upflow is seen along the lane, the opacity, integrated along the flow, makes it visible. On the contrary, if an upflow is oriented so that the line-of-sight is perpendicular to it, then we see "through" the wall.

The visibility of the tails depends critically on the wavelength. Close to the opacity minima (4000 Å, 1.65 μm), we see deeper layers (Fig. 5.7) and the tails vanish from the continuum images.

An example of an umbral dot with a tail is shown in detail in Fig. 5.8. To explain the appearance of UDs at $\mu = 0.2$, we selected a row of pixels in the intensity map and the corresponding vertical cross-section through the simulation snapshot. At disk center, the cross-section goes through the dark lane of an UD, and at $\mu = 0.2$ through the dot and its tail. The variation of the continuum intensity along the selected pixels is plotted in Fig. 5.8 (second row). Limb darkening due to the decrease of temperature with height is evident as the overall decrease of intensity at $\mu = 0.2$. Moreover, the spatial intensity variation close to the limb is smoothed because the line-of-sight crosses through different structures. To illustrate that, three lines-of-sight are selected in Fig. 5.8: a line at the edge of a dot, one at the base of its tail and one at the top of the tail. If we follow these lines through the temperature stratification of the snapshot (Fig. 5.8, third row), all of them pass through both hot and cool material.

A band of geometrical heights at which the contribution function of the contin-

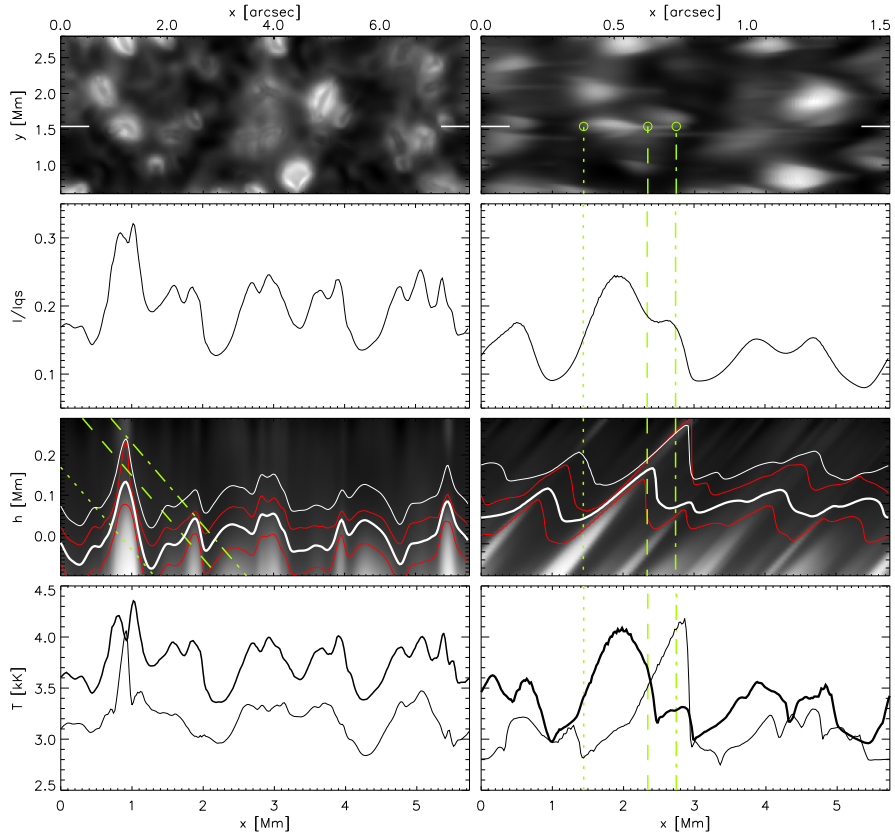

Figure 5.8: Umbral dots at disk center (*left column*) and at $\mu = 0.2$ (*right column*). In the righthand panels, the images and plots are not shrunk to account for the foreshortening. The green lines show the selected lines-of-sight: bottom of a UD (dotted); a point in the UDs "tail" (dashed); close to the top of the "tail" (dash-dotted). In the righthand panels these lines are perpendicular to the x-axis. All panels in both columns have a common x-axis (shown at the bottom). The axis at the top shows the foreshortening effect. *First row*: the intensity map (at 6300 Å) with the three UDs analyzed in Fig. 5.6. The center-limb direction is along the x-axis. The small green circles show the locations of the selected lines of sight in the intensity maps. *Second row*: intensity along the cross-section at $y \approx 1.5$ Mm. *Third row*: vertical cross-section of temperature at $y \approx 1.5$ Mm. The zero level of the height scale is at the mean $\tau_{6300} = 1$ level, averaged over the whole snapshot. The red curves show levels where the integrated continuum contribution function at 6300 Å reaches 10% (upper curve) and 90% (lower). The levels of constant continuum optical depth are shown in white: $\tau_{6300} = 1$ (thick) and $\tau_{6300} = 0.1$ (thin). *Forth row*: temperature along the $\tau_{6300} = 1$ (thick curve) and $\tau_{6300} = 0.1$ (thin).

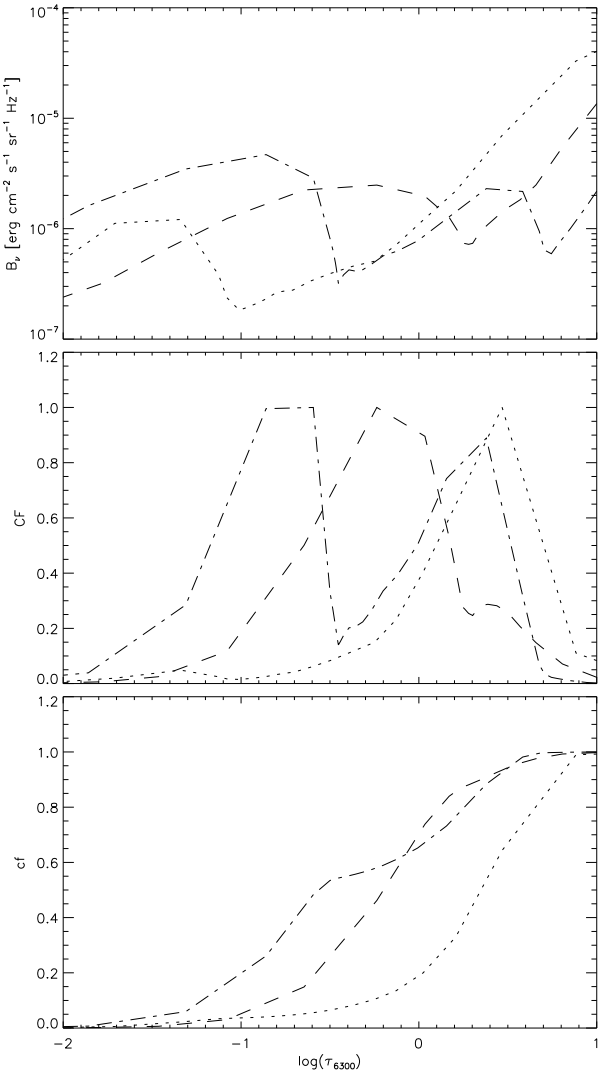

Figure 5.9: The integration of the intensity along the three lines-of-sight indicated in Fig. 5.8 (UD base, dotted; tail, dashed, top of the tail, dash-dotted) at $\mu = 0.2$. *Upper panel*: Planck function, B_ν; *middle panel*: continuum contribution function (CF); *lower panel*: the integrated continuum contribution function (cf = $\int_\infty^\tau$ CF $d\tau$). The contribution functions are normalized to their maximal values and the integrated contribution functions to the local continuum intensity.

uum intensity integrated over optical depth reaches 10% and 90% is plotted over the temperature stratification. The UD brightening (the region between the dotted and dashed line-of-sight) at the limb originates from a very narrow band in geometrical-height scale. The region above has lower density and temperature (and lower opacity), and hence the border between magnetic and nonmagnetic (less-magnetic) structure is characterized by steep gradients in both temperature and density. The vertical boundary of an UD is analogous to the granular boundary responsible for the facular brightening (compare our Fig. 5.8 to Fig. 2 of Keller et al. (2004)).

The UD tail extends between the dashed and the dash-dotted line-of-sight in Fig. 5.8. The higher temperature and density along the upflow increase the opacity and make the tail visible. The source function B_ν, the continuum intensity contribution function (CF) and its integrated value (cf) over τ_{6300} along the three lines-of-sight are shown in Fig. 5.9. The source function in the UD (dotted curve) at $\mu = 0.2$ is dominated by the regions below $\log \tau_{6300} = 0$ with a negligible contribution in the higher layers from an upflow of another UD. The corresponding contribution function peaks at $\log \tau_{6300} = 0.4$, and the integrated contribution function increases smoothly with increasing τ_{6300}. If we look toward the base of the tail, the source function (dashed curve) has a broad peak between $\log \tau_{6300} = -1$ and 0 before it starts to increase monotonically. From the contribution function plot, it is clear that most of the intensity originates from the region of the broad peak and only a small fraction from the layers below it. Further out in the tail, the contributing band rapidly broadens in the geometrical scale due to the hot material present in the higher layers and a larger fraction of cooler and less dense and less opaque material under the upflow. In Fig. 5.9 (dash-dotted curve), the source function has two peaks before it starts to increase monotonically with τ_{6300}. The first peak is located in the upflow of the analyzed UD and the second one comes from the next UD in the limb direction. The contribution function shows two similar peaks and the integrated CF consequently has a plateau between $\log \tau_{6300} = -0.5$ and 0 showing the clear separation between the tail and the background contribution (lower panel of Fig. 5.9).

5.5.2 Intensity ratio

With the currently available solar telescopes, the detailed imaging of umbrae at small μ is still beyond reach. Therefore, there are no observations to compare the results of Sect. 5.5.1 with. However, we can compare intensities averaged over the whole snapshot seen at $\mu = 0.2, \ldots, 1.0$ with the available observations of the umbral CLV. We define the absolute CLV of a model atmosphere as the variation of the continuum intensity with μ normalized to the quiet-sun intensity at disk center:

$$i(\lambda, \mu) = \frac{I(\lambda, \mu)}{I_{\mathrm{QS}}(\lambda, \mu = 1)}.$$

The absolute CLV averaged over the snapshot (at 4000 Å, 6300 Å, and 1.65μm) is shown in the upper panels of Fig. 5.10. The same quantity computed from the models ⟨3D⟩ and Maltby M is shown for comparison. The decrease of the umbral

continuum intensity with μ is due to the elevation of the $\tau = 1$ surface to higher and cooler layers (cf. upper panel of Fig. 5.5).

To define the relative CLV, we normalize $i(\lambda, \mu)$ to its value at disk center $i(\lambda, \mu = 1)$:

$$j(\lambda, \mu) = \frac{i(\lambda, \mu)}{i(\lambda, 1)}.$$

The relative CLV averaged over the snapshot and computed from the two models is shown in the lower panels of Fig. 5.10. It is particularly interesting to note the opposite behavior of relative CLV's computed from the 3D snapshot and from the $\langle 3D \rangle$ model in respect to the quiet sun. While the 3D snapshot darkens less than the quiet sun at all wavelengths and for all heliocentric angles, the $\langle 3D \rangle$ model appears relatively darker than the quiet sun at every λ and μ. The $\langle 3D \rangle$ model also behaves remarkably similar to the Maltby M model.

5.5.3 Comparison with observations

The sunspot intensity at disk center is not always known because a sunspot umbra changes significantly as the spot rotates from close to disk center fo the limb. Therefore, the $j(\lambda, \mu)$ variation is difficult to measure. It is observationally more convenient to define a measure that does not depend on the umbral intensity at the disk center:

$$k(\lambda, \mu) = \frac{I(\lambda, \mu)}{I_{\rm QS}(\lambda, \mu)} \equiv \frac{i(\lambda, \mu)}{i_{\rm QS}(\lambda, \mu)}.$$

The function $k(\lambda, \mu)$ represents the ratio of the umbral and quiet sun intensities measured locally at a given value of μ.

Since Minnaert & Wanders (1932) pointed out the significance of the CLV determination for sunspot modeling, the function $k(\lambda, \mu)$ has been measured over limited wavelength ranges by a number of authors. Earlier observations (see Albregtsen et al. (1984) for a list of references) suggested that the ratio $k(\lambda, \mu)$ is either independent of μ within the limits of observational error (Staveland (1970), Albregtsen & Maltby (1981)), or increases toward the limb (Rödberg (1966), Wittmann & Schröter (1969), Stellmacher & Wiehr (1972)). The most extensive observations, however, are those of Albregtsen et al. (1984) who measured $k(\lambda, \mu)$ of 22 large sunspots in a wide wavelength range (3870 Å to 2.35 μm), and corrected the measurements for stray light. Contrary to the previous observations, these authors found that the observed function $k(\lambda, \mu)$ decreases linearly with μ, particularly in the infrared, and determined the best-fit coefficients (their Table IV). More recently, Norton & Gilman (2004) studied the CLV of the continuum intensity at 6768 Å from MDI data. They analyzed data for two sunspots observed in June 2003 (active regions 0373 and 0375), and found an overall increase of $k(\lambda, \mu)$ toward the limb for both sunspots, although "in an unpredictable manner as a result of evolution".

To compare our results to the measurements of Albregtsen et al. (1984), we computed the linear fits of the $k(\lambda, \mu)$ variation of the 3D snapshot, its 1D average and

the Maltby M model. The slopes of the linear fit, b_λ, are compared to the values of Albregtsen et al. in Fig. 5.11. The computed values of b_λ from the 3D snapshot are negative as the 3D snapshot darkens with μ less than the quiet sun. They are systematically smaller than the observed values. On the other hand, the values derived from the Maltby M and $\langle 3D \rangle$ models agree well with the observations. The difference between b_λ computed from $\langle 3D \rangle$ and the Maltby M model, even at the wavelengths where the two models predict very similar $j(\lambda, \mu)$, is due to the difference in the continuum intensities of the two models computed at disk center.

5.5.4 Discussion

How to explain the described discrepancy between the CLV computed from the 3D snapshot on the one hand, and the CLV computed from the two 1D models and the CLV observed by Albregtsen et al. (1984) on the other hand?

First of all, the CLV of a 1D model is fully defined by its temperature and density gradients. The same would be true for a 3D snapshots with a nearly-homogeneous distribution of temperature and density on surfaces with constant optical depth. On the other hand, the CLV computed from an inhomogeneous 3D snapshot is not determined by the mean vertical temperature gradient, but by temperature distribution along lines-of-sight that pass through the fine structure in the snapshot (Fig. 5.6). More precisely, the filling factor of UDs increases with decreasing μ because of their positive differential Wilson depression: at small values of μ, UDs "shadow" the limbward background. The increase in filling factor of the bright component toward the limb reduces the limb darkening. This effect is obviously absent from the $\langle 3D \rangle$ model that predicts systematically smaller intensities toward the limb.

The basic understanding of the umbral appearance away from disk center was already anticipated by Wilson (1969) who pointed out that "...when the inhomogeneous nature of umbra is considered, the limb darkening of the cool component (and thus the temperature gradient in this region) cannot be derived from the mean limb darkening without knowledge of the inhomogeneous structure of the atmosphere."

The difference between the 3D snapshot and the Maltby M model reflects the nature of different regions of a sunspot umbra. The model of Maltby et al. (1986) was constructed to represent umbral cores, the darkest and the most homogeneous parts of large sunspot, where UDs are infrequent or completely absent (Sobotka et al. 1992). The 3D effects on the observed intensity CLV computed from a largely homogeneous atmosphere would be insignificant, so even a 3D simulation of an umbral core would reproduce similar CLV as its 1D mean.

The agreement between CLVs computed from the Maltby M and $\langle 3D \rangle$ models is due the general agreement in temperature gradients of the two models in the continuum formation layers (Fig. 5.4). This agreement should be treated with caution, since the $\langle 3D \rangle$ model is obtained by averaging of an inhomogeneous atmosphere.

One might also ask how the CLV of the continuum intensity ratio between UDs and DB ($I_{\rm UD}(\mu, \lambda)/I_{\rm DB}(\mu, \lambda)$) changes with wavelength. When umbral inhomogeneities are viewed away from disk center, the line-of-sight crosses through both

hot and cool components making them virtually inseparable in the intensity maps even at the intrinsic resolution of the simulation. The effect is obviously more pronounced close to the solar limb where the intensity along a single line-of-sight can originate even from different UDs (cf. Fig. 5.9). In principle, the separation of the two components could be facilitated more easily in the infrared where we see deep layers and where the continuum contribution function is less extended. On the other hand, in the infrared, the diffraction-limited resolution would be an unavoidable obstacle to identify UDs. Moreover, a small intensity ratio $I_{\rm UD}(\mu,\lambda)/I_{\rm DB}(\mu,\lambda)$ in the infrared (Fig. 5.5) would make such an observation very uncertain.

5.6 Conclusions

We analyzed the monochromatic continuum radiation (4000 to 16500 Å) computed from a 3D radiative MHD simulation of a sunspot umbra. There is general agreement between the morphology of the simulated umbra and observations. The typical size and filling factor of the simulated umbral dots are consistent with the most recent observations (Sobotka & Hanslmeier 2005, Riethmüller et al. 2008b).

A simple procedure for automatic identification of umbral dots is sufficient to separate bright dots from the dark background (at least) when there are no global intensity gradients over the field of view. The dark background in the simulation is inhomogeneous, covered with grainy structure of decaying umbral dots, and with dark elongated features that coincide with areas of the strongest magnetic field. The intensity ratio between umbral dots and dark background predicted in the simulation is the largest in the blue part of the spectrum (≈ 4) and in the infrared drops to ≈ 1.3. That ratio decreases after the effects of the diffraction limited resolution, pixel size and the stray light are taken into account. In the blue continuum of SOT/Hinode it agrees quite well with the measurement of Watanabe et al. (2009a).

When the simulation snapshot is skewed to mimic a sample of a sunspot umbra seen away from disk center, the umbral dots become more elongated and their total filling factor increases. At large heliocentric angles, the typical coffee-bean shape seen at disk center completely vanishes. In addition, many dots show tiny limbward "tails". The tails appear due to the jet-like upflows predicted in the simulation by Schüssler & Vögler (2006). The visibility of a tail depends on the temperature and density in the upflow, on its geometrical shape, orientation relative to the center-limb direction, and on the brightness of the background seen below the jet at small μ. It also strongly depends on the wavelength at which the tail is observed. Because of their small size and low contrast, the described tails are below the resolving power of the largest, currently available solar telescopes. However, it might be possible that similar tails are related to umbral upflows on larger scales that are not covered in this study (e.g., in light bridges). An observational confirmation of this phenomenon would be an argument in favor of the validity of the considered 3D MHD simulation of the umbral magnetoconvection.

The simulated 3D umbra analyzed in this paper is generally cooler and darker

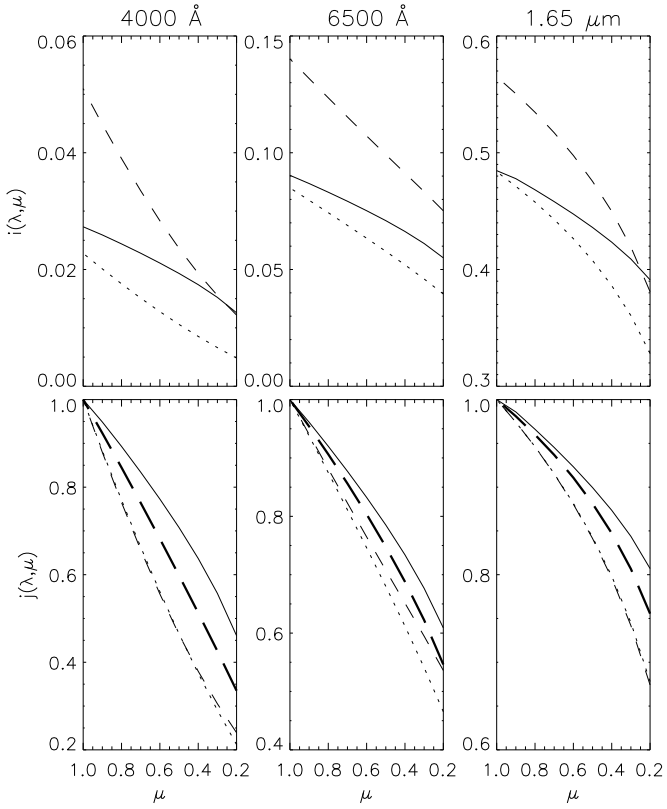

Figure 5.10: CLV of the continuum intensity as a function of μ at different wavelengths (4000 Å, left; 6500 Å, center; 1.65 μm, right). *Upper panels*: the absolute CLV $i(\lambda, \mu)$ normalized to the quiet sun intensity at disk center. The CLV is computed from the skewed 3D snapshot (solid curves). For the comparison, the CLV of the continuum intensity computed from two 1D plane-parallel models is also shown: Maltby M (dashed), ⟨3D⟩ (dotted). *Lower*: the relative CLV normalized to the intensity at the disk center computed in the corresponding model. The CLV computed from the quiet sun HSRA model is added as a reference (long-dashed).

than observed umbrae. On average, it is also cooler than the semi-empirical 1D models of Maltby et al. (1986). That might be a surprising result because the Maltby M model is based on observations of dark umbral cores and, therefore, the 3D snaphot covered with umbral dots should be brighther. Part of the explanation may be in the stray light that is not completely removed from the observational data. On the other hand, we cannot rule out that by choosing different model parameters (e.g., like combining different average magnetic field strength with higher energy influx at the bottom boundary) one may achieve better agreement in the overall brigthness

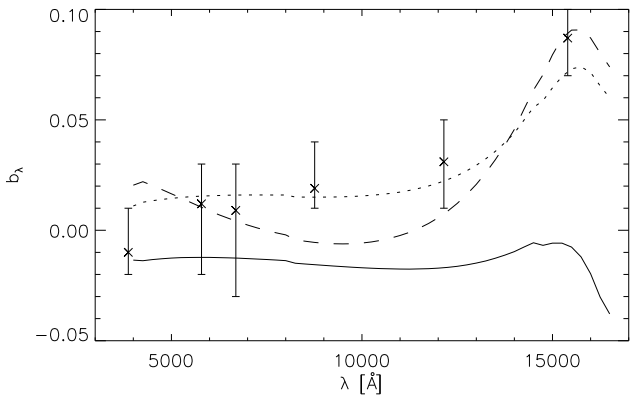

Figure 5.11: Slopes b_λ of the best linear fits through the relative umbra/quiet sun CLV $k(\lambda, \mu)$: averaged 3D snapshot (solid curve), ⟨3D⟩ model (dotted) and the Maltby M model (dashed). The slopes measured by Albregtsen et al. (1984) are shown (crosses) with the corresponding uncertainties.

between the simulation and observations and still preserve the good agreement in the morphology of the fine structure. However, this is subject of a current research, and beyond the scope of this paper.

The CLV of umbral intensity computed from the 3D snapshot predicts, due to inhomogeneities in the temperature distribution, relatively smaller limb darkening than in the quiet sun, what is opposite to the results computed from the 1D Maltby M model. This discrepancy comes from the fact that the 3D snapshot represents a structure of umbra between a dark umbral core and umbral periphery, while the Maltby M model represents average umbral core that is homogeneous and without UDs. The importance of inhomogeneities for CLV computation was already suggested by Wilson (1969). Alhough the observations of Albregtsen et al. (1984) are in agreement with the Maltby M model, significant intensity differences do exist between individual sunspots (e.g., Norton & Gilman (2004)), and between different regions in every large sunspot, and it seems difficult, if not impossible, to define a single CLV function for all.

The next step in the study of the umbral structure is to compare synthetic spectropolarimetric signal with the high-resolution observations. Since the simulation run described here does not extend high enough for that kind of analysis, we leave this topic for a forthcoming paper.

Acknowledgments

We thank R. J. Rutten and M. Schüssler for carefully reading the manuscript. N.V. thanks G. Scharmer, H. Socas-Navarro and A. Norton for helpful and constructive

discussions. This research is supported by a Marie Curie Early Stage Research Training Fellowship of the EC's Sixth Framework Programme under contract number MEST-CT-2005-020395. This research has made use of NASA's Astrophysics Data System.

Life can only be understood backwards;
but it must be lived forwards.
— Søren Kierkegaard

Chapter 6

Observational signatures of a simulated sunspot umbra: II. Stokes profiles of the Fe I 6302 Å lines

N. Vitas, A. Vögler and C. U. Keller*

Abstract

Magneto-convection in sunspot umbrae has been qualitatively reproduced in 3D radiative MHD simulations, in particular by Schüssler and Vögler (2006). As a natural consequence of convection process in the strong magnetic field typical for sunspot umbra, plumes of weakly magnetized gas reach the surface and form small bright dots superimposed on a dark background. These are called umbral dots. Our aim is to compute and analyze the spectropolarimetric signatures of simulated umbral dots and to compare them to recent high-resolution observations. A sunspot umbra is simulated with sufficient vertical extent to permit synthesis of Fe I 6301.5 Åand Fe I 6302.5. Emergent line profiles are computed assuming local thermodynamical equilibrium and degraded to the Hinode and SST resolution, and used to synthesize and evaluate commonly used diagnostics. In addition, the degraded line profiles are used as input to both a Milne-Eddington and a height-dependent LTE inversion code and the inversion results are compared to the original simulation snapshot and to actual observations by other authors. This comparison yields the conclusion that the simulated umbral dots are consistent with observed central umbral dots, but systematically different from umbral dots at umbral periphery. The analyzed diagnostics provide reliable information on the umbral structure only in the deep photosphere where the considered lines are formed.

*To be submitted.

6.1 Introduction

In continuum images, sunspot umbrae contain tiny bright features called umbral dots (UD). The observational and theoretical aspects of these UDs have been reviewed by Solanki (2003) and Thomas & Weiss (2004, 2008). Recently, the highly realistic numerical MHD simulation by Schüssler & Vögler (2006) has explained UDs as the natural consequence of magnetoconvection in umbrae. In Vitas et al. (2010, hereafter Paper I), we synthesized and analyzed the emergent continuum radiation at visible and near infrared wavelengths for a snapshot taken from a similar umbral simulation.

Although there is a long history of photometric and spectroscopic observations of UDs (see e.g., reviews by Sobotka (1997) and Solanki (2003)), the more recent improvement of the observational facilities enables detailed spectropolarimetric study of the UD phenomenon and to establish the physical differences between UDs and the surrounding dark background (DB). This is the topic of this paper, in which we exploit a new MHD simulation that extends higher up into the atmosphere than the one used in Paper I. Specifically, we use this new simulation to study what the UD–DB differences are in the magnetic field strength and inclination, and in the line-of-sight (LOS) velocities. In addition, we study how high UDs extend into the overlying atmosphere.

Recent studies agree that UDs exhibit a magnetic-field reduction relative to their surroundings, but the quantitative results disagree between studies (e.g., Riethmüller et al. (2008a), Socas-Navarro et al. (2004), Watanabe et al. (2009b)). Moreover, different UDs within one sunspot show a large variety in brightness and magnetic field strength (cf. Table 2. of Socas-Navarro et al. (2004) and Fig. 6 of Riethmüller et al. (2008a)). Socas-Navarro et al. (2004) measured the full Stokes vector in UDs and found that their fields are weaker and more inclined than in the field in the DB. This result has been confirmed by Riethmüller et al. (2008a) and Ortiz et al. (2010). The analysis of Socas-Navarro et al. (2004) also indicates that UDs merge with the surrounding DB at about $\log \tau_{5000} = -1$. The study of Riethmüller et al. (2008a) confirmed this merging, but placed it at $\log \tau_{5000} = -2$.

The variation between different UD measurements is largest for the velocities. The LOS velocities are generally rather small in the DB (e.g., < 100 m/s, Sankarasubramanian & Rimmele (2002)), so that the measure UD velocities relative to the DB nearly represent absolute motions. Some authors measured upflows at UD locations (≈300 m/s, Lites et al. (1991); ≈250 m/s in peripheral UDs, Socas-Navarro et al. (2004), ≈1.2 km/s, Pahlke & Wiehr (1990), 3 km/s, Kneer (1973)), whereas others measured no significant UD velocities (Zwaan et al. 1985, Wiehr 1994, Schmidt & Balthasar 1994). Hartkorn & Rimmele (2003) made a distinction between peripheral UDs, found near the umbral edge, associated with upflows (≈200m/s) and central UDs which show no upflows or even, occasionally, downflows. A similar result was found by Riethmüller et al. (2008a): upflows of ≈800 m/s in peripheral UDs and no significant velocity in central ones. Ortiz et al. (2010) observed both upflows (≈1 km/s) and downflows (≈500 m/s) within a single UD.

In this paper, we use a snapshot from a MHD simulation of umbral magneto-

convection to synthesize and analyze the full Stokes vector for the Fe I 6301.5 Å and 6302.5 Å lines. We apply four different methods to distill the UD and DB properties from these synthetic observations as if they were actual observations, and then compare these results with the actual simulation quantities. The profile-integrated polarization diagnostics and the magnetic field and velocity determined by center-of-gravity measurement are compared with the measurements of Ortiz et al. (2010). The results of the bisector analysis of the simulated Stokes *V* profiles are compared to the results of Sankarasubramanian & Rimmele (2002). The Milne-Eddington inversions and SIR inversions of the synthetic profiles are compared to the corresponding observations of Watanabe et al. (2009b), Socas-Navarro et al. (2004) and Riethmüller et al. (2008a).

The current study is motivated by three questions: (*i*) Is the simulation of an isolated umbra consistent with the available observations in Fe I 6301.5 Å and 6302.5 Å? (*ii*) What is the effect of limited spectral and angular resolution on measurements of the physical parameters of UDs? (*iii*) Do the different methods provide consistent measurements of UD properties? This research was partly inspired by Westendorp Plaza et al. (1998) who presented a comparison between the results of two inversion techniques applied to the spectral line profiles synthesized in one-dimensional model atmospheres.

6.2 Method

6.2.1 Simulation

The MURaM (MPS/University of Chicago Radiative MHD) (Vögler & Schüssler 2003, Vögler et al. 2005) code has been used to simulate magnetoconvection in a sunspot umbra. The code solves the non-linear system of time-dependent radiative MHD equations on a 3D, uniform Cartesian grid taking into account the effects of non-gray radiative transfer and partial ionization.

The simulation domain is covered by 288×180×288 grid points. In the horizontal and vertical direction the extent of the simulation box is 5.76 Mm and 1.8 Mm, respectively. These new simulations have 20 additional vertical grid points with respect to the simulations in Paper I. The initial snapshot of the new simulation is constructed by extending the snapshot used in Paper I by an additional 200 km. The additional layers of the initial snapshot are static, isothermal and in hydrostatic equilibrium with respect to the density. The magnetic field is given by a potential field extrapolation of the magnetic field at the top of the Paper I snapshot. We run the simulation for about 20 minutes of solar time and select the last snapshot for further analysis.

The logarithm of the continuum optical depth at 5000 Å at the top of the selected snapshot is smaller than −4.5 at every point. That is a requirement for the succesful synthesis of the two Fe I lines from the snapshot.

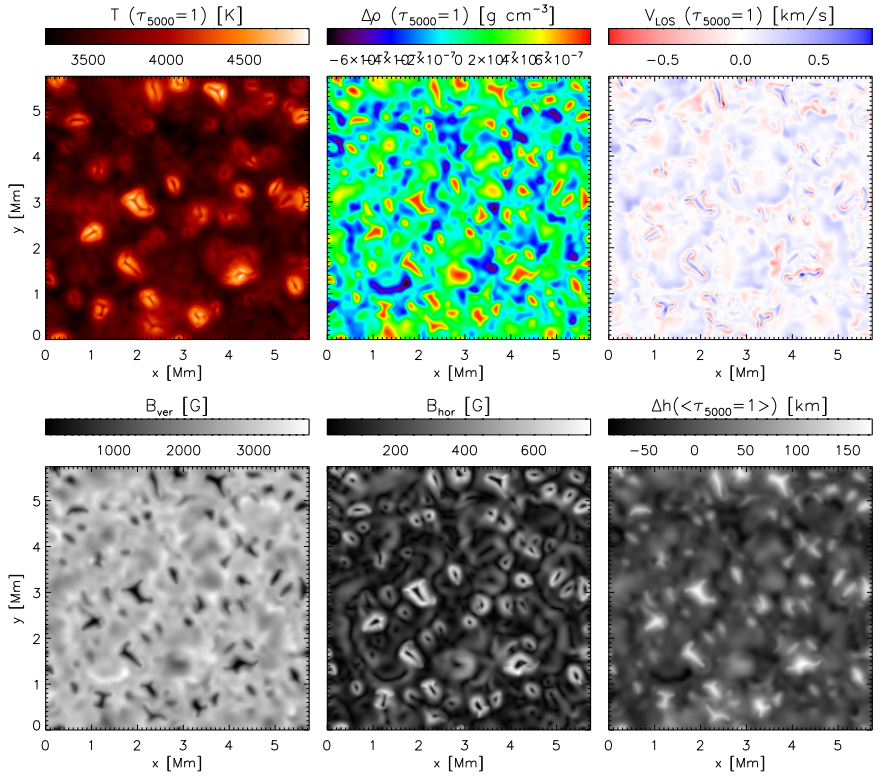

Figure 6.1: Cross-sections through a snapshot of a simulated sunspot umbra at constant optical depth $\tau_{5000} = 1$. *Upper row*: temperature (left), deviation from the local mean density (center) and line-of-sight velocity (right; upflows, blue; downflows, red). *Lower row*: vertical (left) and horizontal (center) component of the magnetic field vector; deviation of the iso-τ_{5000} surface from the horizontal plane where $\langle\tau_{5000}\rangle = 1$, the so-called differential Wilson depression (right).

6.2.2 Line synthesis and smearing

Line synthesis. The Stokes profiles of the Fe I 6301.5 Å and 6302.5 Å lines are computed using the forward-synthesis mode of the LILIA code (Socas-Navarro 2001). The lines are sampled in 320 wavelength points in step of 12 mÅ. The spectral lines are synthesized assuming the validity of the local thermodynamical equilibrium (LTE). The atomic data for the two lines are adopted from Khomenko et al. (2005b). All other atomic or molecular lines in this wavelength range are ignored.

Smearing. To compare our synthetic observations to real observations obtained by the Solar Optical Telescope (SOT) on Hinode (Suematsu et al. 2008), we convolve the

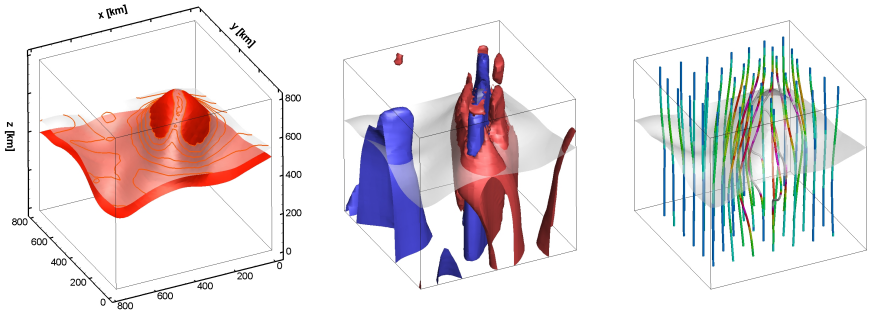

Figure 6.2: The 3D structure of a simulated umbral dot. *Left:* the iso-surface of the temperature at $T = 4400$ K (red), the optical depth surface of $\tau_{5000} = 1$ (semi-transparent); the contours show iso-temperature levels on the iso-τ surface. *Center:* The iso-surfaces of the velocity, upflows are shown in blue, downflows in blue. *Right:* The curves represent magnetic field lines. They are colored according to the local field inclination.

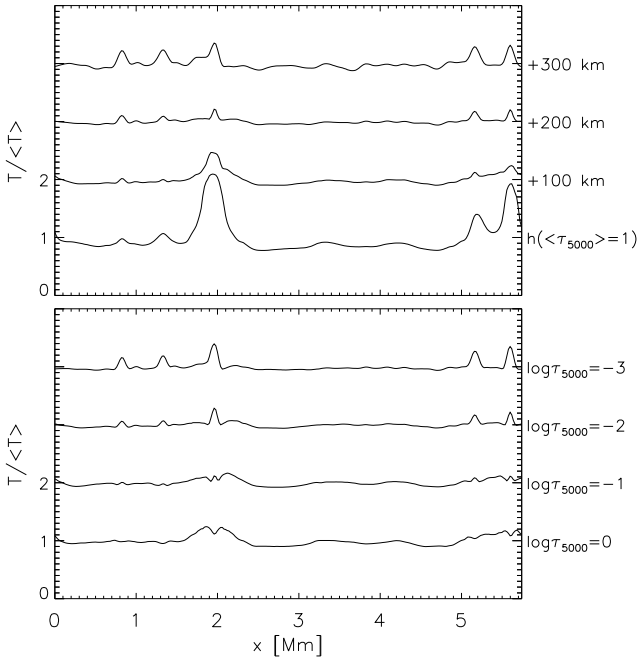

Figure 6.3: Temperature cuts at different geometrical heights (*upper panel*) and optical depths (*lower*) from a vertical slice through the snapshot. The zero value of the height scale is the height at which τ_{5000} averaged over the snapshot equals one.

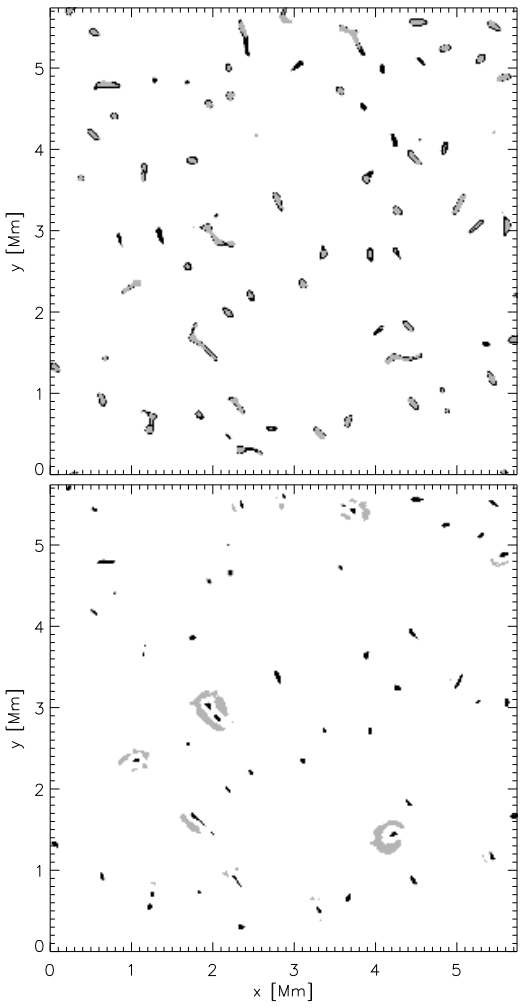

Figure 6.4: Number of lobes of the synthetic Stokes V profiles of Fe I 6301.5 Å (*upper panel*) and Fe I 6302.5 Å (*lower*) at the MURaM resolution. Locations of the profiles with 2, 4 and 6 lobes are shown *white*, *gray*, and *black*, respectively.

images at every wavelength point with the ideal part of the empirical point spread function (PSF) derived for SOT by Wedemeyer-Böhm (2008). The smeared images for every wavelength are resampled to a pixel size of 0.16″. After the resampling in the x-y plane, the Stokes profiles are degraded in the spectral dimension with the instrumental profile of the SP/SOT instrument to account for its spectral resolution and wavelength sampling (112 wavelength points with $\Delta\lambda$=21 mÅ).

The same procedure is applied to simulate observations with the CRISP instrument (van Noort & Rouppe van der Voort 2008) at the Swedish Solar Telescope (Scharmer et al. 2003). The PSF of the SST ($\mathrm{PSF_{SST}}$) is modeled as the convolution of the "atmospheric" part ($\mathrm{PSF_{atm}}$) and "diffraction" part ($\mathrm{PSF_{diff}}$) (see (Pereira et al. 2009b)):

$$\mathrm{PSF_{atm}}(r,a,b) = \frac{a}{r^2+a^2} + \frac{b}{r^2+b^2}, \tag{6.1}$$

$$\mathrm{PSF_{diff}}(r) = \left[\frac{2\lambda}{\pi\, D\, r} J_1\left(\frac{\pi\, D\, r}{\lambda}\right)\right]^2, \tag{6.2}$$

$$\mathrm{PSF_{SST}}(r,a,b) = \mathrm{PSF_{atm}} * \mathrm{PSF_{diff}}, \tag{6.3}$$

where a and b ($a > b$) are free parameters, r the angular distance, λ the wavelength, D the diameter of the telescope, and J_1 is the first order Bessel function of the first kind. However, intensity distribution of umbra is not well defined as in the quiet-sun case, so we cannot compare the continuum intensity distributions for the smeared simulation and the observation to obtain the best-fit values of the free parameters a and b. Instead, we adopt the values used by Pereira et al. (2009b). Note that the observations of Pereira et al. (2009b) were obtained by a spectrograph at SST and not by the CRISP tunable filter instrument. Even if the instrument would have been the same, the true PSF of ground-based observations depends on the actual terrestrial atmosphere at the time of the observations. However, even if the true PSF was known, its application to the simulation of an isolated umbra would lead to an underestimation of the stray-light contribution as the bright surrounding of the umbra (penumbra, faculae, quiet Sun) is not present in the simulation.

The smeared images are resampled to a pixel size of 0.07″. To account for limited spectral resolution of the CRISP instrument, we convolved the Stokes profiles in the spectral dimension with a Gaussian with FWHM = 64 mÅ and resampled them at wavelength steps of 48 mÅ. The wavelength points are distributed in the ±336 mÅ intervals around 6301.5 and 6302.5 Å. The noise is added at the level of 10^{-3} in Stokes I and 2×10^{-3} in Q, U and V to the degraded Stokes profiles to mimic actual CRISP and SP/SOT observations.

In this paper we use three synthetic observations: the profiles computed from the snapshot at the full spectral resolution ("MURaM resolution"), the profiles degraded to mimic an observation with SP/SOT ("SP/SOT resolution"), and the profiles degraded to mimic an observation with CRISP ("CRISP resolution").

Stray light. Stray-light significantly affects real sunspot observations; the contribution of the stray-light is determined by the far wings of the PSF. However, the real

umbra is always surrounded by the quiet Sun and often by the penumbra. In contrast, the umbra in our simulation is isolated, so no matter how extended the wings of the assumed PSF are, the main sources of stray light are omitted. Moreover, the far wings of the PSFs of CRISP and SP/SOT are known only approximately. Applying an inversion technique to a synthetic observation with a posteriori added stray light would be easy but also misleading if the stray-light profiles assumed in the inversion code are identical to the ones added to the synthetic observations. Realistic modeling of the stray light is indeed beyond the scope of this paper, and we threrefore choose to neglect it.

6.2.3 Diagnostics

Profile-integrated diagnostics. Integrated linear (LP), circular (CP) and net circular polarization (NCP) are evaluated from the synthesized Stokes profiles as:

$$\mathrm{LP} = \int_{\lambda_b}^{\lambda_r} \frac{(Q_\lambda^2 + U_\lambda^2)^{1/2}}{I_\mathrm{c}}\, \mathrm{d}\lambda, \tag{6.4}$$

$$\mathrm{CP} = \int_{\lambda_b}^{\lambda_r} \frac{|V_\lambda|}{I_\mathrm{c}}\, \mathrm{d}\lambda, \tag{6.5}$$

$$\mathrm{NCP} = \int_{\lambda_b}^{\lambda_r} \frac{V_\lambda}{I_\mathrm{c}}\, \mathrm{d}\lambda, \tag{6.6}$$

where λ_b and λ_r are integration limits at the blue and red side of the spectral line profile, and I_c is the local continuum intensity. The integration limits are infinite in theory, but in practice they are specified by the observed wavelength range. We adopt the integration limits used by Ortiz et al. (2010), $\lambda_{\mathrm{r,b}} = 6301.5 \pm 0.336$ Å and 6302.5 ± 0.336 Å, and consistently apply them to any profile integration throughout this paper. The three quantities defined in Eqs. (6.4)-(6.6) are expressed in mÅ. The CP defined in this way is identical to the unsigned Stokes V area. The ratio of NCP and CP is also known as Stokes V area asymmetry (cf. Shelyag et al. (2007). The mean linear and circular polarization used by Ortiz et al. (2010) differ from our definitions by the constant factor $\lambda_\mathrm{r} - \lambda_\mathrm{b}$.

Center-of-gravity method We apply the center-of-gravity (COG) method of Rees & Semel (1979) to measure the LOS components of the velocity and magnetic field from the three sets of synthetic observations. The wavelength position of the COG of Stokes I is defined as:

$$\lambda_\mathrm{COG} = \frac{\int_{\lambda_b}^{\lambda_r} (I_\mathrm{c} - I_\lambda)\, \lambda\, \mathrm{d}\lambda.}{\int_{\lambda_b}^{\lambda_r} (I_\mathrm{c} - I_\lambda)\, \mathrm{d}\lambda}. \tag{6.7}$$

The Doppler shift of the COG in respect to the rest wavelength of the line represents a measure of the LOS velocity, $V_{\rm COG}$:

$$\mathrm{V_{COG}} = \frac{c(\lambda_0 - \lambda_{\rm COG})}{\lambda_0}, \tag{6.8}$$

where c is speed of light, λ_0 the rest wavelength of the line, and $\lambda_{\rm COG}$ the position of the COG of the line by Eq. (6.7). The LOS component of the magnetic field is measured by the difference of the centroids of the right and left circularly polarized line components, $I_\lambda \pm V_\lambda$:

$$\mathrm{B_{COG}} = \frac{0.5(\lambda_+ - \lambda_-)}{4.67 \times 10^{-13} g_{\rm L} \lambda_0^2}, \tag{6.9}$$

where $g_{\rm L}$ is the Landé factor and λ_0 is the rest wavelength in Å. The centroids $\lambda_\pm$ (in mÅ) are defined as:

$$\lambda_\pm = \frac{\int [I_{\rm c} - (I_\lambda \pm V_\lambda)\lambda] {\rm d}\lambda}{\int [I_{\rm c} - (I_\lambda \pm V_\lambda)] {\rm d}\lambda}. \tag{6.10}$$

Bisectors More detailed diagnostic information can be obtained with the line-bisector analysis. The bisector of a Stokes I profile connects the midpoints between the two halves of the spectral line at a number of intensity levels (see e.g. Gray (2008)). The bisector analysis was applied to spectropolarimetric observations by Rayrole (1967). A detailed description of the method applied to Stokes V observations of sunspot umbrae is given by Sankarasubramanian & Rimmele (2002, Fig. 6). This method is potentially capable of detecting gradients in the LOS velocity and magnetic fields with height as the different intensity levels of a spectral line are sensitive to different layers in the atmosphere. However, it is not trivial to assign a height scale to the measured values. Another difficulty is that the method cannot be directly applied to the fully split Stokes I profiles and to the multi-lobed Stokes V profiles. As almost all Stokes I profiles in our synthetic observations show a clear Zeeman split, we apply the bisector analysis to Stokes V profiles only. Furthermore, we exclude from all Stokes V profiles with more than 2 lobes (see Fig.6.4) from the bisector analysis. For two-lobed profiles we determine bisectors of the red and blue lobes at seven intensity levels (0.2 to 0.8 in steps of 0.1).

Milne-Eddington inversions The Milne-Eddington (ME) inversions of Stokes profiles assume that the signal is formed in an atmosphere characterized by a source function that is linear in optical depth and that other physical parameters are constant along the LOS (Skumanich & Lites 1987). For the ME inversions performed here we use the MELANIE code (Socas-Navarro 2001).

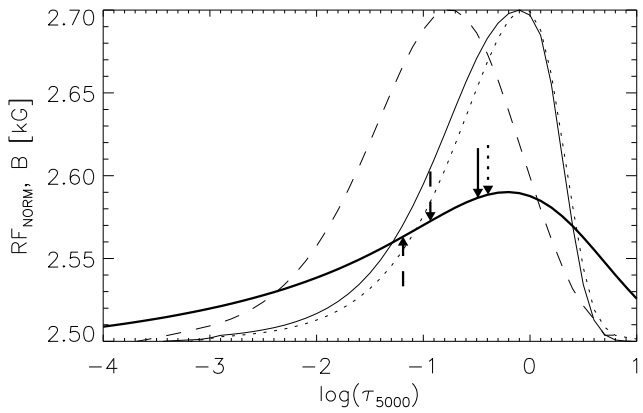

Figure 6.5: The generalized response functions of the circular polarization (thin solid), $B_{\rm LOS}$ determined by the COG method (dotted) and $B_{\rm LOS}$ determined by the ME inversion (dashed) to the perturbation of magnetic field strength. The 1D average of the magnetic field in the snapshot is specified by the thick solid curve. All functions are evaluated by perturbing the 1D average of the snapshot and normalized to their maxima. The arrows pointing down specify the theoretical HOFMs of the three measurements. The arrow pointing up specifies the experimental HOFM for the ME inversion.

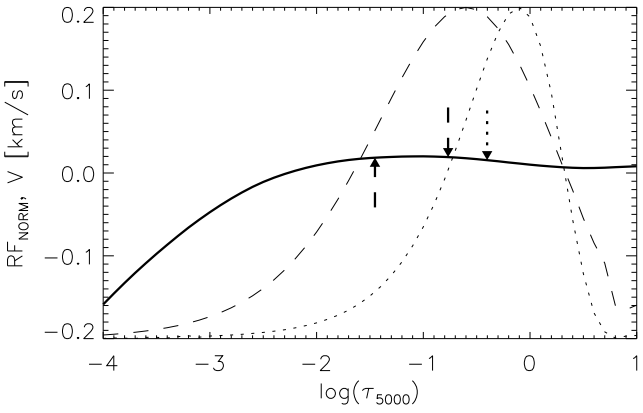

Figure 6.6: Same format as Fig.6.5 for the generalized response functions of $V_{\rm LOS}$ determined by the COG method (dotted) and $V_{\rm LOS}$ determined by the ME inversion (dashed) to the perturbation of LOS velocity. The 1D average of the LOS velocity in the snapshot is specified by the thick solid curve.

Westendorp Plaza et al. (1998) performed ME inversions of line profiles synthesized from 1D models (including models representing an umbra) and compared the

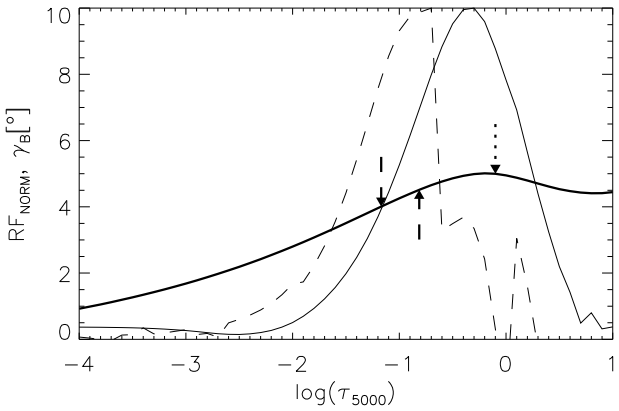

Figure 6.7: Same format as Fig.6.5 for the generalized response functions of the linear polarization (thin solid) and the inclination of the magnetic field inferred by the ME inversion (dashed) to the perturbation of the inclination. The 1D average of the inclination in the snapshot is specified by the thick solid curve.

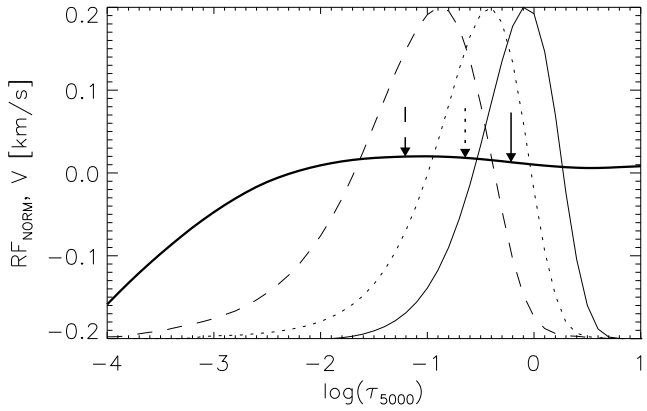

Figure 6.8: Generalized response functions of the LOS velocity measured by the Stokes V bisector shifts to the perturbation of the $V_{\rm LOS}$ in the 1D average of the snapshot. Different curves correspond to different intensity levels: 0.2 (solid), 0.5 (dotted), 0.8 (dashed). The arrows show the theoretical HOFM at the three intensity levels. The 1D average of the LOS velocity in the snapshot is specified by the thick solid curve.

results to the actual stratifications. The ME inversions have also been succesfully tested on synthetic observations based on quiet-Sun MURaM simulations (Orozco Suárez et al. 2007a, 2010b).

SIR inversions Inversions based on response functions (SIR inversions, Ruiz Cobo & del Toro Iniesta (1992)) allow the reconstruction of height-dependent plane-parallel model atmospheres from observed Stokes profiles. The model atmosphere is iteratively adjusted in a prescribed set of points, so-called nodes, starting from an initial model. The merit function is the sum of squared differences between the observed and synthesized profile weighted by the uncertainties of the observation. It is minimized using a non-linear least squares algorithm (e.g. Levenberg-Marquardt algorithm). The advantages and disadvatages of this method in comparison to other widely used techniques are summarized in the review of Ruiz Cobo (2007). To invert the synthetic observations at the three resolutions we employ the LILIA code (Socas-Navarro 2001).

The number of inversion nodes determines the number of free parameters in SIR inversions. A simple procedure to determine the optimal distribution of nodes was suggested by Socas-Navarro (2004). However, this optimal distribution critically depends on the amount of information contained in the observed profiles; lower spectral and angular resolution reduces the amount of information in the observed data, implying that a smaller number of free parameters can be retrieved. The optimal number of the inversion nodes also depends strongly on the model atmosphere and the selected spectral lines.

Nevertheless, as we compare the results of the inversions applied to the synthetic data at three different angular and spectral resolutions, we choose the same inversion scheme for all three data sets. The HSRA atmosphere (Gingerich et al. 1971) is used as the initial model. The model is artificially extrapolated beyond the temperature minimum to obtain a monothonically decreasing temperature stratification. The number of nodes in the temperature is 6, 4 in the velocity and magnetic field strength and 2 in the azimuth and inclination stratifications.

6.2.4 Height of formation of the measurement

To compare the physical parameters inferred from the synthetic observations to the actual values of these parameters in the simulation snapshot, it is neccessary to estimate the height of formation of the measurement (HOFM, Sanchez Almeida et al. (1996)). Every diagnostic measurement technique samples a slightly different range of heights in the atmosphere. The HOFM can be determined either "experimetally"

Figure 6.9 (facing page): Five examples of synthesized Stokes *I* and *V* profiles of Fe I 6301.5 Å and Fe I 6302.5 Å normalized to the local continuum intensity and the stratifications of the corresponding 1D atmospheres in the snapshot. The locations of the five pixels are indicated in the top-left panel of Fig.6.10. *First and second row*: Stokes *I* and *V* at the MURaM resolution; *third and fourth*: Stokes *I* and *V* at the CRISP resolution; *fifth and sixth*: Stokes *I* and *V* at the SP/SOT resolution; *seventh*: temperature; *eight*: total magnetic field strength; *nineth*: LOS velocity (downflow negative; upflow positive); *tenth*: inclination of magnetic field vector (0° vertical; 90° horizontal).

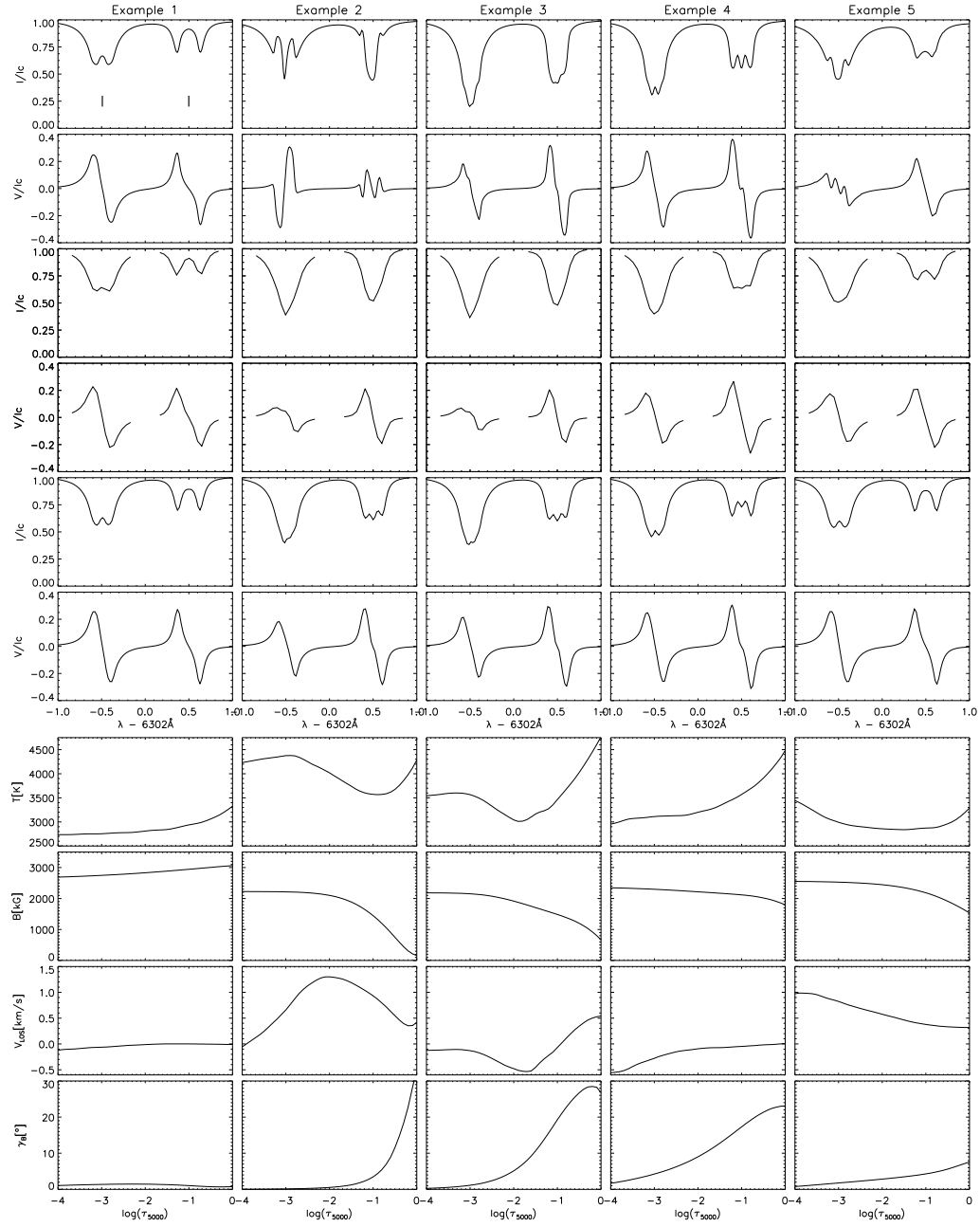
Example 1
Example 2
Example 3
Example 4
Example 5
I/Ic
V/Ic
λ − 6302Å
T[K]
B[kG]
v_{LOS}[km/s]
γ_B[°]
log(τ_{5000})

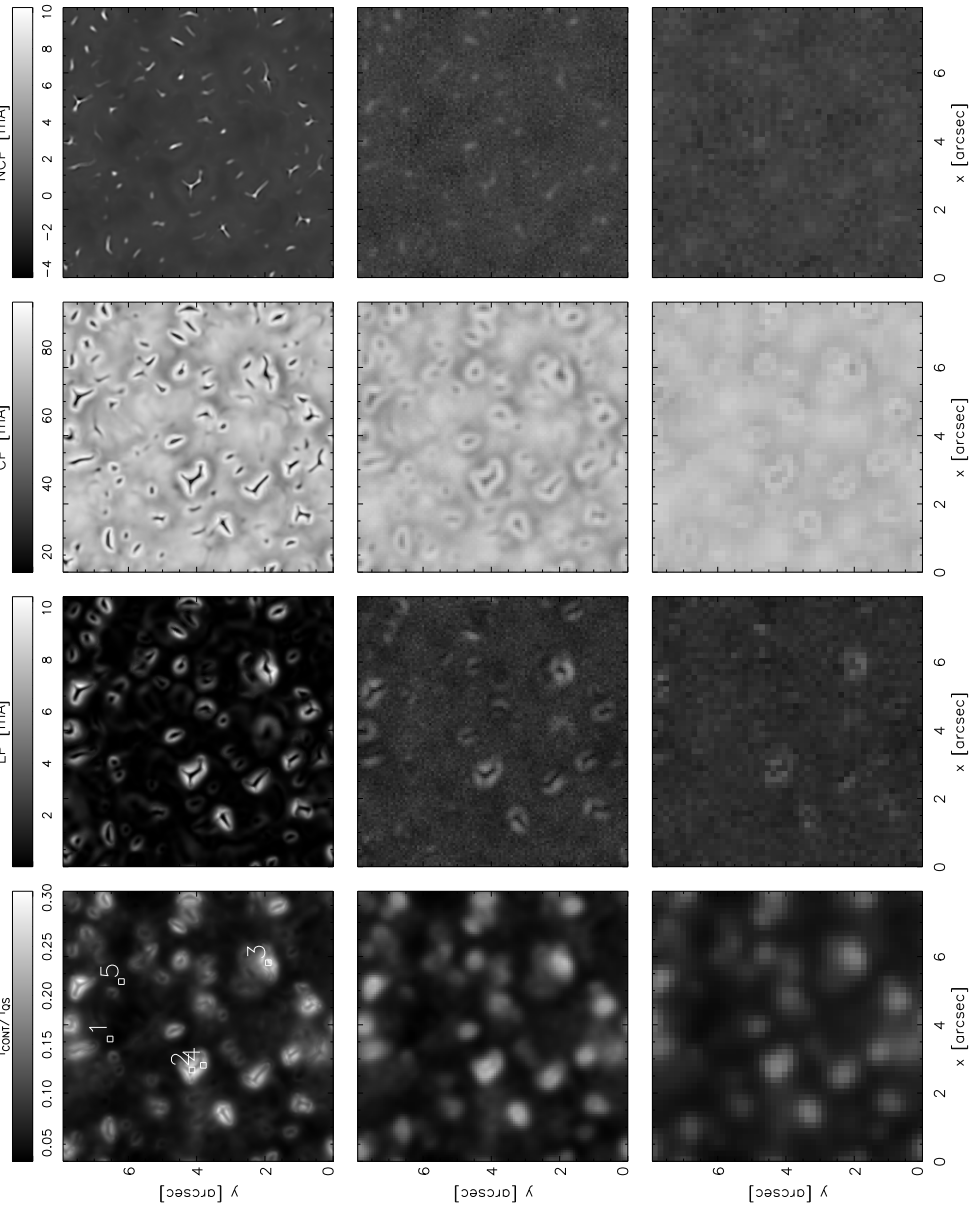

Figure 6.10: Continuum intensity and spectral line diagnostics derived from the synthetic observation at the MURaM resolution (*top row*) and at the resolutions of CRISP (*middle*) and SP/SOT (*bottom*). *First column:* continuum intensity at 6300 Å; *second column:* linear polarization; *third column:* circular polarization; *fourth column:* net circular polarization.

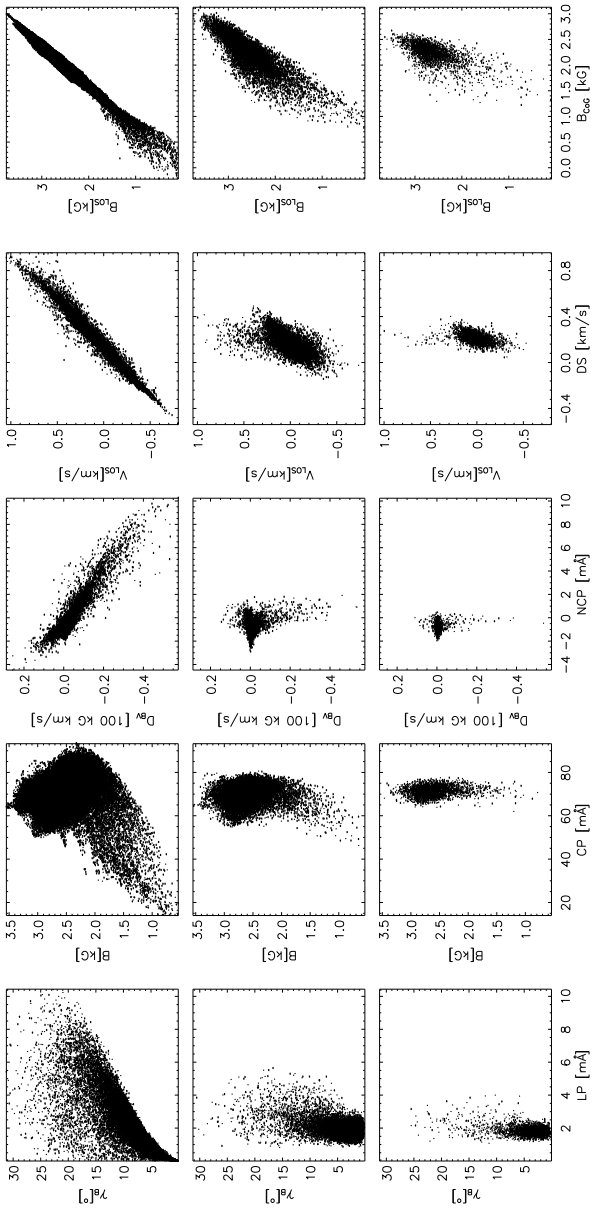

Figure 6.11: Scatter plots between spectral line diagnostics derived from the synthetic observations (MURaM resolution, top row; CRISP, medium; SP/SOT, bottom) and physical parameters taken from the simulation snapshot at the HOFM. *First column:* magnetic field inclination versus linear polarization. *Second column:* total magnetic field strength versus circular polarization. *Third column:* multiplication of velocity and magnetic field gradients with optical depth versus net circular polarization. *Fourth column:* LOS velocity versus Doppler shift. *Fifth column:* LOS magnetic field in the simulation versus the value obtained by the COG measurement .

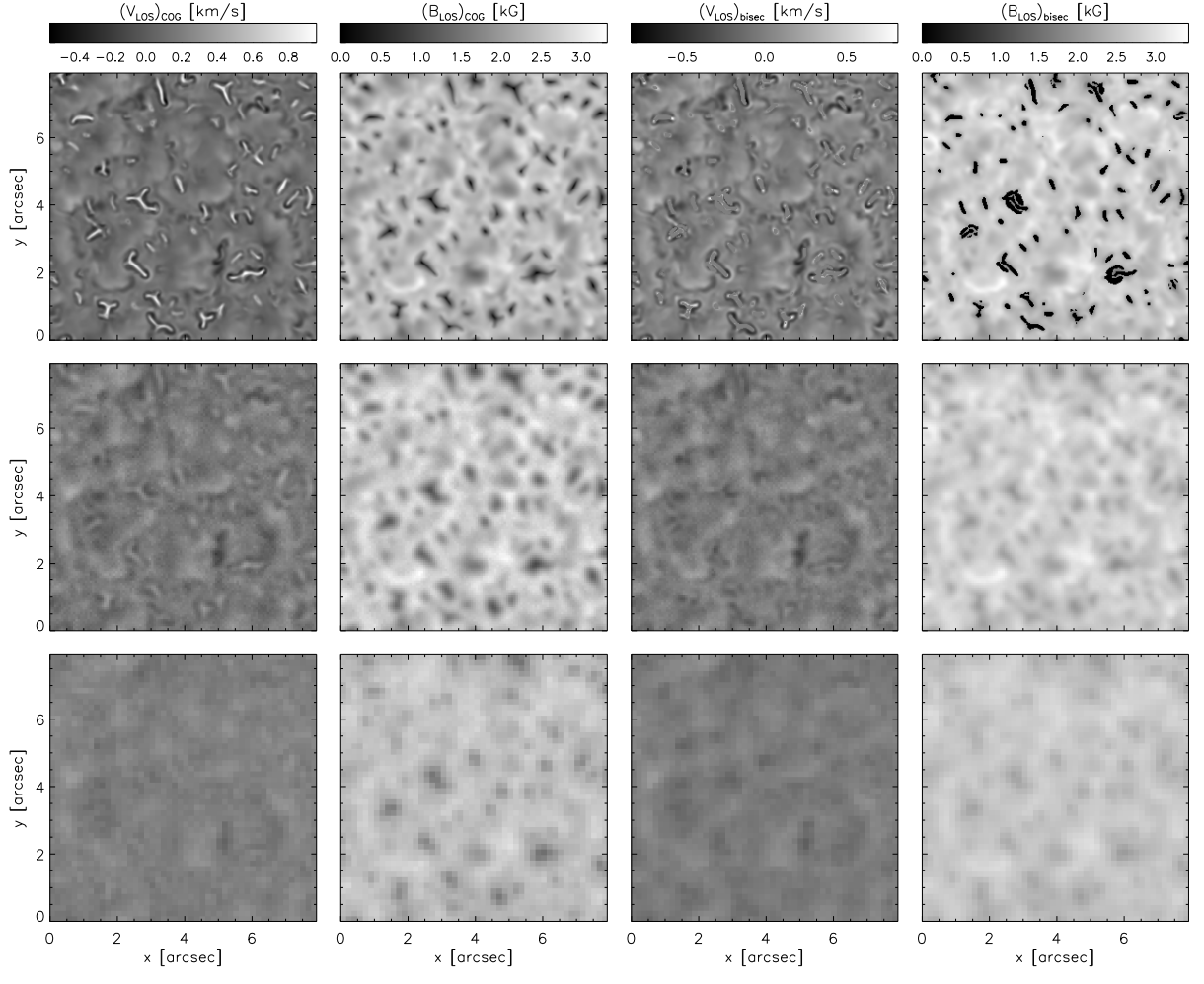

Figure 6.12: The LOS components of the velocity and magnetic field evaluated from the synthetic observations at the MURaM resolution (top row) and at the resolutions of CRISP (medium) and SP/SOT (bottom). Quantities in the *first* and *second column* are obtained by the COG method; quantities in the *third* and *fourth column* are averages of the values obtained through the bisector analysis.

as a height at which the measured value of a parameter matches the actual value (Eq. (3) of Sanchez Almeida et al.), or "theoretically" as (Eq. (12) of Sanchez Almeida et al.):

$$\mathrm{HOFM} = f^{-1}\left[\int_0^\infty f(\tau)\ \mathrm{gRF}(\tau)\ d\tau\right] \tag{6.11}$$

where $f(\tau)$ is the actual stratification of the parameter in the model or an approximative function and gRF is the generalized response functions defined as in (Ruiz Cobo & del Toro Iniesta 1994).

In practice, the HOFM concept has its own limitations. (1) The HOFM is always model-dependent. A small change in the model atmosphere can cause a significant change in the HOFM. (2) If more than one physical parameter influences the measured value, it is more difficult to interpret the gRFs. The same applies to the measured parameters that are predominantly determined by the gradients of physical quantities as it isimpossible to perturb gradients in the stratification with a δ-function. An obvious example is NCP, which is determined by joint contributions of gradients of LOS velocity and magnetic fields. (3) The smaller the gradient of a physical parameter, the less precise the HOFM evaluation is. In an extreme case, when the physical parameter is constant with height, the experimental HOFM is obviously undetermined as the measured value is either equal to or different from the actual value at every height. Nevertheless, the HOFM concept in many cases provides a quantitative estimate of a layer in the atmosphere that contributes the most to the inferred value.

6.3 Results

6.3.1 Snapshot

The $\tau_{5000} = 1$ maps of the temperature, density fluctuation, LOS velocity, differential Wilson depression and the vertical and horizontal magnetic fields of the snapshot selected for analysis are shown in Fig. 6.1. Figure 6.2 shows the 3D structure of the temperature, velocity and magnetic field of a typical UD. The appearance of the simulated umbra is similar to the results of Schüssler & Vögler (2006), Bharti et al. (2010) and **?**. UDs can easily be distinguished from the DB as the locations where the temperature and density are enhanced, while the magnetic field is weaker and more inclined. If the temperature and magnetic field are averaged over the UDs identified in the continuum intensity (as in Paper I), the mean temperature enhancement at $\log \tau_{5000} = 0$ is $\approx$650 K; the mean differences in the magnetic field strength and inclination at the same level are $\approx$600 G and $\approx 10^\circ$, respectively. However, the individual 1D atmospheres corresponding to the two components exhibit a wide range of temperatures ($\approx$1000 K) and magnetic field strengths ($\approx$3 kG) at $\log \tau_{5000} = 0$. In the temperature map (Fig. 6.1), the UDs show characteristic "coffee-bean"

shapes with narrow, dark lanes. Upflows coincide with the dark lanes; they turn to downflows roughly in the bright parts of the UDs (Fig. 6.2). The magnetic field lines enclose the UDs.

The simulation box represents an isolated umbra. Observed UDs are often divided by their location into two categories (Grossmann-Doerth et al. 1986): central UDs (in the inner part of the umbra) and peripheral UDs (in the outer umbra close to the penumbra). The simulated UDs thus represent central UDs.

Figure 6.3 shows the variation of the temperature along a vertical cross-section of the simulated box. The variation is shown for different geometrical heights (upper panel) and optical depths (lower) relative to the mean value at the corresponding level. The UD at $x \approx 2$ Mm is a factor of ≈2 hotter than the surrounding atmosphere at the height where the mean optical depth equals zero. However, the temperature variation along the cross-section is much smaller on the optical-depth scale. In the deep photosphere the relative temperature of the UD decreases with height; at $h = +200$ km, in the center of the UD, the temperature is ≈15% above the average. Higher up in the atmosphere, the relative temperature increases in the central part of the UD. That increase corresponds to the "narrow jetlike upflow above the cusp" described by Schüssler & Vögler (2006). In the optical-depth scale, the relative temperature in the center of the UD increases between $\log \tau_{5000} = 0$ and -3 and decreases in the bright flanks of the UD.

6.3.2 Individual line profiles

We classify the computed Stokes V profiles of the two iron lines according to the total number of positive and negative lobes they exhibit. Figure 6.4 shows the number of lobes in the Stokes V profiles of Fe I 6301.5 Å and 6302.5 Å for a 1D atmosphere extracted from the snapshot. The large majority (≈95%) of the computed profiles at the MURaM resolution show two lobes in both Fe lines. The multi-lobe profiles (4 or 6 lobes) appear exclusively in UDs and, in particular, along their central, dark lanes. The most complex profiles are found in Fe I 6302.5 Å at the end-points of the dark lanes. At the CRISP and SP/SOT angular and spectral resolution, all Stokes V profiles are two-lobed.

Examples of characteristic profiles are shown in Fig. 6.9 together with the corresponding stratifications of temperature, total magnetic field strength, magnetic field inclination and LOS velocity. Profiles degraded to the SP/SOT and CRISP resolutions are shown for comparison. The locations of the selected examples are indicated in the continuum intensity image in Fig. 6.9. White boxes indicate the pixel size of the two instruments.

Example 1 is characteristic for the dark background. The field is strong and almost vertical; its gradient with optical depth is small. The temperature decreases monothonically with height. The velocity is very small, with a downflow velocity of ≈100 m/s. The line profile is symmetric with a clear Zeeman splitting of the two σ components. The degraded profiles look very similar due to the rather similar neighbouring pixels in the simulation box.

Example 2 comes from the dark UD lane. The temperature increases with height in the narrow, jet-like flow above the UD (cf. Schüssler & Vögler (2006)). The total magnetic field strength also increases with height as the LOS passes through the weakly magnetized top of the UD in the deep layers ($\log \tau_{5000} > -2$). The field bends around the UD, becoming vertical in the jet. The velocity of the upflow increases along the jet to ≈1 km/s at $\log \tau \ -2$ and decreases in the higher layers. Such a distribution of the physical parameters along the LOS leads to the complex Stokes I and V profiles at the MURaM resolution. The Stokes I profiles of both Fe I lines show emission reversals in the wings. The temperature rise produces the reversal of the Stokes V profile of Fe I 6301.5 Å, as well as the complex 6-lobe profile in Fe I 6302.5 Å. The difference between the two profiles reflects the difference in their formations heights and their different sensitivities to the magnetic field. At the CRISP resolution the Stokes V profile shows a clear asymmetry between the red and blue wing, but only in Fe I 6301.5 Å. At the resolution of the SP/SOT the peculiarities of the profiles are largely smeared out.

The magnetic field of Example 3 is similar to the magnetic field of Example 2. The velocity along the LOS turns from negative (downflow) in deep layers to positive (upflow) in higher layers. Although the temperature increases with height, as in the Example 2, the gradient of this increase is smaller and occurs higher up. As a consequence, the emission reversals are not visible in the Stokes profiles at the MURaM resolution. The profiles after the degradations are almost identical to the profiles in Example 2.

Example 4 is located in the same UD as Example 2, but in its bright part, which is associated with a downflow. The temperature decreases smoothly with height. The magnetic field is stronger here than in the dark-lane area, while its inclination and its gradient are smaller. The magneto-optical effect under these conditions leads to the small wiggle in the center of the Stokes V profile of Fe I 6302.5 Å. The Stokes I profile of Fe I 6302.5 Å clearly shows the two σ and the π component of the Zeeman triplet. The three components are still visible at SP/SOT resolution, while they produce only a boxy line core at the CRISP resolution.

In the continuum intensity image (Fig. 6.10) Example 5 is located in one of the darkest regions. Nevertheless, a density excess is visible in the density variation map (Fig. 6.1) at that location. Inspection of the vertical stratification of that area reveals a characteristic UD structure just below the surface. Based on a single snapshot, we cannot be certain whether this is an rising or decaying UD. There are several similar examples in the snapshot, e.g. at (x, y) ≈(1.3,5.9), ≈(2.6,1.7) and ≈(1.8,0.7) Mm. The corresponding Stokes I profile of Fe I 6301.5 Å shows a small emission reversal close to the line core, while the 6303.5 Å profile shows only a small amount of Zeeman splitting. In circular polarization, Fe I 6302.5 Å exhibits a distorted profile with double-peaked lobes, Fe I 6301.5 Å a regular two-lobed profile.

6.3.3 Profile-integrated diagnostic

Figures 6.5, 6.6 and 6.7 show the generalized response functions (gRF) of the profile-integrated diagnostics to the perturbation of the 1D average of the snapshot. The corresponding theoretical values of the HOFM are indicated by arrows. The gRFs of the CP and the LOS component of the magnetic field measured by the COG method to the perturbation of the magnetic field strengt are shown in Fig. 6.5; the gRFs of the LOS velocity measured by the COG method to the perturbation of the LOS velocity are shown in Fig. 6.6; and the gRF of the LP to the perturbation of the magnetic field inclination is shown in Fig. 6.7. The measured values of CP and LP are formed around $\log \tau_{5000} = -0.5$ and 0.1, respectively, and the values of $V_{\rm LOS}$ and $B_{\rm LOS}$ measured by the COG method around $\log \tau_{5000} = -0.4$.

Figure 6.10 shows the continuum intensity at 6300 Å and the three parameteres defined by Eqs. (6.4), (6.5) and (6.6), evaluated for every pixel at the three resolutions. The scatter-plots between these parameters and the actual physical variables at the HOFMs are shown in Fig. 6.11.

Linear polarization. In the dark background and the central dark lanes in UDs, the linearly polarized signal is very small ($\approx$ 1%). The linear polarization (LP) is only larger in the bright parts of UDs where the magnetic field is more inclined. The scatterplot at the MURaM resolution (Fig. 6.11) shows a clear correlation between the derived LP and the actual magnetic field inclination at $\log \tau_{5000} = 0.1$. At the CRISP resolution, the LP is smeared out and remains above the noise level only in the bright parts of large UDs. At the SP/SOT resolution, the variation of the LP over the field of view (FOV) is further reduced, so that UDs are barely visible. The correlation between the LP and the inclination is reduced at the CRISP resolution; it disappears at the resolution of the SP/SOT.

Circular polarization. The circular polarization (CP), at the MURaM resolution, is largest in the bright areas of UDs and the smallest in their dark lanes; the CP has intermediate values in the dark background. The fact that UDs, having reduced magnetic field, exhibit larger Stokes V amplitudes than the dark background with its larger magnetic field has been explained by the difference in the thermodynamic properties of the two components (Socas-Navarro et al. 2004). UDs are hotter than the surrounding, and the temperature gradients are larger, so that the emergent spectral lines are stronger in intensity leading to values of CP larger than in the dark background. The effect becomes less visible when the resolution is reduced, as is also shown by the horizontal shrinking of the cloud of points in Fig. 6.11.

Net circular polarization. At the MURaM resolution, the net circular polarization shows an excess only at the locations of the dark umbral lanes; the profiles in the rest of the simulated FOV show very small asymmetries ($|NCP| \lesssim \pm 2\%$). The presence of non-zero NCP is a consequence of LOS gradients of the magnetic field and the

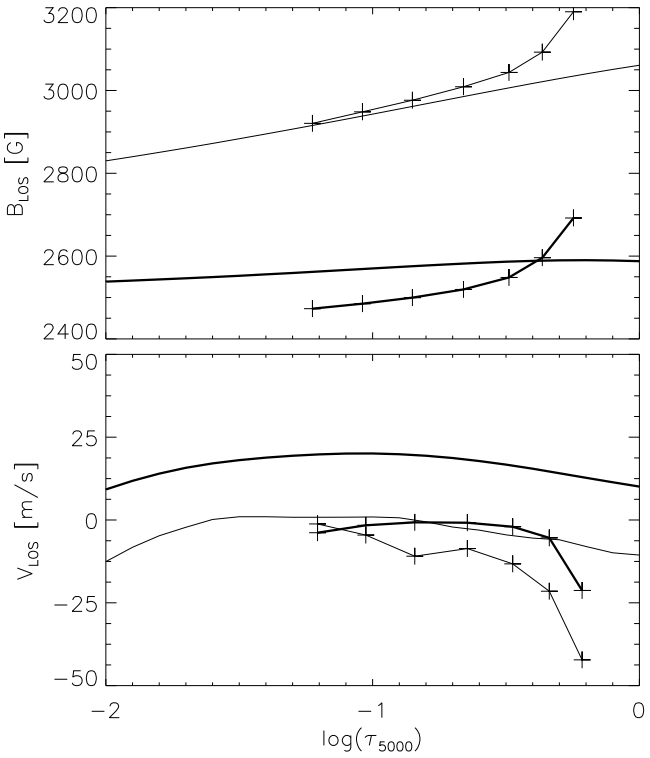

Figure 6.13: The results of bisector analysis (curves with crosses) compared to the actual stratifications (curves without crosses). The crosses indicate the heights of formation for the bisector measurements at different intensity levels. Results are shown for the 1D average of the snapshot (thick curve) and for example 1 in Fig.6.9 (thin). *Upper panel:* LOS component of the magnetic field; *lower panel:* LOS velocity.

velocity. A simple model discussed by Sanchez Almeida & Lites (1992) predicts that the sign of the NCP depends on the signs of these gradients:

$$\mathrm{sign(NCP)} = -\mathrm{sign}\left(V_{\mathrm{blue}} \frac{\mathrm{d}V_{\mathrm{LOS}}}{\mathrm{d}\tau} \frac{\mathrm{d}|B|}{\mathrm{d}\tau}\right), \tag{6.12}$$

where V_{blue} is the sign of the Stokes V blue lobe ($V_{\mathrm{blue}} > 0$ in our simulation). The trend of Eq. (6.12) is indeed visible in the scatterplot (Fig. 6.11, third column): at the MURaM resolution, the combination of gradients on the horizontal axis has a negative trend with NCP shown in the vertical axis. This plot suggests that the Eq. (6.12) holds even for the complex profiles synthesized from the umbral dark lanes, although the equation was derived from a simplified model. After smearing to the SP/SOT and CRISP resolutions, the NCP disappears almost completely.

Center-of-gravity The first column of Fig. 6.12 shows the velocity derived from the Doppler-shift of the COG of the synthesized Stokes I profiles. The upflows coinciding with dark UD lanes are clearly visible at the MURaM resolution along with the adjacent downflows; they still remain visible after degradation to the CRISP resolution, but largely disappear at the resolution of the SP/SOT. The magnitude of the Doppler velocities is between 0.5 km/s in the downflows and 1 km/s in the upflows. The scatter plots between the Doppler velocity and the actual velocity at the HOFM are shown in the fourth column of Fig.6.11. At the MURaM resolution, the correlation is obvious in the full range of the actual velocities; at the resolution of the CRISP the method cannot detect the fastest upflows. At the SP/SOT resolution, the wide range of velocities in the snapshot translates into a narrow range of Doppler velocities around 200 m/s toward the observer.

The second column of Fig.6.12 represents the LOS component of the magnetic field measured by the COG method at the three resolutions. At the MURaM resolution, the retrieved distibution over the field-of-view compares well with the distribution in the simulation snapshot (Fig. 6.1). The scatter plot of the actual versus retrieved values (first row, last column, Fig.6.11) shows a clear correlation with the largest dispersion for the weak fields. At the CRISP and SP/SOT resolutions, the local reduction of the magnetic field in UDs is still visible. However, the dispersion of the cloud of points increases with decreasing resolution, and the contrast is strongly reduced. Magnetic fields weaker than 1 kG at the CRISP resolution and weaker than 1.5 kG at the SP/SOT resolution remain virtually invisible due to the spatial smearing.

6.3.4 Bisector analysis

Figure 6.8 shows the generalized response functions of the velocity measured by the bisector analysis of Stokes V profiles to the LOS-velocity perturbation in the average 1D atmosphere. The gRFs for the three intensity levels are shown (I = 0.2, 0.5, 0.8); the derived values of HOFM are indicated by arrows. We apply the same procedure to the $B_{\rm LOS}$ measurements where the magnetic field is perturbed. The gRFs for the $B_{\rm LOS}$ and $V_{\rm LOS}$ measurements are similar: the measured values are formed between $\log\tau \approx -0.25$ (I = 0.2) and ≈ -1.23 (I = 0.8). The distributions of the measured velocity and magnetic fields averaged over bisectors are displayed in the third and fourth columns of Fig.6.12, respectively.

The range of retrieved positive velocities at the MURaM resolution is smaller than for the COG measurements because the method is not applicable to the pixels with the fastest upflows (corresponding to the dark UD lanes that exhibit multi-lobed profiles). At the CRISP and SP/SOT resolutions the distributions of the retrieved velocity are very similar to the results obtained by the COG method. The upper panel of Fig.6.13 shows the retrieved stratification of the LOS velocity with optical depth compared to the velocity in the snapshot. The results are plotted for the 1D average of the snapshot and for the model atmosphere of Example 1 in Fig.6.9. The rertieved values match the actual values well between $\log\tau = -1.2$ and 0.5. The discrepancy increases close to $\tau_{5000} = 1$. Note that the range of values in the plot is

very small, ≈ 50 m/s.

At the MURaM resolution, the distribution of the measured $B_{\rm LOS}$ is similar to the actual distribution in the snapshot. However, the values are slightly lager than those obtained by the COG method mainly due to the COG averaging over the whole spectral line. The lower panel of Fig.6.13 shows the retrieved stratification of $B_{\rm LOS}$ versus the vertical component of the field in the simulation snapshot. Analogous to the velocity measurement, the values in the higher layers ($\log \tau_{5000} \approx -1.2$) are more reliable than those at $\log \tau_{5000} \approx -0.2$ where the methods tends to overestimate the magnetic field.

6.3.5 Milne-Eddington inversions

The gRFs for ME measurements of the magnetic field strength and inclination and of the LOS velocity are shown in Figs. 6.5, 6.6 and 6.7. The corresponding theoretical values of the HOFM (marked by downward pointing arrows) are close to $\log \tau_{5000} = -1$. For the magnetic field measurement, the experimental value closely matches the theoretical value. In contrast, there is a significant discrepancy between the experimental and theoretical HOFM for the $V_{\rm LOS}$ measurement caused by the rather small velocity gradient and consequently the uncertainty of the experimental HOFM. Note that we invert both iron lines, while we used only Fe I 6302.5 Å in the COG and bisector analyses. The Fe I 6301.5 Å is formed slightly higher, thereby increasing the evaluated HOFM for the ME inversions.

The gRFs for ME measurements of the magnetic field strength and inclination and of the LOS velocity are shown in Figs. 6.5, 6.6 and 6.7. The corresponding theoretical values of the HOFM (marked by downward pointing arrows) are close to $\log \tau_{5000} = -1$. For the magnetic field measurement, the experimental value closely matches the theoretical value. In contrast, there is a significant discrepancy between the experimental and theoretical HOFM for the $V_{\rm LOS}$ measurement caused by the rather small velocity gradient and consequently the uncertainty of the experimental HOFM. Note that we invert both iron lines, while we used only Fe I 6302.5 Å in the COG and bisector analyses. The Fe I 6301.5 Å is formed slightly higher, thereby increasing the evaluated HOFM for the ME inversions.

The results of ME inversions of the three synthetic observations are presented in Fig.6.15. Horizontal cuts through the simulation box at the HOFMs for the three parameters are displayed for comparison. The corresponding scatter plots are shown in Fig.6.16. At the MURaM resolution, a clear correlation is present for the strongest magnetic fields (> 2.5 kG). With decreasing field the method tends to underestimate the field strength. The correlation at the CRISP resolution is rather good with a linear correlation coefficient of 0.92. At the SP/SOT resolution, the range of the retrieved values is significantly reduced, with a trend to overestimating for fields weaker than B=2.5 kG and underestimating the strong fields. The inclination measurement at the full resolution (Fig.6.16) shows a small fraction of pixels with opposite polarities due to profiles similar to Example 2 in Fig.6.9; otherwise, the two distributions match rather well at all resolutions. At the MURaM resolution, the scatter plot for the

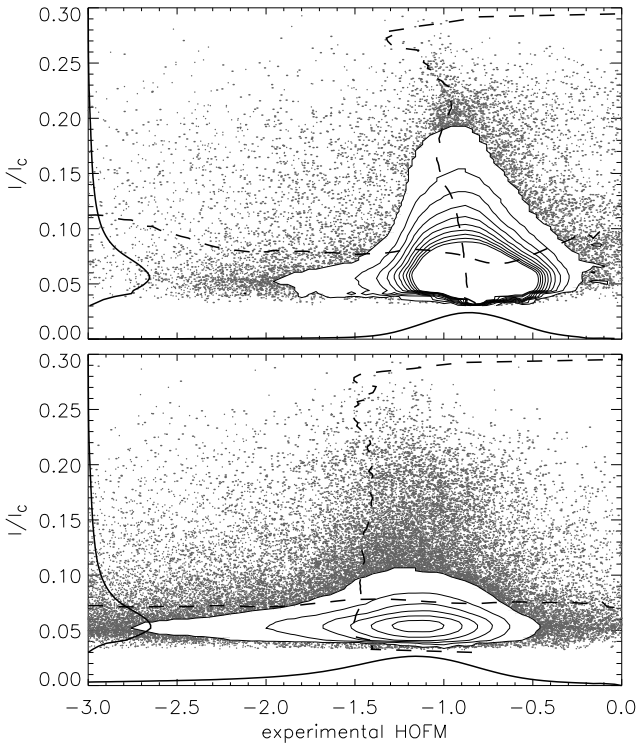

Figure 6.14: Scatter plots of the experimental HOFM of $B_{\rm LOS}$ (*upper panel*) and $V_{\rm LOS}$ (*lower*) versus the continuum intensity. The solid curves show the occurrence distributions. The dashed lines show the first moments of the sample density distribution.

velocity measurements shows a trend to underestimating the actual values. At the smeared resolutions, the distribution of upflows and downflows in Fig.6.15 is still visible, though the range of measured velocities is reduced significantly.

6.3.6 SIR inversions

The result of the SIR inversions is a height-dependent stratification of the physical parameters, which renders the HOFM concept obsolete. Instead, we evaluate the standard deviations of the difference between the original snapshot and the results of the inversions as a function of height. Figure 6.19 shows the results for the three synthetic observations.

At the MURaM resolution, the inversion failed in ≈5% of all profiles. These profiles correspond to the darkest pixels in the continuum intensity map. In the corresponding atmospheres the temperature drops below the temperature threshold

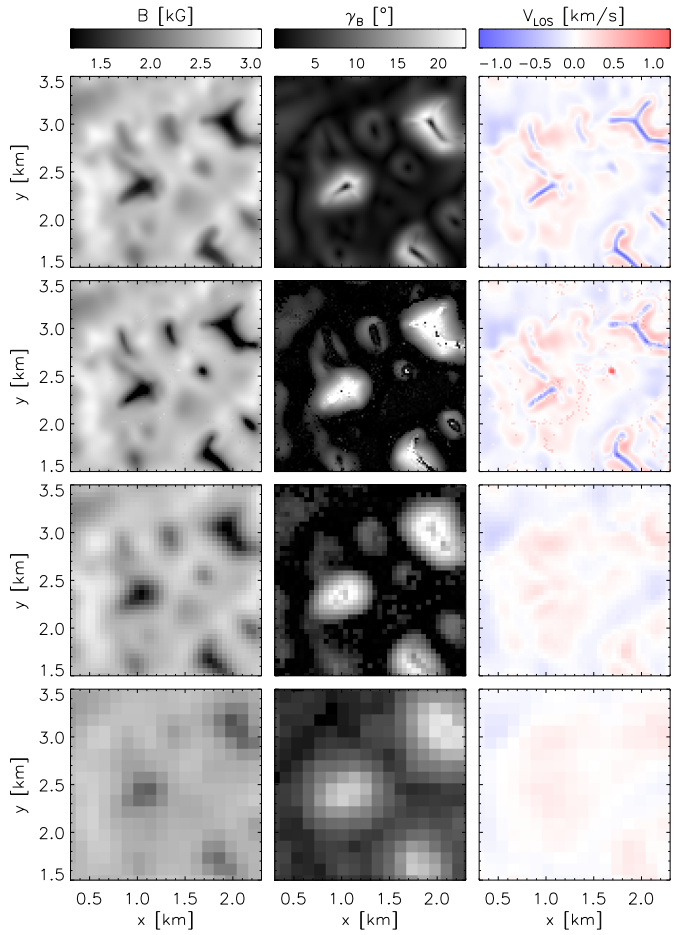

Figure 6.15: Comparison between magnetic field strength (*left*), inclination, (*center*), and LOS velocity (*right*) of the simulation (*first row*) and retrieved from the synthetic observations at the resolutions of MURaM (*second row*, CRISP *third row* and SP/SOT *fourth row*. The horizontal cuts through the simulation snapshot are taken at the theoretical HOFMs for the three parameters (see Figs.6.5, 6.6 and 6.7). Portions of 2 Mm×2 Mm of the full x-y maps are shown. The color scales are clipped at the minimal and maximal parameter values in the corresponding simulation map.

(2000 K) that the inversion code can handle. These pixels are removed from the sample. In the temperature panel of Fig. 6.19, at the MURaM and CRISP resolutions, the deviation is smallest (≈50 K) at the locations of the nodes at $\log \tau_{5000} = 0.3$ and -0.8; it increases with height in the layers above this range of τ_{5000}, and with depth in the layers below. At the SP/SOT resolution the deviation is slightly larger (≈150 K)

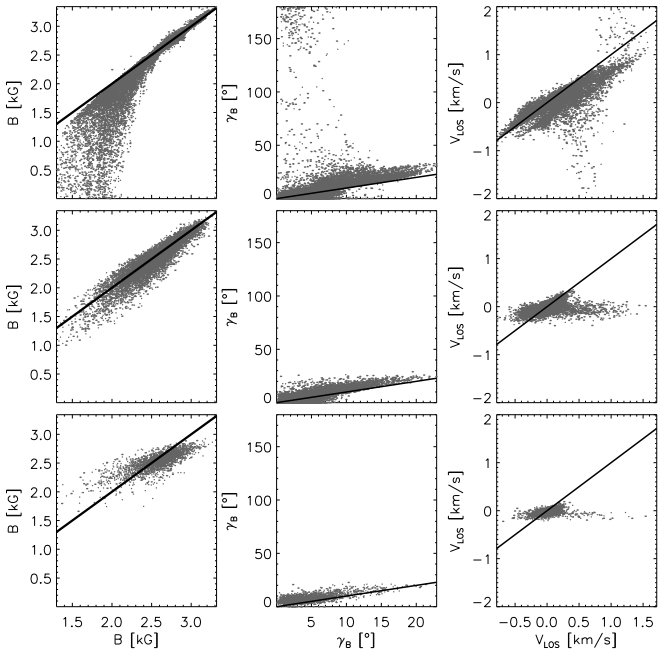

Figure 6.16: Scatterplots of the results from the ME inversions of the synthetic observations against the corresponding simulation quantities for: magnetic field strength (*left*), inclination (*center*) and LOS velocity (*right*). *Top row:* at MURaM resolution; *middle:* at CRISP resolution; *bottom:* at SP/SOT resolution.

in the same range.

The standard deviation of the magnetic field strength has a similar minimum at any resolution (≈100 G), but the height where the minimum is reached increases with decreasing angular resolution. The expansion of the magnetic field with height smears the magnetic features and, therefore, leads to a closer match at lower resolution. The standard deviation of the magnetic field inclination is largest at the MURaM resolution due to the profiles with inverse sign of Stokes V that are present at that resolution (Example 2 in Fig.6.9). In these pixels the code retrieves inclinations ≈180° increasing standard deviation. In addition, the standard deviation of the inclination does not show a rise with height due to the very small inclination gradient present in the vast majority of 1D atmospheres in the snapshot. Therefore, once the inclination is correctly retrieved in the region of line formation and extrapolated as nearly constant into the layers above, it also matches the actual values in those layers. The standard deviation of the velocity has its minimum between $\log \tau_{5000} = 0$ and -0.5. The deviation of the measurement at the CRISP resolution has a larger deviation than at the SP/SOT resolution due to the limited spectral resolution.

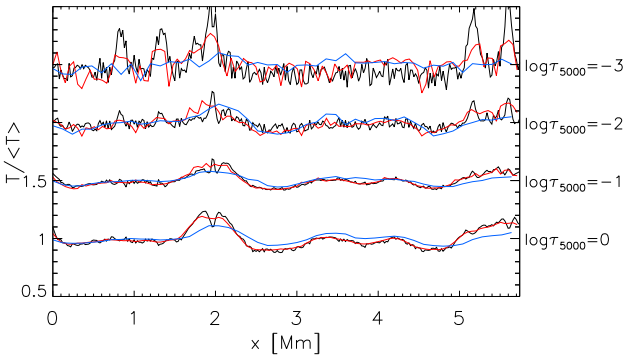

Figure 6.17: Temperature variation at different optical depths in a vertical cut through the 3D stratification obtained by SIR inversions at the three resolutions: MURaM, *black*; CRISP, *red*; SP/SOT, *blue*. The temperature variation is shown relative to the average temperature at every level.

Figure 6.20 shows how the range of temperature, magnetic field strength and velocity varies with optical depth in the snapshot and in the inversion results at the SP/SOT resolution. The results for the UDs and for the DB are shown separately (upper and middle row, respectively). The derived mean 1D stratifications are also presented. They match remarkably well all three parameters and both components (bottom row). In the deepest layers the temperatures of UDs are underestimated due to the smearing of the intensity. Above $\log \tau_{5000} = -1$ the high temperatures in the jets remain completely hidden at the SP/SOT resolution. On the other hand, in the DB, the ranges of the orginal and inferred temperatures are in agreement. The inversion technique is not capable of reproducing the large range of magnetic field strengths in the deep layers of the original snapshot, while above $\log \tau_{5000} \approx -1.5$ it results in a range of values larger than in the snapshot. The systematic errors in the deep layers are due to the spatial smearing; in the high layers they are due to the lack of sensitivity of the spectral lines to the magnetic field. The velocity panels show that the fast upflows are not detected by this method. Moreover, downflows are favored. This effect is more pronounced in UDs.

6.4 Comparison with observations

ME inversions. Watanabe et al. (2009b) observed sunspot umbrae performed with SP/SOT and applied ME inversions to the recorded profiles. The observed Stokes V profiles are all virtually symmetric, which is in accordance with our synthetic observation at the SP/SOT resolution (Fig.6.9). The results of their inversions suggest that, in the statistical average, UDs do not show different magnetic properties from their surroundings, while they show small blue shifts relative to the DB. Figures 6.15

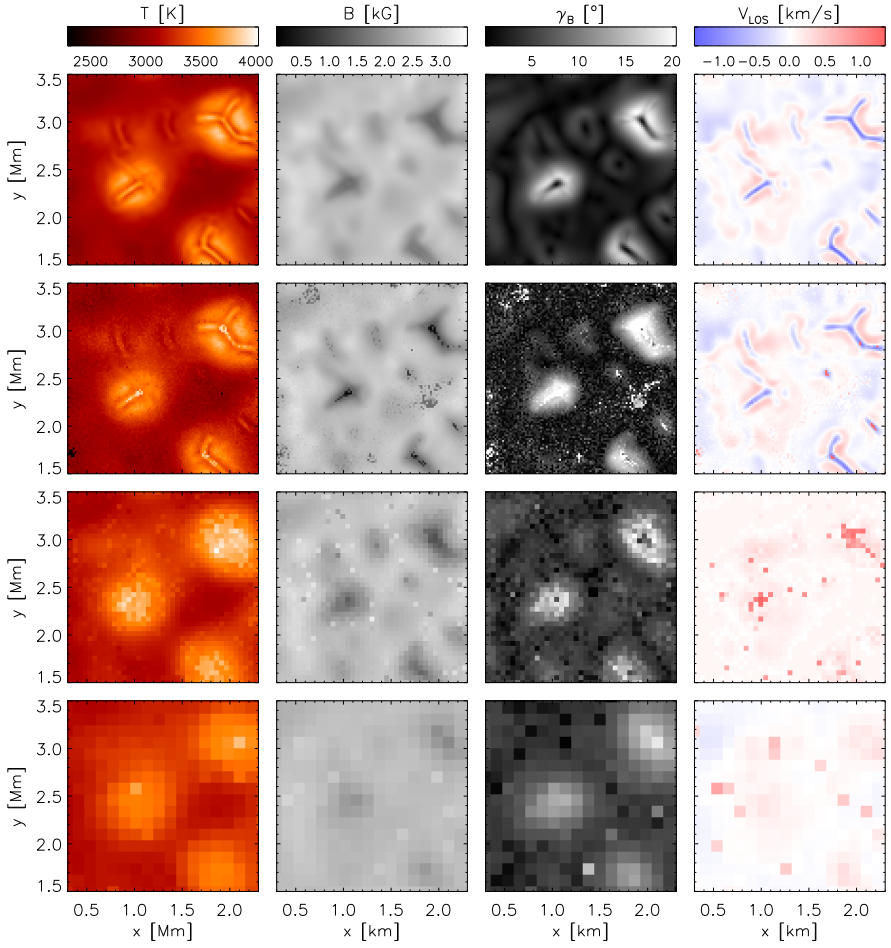

Figure 6.18: Cross-sections at $\tau_{5000} = 1$ through the simulation box and through the 3D models obtained by inversions of the synthetic observations, for the temperature, magnetic field strength, inclination angle, and LOS velocity.

and 6.16 demonstrate that the differences in magnetic field and velocity between UDs and the DB vanish in the ME inversions at the SP/SOT resolution. Therefore, the measurement of Watanabe et al. (2009b) is consistent with our simulation. On the other hand, Watanabe et al. found weak positive correlation between the UD brightness and the observed blueshifts. We cannot confirm that correlation, but we speculate that the UDs causing the observed correlation at the SP/SOT resolution (the brightest UDs with measurable upflow velocities) represent peripheral UDs which are not present in our simulation. s

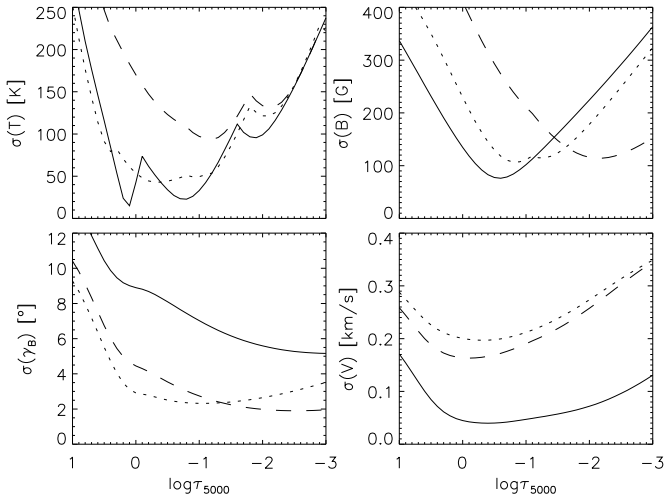

Figure 6.19: Standard deviations of the difference between the original snapshot and the inversion results at the three resolutions (MURaM, *solid*; CRISP *dotted*; SP/SOT *dashed*) as a function of optical depth, for the temperature (*upper left*), magnetic field strength (*upper right*), inclination angle (*lower left*), and LOS velocity (*lower right*).

SIR inversions. Socas-Navarro et al. (2004) obtained the full Stokes vector for a sunspot umbra with the La Palma Stokes Polarimeter at the former Swedish Vacuum Solar Telescope. Riethmüller et al. (2008a) performed a similar observation using SP/SOT on Hinode. Both groups inverted the observed profiles using SIR-like inversions. The observation of Riethmüller et al. has the advantage of better angular resolution. Socas-Navarro et al. (2004) studied peripheral UDs exclusively, while Riethmüller et al. (2008a) analyzed both peripheral and central UDs.

Socas-Navarro et al. (2004) found that (1) the magnetic field in the UDs is more inclined than in the DB for ≈5° to ≈15°; (2) UDs show reduction of the magnetic field strength up to 1 kG; (3) UDs are hotter than the background with the temperature difference is between 500 and 2500 K; (4) the temperature stratification of UDs and the DB merge at $\log \tau_{5000} = -1$; (5) UDs exhibit slow upflows (≈200 m/s) relative to the DB. Riethmüller et al. (2008a) confirmed that peripheral UDs show field inclination (≈5°) while central ones do not. The reduction of the magnetic field strength for both types of UDs is found to be ≈500 G, whereas the temperature enhancement is ≈500 K. The temperature of the UDs reaches the ambiental temperature in the layers above $\log \tau_{5000} = -2$. Upflows up to 800 m/s are found in the peripheral UDs; the central UDs are nearly static. They found weak downflows in the vicinity of upflows associated to some UDs.

We simulated the observation of Riethmüller et al. (2008a). Figure 6.18 shows the results of the inversions of the synthetic observations at $\log \tau_{5000} = -1$. The comparison with the original snapshot shows that the contrasts in the temperature,

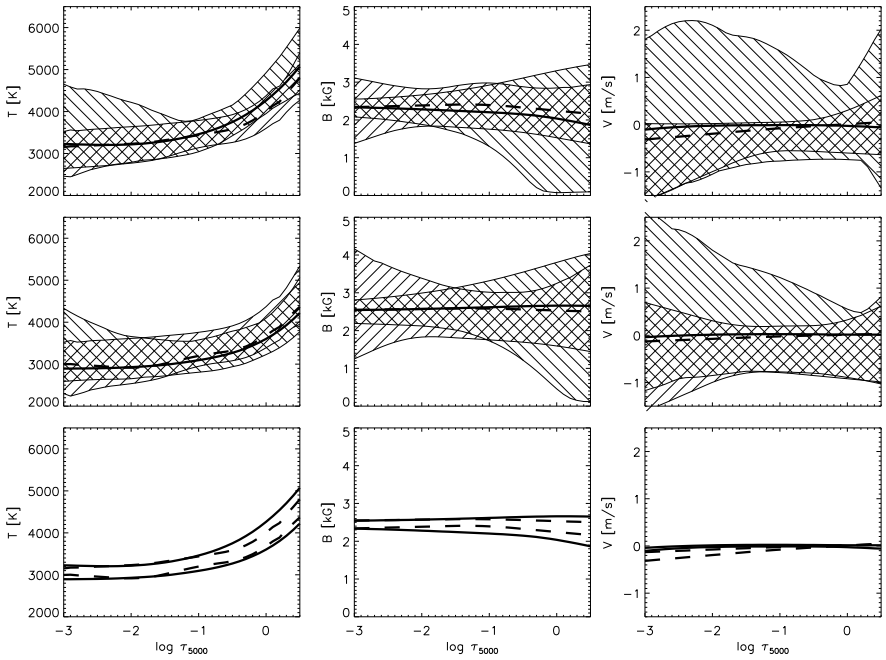

Figure 6.20: Range of the temperature (*left*), magnetic field strength (*center*) and LOS velocity (*right*) with height. Areas filled with the \\\ pattern correspond to the simulation snapshot; areas filled with /// to the results inferred from the synthetic SP/SOT observation. The *solid* curves show the mean models at the MURaM resolution; *dashed* at the resolution of SP/SOT. The results are shown separately for the UDs (*top panels*) and for the DB (*middle*). The bottom panels show the comparison between the mean models of the two components.

magnetic field strength and LOS velocity are reduced in the data retrieved from the synthetic observation at the SP/SOT resolution. However, the averages over the UDs and the DB are rather well reproduced as is shown in Fig.6.20. The temperature and magnetic field values found by Socas-Navarro et al. and Riethmüller et al. are therefore confirmed.

The strong upflows present in the simulation are absent from the inferred velocities. Weak downflows are detected instead at the UD locations. The main reason for this is the insufficient angular resolution. The velocity signal in an UD is dominated by the bright pixels which are largely co-spatial with downflows. Figure 6.20 shows that the large variety of upflows in UDs and the DB remains invisible at the SP/SOT resolution. This is in agreement with the results of Riethmüller et al. for the central UDs, and also with the measurements of Hartkorn & Rimmele (2003) who detected measurable upflows in peripheral UDs identified as penetrating penumbral grains, while the "normal" central UDs showed no motion, weak downflows and occasionally downflows up to ≈300 m/s.

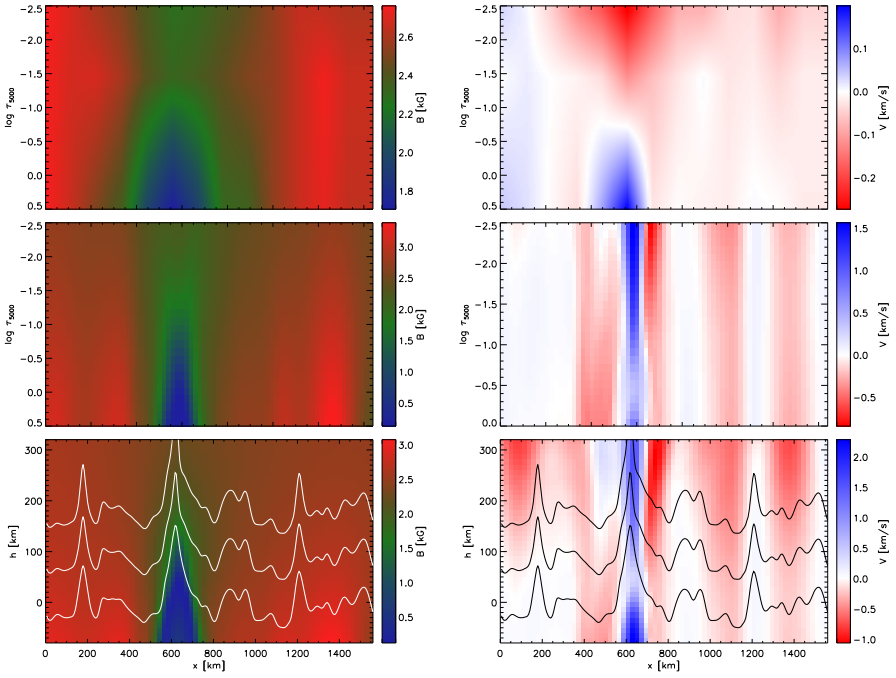

Figure 6.21: Vertical cross-sections through the magnetic field strength (*left*) and LOS velocity (*right*) of a simulated UD. *Top row:* cut through the results of the SIR inversion applied to the synthetic observation at the SP/SOT resolution (analogous to Fig. 5 of Riethmüller et al. (2008a)); *middle:* cut through the simulation snapshot shown in the optical depth scale; *bottom:* cut through the simulation snapshot shown in the geometrical height scale. The curves show the levels where $\log \tau_{5000} = 0, -1$ and -2.

Profile-integrated diagnostics. Ortiz et al. (2010) used the CRISP instrument at the SST to observe a pore at $\mu = 0.85$. We simulated an observation of a sunspot umbra at disk center with CRSIP and evaluated the diagnostics they used. The size of the observed pore is comparable to the area covered by our snapshot. The results shown in Fig.6.10 qualitatively match the findings of Ortiz et al.: the LP is only relatively large at the locations of the bright parts of the UDs; the central dark lanes show a reduction of the CP, whereas the brigh parts show a CP similar as the one in the DB; the NCP at this resolution is fairly homogeneous. These authors observed upflows associated with UDs and downflows at the end-points of the UDs. The simulation indeed predicts upflows roughly co-spatial with the dark lanes and surrounding downflows. However, the upflowing regions in the simulated UDs are quite narrow (Figs.6.1 and 6.2). As they correspond to relatively dark pixels, the upflows become barely visible with decreasing spatial resolution. We tested several methods for the detection of the upflows in the synthetic observations at the CRISP

and SP/SOT resolutions (Figs.6.12, 6.15, 6.18). The results show that the clearest detection of the upflows is obtained with the COG method applied to the Stokes V profiles. However, the range of the retrieved velocities is significantly reduced relative to the range found in the simulations. The COG method gives the best UD velocity measurement, because the peak of its sensitivity is slightly deeper than for the ME inversions and the bisector analysis.

However, note that our determination of the LOS velocity is not identical to the method used by Ortiz et al.; we perform the measurement with Stokes V profiles, whereas they used intensity profiles. The Stokes I profiles in their observations do not show clear Zeeman splitting. This is not the case with the simulated profiles at disk center, which is why we cannot repeat their measurements with our synthetic observations in an identical way. To figure out what causes the lack of the split in the real CRISP observations, we skew[1] the snapshot to $\mu = 0.85$ and computed the line profiles at that viewing angle. The result is shown in Fig.6.22. The thick, black curve represents the Stokes I profile at $\mu = 1$ (upper panel) and $\mu = 0.85$ (lower panel) averaged over the entire snapshot. Away from disk center the π component is more pronounced. The red curve shows the profiles after the spectral and spatial smearing to the CRISP resolution; pluses specify the actual filter positions. At $\mu = 0.85$ the clear Zeeman splitting almost disappeared, though the shape of the profile remains boxy. If the profile is contaminated with a fraction of the quiet-Sun stray-light[2] ($\alpha = 5\%$), the boxy shape is no longer present, so that the profiles become similar to those shown in Fig. 5 of Ortiz et al. (2010). As the Stokes I profiles of Ortiz et al. contain an unknown stray-light contribution, we are unable to reproduce their measurements, instead we apply the COG method to the Stokes V profiles as described above.

Limitations. There are several limitations to this study. First, we simulate an isolated umbra neglecting the surrounding penumbra and quiet sun, so that our UDs are central UDs by definition.

Second, the size and properties of the simulated UDs depend on the boundary conditions. Particularly, the closed top boundary of our simulation box affects the solution in the high layers. However, as shown above, all our diagnostics form largely below $\log \tau_{5000} = -2$, more than one scale height below the upper boundary.

The third limitation is the assumption of LTE for the line synthesis. Shchukina & Trujillo Bueno (1998) analyzed the NLTE effects on the formation of iron lines in the semi-empirical model of Maltby et al. (1986). They found that the NLTE effects are rather marginal, though more important for the lines with intermediate and high excitation potentials. As our snapshot is cooler than the model of Maltby et al. (1986) (Fig. 4 in Paper I), the NLTE populations of the Fe I 6302 Å lines ($\chi \approx 3.7$ eV) are very close to the LTE ones.

Fourth, we use the same set of atomic parameters for forward modeling and for inversions. In that respect, we neglect any ambiguity due to uncertainties in the

[1] The skewing procedure is described in detail in Paper I.

[2] As a stray-light component we use the synthetic profile of Fe I 6301 and 6302 Å at $\mu = 0.85$ computed by de la Cruz Rodríguez et al. (2010).

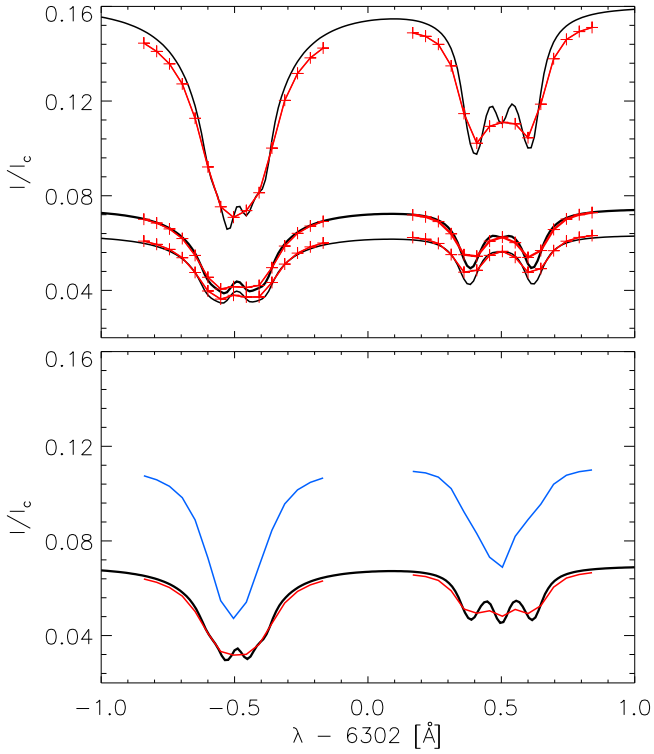

Figure 6.22: *Upper panel:* Average line profiles at disk center. The three black curves show averages at the MURaM resolution. The middle one is the average over the entire snapshot, whereas the top and bottom curves show averages over the UDs and the DB, respectively. The red curves show the same profiles after averaging the synthetic observation at the CRISP resolution. The crosses specify the CRISP wavelength positions. In this averaging, the UDs and the DB are defined by setting a threshold at 1.6 of the mean continuum intensity. *Lower panel*: line profiles averaged over the entire snapshot at $\mu = 0.85$. The black and red curves correspond to synthetic observations at the MURaM and CRISP resolution, respectively. The blue curves show the synthetic CRISP observation after a stray-light contamination with 5% of the quiet-sun spectrum.

atomic input data. We also neglect all other atomic or molecular lines that might contaminate the real observations.

Fifth, the point spread functions used to smear the synthetic profiles to the resolution of the real instruments are not completly realistic. The main discrepancy is in the far wings of the PSFs affecting the brightness ratio in the synthetic observations.

Sixth, the stray light originating from the surrounding penumbra and quiet sun is neglected both in the degradation of the synthetic observations and when different diagnostics are applied to these synthetic data. This is a serious limitation since all

intensities measured in a real umbra are dominated by stray light. One should consider multiple lines of different ionization species and different excitation potentials to address the stray light issue properly.

Seventh, the scheme we employ for the SIR inversion is rather simple. More sophisticated approaches (e.g., cycles with increasing number of nodes, initial models closer to the expected solution or repeated inversions) would probably improve the results. However, no matter how sophisticated the inversion setup, the retrieved physical parameters can be trusted only where the lines are actually formed. There, even the simple scheme employed here performs rather well (Fig.6.19).

6.5 Conclusions

We have synthesized spectral line profiles of Fe I 6301.5 Å and 6302.5 Å from a MURaM simulation snapshot sampling a sunspot umbra. Various diagnostics were applied to the synthetic profiles after degradation to match the angular and spectral resolutions of the CRISP and SP/SOT instruments. Our comparison of physical parameters between the original snapshot and the corresponding ones retrieved from the synthetic observations yield the following conclusions:

(1) Most of the Stokes V profiles at the MURaM resolution (≈95%) show regular two-lobed shapes in both lines. The UDs often cause anomalous profiles, particular in their dark lanes. Some of these anomalous profiles show sign reversals in Stokes V due to the temperature rise with height along upflowing plumes. Similar anomalous profiles with Stokes V reversal are observed in umbral flashes (Socas-Navarro et al. 2000). The asymmetries are become much smaller at the CRISP resolution and vanish at the SP/SOT resolution.

(2) At the CRISP resolution, the spatial distributions of the integrated polarization diagnostics (LP, CP, NCP) agree qualitatively with the results of Ortiz et al. (2010). However, we do not find as high NCP values as measured by these authors. This discrepancy may partly be due to viewing angle ($\mu = 0.85$ in their observation). However, other observational studies suggest that the NCP nearly vanishes in umbrae (e.g., Tritschler et al. (2007), Ichimoto et al. (2009)).

(3) The values of the LOS velocity and magnetic field strength retrieved at the MURaM resolution by the COG method show a remarkable correlation with the simulation parameters at the corresponding height of formation ($\log \tau_{5000} \approx -0.5$). The upflows and downflows corresponding to the UDs are clearly visible in the inferred velocity maps. They remain visible at the CRISP resolution, though the range of the velocities is strongly reduced (especially for the upflows). Therefore, we conclude that the UDs with upflows and downflows observed by Ortiz et al. (2010) are more similar to peripheral UDs which exhibit faster flows than central UDs.

(4) Our bisector analysis of the synthetic Stokes V profiles provides a reasonable estimate of the LOS velocity and magnetic field and their gradients between $\log \tau_{5000} \approx -0.5$ and $\log \tau_{5000} \approx -1.5$. However, it tends to overestimate gradients in deeper layers. This is consistent with the observations of Sankarasubramanian & Rimmele (2002).

(5) ME inversions are suitable to measure the DB magnetic field at the height of formation for all three resolutions. The results for UD magnetic fields depend on angular resolution. At high resolution, the field is underestimated because the ME simplification cannot reproduce complex irregular profiles. At low resolution, the field is overestimated due to the spatial smearing. Our results are in agreement with the observations of Watanabe et al. (2009b).

(6) Although extended patches of upflows and downflows are correctly identified by the ME inversions, the retrieved contrast between upflows and downflows is much too small.

(7) The SIR inversions of the synthetic observations at the SP/SOT resolution recover the average height-dependent stratification of the UDs and the DB remarkably well. Nevertheless, in deep layers extreme values of the LOS velocity and magnetic field strength remain undetected. The relatively fast upflows in the plumes are also invisible for this method. In high layers, the method yields a range of magnetic field strengths in excess of the actual snapshot values due to insufficient sensitivity.

(8) The deviations in temperature, LOS velocity and magnetic field strength and inclination between the results from the SIR inversions and the simulation input become large above $\log \tau_{5000} \approx -2$. They also worsen for decreasing angular and spectral resolution. However, they provide only a lower limit because stray-light in actual observations increases the error. For this reason, the results of Socas-Navarro et al. (2004) and Riethmüller et al. (2008a) showing no difference between the bright and dark component above $\log \tau_{5000} \approx -2$ remain inconclusive.

(9) The spatially averaged difference in the temperature and magnetic field strength and inclination between the UDs and the DB in the snapshot matches the observations of Socas-Navarro et al. (2004) and Riethmüller et al. (2008a) remarkably well. The measured velocities in these observations also agree with the snapshot values, although the velocities inferred by our inversions of the spatially smeared synthetic observations are significantly smaller. However, our results are in good agreement with Riethmüller et al. (2008a) who observed almost no motions in central UDs.

Acknowledgments

We thank J. Sánchez Almeida, H. Socas-Navarro, J. Trujillo Bueno and T. Perreira for useful discussions. NV thanks B. Viticchiè for his friendly coercion to complete this research and R. J. Rutten for improvements to the text. The authors thankfully acknowledge the technical expertise and assistance provided by the Spanish Supercomputing Network (Red Española de Supercomputación), and the use of the LaPalma Supercomputer, located at the Instituto de Astrofísica de Canarias. This research was supported by a Marie Curie Early Stage Research Training Fellowship of the EC's Sixth Framework Programme under contract number MEST-CT-2005-020395. This research has made use of NASA's Astrophysics Data System.

Bibliography

Abt, A. 1952, Astrophys. J., 115, 199 (cited on page 30)

Albregtsen, F., Joras, P. B., & Maltby, P. 1984, Sol. Phys., 90, 17 (cited on pages 99, 100, and 103)

Albregtsen, F. & Maltby, P. 1981, Sol. Phys., 71, 269 (cited on page 99)

Allen, M. S. 1978, Astrophys. J., 219, 307 (cited on pages 14, 15, 16, and 24)

Arlandini, C., Käppeler, F., Wisshak, K., et al. 1999, Astrophys. J., 525, 886 (cited on page 15)

Asensio Ramos, A. 2009, Astrophys. J., 690, 416 (cited on page 7)

Asensio Ramos, A., Martínez González, M. J., López Ariste, A., Trujillo Bueno, J., & Collados, M. 2007, Astrophys. J., 659, 829 (cited on page 30)

Asplund, M. 2000, Astron. Astrophys., 359, 755 (cited on page 6)

Asplund, M., Grevesse, N., & Sauval, A. J. 2005, in ASP Conf. Ser., Vol. 336, Cosmic Abundances as Records of Stellar Evolution and Nucleosynthesis, ed. T. G. Barnes, III & F. N. Bash, 25 (cited on pages 14, 15, and 21)

Asplund, M., Grevesse, N., Sauval, A. J., Allende Prieto, C., & Kiselman, D. 2004, Astron. Astrophys., 417, 751 (cited on page 6)

Asplund, M., Nordlund, Å., Trampedach, R., Allende Prieto, C., & Stein, R. F. 2000a, Astron. Astrophys., 359, 729 (cited on page 6)

Asplund, M., Nordlund, Å., Trampedach, R., & Stein, R. F. 2000b, Astron. Astrophys., 359, 743 (cited on page 6)

Auer, L. H., House, L. L., & Heasley, J. N. 1977, Sol. Phys., 55, 47 (cited on page 50)

Bellot Rubio, L. R. 2009, Astrophys. J., 700, 284 (cited on pages 58, 59, 71, 72, 73, 74, and 77)

Berdyugina, S. V., Solanki, S. K., & Frutiger, C. 2003, Astron. Astrophys., 412, 513 (cited on page 24)

Bergemann, M. & Gehren, T. 2007, Astron. Astrophys., 473, 291 (cited on page 36)

Bharti, L., Beeck, B., & Schüssler, M. 2010, Astron. Astrophys., 510, A12 (cited on pages 82, 86, 87, and 123)

Bharti, L., Joshi, C., & Jaaffrey, S. N. A. 2007, Astrophys. J. Lett., 669, L57 (cited on page 82)

Biermann, L. 1941, Vierteljahresschr. Astron. Ges., 76, 194 (cited on page 82)

Blackwell-Whitehead, R. J., Pickering, J. C., Pearse, O., & Nave, G. 2005, Astrophys. J. Suppl., 157, 402 (cited on page 35)

Bord, D. J. & Cowley, C. R. 2002, Sol. Phys., 211, 3 (cited on page 15)

Bruls, J. H. M. J. & Solanki, S. K. 1993, Astron. Astrophys., 273, 293 (cited on page 37)

Buente, M., Solanki, S. K., & Steiner, O. 1993, Astron. Astrophys., 268, 736 (cited on pages 38 and 52)

Cabrera Solana, D., Bellot Rubio, L. R., & del Toro Iniesta, J. C. 2005, Astron. Astrophys., 439, 687 (cited on page 69)

Cameron, R., Schüssler, M., Vögler, A., & Zakharov, V. 2007, Astron. Astrophys., 474, 261 (cited on pages 59 and 83)

Canfield, R. C. 1971, Astron. Astrophys., 10, 64 (cited on page 32)

Carlsson, M. 1992, in ASP Conf. Ser., Vol. 26, Cool Stars, Stellar Systems, and the Sun, ed. M. S. Giampapa & J. A. Bookbinder, 499 (cited on page 20)

Carlsson, M. 2009, Mem. Soc. Astron. Italiana, 80, 606 (cited on page 8)

Carlsson, M., Stein, R. F., Nordlund, Å., & Scharmer, G. B. 2004, Astrophys. J. Lett., 610, L137 (cited on pages 8 and 33)

Cattaneo, F., Hurlburt, N. E., & Toomre, J. 1990, Astrophys. J. Lett., 349, L63 (cited on page 58)

Chen, Q.-S. & Weinhous, M. S. 1999, in SPIE Conf. Ser., Vol. 3661, SPIE Conf. Ser., ed. K. M. Hanson, 728 (cited on page 84)

Cheung, M. C. M., Rempel, M., Title, A. M., & Schüssler, M. 2010a, Astrophys. J., 720, 233 (cited on page 8)

Cheung, M. C. M., Rempel, M., Title, A. M., & Schüssler, M. 2010b, ArXiv e-prints (cited on page 59)

Cheung, M. C. M., Schüssler, M., & Moreno-Insertis, F. 2007a, Astron. Astrophys., 467, 703 (cited on pages 8, 59, 77, and 83)

Cheung, M. C. M., Schüssler, M., & Moreno-Insertis, F. 2007b, Astron. Astrophys., 461, 1163 (cited on pages 7, 58, and 63)

Cheung, M. C. M., Schüssler, M., Tarbell, T. D., & Title, A. M. 2008, Astrophys. J., 687, 1373 (cited on page 8)

Corliss, C. H. & Bozman, W. R. 1962, Experimental transition probabilities for spectral lines of seventy elements (NBS Monograph, US Department of Commerce, National Bureau of Standards, Washington) (cited on page 20)

Cram, L. E., Lites, B. W., & Rutten, R. J. 1980, Astrophys. J., 241, 374 (cited on page 32)

Curdt, W., Brekke, P., Feldman, U., et al. 2001, Astron. Astrophys., 375, 591 (cited on page 19)

Danielson, R. 1965, in IAU Symposium, Vol. 22, Stellar and Solar Magnetic Fields, ed. R. Lust, 314 (cited on page 82)

Danilovic, S., Gandorfer, A., Lagg, A., et al. 2008, Astron. Astrophys., 484, L17 (cited on pages 6, 8, and 90)

Danilovic, S., Schüssler, M., & Solanki, S. K. 2010, Astron. Astrophys., 513, A1+ (cited on page 8)

Danilović, S., Solanki, S. K., Livingston, W., Krivova, N., & Vince, I. 2007, in Modern solar facilities - advanced solar science, ed. F. Kneer, K. G. Puschmann, & A. D. Wittmann, 189–+ (cited on pages 30, 34, 51, and 52)

Danilovic, S. & Vince, I. 2004, Serbian Astronomical Journal, 169, 47 (cited on page 30)

Danilovic, S. & Vince, I. 2005, Mem. Soc. Astron. Italiana, 76, 949 (cited on page 30)

Danilovic, S., Vince, I., Vitas, N., & Jovanovic, P. 2005, Serbian Astronomical Journal, 170, 79 (cited on page 30)

de la Cruz Rodríguez, J., Kiselman, D., & Carlsson, M. 2010, in preparation (cited on page 138)

de Wijn, A. G., Rutten, R. J., Haverkamp, E. M. W. P., & Sütterlin, P. 2005, Astron. Astrophys., 441, 1183 (cited on page 33)

Deinzer, W. 1965, Astrophys. J., 141, 548 (cited on page 82)

Delbouille, L., Roland, G., & Neven, L. 1973, Atlas photométrique du spectre solaire de λ 3000 Å à λ 10000 Å (Institut d'Astrophysique, Université de Liège) (cited on page 16)

Doyle, J. G., Jevremović, D., Short, C. I., et al. 2001, Astron. Astrophys., 369, L13 (cited on pages 30, 31, 32, and 52)

Elste, G. 1987, Sol. Phys., 107, 47 (cited on pages 30 and 31)

Elste, G. & Teske, R. G. 1978, Sol. Phys., 59, 275 (cited on pages 30, 31, and 34)

Farouqi, K. 2005, Ph.D. Thesis, University of Mainz, Germany (cited on page 16)

Fligge, M., Solanki, S. K., & Unruh, Y. C. 2000, Astron. Astrophys., 353, 380 (cited on page 51)

Fontenla, J. M., Avrett, E., Thuillier, G., & Harder, J. 2006, Astrophys. J., 639, 441 (cited on page 52)

Fontenla, J. M., Avrett, E. H., & Loeser, R. 1993, Astrophys. J., 406, 319 (cited on pages 51 and 52)

Freytag, B., Allard, F., Ludwig, H., Homeier, D., & Steffen, M. 2010, Astron. Astrophys., 513, A19+ (cited on page 8)

Freytag, B. & Höfner, S. 2008, Astron. Astrophys., 483, 571 (cited on page 8)

Fuhr, J. R. & Wiese, W. L. 2006, in CRC Handbook of Chemistry and Physics (87th edition), ed. D. R. Lide (CRC Press, Inc., Boca Raton, FL) (cited on pages 19, 20, and 21)

Gadun, A. S. & Hanslmeier, A. 2000, Kinematika i Fizika Nebesnykh Tel, 16, 130 (cited on page 58)

Gadun, A. S., Hanslmeier, A., Pikalov, K. N., et al. 2000, A&A Suppl., 146, 267 (cited on page 61)

Gingerich, O., Noyes, R. W., Kalkofen, W., & Cuny, Y. 1971, Sol. Phys., 18, 347 (cited on pages 88 and 118)

Gizon, L., Birch, A. C., & Spruit, H. C. 2010, Annu. Rev. Astron. Astrophys., 48, 289 (cited on page 8)

Gokhale, M. H. & Zwaan, C. 1972, Sol. Phys., 26, 52 (cited on page 82)

Goldberg, L., Muller, E. A., & Aller, L. H. 1960, Astrophys. J. Suppl., 5, 1 (cited on pages 14 and 15)

Gonzalez, G. 2006a, MNRAS, 371, 781 (cited on pages 14, 17, 18, and 25)

Gonzalez, G. 2006b, MNRAS, 370, L90 (cited on page 14)

Gray, D. F. 2008, The Observation and Analysis of Stellar Photospheres, ed. Gray, D. F. (Cambridge University Press) (cited on pages 92 and 115)

Grevesse, N. & Sauval, A. J. 1998, Space Sci. Rev., 85, 161 (cited on page 15)

Grossmann-Doerth, U. 1994, Astron. Astrophys., 285, 1012 (cited on page 71)

Grossmann-Doerth, U., Schmidt, W., & Schroeter, E. H. 1986, Astron. Astrophys., 156, 347 (cited on page 124)

Gurtovenko, E. A. & Kostyk, R. I. 1989a, Fraungoferov spektr i sistema solnechnykh sil ostsilliatorov (Nauk. dumka, Kyiv) (cited on page 20)

Gurtovenko, E. A. & Kostyk, R. I. 1989b, Kiev Izdatel Naukova Dumka (cited on page 32)

Hartkorn, K. & Rimmele, T. 2003, in Astronomical Society of the Pacific Conference Series, Vol. 286, Current Theoretical Models and Future High Resolution Solar Observations: Preparing for ATST, ed. A. A. Pevtsov & H. Uitenbroek, 193–+ (cited on pages 108 and 136)

Holweger, H. & Müller, E. A. 1974, Sol. Phys., 39, 19 (cited on page 21)

Ichimoto, K., Suematsu, Y., Katsukawa, Y., et al. 2009, in Astronomical Society of the Pacific Conference Series, Vol. 405, Astronomical Society of the Pacific Conference Series, ed. S. V. Berdyugina, K. N. Nagendra, & R. Ramelli, 167–+ (cited on page 140)

Jackson, D. A. 1981, Physica, 103, 437 (cited on page 19)

Kasting, J. F., Whitmire, D. P., & Reynolds, R. T. 1993, Icarus, 101, 108 (cited on page 1)

Keller, C. U. 2006, in ASP Conf. Ser., Vol. 354, Solar MHD Theory and Observations: A High Spatial Resolution Perspective, ed. J. Leibacher, R. F. Stein, & H. Uitenbroek, 3 (cited on page 74)

Keller, C. U., Schüssler, M., Vögler, A., & Zakharov, V. 2004, Astrophys. J. Lett., 607, L59 (cited on pages 8, 33, 60, 83, 84, and 98)

Khomenko, E. & Collados, M. 2007a, in Modern solar facilities - advanced solar science, ed. F. Kneer, K. G. Puschmann, & A. D. Wittmann, 303–+ (cited on page 7)

Khomenko, E. & Collados, M. 2007b, Mem. Soc. Astron. Italiana, 78, 166 (cited on page 7)

Khomenko, E., Martinez Pillet, V., Solanki, S. K., et al. 2010, ArXiv e-prints (cited on page 58)

Khomenko, E. V., Martínez González, M. J., Collados, M., et al. 2005a, Astron. Astrophys., 436, L27 (cited on page 7)

Khomenko, E. V., Shelyag, S., Solanki, S. K., & Vögler, A. 2005b, Astron. Astrophys., 442, 1059 (cited on pages 7, 59, 61, and 110)

Kitai, R., Watanabe, H., Nakamura, T., et al. 2007, PASJ, 59, 585 (cited on page 91)

Kneer, F. 1973, Sol. Phys., 28, 361 (cited on page 108)

Knobloch, E. & Weiss, N. O. 1984, MNRAS, 207, 203 (cited on page 82)

Kochukhov, O., Freytag, B., Piskunov, N., & Steffen, M. 2007, in IAU Symposium, Vol. 239, IAU Symposium, ed. T. Kuroda, H. Sugama, R. Kanno, & M. Okamoto, 68–70 (cited on page 8)

Kratz, K.-L., Farouqi, K., Pfeiffer, B., et al. 2007, Astrophys. J., 662, 39 (cited on pages 15 and 16)

Krivova, N. A., Solanki, S. K., Fligge, M., & Unruh, Y. C. 2003, Astron. Astrophys., 399, L1 (cited on page 51)

Kupka, F., Piskunov, N., Ryabchikova, T. A., Stempels, H. C., & Weiss, W. W. 1999, A&A Suppl., 138, 119 (cited on page 18)

Kurucz, R. & Bell, B. 1995, 23 (cited on pages 16, 18, 19, and 20)

Kurucz, R. L. 1979, Astrophys. J. Suppl., 40, 1 (cited on page 51)

Kurucz, R. L. 1992a, Rev. Mexicana Astron. Astrofis., 23, 181 (cited on page 51)

Kurucz, R. L. 1992b, Rev. Mexicana Astron. Astrofis., 23, 187 (cited on page 51)

Kurucz, R. L. 1993, ATLAS9 Stellar Atmosphere Programs and 2 km/s grid, CD-ROM No 13 (CD-ROM No 13) (cited on page 83)

Lambert, D. L., Mallia, E. A., & Warner, B. 1969, MNRAS, 142, 71 (cited on pages 15 and 20)

Landi degl'Innocenti, E. 1975, Astron. Astrophys., 45, 269 (cited on page 21)

Landi degl'Innocenti, E. 1978, A&A Suppl., 33, 157 (cited on pages 21 and 35)

Leenaarts, J., Rutten, R. J., Carlsson, M., & Uitenbroek, H. 2006a, Astron. Astrophys., 452, L15 (cited on page 53)

Leenaarts, J., Rutten, R. J., Sütterlin, P., Carlsson, M., & Uitenbroek, H. 2006b, Astron. Astrophys., 449, 1209 (cited on pages 34 and 53)

Leenaarts, J., Sütterlin, P., Rutten, R. J., Carlsson, M., & Uitenbroek, H. 2005, in ESA Special Publication, Vol. 596, Chromospheric and Coronal Magnetic Fields, ed. D. E. Innes, A. Lagg, & S. A. Solanki (cited on page 34)

Leenaarts, J. & Wedemeyer-Böhm, S. 2005, Astron. Astrophys., 431, 687 (cited on page 7)

Lemaire, P. & Skumanich, A. 1973, Astron. Astrophys., 22, 61 (cited on page 32)

Lites, B. W., Bida, T. A., Johannesson, A., & Scharmer, G. B. 1991, Astrophys. J., 373, 683 (cited on page 108)

Livingston, W. & Wallace, L. 1987, Astrophys. J., 314, 808 (cited on page 30)

Livingston, W., Wallace, L., White, O. R., & Giampapa, M. S. 2007, Astrophys. J., 657, 1137 (cited on page 30)

Lodders, K. 2003, Astrophys. J., 591, 1220 (cited on pages 14 and 15)

López Ariste, A., Ramírez Vélez, J. C., Tomczyk, S., Casini, R., & Semel, M. 2006a, in Astronomical Society of the Pacific Conference Series, Vol. 358, Astronomical Society of the Pacific Conference Series, ed. R. Casini & B. W. Lites, 54–+ (cited on page 30)

López Ariste, A., Tomczyk, S., & Casini, R. 2002, Astrophys. J., 580, 519 (cited on page 30)

López Ariste, A., Tomczyk, S., & Casini, R. 2006b, Astron. Astrophys., 454, 663 (cited on page 30)

Malagoli, A., Cattaneo, F., & Brummell, N. H. 1990, Astrophys. J. Lett., 361, L33 (cited on pages 58 and 61)

Malanushenko, O., Jones, H. P., & Livingston, W. 2004, in IAU Symposium, Vol. 223, Multi-Wavelength Investigations of Solar Activity, ed. A. V. Stepanov, E. E. Benevolenskaya, & A. G. Kosovichev, 645–646 (cited on pages 30, 33, 34, and 50)

Maltby, P., Avrett, E. H., Carlsson, M., et al. 1986, Astrophys. J., 306, 284 (cited on pages 22, 36, 38, 87, 89, 90, 100, 102, and 138)

Martinez Pillet, V. 1992, Sol. Phys., 140, 207 (cited on page 91)

Martínez-Sykora, J., Hansteen, V., & Carlsson, M. 2008, Astrophys. J., 679, 871 (cited on page 8)

Martínez-Sykora, J., Hansteen, V., & Carlsson, M. 2009, Astrophys. J., 702, 129 (cited on page 8)

Meyer, B. S. 1994, Annu. Rev. Astron. Astrophys., 32, 153 (cited on page 14)

Milkey, R. W. & Mihalas, D. 1974, Astrophys. J., 192, 769 (cited on page 32)

Minnaert, M. & Wanders, A. J. M. 1932, Zeitschrift fur Astrophysik, 5, 297 (cited on page 99)

Morton, D. C. 2000, Astrophys. J. Suppl., 130, 403 (cited on page 20)

Neckel, H. 1999, Sol. Phys., 184, 421 (cited on page 37)

Nesis, A., Bogdan, T. J., Cattaneo, F., et al. 1992, Astrophys. J. Lett., 399, L99 (cited on pages 73 and 74)

Nesis, A., Hanslmeier, A., Hammer, R., et al. 1993, Astron. Astrophys., 279, 599 (cited on pages 58 and 74)

Nordlund, A. 1982, Astron. Astrophys., 107, 1 (cited on page 6)

Nordlund, Å., Stein, R. F., & Asplund, M. 2009, Living Reviews in Solar Physics, 6, 2 (cited on pages 2, 58, 82, and 162)

Norton, A. A. & Gilman, P. A. 2004, Astrophys. J., 603, 348 (cited on pages 99 and 103)

Obridko, V. N. 1974, Astron. Zhur., 51, 1272 (cited on page 82)

Orozco Suárez, D., Bellot Rubio, L. R., & del Toro Iniesta, J. C. 2007a, Astrophys. J. Lett., 662, L31 (cited on pages 7 and 117)

Orozco Suárez, D., Bellot Rubio, L. R., del Toro Iniesta, J. C., et al. 2007b, Astrophys. J. Lett., 670, L61 (cited on page 50)

Orozco Suárez, D., Bellot Rubio, L. R., Martínez Pillet, V., et al. 2010a, ArXiv e-prints (cited on page 7)

Orozco Suárez, D., Bellot Rubio, L. R., Vögler, A., & Del Toro Iniesta, J. C. 2010b, Astron. Astrophys., 518, A2+ (cited on pages 7 and 117)

Ortiz, A., Bellot Rubio, L. R., & Rouppe van der Voort, L. 2010, Astrophys. J., 713, 1282 (cited on pages 82, 108, 109, 114, 137, 138, and 140)

Pahlke, K.-D. & Wiehr, E. 1990, Astron. Astrophys., 228, 246 (cited on page 108)

Parker, E. N. 1979, Astrophys. J., 234, 333 (cited on page 82)

Pereira, T. M. D., Asplund, M., & Kiselman, D. 2009a, Astron. Astrophys., 508, 1403 (cited on page 6)

Pereira, T. M. D., Kiselman, D., & Asplund, M. 2009b, Astron. Astrophys., 507, 417 (cited on page 113)

Rayrole, J. 1967, Annales d'Astrophysique, 30, 257 (cited on page 115)

Rees, D. E. & Semel, M. D. 1979, Astron. Astrophys., 74, 1 (cited on page 114)

Rempel, M., Schüssler, M., Cameron, R. H., & Knölker, M. 2009a, Science, 325, 171 (cited on pages 8, 59, 82, and 83)

Rempel, M., Schüssler, M., & Knölker, M. 2009b, Astrophys. J., 691, 640 (cited on pages 8, 82, and 83)

Riethmüller, T. L., Solanki, S. K., & Lagg, A. 2008a, Astrophys. J. Lett., 678, L157 (cited on pages 108, 109, 135, 136, 137, and 141)

Riethmüller, T. L., Solanki, S. K., Zakharov, V., & Gandorfer, A. 2008b, Astron. Astrophys., 492, 233 (cited on pages 86, 87, 91, and 101)

Rimmele, T. 2008, Astrophys. J., 672, 684 (cited on page 82)

Rödberg, H. 1966, Nature, 211, 394 (cited on page 99)

Ruiz Cobo, B. 2007, in Modern solar facilities - advanced solar science, ed. F. Kneer, K. G. Puschmann, & A. D. Wittmann, 287–+ (cited on page 118)

Ruiz Cobo, B. & del Toro Iniesta, J. C. 1992, Astrophys. J., 398, 375 (cited on page 118)

Ruiz Cobo, B. & del Toro Iniesta, J. C. 1994, Astron. Astrophys., 283, 129 (cited on pages 69 and 123)

Rutten, R. 2003, Radiative Transfer in Stellar Atmospheres (Utrecht University lecture notes, 8th edition) (cited on pages 48 and 51)

Rutten, R. J. 1988, in Astrophysics and Space Science Library, Vol. 138, IAU Colloq. 94: Physics of Formation of FE II Lines Outside LTE, ed. R. Viotti, A. Vittone, & M. Friedjung, 185–210 (cited on page 35)

Rutten, R. J. 1999, in Astronomical Society of the Pacific Conference Series, Vol. 184, Third Advances in Solar Physics Euroconference: Magnetic Fields and Oscillations, ed. B. Schmieder, A. Hofmann, & J. Staude, 181–200 (cited on page 33)

Rutten, R. J. 2002, The Journal of Astronomical Data, 8, 8 (cited on page 21)

Rutten, R. J. & Kostik, R. I. 1982, Astron. Astrophys., 115, 104 (cited on page 50)

Rutten, R. J. & Stencel, R. E. 1980, A&A Suppl., 39, 415 (cited on page 32)

Rutten, R. J. & van der Zalm, E. B. J. 1984, A&A Suppl., 55, 143 (cited on page 51)

Rybák, J., Wöhl, H., Kučera, A., Hanslmeier, A., & Steiner, O. 2004, Astron. Astrophys., 420, 1141 (cited on page 58)

Sanchez Almeida, J. & Lites, B. W. 1992, Astrophys. J., 398, 359 (cited on page 127)

Sanchez Almeida, J., Ruiz Cobo, B., & del Toro Iniesta, J. C. 1996, Astron. Astrophys., 314, 295 (cited on pages 118 and 123)

Sánchez Almeida, J., Viticchié, B., Landi Degl'Innocenti, E., & Berrilli, F. 2008, Astrophys. J., 675, 906 (cited on pages 30, 35, 38, and 53)

Sankarasubramanian, K. & Rimmele, T. 2002, Astrophys. J., 576, 1048 (cited on pages 108, 109, 115, and 141)

Scharmer, G. B., Bjelksjo, K., Korhonen, T. K., Lindberg, B., & Petterson, B. 2003, in Society of Photo-Optical Instrumentation Engineers (SPIE) Conference Series, Vol. 4853, Society of Photo-Optical Instrumentation Engineers (SPIE) Conference Series, ed. S. L. Keil & S. V. Avakyan, 341–350 (cited on page 113)

Schlüter, A. & Temesváry, S. 1958, in IAU Symposium, Vol. 6, Electromagnetic Phenomena in Cosmical Physics, ed. B. Lehnert, 263 (cited on page 82)

Schmidt, W. & Balthasar, H. 1994, Astron. Astrophys., 283, 241 (cited on page 108)

Schüssler, M. & Vögler, A. 2006, Astrophys. J. Lett., 641, L73 (cited on pages 8, 59, 82, 83, 84, 85, 86, 94, 101, 108, 123, 124, and 125)

Schüssler, M. & Vögler, A. 2008, Astron. Astrophys., 481, L5 (cited on pages 7, 59, and 83)

Severnyi, A. B. 1965, Soviet Astronomy, 9, 171 (cited on page 82)

Shchukina, N. G. & Trujillo Bueno, J. 1998, Inf. Bull. Ukrainian Astron. Assoc., No. 12, p. 32 - 33, 12, 32 (cited on page 138)

Shelyag, S., Schüssler, M., Solanki, S. K., Berdyugina, S. V., & Vögler, A. 2004, Astron. Astrophys., 427, 335 (cited on pages 7 and 33)

Shelyag, S., Schüssler, M., Solanki, S. K., & Vögler, A. 2007, Astron. Astrophys., 469, 731 (cited on pages 8 and 114)

Sheminova, V. A., Rutten, R. J., & Rouppe van der Voort, L. H. M. 2005, Astron. Astrophys., 437, 1069 (cited on page 36)

Simmerer, J., Sneden, C., Cowan, J. J., et al. 2004, Astrophys. J., 617, 1091 (cited on page 15)

Skumanich, A. & Lites, B. W. 1987, Astrophys. J., 322, 473 (cited on pages 50 and 115)

Sobelman, I. I. 1992, Atomic spectra and radiative transitions (Springer, Berlin) (cited on page 20)

Sobotka, M. 1997, in ASP Conf. Ser., Vol. 118, 1st Advances in Solar Physics Euroconference. Advances in Physics of Sunspots, ed. B. Schmieder, J. C. del Toro Iniesta, & M. Vazquez, 155 (cited on pages 82 and 108)

Sobotka, M., Bonet, J. A., & Vazquez, M. 1992, Astron. Astrophys., 257, 757 (cited on page 100)

Sobotka, M., Bonet, J. A., & Vazquez, M. 1993, Astrophys. J., 415, 832 (cited on page 91)

Sobotka, M., Brandt, P. N., & Simon, G. W. 1997, Astron. Astrophys., 328, 682 (cited on page 86)

Sobotka, M. & Hanslmeier, A. 2005, Astron. Astrophys., 442, 323 (cited on pages 87, 91, and 101)

Sobotka, M. & Puschmann, K. G. 2007, in Modern solar facilities - advanced solar science, ed. F. Kneer, K. G. Puschmann, & A. D. Wittmann, 205 (cited on page 91)

Sobotka, M. & Puschmann, K. G. 2009, Astron. Astrophys., 504, 575 (cited on pages 82 and 86)

Socas-Navarro, H. 2001, in ASP Conf. Ser., Vol. 236, Advanced Solar Polarimetry – Theory, Observation, and Instrumentation, ed. M. Sigwarth, 487 (cited on pages 60, 84, 110, 115, and 118)

Socas-Navarro, H. 2004, Astrophys. J., 614, 457 (cited on page 118)

Socas-Navarro, H., Pillet, V. M., Sobotka, M., & Vázquez, M. 2004, Astrophys. J., 614, 448 (cited on pages 86, 91, 108, 109, 126, 135, 136, and 141)

Socas-Navarro, H., Trujillo Bueno, J., & Ruiz Cobo, B. 2000, Science, 288, 1396 (cited on page 140)

Solanki, S. K. 1986, Astron. Astrophys., 168, 311 (cited on page 37)

Solanki, S. K. 2003, A&AR, 11, 153 (cited on pages 87 and 108)

Solanki, S. K., Barthol, P., Danilovic, S., et al. 2010, Astrophys. J. Lett., 723, L127 (cited on page 2)

Solanki, S. K. & Brigljevic, V. 1992, Astron. Astrophys., 262, L29 (cited on pages 36 and 37)

Solanki, S. K., Rueedi, I., Bianda, M., & Steffen, M. 1996, Astron. Astrophys., 308, 623 (cited on pages 58, 73, and 76)

Solanki, S. K. & Steenbock, W. 1988, Astron. Astrophys., 189, 243 (cited on page 37)

Spruit, H. 1997, Mem. Soc. Astron. Italiana, 68, 397 (cited on page 6)

Spruit, H. C. 1976, Sol. Phys., 50, 269 (cited on page 33)

Spyak, P. R. & Wolfe, W. L. 1992a, Optical Engineering, 31, 1746 (cited on page 91)

Spyak, P. R. & Wolfe, W. L. 1992b, Optical Engineering, 31, 1775 (cited on page 91)

Staath, E. & Lemaire, P. 1995, Astron. Astrophys., 295, 517 (cited on page 32)

Staveland, L. 1970, Sol. Phys., 12, 328 (cited on pages 24 and 99)

Stein, R. F., Lagerfjärd, A., Nordlund, Å., & Georgobiani, D. 2010, Sol. Phys., 34 (cited on page 8)

Stein, R. F. & Nordlund, A. 1998, Astrophys. J., 499, 914 (cited on pages 6, 58, 61, 63, and 77)

Stein, R. F. & Nordlund, Å. 2006, Astrophys. J., 642, 1246 (cited on page 6)

Steiner, O. 2005, Astron. Astrophys., 430, 691 (cited on page 8)

Steiner, O., Franz, M., Bello González, N., et al. 2010, ApJL, in press (cited on pages 63 and 68)

Steiner, O., Grossmann-Doerth, U., Knoelker, M., & Schuessler, M. 1998, Astrophys. J., 495, 468 (cited on page 64)

Stellmacher, G. & Wiehr, E. 1972, Astron. Astrophys., 19, 293 (cited on page 99)

Suematsu, Y., Tsuneta, S., Ichimoto, K., et al. 2008, Sol. Phys., 249, 197 (cited on pages 2, 59, 110, and 162)

Thackeray, A. D. 1937, Astrophys. J., 86, 499 (cited on pages 25 and 30)

Thiessen, G. 1950, The Observatory, 70, 234 (cited on page 82)

Thomas, J. H. & Weiss, N. O. 2004, Annu. Rev. Astron. Astrophys., 42, 517 (cited on page 108)

Thomas, J. H. & Weiss, N. O. 2008, Sunspots and Starspots (Cambridge University Press) (cited on pages 82 and 108)

Tortosa-Andreu, A. & Moreno-Insertis, F. 2009, Astron. Astrophys., 507, 949 (cited on page 8)

Travaglio, C., Gallino, R., Arnone, E., et al. 2004, Astrophys. J., 601, 864 (cited on page 15)

Tritschler, A., Müller, D. A. N., Schlichenmaier, R., & Hagenaar, H. J. 2007, Astrophys. J. Lett., 671, L85 (cited on page 140)

Tritschler, A. & Schmidt, W. 1997, Astron. Astrophys., 321, 643 (cited on page 91)

Unruh, Y. C., Solanki, S. K., & Fligge, M. 1999, Astron. Astrophys., 345, 635 (cited on pages 36, 38, 51, and 52)

van Noort, M. J. & Rouppe van der Voort, L. H. M. 2008, Astron. Astrophys., 489, 429 (cited on page 113)

Vernazza, J. E., Avrett, E. H., & Loeser, R. 1981, Astrophys. J. Suppl., 45, 635 (cited on page 25)

Vince, I. & Erkapic, S. 1998, in IAU Symposium, Vol. 185, New Eyes to See Inside the Sun and Stars, ed. F.-L. Deubner, J. Christensen-Dalsgaard, & D. Kurtz, 459–+ (cited on page 30)

Vince, I., Gopasyuk, O., Gopasyuk, S., & Vince, O. 2005a, Serbian Astronomical Journal, 170, 115 (cited on pages 30 and 31)

Vince, I., Vince, O., Ludmány, A., & Andriyenko, O. 2005b, Sol. Phys., 229, 273 (cited on pages 30 and 32)

Vitas, N. 2005, Memorie della Societa Astronomica Italiana Supplementi, 7, 164 (cited on page 32)

Vitas, N. & Vince, I. 2007, in Astronomical Society of the Pacific Conference Series, Vol. 368, The Physics of Chromospheric Plasmas, ed. P. Heinzel, I. Dorotovič, & R. J. Rutten, 543–+ (cited on page 32)

Vitas, N., Vögler, A., & Keller, C. U. 2010, accepted for publication in A&A, Chapter 4 of this thesis (cited on pages 60 and 108)

Vögler, A. 2003, Three-dimensional simulations of magneto-convection in the solar photosphere (PhD thesis, Göttingen) (cited on page 7)

Vögler, A. 2004, Astron. Astrophys., 421, 755 (cited on pages 7, 38, and 83)

Vögler, A. 2005, Mem. Soc. Astron. Italiana, 76, 842 (cited on page 7)

Vögler, A. & Schüssler, M. 2003, Astronomische Nachrichten, 324, 399 (cited on pages 4, 7, 38, 58, 59, 83, and 109)

Vögler, A. & Schüssler, M. 2007, Astron. Astrophys., 465, L43 (cited on pages 7, 59, and 83)

Vögler, A., Shelyag, S., Schüssler, M., et al. 2005, Astron. Astrophys., 429, 335 (cited on pages 4, 7, 38, 59, 60, 83, and 109)

Wallace, L., Hinkle, K., & Livingston, W. 1998a, An Atlas of the Spectrum of the Solar Photosphere from 13 500 to 28 000 cm^{-}1 (3570 to 7405 Å, Technical Report 98-001 (National Solar Observatory, Tucson) (cited on page 37)

Wallace, L., Hinkle, K., & Livingston, W. 1998b, An atlas of the spectrum of the solar photosphere from 13,500 to 28,000 cm^{-1} (3570 to 7405 Å) (NOAO, Tucson, AZ) (cited on pages 16 and 19)

Wallace, L., Hinkle, K., & Livingston, W. 2000, An atlas of sunspot umbral spectra in the visible, from 15,000 to 25,500 $^{-1}$ (3920 to 6664 Å) (NOAO, Tucson, AZ) (cited on pages 17 and 24)

Watanabe, H., Kitai, R., & Ichimoto, K. 2009a, Astrophys. J., 702, 1048 (cited on pages 91, 92, and 101)

Watanabe, H., Kitai, R., Ichimoto, K., & Katsukawa, Y. 2009b, PASJ, 61, 193 (cited on pages 86, 108, 109, 133, 134, and 141)

Wedemeyer, S., Freytag, B., Steffen, M., Ludwig, H., & Holweger, H. 2004, Astron. Astrophys., 414, 1121 (cited on page 58)

Wedemeyer-Böhm, S. 2008, Astron. Astrophys., 487, 399 (cited on pages 61, 90, 92, and 112)

Wedemeyer-Böhm, S. & Rouppe van der Voort, L. 2009, Astron. Astrophys., 503, 225 (cited on page 8)

Weiss, N. O., Brownjohn, D. P., Hurlburt, N. E., & Proctor, M. R. E. 1990, MNRAS, 245, 434 (cited on page 82)

Wenzler, T., Solanki, S. K., & Krivova, N. A. 2005, Astron. Astrophys., 432, 1057 (cited on page 51)

Wenzler, T., Solanki, S. K., Krivova, N. A., & Fröhlich, C. 2006, Astron. Astrophys., 460, 583 (cited on page 51)

Westendorp Plaza, C., del Toro Iniesta, J. C., Ruiz Cobo, B., et al. 1998, Astrophys. J., 494, 453 (cited on pages 50, 109, and 115)

Wiehr, E. 1994, Astron. Astrophys., 287, L1 (cited on page 108)

Wilson, P. R. 1969, Sol. Phys., 9, 391 (cited on pages 100 and 103)

Wittmann, A. & Schröter, E. H. 1969, Sol. Phys., 10, 357 (cited on page 99)

Yelles Chaouche, L., Cheung, M. C. M., Solanki, S. K., Schüssler, M., & Lagg, A. 2009, Astron. Astrophys., 507, L53 (cited on page 8)

Zaal, G. J., Hogervorst, W., Elie, E. R., Bouma, J., & Blok, J. 1978, J. Phys. B: At., Mol. Opt. Phys., 11, 2821 (cited on page 19)

Zwaan, C. 1965, Sunspot models; a study of sunspot spectra (Drukkerij D. Reidel, Dordrecht) (cited on pages 18 and 91)

Zwaan, C. 1967, Sol. Phys., 1, 478 (cited on page 33)

Zwaan, C., Brants, J. J., & Cram, L. E. 1985, Sol. Phys., 95, 3 (cited on page 108)

Nederlandse samenvatting

De zonnefotosfeer

De zon is een ster. Het is een gele dwerg, een nogal gewone kleine ster halverwege zijn leven. Astronomisch gezien is de zon een ster van spectraalklasse G2 en lichtkrachtklasse V. Ruwweg kan de zon verdeeld worden in het zonsinwendige en de zonsatmosfeer. Het inwendige bestaat uit drie zones: van binnen naar buiten de kern, de stralingszone en de convectiezone. De atmosfeer is verdeeld in de fotosfeer, de chromosfeer en de corona. De zonnewind waait vanuit de corona en vult de gehele heliosfeer, die het gehele zonnestelsel omvat.

De fotosfeer is een dunne schil die het inwendige scheidt van de verdere atmosfeer. De dikte van deze schil is slechts een paar honderd kilometer. Het plasma in de fotosfeer verandert van optisch dicht onderaan in optisch ijl aan de bovenkant, wat fotonen die in de fotosfeer worden uitgezonden in staat stelt de zon te verlaten en daarbij hun energie weg te dragen. De belangrijkste energie-overdracht verandert van zo convectie in de lagen onder de fotosfeer naar straling in de atmosfeer en daarbuiten.

Er zijn twee belangrijke observationele gevolgen van de plotselinge verandering in opaciteit. Ten eerste is de rand van de zichtbare zonneschijf scherp: de straal van de fotosfeer (696 000 km) wordt algemeen beschouwd als de straal van de zon[1]. Ten tweede is bijna alle straling die de zon verlaat afkomstig van de fotosfeer[2]. De temperatuurverdeling van de fotosfeer bepaalt dus de effectieve temperatuur van de zon als ster (5775 K).

De afstand van de aarde tot de zon is gemiddeld 149 miljoen kilometer, of één astronomische eenheid. Vanuit het perspectief van leven op aarde is dit voldoende dichtbij om globale bevriezing te voorkomen, en voldoende ver om condensatie van oceanen mogelijk te maken[3]. Vanuit het perspectief van een astronoom is de zon de enige ster in het universum die voldoende dichtbij staat om directe waarnemingen

[1] Ter illustratie: de verhouding tussen de straal van de zon en de dikte van de fotosfeer is ongeveer tien keer groter dan de verhouding tussen de grootte van een appel en de dikte van zijn schil.

[2] Het gemiddeld gentegreerde stralingsverlies van de fotosfeer is $\approx 6{,}4\times10^{10}$ erg cm^{-2}s^{-1}; Het verlies van alle andere lagen is ongeveer $\sim 6\times10^{6}$ erg cm^{-2}s^{-1}.

[3] De bewoonbare zone (zone waar leven mogelijk is) in het zonnestelsel strekt zich uit tussen de 0.95 en 1.37 astronomische eenheden (Kasting et al, 1993).

toe te staan van details van zijn oppervlak. Voor de hoogst momenteel mogelijke hoekresolutie is de lineaire dimensie van het kleinste detail van de zonnefotosfeer dat direct kan worden waargenomen rond 35 km[4] (Solanki et al. 2010).

Figuur 1.1 toont een opname van de zonnefotosfeer verkregen met de Broadband Filter Imager (BFI) van de Hinode satelliet (Suematsu el al. 2008). Op ieder tijdstip is de fotosfeer grotendeels of volledig bedekt met een granulair patroon van heldere cellen afgewisseld met donkere stroken. Het patroon toont de bovenkant van de convectiezone: het materiaal in de heldere granulen beweegt naar boven; het materiaal in de donkere stroken naar beneden. Het magneetveld dat wordt geassocieerd met dit patroon is zwak (10–100 G, Nordlund et al. (2009)). Evenwel creëert magnetische activiteit in de zon zo nu en dan actieve gebieden die zichtbaar worden in continuümlicht als donkere zonnevlekken en heldere faculae. Het donkerst centrale gebied van een zonnevlek is de umbra; deze is omringd door een helderder penumbra. De grootte van de granulen is rond de 1000 km, terwijl de afmeting van zonnevlekken varieert van enkele duizenden kilometers (kleine zonnevlekken zonder penumbra, zogenaamde poriën) tot enkele honderdduizenden kilometers (voor groepen zonnevlekken in grote actieve gebieden). Op schalen onder 1000 km tonen continuümbeelden de grote verscheidenheid van fijnstructuur, in zowel rustige als in actieve gebieden. De structuur en evolutie van de zonnefotosfeer wordt vooral beheerst door de gasdruk. De lagen hogerop in de atmosfeer, waar de magnetische druk overheersend wordt, tonen meer dynamiek en een nogal verschillende organisatie van het plasma.

De fotosfeer is het best waargenomen deel van de zon, dankzij het grote aantal zichtbaar-licht fotonen dat hun oorsprong vindt in deze laag. Desalniettemin is de straling afkomstig van de fotosfeer ook belangrijk voor het indirect waarnemen van de lagen er onder en er boven. Eén voorbeeld hiervan is het verkrijgen van de structuur van de convectiezone uit de waargenomen variaties van fotosferische spectraallijnen middels de technieken van helioseismologie. Een ander voorbeeld is de reconstructie van het magneetveld in de chromosfeer en corona door extrapolatie van het waargenomen fotosferische magneetveld. In studies van het ruimteweer bestaat de eerste stap natuurlijk uit analyse van fotosferische beelden: veel belangrijke fenomenen vinden hun oorsprong of laten vingerafdrukken achter in de fotosfeer. Figuur 1.2 toont een samengestelde afbeelding van het magneetveld gemeten in de fotosfeer (de gele en blauwe vlakken) en de nagenoeg simultane opname van de buitenste atmosfeer. De bogen in de hogere lagen zijn duidelijk verbonden aan de fotosferische concentraties van het magnetisch veld.

Hoge-resolutie studies van de zonnefotosfeer bieden tevens een richtsnoer voor het bestuderen van de fotosfeer van andere sterren die een vergelijkbare convectiezone hebben.

Hoewel de waarnemingen een enorme hoeveelheid data leveren zijn ook passende algoritmes nodig die de waarnemingsgegevens vertalen naar de fysische parameters die de toestand van de fotosfeer beschrijven. Bovendien hebben we theoretische

[4]Dit is ongeveer de grootte van de provincie Utrecht.

modellen nodig om ons een dieper inzicht te verschaffen in de fysische processen op schalen en in lagen die niet direct waar te nemen zijn. Inversie van waarnemingen en voorwaarts modelleren worden vaak gezien als afzonderlijke manieren van aanpak, maar feitelijk zijn zij complementair zo niet onscheidbaar. Voordat ik de inhoud van dit proefschrift samenvat behandel ik kort de basisconcepten van deze twee aanpakken en geef ik een overzicht van recent er mee verkregen resultaten.

Indeling van het proefschrift

De vijf studies die in dit proefschrift zijn verzameld vormen verschillende voorbeelden van de vergelijking tussen theorie en waarnemingen van de zonnefotosfeer. Elke analyse gebruikt andere modellen en verschillende waarnemingsdiagnostieken. Hoofdstuk 2 is gebaseerd op semi-empirische 1D modellen, terwijl hoofdstukken 3 tot en met 6 gebruik maken van vier verschillende 3D simulaties met de MURaM code (voor een fakkelveld, rustige zon, een geïsoleerde umbra, en een geïsoleerde umbra uitgebreid met de atmosfeer er boven). Het laatste geval (Hoofdstuk 6) is niet eerder gesimuleerd.

In Hoofdstukken 2, 3 en 4 analyseer ik ongepolariseerde spectraallijnen (In I 4511.3 Å, Mn I 5394.7 Å en Fe I 6301.5 Å); in Hoofdstuk 5 continum intensiteiten in het zichtbare en nabij-infrarood; in Hoofdstuk 6 complete Stokes vectoren van Fe I 6301.5 Å en Fe I 6302.5 Å. De studie die in Hoofdstuk 2 wordt gepresenteerd is de enige abundantie-analyse in dit proefschrift. De lijnvorming in Hoofdstuk 3 wordt alleen geanalyseerd voor de (hoge) ruimtelijke resolutie van de simulatie omdat de bestudeerde fenomenen afhangen van de activiteitscyclus en niet direct kunnen worden gereproduceerd met hoge-resolutie simulaties van de fotosfeer. In Hoofdstuk 4 bespreken we synthetische waarnemingen op de SP/SOT Hinode resolutie; in Hoofdstuk 6 voor de resolutie van SP/SOT en ook voor de resolutie van CRISP van de SST. In Hoofdstuk 5 worden de synthetische waarnemingen ruimtelijk en spectraal versmeerd om echte waarnemingen met verschillende telescopen en bij verscheidene resoluties na te bootsen.

Over de zonne-abundantie van indium. De motivatie voor het presenteren van de studie in Hoofdstuk 2 is de grote fotosferische overabundantie van indium (ten opzichte van de waarde in meteorieten) die is gerapporteerd door verscheidene auteurs. We gebruiken semi-empirische 1D modellen van een zonnevlek voor synthese van de enkele spectraallijn van indium in het zonnespectrum. Het synthetische profiel wordt vergeleken met dat in een spectrumatlas van een umbra. Een synthetisch profiel voor de lijn in een umbra waarbij de meteorische abundantie wordt gebruikt past goed bij de atlas nadat kunstmatige vervuiling door strooilicht aan het synthetische profiel wordt toegevoegd. We concluderen dat de waargenomen lijn in het rustige-zon spectrum die gebruikt werd in de voorgaande bepalingen van de indium abundantie foutief aan indium werd toegeschreven, terwijl de feitelijke fotosferische abundantie overeenkomt met de meteorische waarde.

Verklaring van de activiteitsgevoeligheid van Mn I 5394.7 Å. De ongebruikelijke activiteitsgevoeligheid van de fotosferische Mn I 5394.7 Å spectraallijn is het onderwerp van Hoofdstuk 3. Smalle fotosferische lijnen verliezen hun gevoeligheid voor activiteit vanwege hun thermische en granulaire Dopplerverbreding. In het geval van Mn I 5394.7 Å domineert de hyperfijnstructuur echter over deze verbredingsmechanismen en dit verschil verklaart de waargenomen variatie in intensiteit gedurende de zonnecyclus. De activiteitsgevoeligheid van de Mn I lijn is dus zuiver fotosferisch, in tegenstelling tot eerdere hypotheses. Deze conclusie wordt eerst aannemlijk gemaakt met 1D modellen en dan geverifieerd met 3D simulaties van fotosferische fakkels.

Snelle horizontale stromen en hun spectroscopische signatuur. In Hoofdstuk 4 bestuderen we supersone granulaire stromen in een MHD simulatie voor de rustige zon. We synthetiseren Stokes *I* profielen van Fe I 6301.5 Å voor momentopnames bij verschillende gezichtshoeken en selecteren gezichtslijnen waarlangs supersonische horizontale stromen worden bemonsterd. Op de ruimtelijke oplossing van de simulatie tonen de profielen grote variaties in hun asymmetriën, afhankelijk van de gezichtshoek en de specifieke stromingseigenschappen. Op de Hinode resolutie zijn de profielen significant gladder, hoewel verschillende diagnostieken van supersonische beweging meetbaar blijven. De synthetische waarnemingen worden gebruikt om een recentelijk voorgesteld criterium voor de detectie van zulke stromen te testen. We concluderen dat het criterium inderdaad toepasbaar is, hoewel gevoelig voor ad-hoc parameter keuzes.

Observationele diagnostieken van een gesimuleerde umbra. In Hoofdstukken 5 en 6 bestuderen we waarnemingsdiagnostieken middels simulaties van een geïsoleerde umbra. In Hoofdstuk 5 demonstreren we dat de morfologie, de vorm en het contrast van "umbrale stippen" (umbral dots) in de synthetische waarnemingen overeenkomt met recente hoge-resolutie waarnemingen voor het geval van een umbra op het midden van de zichtbare zonneschijf. Weg van het schijfcentrum verandert de morfologie van umbrale stippen afhankelijk van hun oriëntatie ten opzichte van de centrum-rand richting. We voorspellen dat met het scheidend vermogen van toekomstige zonnetelescopen opwaartse stromingen geassocieerd met umbrale stippen waarneembaar zullen zijn in continuümbeelden nabij de schijfrand. Naast de morfologie van umbrale stippen evalueren we ook de centrum-rand variatie van de umbrale intensiteit op verschillende golflengtes. Het resultaat wordt besproken in de context van bestaande waarnemingen.

Het onderzoek dat wordt gepresenteerd in Hoofdstuk 6 werd gemotiveerd door recente waarnemingspogingen om de snelheid en magneetvelden geassocieerd met umbrale stippen te bepalen. Vier verschillende spectropolarimetrische diagnostieken worden toegepast op de synthetische spectra van Fe I 6301.5 Å en Fe I 6302.5 Å die werden geproduceerd met de gesimuleerde umbra. De resultaten van de verschillende diagnostieken worden vergeleken en de optimale strategie voor het meten van

het magneetveld en de snelheid in de umbra wordt aangegeven. In de lagen waar de spectraallijnen gevoelig zijn voor de fysische parameters van de atmosfeer is de structuur van umbrale stippen, zoals die wordt gereconstrueerd met de synthetische waarnemingen, consistent met de simulaties en met de werkelijke waarnemingen. In de lagen er boven en er onder zijn de verkregen waarden echter niet betrouwbaar, zodat de werkelijke structuur van de umbrale stippen in die lagen niet kan worden verkregen uit waarnemingen van de Fe I 6302.5 Å lijnen.

Sažetak na srpsko-hrvatskom

Fotosfera Sunca

Sunce je zvezda. Ono je žuti patuljak, sasvim obična mala zvezda na sredini svog života. Astronomskim rečnikom, njegova spektralna klasa je G2, a klasa luminoznosti V. Sunce grubo možemo da podelimo na sunčevu unutrašnjost i atmosferu. U unutrašnjosti se izdvajaju tri oblasti (od centra ka spolja): jezgro, zona zračenja i zona konvekcije. Atmosfera se deli na fotosferu, hromosferu i koronu. Sunčev vetar razduvava koronu i ispunjava heliosferu koja obavija čitav sunčev sistem.

Fotosfera je uska ljuska koja razdvaja unutrašnjost od spoljne atmosfere. Debljina ove ljuske je svega nekoliko stotina kilometara. Plazma se u fotosferi menja od optički debele (neprozračne) na donjoj granici do optički tanke (prozračne) na gornjoj, omogućavajući fotonima emitovanim u fotosferi da napuste Sunce odnoseći odredjenu energiju sa sobom. Glavni mehanizam prenosa energije se menja na donjoj granici fotosfere. U slojevima ispod to je konvekcija, u slojevima iznad zračenje.

Nagla promena u prozračnosti ima dve važne posledice. Prvo, ivica vidljivog sunčevog diska je veoma oštra: obično se uzima da poluprečnik fotosfere (696 000 km) definiše poluprečnik Sunca[1]. Drugo, gotovo svo zračenje koje napušta Sunce potiče iz fotosfere[2]. Teperature fotosfere odredjuje efektivnu temperaturu zvezde (5778 K).

Srednja razdaljina izmedju Zemlje i Sunca je 149 miliona kilometara ili jedna astronomska jedinica. Iz perspektive života na Zemlji, Sunce je dovoljno blizu da ne dodje do globalnog zaledjivanja i dovoljno daleko da omogući kondenzaciju okeana[3]. Iz perspektive astronoma, Sunce je jedina zvezda u Vasioni dovoljno blizu da omogući neposredna posmatranja detalja na njenoj površini. Sa najvećom trenutno raspoloživom rezolucijom, linearna dimenzija najmanjih detalja sunčeve atmosfere koji se mogu neposredno posmatrati je oko 35 km[4].

Slika 1.1 prikazuje fotografiju sunčeve fotosfere snimljenu pomoću instrumenta

[1] Ilustracije radi, odnos izmedju sunčevog poluprečnika i debljine fotosfere je približno deset puta veći nego odnos izmedju veličine jabuke i debljine njene kore.

[2] U srednjem, ukupni energetski gubici usled zračenja iz fotosfere iznose $\sim 6.4\times10^{10}$ erg cm^{-2}s^{-1}; gubici iz svih drugih slojeva zajedno iznose samo $\sim 6\times10^{6}$ erg cm^{-2}s^{-1}.

[3] Zona sunčevog sistema u kojoj je život moguć prostire se izmedju 0.95 i 1.37 astronomskih jedinica (Kasting et al, 1993).

[4] Linearna dimenzija gradskog jezgra Beograda je oko dva puta manja.

Broadband Filter Imager (BFI) na satelitu Hinode (Suematsu et al. 2008). U svakom trenutku, fotosfera je potpuno ili gotovo potpuno prekrivena svetlim granularnim ćelijama i tamnim trakama izmedju njih. Taj obrazac otkriva sam vrh zone konvekcije: u svetlim granulama materijal se kreće na gore, dok u tamnim trakama pada na dole. Magnetno polje povezano sa granulacijom je slabo (10-100 G, Nordlund et al. (2009)). Medjutim, magnetna aktivnost na Suncu povremeno stvara aktivne oblasti koje se na fotografijama vidi u obliku tamnih pega i svetlih fakula. Najtamnija oblast jedne pege je senka (umbra); ona je okružena svetlijom polusenkom (penumbrom). Veličina granula je oko 1000 km, dok veličina pega varira od nekoliko hiljada kilometara (male pege bez polusenke, takozvane pore) do nekoliko stotina hiljada kilometara (grupe pega u velikim aktivnim oblastima). Na skalama manjim od 1000 km, fotografije otkrivaju veliku raznovrsnost fine strukture, kako u oblastima mirnog Sunca, tako i u aktivnim oblastima. Struktura i evolucija sunčeve fotosfere je pre svega odredjena gasnim pritiskom. Viši slojevi atmosfere u kojima magnetni pritisak postaje dominantan pokazuju složenija kretanja i veoma drugačiju organizaciju plazme.

Fotosfera je očigledno najviše posmatran deo Sunca zahvaljujući broju fotona koji potiču iz ovog sloja. Pored toga, zračenje koji dolazi iz fotosfere takodje je važno za indirektna ispitivanja slojeva koji se nalaze ispod i iznad. Jedan primer je dobijanje informacija o strukturi zone konvekcije na osnovu promena u fotosferskim spektralnim linijama. Odgovarajuća tehnika poznata je kao helioseizmologija. Drugi primer je rekonstrukcija magnetnog polja u hromosferi i koroni na osnovu fotosferskog magnetnog polja odredjenog iz direktnih posmatranja. Ništa manje značajan primer nalazimo u istraživanjima vasionske klime (space weather) gde je prirodni prvi korak proučavanje slika fotosfere: mnogi važni fenomeni imaju svoje korene u fotosferi ili u njoj ostavljaju svoje tragove.

Slika 1.2 pokazuje kompozitni prikaz magnetnog polja izmerenog u fotosferi (žute i plave oblasti) i gotovo istovremenu sliku spoljne atmosfere. Lukovi u višim slojevima očigledno su povezani sa koncentracijama magnetnog polja u fotosferi. Proučavanje sunčeve fotosfere u visokoj rezoluciji takodje predstavlja vodič za proučavanje fotosfera drugih zvezda koje imaju sličnu zonu konvekcije.

I pored ogromne količine raspoloživih posmatračkih podataka, za opis fizičkih uslova u fotosferi je neophodno naći i odgovarajuće algortime za merenje fizičkih veličina na osnovu dostupnih opservabli. Štaviše, za dublje razumevanje fizičkih procesa na skalama i u slojevima koji nisu dostupni direktnim posmatranjima, neophodni su teorijski modeli. Inverzija posmatranja i modeliranje su često vidjeni kao odvojeni pristupi. Ipak, ti pristupi su komplementarni i zapravo nerazdvojivi. Njihovo mesto susreta je poredjenje izmedju sintetičkih posmatranja izračunatih iz teorijskih modela i stvarnih posmatrnja.

Pregled disertacije

Pet studija skupljenjih u ovoj disertaciji predstavljaju različite primere poredjenja teorije i posmatranja sunčeve fotosfere. U svakoj od njih korišćeni su različiti mo-

deli i različite tehnike dijagnostike. Glava 2 zasnovana je na semi-empirijskim 1D modelima, dok su u ostalim glavlama korišćeni rezultati numeričkih 3D simulacija izračunatih uz pomoć MURaM koda (plaža, mirno Sunce, dva modela izolovane umbre sunčeve pege). Simulacija izolovane umbre opisana u Glavi 6 je prvi put predstavljena u ovoj tezi. U Glavama 2, 3 i 4, analizirane su nepolarizovane spektralne linije (In I 4511.3 Å, Mn I 5394.7 Å i Fe I 6301.5 Å); u Gl. 5 kontinualno zračenje u vidljivoj i infracrvenoj oblasti; u Gl. 6 Stokesovi profili linija Fe I 6301.5 Å i Fe I 6302.5 Å. Studija predstavljena u Gl. 2 je jedina studija zastupljenosti nekog elementa u ovoj disertaciji. S obzirom da fenomen proučavan u Gl. 3 zavisi od ciklusa sunčeve aktivnosti i ne može biti neposredno modeliran u simulacijama visoke rezolucije, analiza je ograničena isključivo na formiranje spektralne linije na numeričkoj rezoluciji simulacije. U Gl. 4 diskutovana su sintetička posmatranja na rezoluciji SP/SOT Hinode instrumenta; u Gl. 6 na rezoluciji instrumenata SP/SOT Hinode i CRISP SST. U Gl. 5 sintetička posmatranja su degradirana tako da oponašaju različite generičke teleskope sa različitim ugaonim i spektralnim rezolucijama.

O zastupljenosti indijuma na Suncu. Motiv za ovo istraživanje bila je značajna razlika izmedju fotosferske i meteoritske zastupljenosti indijuma koju su utvrdili različiti autori. Iskoristili smo semi-empirijske 1D modele pege da izračunamo jedinu spektralnu liniju indijuma u sunčevom spektru pretpostavljajući da je fotosferska zastupljenost jednaka meteoritskoj. Izračunati profil linije uporedjen je sa profilom u spektralnom atlasu umbre. Dobro slaganje izmedju izračunatog profila i atlasa postignuto je tek kad je izračunati profil veštački kontaminiran rasejanom svetlošću. Zaključili smo da je linija koja je posmatrana u spektru mirnog sunca i korišćena u ranijim odredjivanjima zastupljenosti pogrešno identifikovana, te da je stvarna fotosferska zastupljenost indijuma konzistentna sa meteoritskom vrednošću.

Objašnjenje osetljivosti Mn I 5394.7 Å na aktivnost. Neobična osetljivost na aktivnost fotosferske linije Mn I 5394.7 Å tema je Glave 3. Uske fotosferske linije gube svoju osetljivost na aktivnost usled toplotnog širenja i širenja usled granularnih kretanja. Nasuprot tome, rezultati predstavljeni u ovoj glavi pokazuju da hiperfina struktura linije Mn I 5394.7 Å nadmašuje druge mehanizme širenja i dovodi do posmatrane varijacije intenziteta sa ciklusom aktivnosti. U analizi su primenjeni 1D modeli, a rezultati su potvrdjeni korišćenjem 3D simulacije fakule. Zaključak je da je osetljivost na aktivnost ove linije neutralnog mangana u potpunosti fotosferska čime su opovrgnute neke ranije hipoteze.

Brzi horizontalni tokovi i njihovi spektroskopski pokazatelji. U Gl. 4, na osnovu MHD simulacije mirnog Sunca, proučavani su horizontalni supersonični tokovi plazme, tipični za pojavu fotosferske granulacije. Iz 3D modela atmosfere izračunati su profili linije Fe I 6301.5 Å i simulirana posmatranja pri različitim heliocentričnim uglovima. Na numeričkoj rezoluciji simulacije, asimetrije izračunatih profili pokazuju velike varijacije u zavisnosti od ugla gledanja i osobina analiziranog toka plazme.

Na rezoluciji Hinodea, profili su značajno glatkiji, ali odredjeni pokazatelji supersoničnih kretanja su i dalje vidljivi. Na tom setu sintetičkih posmatranja testiran je nedavno predloženi kriterijum za detekciju ovakvih tokova plazme. Zaključak je da je predloženi kriterijum zaista primenjiv, ali da je veoma osetljiv na izbor ad-hoc parametara.

Posmatrački pokazatelji simulirane umbre. U Glavama 5 i 6, proučavani su posmatrački pokazatelji izvedeni iz simulacija izolovane umbre sunčeve pege. U Gl. 5, pokazano je da su morfologija, veličina i kontrast umbralnih sjajnih tačaka u simulaciji konzistentni sa osobinama savremenih posmatranja ovog fenomena u visokoj rezoluciji. Posebno je analiziran izgled umbralnih tačaka u centru sunčevog diska i na lokacijama blizu njegovog limba. Blizu limba, morfologija umbralnih tačaka se menja u zavisnosti od njihove orijentacije u odnosu na prečnik diska. Naši rezultati sugerišu da će visoka ugaona rezolucija nove generacije velikih solarnih teleskopa (na primer, EST i ATST) omogućiti identifikaciju strukturnih detalja umbralnih tačaka na snimcima načinjenim blizu limba. Na osnovu iste simulacije procenjena je i centar-limb varijacija intenziteta zračenja umbre u funkciji talasne dužine. Rezultat je razmatran u kontekstu raspoloživih posmatranja.

Istraživanje predstavljeno u Gl. 6 motivisano je nedavnim posmatračkim nastojanjima da se rekonstruiše struktura brzine i magnetnog polja u umbralnim tačkama. Četiri različita dijagnostička pristupa primenjena su na posmatranja u linijama Fe I 6301.5 Å i Fe I 6302.5 Å sintetisanim na osnovu 3D simulacije umbre. Rezultati različitih dijagnostika su medjusobno uporedjeni i predložena je najbolja strategija za merenje magnetnog polja i brzine u umbri. U slojevima gde su spektralne linije osetljive na fizičke parametre atmosfere, struktura umbralnih tačaka rekonstruisana iz sintetičkih posmatranja u skladu je i sa simulacijom i sa stvarnim posmatranjima. U slojevima ispod i iznad, vrednosti dobijene primenom dijagnostika nisu pouzdane: stvarna struktura umbralnih tačaka u tim slojevima ne može biti pouzdano rekonstruisana ukoliko se koriste isključivo posmatranja u dve Fe I 6302 Å linije.

Acknowledgments

First of all, I would like to thank my promotors Christoph Keller and Rob Rutten for giving me the opportunity to work and study in Utrecht. Rob Rutten, my teacher and friend, guided my first steps here. From him I have not only learned about radiative transfer, but also about many aspects of science: about scientific method, importance of the visual representation of results, scientific writing and, the most important, about scientific ethics. However, he was not able to teach me how to solve the mystery of *the* and *a* randomness in my papers. In Christoph Keller I have again found the best of teacher and colleague. He patiently guided me through the thrilling topic of polarized radiation. His questions during our regular meetings often triggered illuminative discussions sending my research into new and exciting directions.

I am very grateful to Alexander Vögler for introducing me to the fascinating world of solar MHD and the MURaM code, and for sharing his knowledge and energy. His insistence on clarity and deep understanding of physical phenomena shaped the large fraction of this thesis. I look forward to collaborating with him in future.

I am indebted to Manfred Schüssler, Frank Verbunt, Rony Keppens and Alex de Koter for reading the entire manuscript and providing numerous comments and corrections.

Special thanks are due to Dan Kiselman for many useful discussions and for leading the Utrecht-Stockholm-Oslo collaboration in solar physics. It was a real pleasure to be a part of the USO-SP team.

Collaboration with Bartolomeo Viticchiè started during the research described in Ch. 3, continued in many various directions and, most importantly, evolved into a true friendship. I am grateful for our endless discussions and all the fun we had together.

Hector Socas-Navarro, Alfred de Wijn and Andréas Asensio Ramos helped me to explore further some of my scientific interests. Although the ideas we discussed and the projects we worked on were not ready in time to appear as a part of this thesis, they strongly influenced my way of thinking.

I am very grateful to Olexa Andriyenko, Michael Van Noort and Sanja Danilović for sharing many personal and scientific experiences. They belong to the very special category of the solar friends.

I am also greatful to many other colleagues from the solar community for helping

me during the work on this thesis. In particular, Instituto de Astrofísica de Canarias on Tenerife, Institutet for solfysik in Stockholm and Università degli Studi di Roma "Tor Vergata" were places of countless interesting and useful discussions.

I would also like to thank the members of the Utrecht solar group with whom I was privileged to collaborate and share the passion for solar physics: Catherine Fischer, Frans Snik, Jorrit Leenaarts, Pit Sütterlin, Julius Koza and many others. Thanks are also due to Jos de Boer with whom I had the pleasure to collaborate on his bachelor thesis and who was so kind to translate the Nederlandse samenvatting for me.

Many thanks to all my fellows at Sterrenkunding Instituut. The institute was always like a big supporting family. My special thanks are due to Esteban Silva Villa and Hector Canovas Cabrera for being such devoted comrades. I am also grateful to my office-mates Sjoers Broersen and Tim van Werkhoven for being great companions and for tolerating me while I was working on the last bits of this manuscript. Many thanks are due to Marion Wijburg for being always so helpful and kind and for making my life easier.

This thesis closes one chapter of my scientific career, so I would like to remember and thank my teachers from the early days who introduced me into the world of science. In order of appearance: Aleksandar Tomić (AD "Rudjer Bošković"), Nenad Golović (OŠ "Braća Ribar"), Nevenka Krstajić, Nevenka Arsenijević-Majer, Violeta Lujić (Prva beogradska gimnazija), Mirjana Vukićević-Karabin, Stevan Djeniže, Trajko Angelov, Olga Atanacković (Beogradski univerzitet). The last but by no means least in this sequence is Ištvan Vince who is responsible for getting me involved in spectroscopy and physics of solar and stellar atmospheres. He was always a great teacher and a unique friend.

I would like to express special thanks to my wife and fellow traveler Nadežda Miketić. Without her love I would be desperately lost and confused. Without her strong support and interest in my work this thesis would not have been completed.

I reserve this last acknowledgment for my parents, Slavica Miletić and Duško Vitas. They receive my deepest gratitude and love for providing me countless opportunities, for respecting my freedom, for supporting my interests, and for not being just great parents, but also my best friends.

Curriculum vitae

I was born in Belgrade, Socialist Federal Republic of Yugoslavia, on December 12th 1974. The place of my birth has not changed its geographical coordinates, but the country kept changing its name and borders. Currently it is called Republic of Serbia.

My passion for astronomy started during a winter school organized by the Astronomical Society "Rudjer Bošković" in 1985. In 1993 I finished the First Belgrade Gymnasium and started my studies of astrophysics at the Department of astronomy of the University of Belgrade. After I graduated in 1999, I got an opportunity to work as a full-time teaching assistant at the same department for the next seven years. During this period I taught many different astronomical courses and wrote several sets of computational problems and lecture notes. In 2003 I got interested in solar physics and spectroscopy and in 2005 I defended my master thesis on the hyperfine structure of the Mn I spectral lines. This work has been done under the supervision of prof. dr. Ištvan Vince. During those years I attended conferences in Rome, Vršac, Terskol, Leuven and Coimbra, and schools at Observatoire Haute Provence and in Tatranska Lomnica. I also visited the Terskol observatory and participated in an unforgettable (but also unsuccessful) solar eclipse expedition.

On November 2006 I started my Ph.D. research at Sterrenkundig Instituut in Utrecht under the supervision of prof.dr. Christoph U. Keller, prof.dr.Robert J. Rutten and dr. Alexander Vögler. My research was supported by Marie Curie Early Stage Research Training Fellowship as a part of the Utrecht-Stockholm-Oslo collaboration in solar physics. During these four years I attended conferences and workshops in Dublin, Freiburg, Catania, Tammsvik and Palermo, schools in Oslo, Abisko, La Palma, Copenhagen and Dwingeloo, and visited the solar institutes in Tenerife, Stockolm, Oslo, Lindau and Rome.

Starting in March 2011, I will be working for the Netherlands Institute for Space Research on the problems of radiative transfer in the Earth's atmosphere and retrieval of the CO abundance.

In ancient days two aviators procured to themselves wings. Daedalus flew safely through the middle air and was duly honoured on his landing. Icarus soared upwards to the sun till the wax melted which bound his wings and his flight ended in fiasco. The classical authorities tell us, of course, that he was only "doing a stunt"; but I prefer to think of him as the man who brought to light a serious constructional defect in the flying-machines of his day. So, too, in science. Cautious Daedalus will apply his theories where he feels confident they will safely go; but by his excess of caution their hidden weaknesses remain undiscovered. Icarus will strain his theories to the breaking-point till the weak joints gape. For the mere adventure? Perhaps partly, this is human nature. But if he is destined not yet to reach the sun and solve finally the riddle of its construction, we may at least hope to learn from his journey some hints to build a better machine.[†]

—Arthur Eddington, from *Stars & Atoms*, Oxford University Press, 1927

[†]The illustration is a detail of *Landscape with the Fall of Icarus* by Pieter Bruegel the Elder or by another artist after Bruegel.